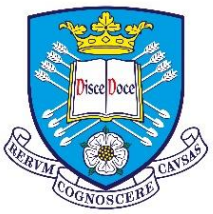

The University Of Sheffield.

Developing zebrafish models to investigate the role of *TCP1* in a rare neurological disease

Kathryn Isabel Adamson

Department of Neuroscience

Faculty of Medicine, Dentistry and Health

University of Sheffield

A thesis submitted to the University of Sheffield in partial fulfilment of the requirements for the degree of Doctor of Philosophy

Submission Date:

March 2020

Statement regarding the reuse of published material in this thesis

The following PhD thesis, entitled 'Developing zebrafish models to investigate the role of *TCP1* in a rare neurological disease', submitted to the University of Sheffield by Kathryn Adamson, contains material that was previously published in the Journal of Medical Genetics, as part of the following review article:

Adamson, K.I., Sheridan, E., Grierson, A.J., 2018. Use of zebrafish models to investigate rare human disease. *J Med Genet* 55, 641–654. (doi:10.1136/jmedgenet-2018-105358)

Article copyright statement: "© Author(s) (or their employer(s)) 2018. No commercial re-use. See rights and permissions. Published by BMJ."

The reuse and adaptation of material from the above article in this thesis are permitted by BMJ under the terms of the author licence. Permission has also been granted by co-authors of the review, Professor Eamonn Sheridan and Dr Andrew Grierson, for the material to be reused in this thesis. Author contributions to the published manuscript were as follows: KIA and AJG planned and wrote the review; KIA created the figures; KIA, ES and AJG edited the document.

Statement from Professor Christopher McDermott, Head of Department of Neuroscience, University of Sheffield:

Given the contributions made by Kathryn Adamson to the above review article, I am happy that the reuse of the material in this thesis is appropriate.

Acknowledgements

I would firstly like to extend my gratitude to Dr Andy Grierson for supervising this project, and for his continued guidance and support over the past few years. I am also grateful to Professor Eamonn Sheridan for co-supervising the project, and for helpful discussions and encouragement.

I would also like to thank the other members of the Grierson lab, as well as Professor Kurt De Vos, Dr Alison Twelvetrees and their teams, for offering useful suggestions and advice at lab meetings over the course of the project.

I am additionally grateful to Dr Ryan MacDonald for teaching me how to cryosection and stain the zebrafish retina and for providing technical advice. I would also like to thank Dr Paweł Łysyganicz for allowing me to use the colour maze he constructed to perform the colour preference assay presented in this thesis. I additionally owe my thanks to the aquarium staff at the Bateson Centre for assistance with zebrafish husbandry.

I would like to acknowledge the support of the Medical Research Council who have funded my project through the Discovery Medicine North (DiMeN) DTP. Thank you to Dr Emily Goodall, Professor Stephen Renshaw, and everybody else from 'Team DiMeN' for providing training opportunities and support throughout my PhD.

Thanks also to my colleagues at the Sheffield Institute for Translational Neuroscience (SITraN) and the Bateson Centre for offering advice, support and friendship over the past few years – it has been a pleasure working with you all.

I could not have got to this point without the support of my wonderful parents and sisters, who have patiently encouraged me from the start. Thank you.

Finally, I would like to dedicate this thesis to my grandmother, Mrs Ellen Speirs (Granny), who has always taught me to strive for the best.

Abstract

Thousands of rare genetic disorders have been reported to date. Together, these conditions affect hundreds of millions of patients worldwide, often presenting with debilitating phenotypes. The identification of rare disease-linked variants has been expedited by modern DNA sequencing technologies; however, poorly understood pathogenesis continues to hamper therapeutic development. We therefore require novel experimental models for these diseases, which may also provide new insights into gene function.

Here, we used the zebrafish to investigate a novel homozygous missense mutation in *TCP1*, encoding a subunit of a highly conserved chaperonin: the TCP1 Ring Complex. The mutation was discovered in three siblings born to consanguineous parents, who developed childhood-onset motor and visual defects with pathology primarily affecting the cerebellum and retina. No other pathogenic *TCP1* mutations have been reported in other families; therefore, we required further evidence to support the pathogenicity of the mutation.

We hypothesised that: a) the *TCP1* missense mutation causes the patients' neurological phenotypes, and b) *TCP1* plays an important role in the cerebellum and retina. To test these hypotheses, we used CRISPR/Cas9 to create one mutant zebrafish line in which the equivalent missense mutation was precisely introduced into zebrafish *tcp1*, and a second mutant line harbouring a frameshift mutation in *tcp1*. We characterised the morphology and behaviour of homozygous mutants to assess the phenotypic consequences of *tcp1* mutations.

Loss of zebrafish *tcp1* caused widespread developmental defects, with abnormalities in tissues implicated in the human disorder and some unrelated tissues. Loss of *tcp1* also resulted in severe motor dysfunction. We did not detect morphological defects or motor dysfunction in zebrafish harbouring the patients' missense mutation; however, they displayed behavioural changes that may be consistent with a colour vision defect. Together, our findings support our hypotheses, but further investigations are required to more robustly confirm the pathogenicity of the novel mutation.

Contents

List of figures

List of tables

List of abbreviations

actb1	-	beta-actin
ANOVA	-	analysis of variance
apaf1	-	apoptotic protease activating factor 1
ARAP1	-	ArfGAP with RhoGAP domain, ankyrin repeat and PH domain 1
ARL6IP1	-	ADP-ribosylation factor-like protein 6-interacting protein 1
AS-PCR	-	allele-specific PCR
Atg5	-	autophagy-related 5
Atg7	-	autophagy-related 7
ATP	-	adenosine triphosphate
ATOH1	-	atonal basic helix-loop-helix transcription factor 1
ATXN3	-	ataxin 3
BBS	-	Bardet-Biedl syndrome
BCIP	-	5-bromo-4-chloro-3-indoyl-phosphate
BLAST	-	Basic Local Alignment Search Tool
bp	-	base pairs
BSA	-	bovine serum albumin
CADD	-	Combined Annotation Dependent Depletion
Cas9	-	CRISPR-associated protein 9
CATSPERG	-	cation channel sperm associated auxiliary subunit gamma
CCT	-	chaperonin containing TCP1
Cdc20	-	cell division cycle protein 20
cDNA	-	complementary DNA
CLPTM1	-	cleft lip and palate transmembrane protein 1
Cobl	-	Cordon-Bleu WH2 repeat protein
CRISPR	-	clustered regularly interspaced short palindromic repeats
CRISPRi	-	CRISPR interference
Ct	-	cycle threshold
CTP	-	cytidine triphosphate
Ctsd	-	cathepsin D
DAPI	-	4′,6-diamidino-2-phenylindole
dCas9	-	catalytically inactive (dead) Cas9
DDD	-	Deciphering Developmental Disorders
d.H_2O	-	distilled water
DIG	-	digoxigenin
DLL3	-	delta-like canonical notch ligand 3
DNA	-	deoxyribonucleic acid
dpf	-	days post-fertilisation
EDTA	-	ethylenediaminetetraacetic acid
eef1a	-	eukaryotic translation elongation factor 1 alpha
ENU	-	*N*-ethyl-*N*-nitrosourea
ERG	-	electroretinogram
EURORDIS	-	European Organisation for Rare Diseases
ExoSAP	-	Exonuclease I and shrimp alkaline phosphatase

EYS - eyes shut homolog
F-actin - filamentous actin
FORGE - Finding of Rare Disease Genes
fps - frames per second
GABA - γ-aminobutyric acid
GBA - glucocerebrosidase
GOLD - Genetic Basis of Learning Disability
GPCR - G-protein coupled receptor
GPAA1 - glycosylphosphatidylinositol anchor attachment 1
GPI - glycosylphosphatidylinositol
gRNA - guide RNA
GTP - guanosine triphosphate
HDR - homology-directed repair
HRM - high-resolution melt
IDT - Integrated DNA Technologies
INL - inner nuclear layer
IPL - inner plexiform layer
IRDiRC - International Rare Diseases Research Consortium
KLHL9 - Kelch-like protein 9
LUT - lookup table
M13F - M13 forward
Map1a - microtubule-associated protein 1a
mRNA - messenger RNA
NBT - nitro blue tetrazolium chloride
NGS - next-generation sequencing
NHEJ - non-homologous end joining
NIH - National Institutes of Health
nt - nucleotide
NTC - no template control
OCT - optimal cutting temperature
ONL - outer nuclear layer
OPL - outer plexiform layer
PAM - protospacer adjacent motif
PBS - phosphate-buffered saline
PBST - 1% Triton X-100 in PBS
PCR - polymerase chain reaction
PFA - paraformaldehyde
PhLP1 - phosducin-like protein 1
PIGG - phosphatidylinositol glycan anchor biosynthesis class G
PNKP - polynucleotide kinase 3’-phosphatase
Plk1 - polo-like kinase 1
PolyPhen-2 - Polymorphism Phenotyping v2
PTF1A - pancreas-associated transcription factor 1a
PTW - 0.1% Tween-20 in PBS
qPCR - quantitative real-time PCR
RFP - red fluorescent protein

RNA	-	ribonucleic acid
RT	-	room temperature
SDS	-	sodium dodecyl sulphate
SHH	-	sonic hedgehog
SIFT	-	Sorting Intolerant From Tolerant
SNAP2	-	Screening for Non-Acceptable Polymorphisms 2
SNP	-	single-nucleotide polymorphism
SSC	-	saline sodium citrate
ssODN	-	single-stranded oligodeoxynucleotide
TALEN	-	transcription activation-like effector nuclease
TCP1	-	T-complex polypeptide 1
TGFβ	-	transforming growth factor-beta
TILLING	-	Targeting Induced Local Lesions in Genomes
TRiC	-	TCP1 ring complex
tRNA	-	transfer RNA
Ttbk2	-	tau tubulin kinase 2
Ucrit	-	critical swimming velocity
UDN	-	Undiagnosed Diseases Network
UDNI	-	Undiagnosed Diseases Network International
UDP	-	Undiagnosed Diseases Program
UTP	-	uridine triphosphate
UV	-	ultraviolet
WDR76	-	WD40-repeat protein 76
ZFIN	-	Zebrafish Information Network
ZFN	-	zinc finger nuclease
zLOST	-	zebrafish long single-stranded DNA template

Chapter 1

Introduction

1.1 The importance of researching rare genetic diseases

Rare diseases often manifest as chronically debilitating illnesses which dramatically decrease life expectancy and quality of life (EURORDIS, 2005). These conditions are individually rare, defined as having a prevalence lower than 1 in 2,000 (Boycott et al., 2013), but over 6,000 distinct rare diseases have been described to date (EURORDIS, 2005). Collectively, these are estimated to affect approximately 30 million people in Europe alone (EURORDIS, 2005), posing a tremendous burden on society (Angelis et al., 2015).

Approximately 80% of rare diseases are genetic (EURORDIS, 2007). The advent of next-generation sequencing (NGS) technology means that the entire human genome can now be sequenced in an unbiased and increasingly cost-effective manner (Figure 1.1), which has been especially advantageous for diagnosing rare genetic diseases. There has been unprecedented discovery of candidate variants for rare conditions in recent years (Koboldt et al., 2013), and several large-scale, collaborative initiatives involving national and international networks of clinical and basic scientific researchers have been established to accelerate the identification and investigation of these rare variants (Table 1.1).

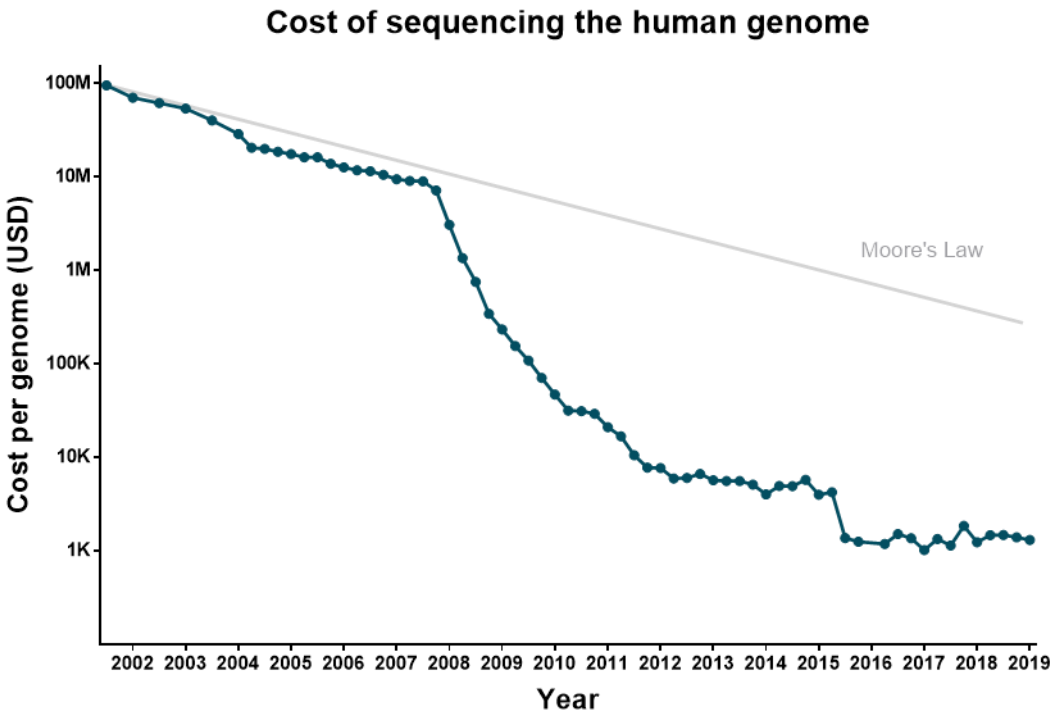

Figure 1.1. The cost of whole genome sequencing has decreased dramatically in recent years. The blue line represents the change in average sequencing cost per human genome over time. The grey line represents hypothetical data based on Moore's Law, which describes a trend of computer power doubling every two years. Technologies are considered to have made extremely good progress if they maintain a pace equivalent to Moore's Law. The decrease in sequencing cost rapidly begins to outpace Moore's Law in 2008, illustrating the transition from traditional Sanger-based sequencing to NGS technology. Data obtained from the National Institutes of Health (NIH) National Human Genome Research Institute (accessible at genome.gov/sequencingcosts).

Table 1.1. National and international collaborative networks aiming to accelerate research into rare genetic diseases

Programme/Network name	Locations	Active years	Aims and specific disease interests	Summary publications
Genetic Basis of Learning Disability (GOLD study)	Based at the Cambridge Institute for Medical Research (UK) Collaborations with Wellcome Trust Sanger Institute (UK), Greenwood Genetic Center (USA), University of Adelaide (Australia) and University of Newcastle (Australia)	2001-2009	Identifying genetic causes of X-linked intellectual disability	(Raymond et al., 2009)
Deciphering Developmental Disorders (DDD) study	Collaborations across 24 regional genetics services (UK and Ireland) and Wellcome Trust Sanger Institute (UK)	2011-2016	Identifying genetic causes of developmental disorders	(Deciphering Developmental Disorders Study, 2017, 2015; Wright et al., 2015)
Finding of Rare Disease Genes (FORGE) Canada Consortium	Network of 21 genetics centres and 3 science and technology innovation centres across Canada, with international collaborations across 17 additional countries	2011-2013	Identifying genes associated with rare monogenic childhood-onset diseases	(Beaulieu et al., 2014)
International Rare Diseases Research Consortium (IRDiRC)	International network of researchers and organisations with an interest in rare disease research	2011-present	Contributing to the development of novel rare disease therapies and the means to uncover the genetic causes of rare diseases	(Dawkins et al., 2017)
Undiagnosed Diseases Program (UDP)/Undiagnosed Diseases Network (UDN)	Network of clinical and scientific sites across the USA, co-ordinated by Harvard Medical School	2008 - present	Accelerating identification of genetic causes of rare diseases, with use of drosophila and zebrafish models to validate candidate genes	(Gahl et al., 2016; Ramoni et al., 2017; Wangler et al., 2017)

Table 1.1 (cont.)

Undiagnosed Diseases Network International (UDNI)	Network of 45 clinical investigators across the globe (23 participating countries in total)	2015 – present	Using collaborative approaches to identify genetic causes for rare diseases and better understand their pathogenesis	(Taruscio et al., 2015)
Solve-RD - Solving the Unsolved Rare Diseases	Network of clinicians, geneticists, translational researchers and rare disease infrastructures across Europe	2018 – present	Using "omics" approaches to identify genetic causes for rare diseases. Implementing a "genetic knowledge web" to share information about rare genotype/phenotype relationships	No summary publications. Full list of publications arising from the initiative available at the Solve-RD website (solve-rd.eu/results/scientific-publications)

(Table adapted from Adamson et al., (2018) under terms of the BMJ author licence)

Despite these advances, treatments for most rare diseases remain scarce (Luzzatto et al., 2015). For 'ultra-rare' diseases, in which a candidate variant has been proposed for only one individual or a handful of individuals from a single pedigree, it can be challenging to validate the pathogenicity of the variant. Moreover, because common disorders have historically taken priority over rare diseases with regard to translational research (Shen et al., 2015), the pathogenic mechanisms that contribute to rare diseases are often unclear, even once a genetic cause has been identified.

Considering the increasing number of candidate variants being identified by NGS, there is a growing need for experimental research into these diseases. These investigations will enable ultra-rare variants to be experimentally validated, facilitating more robust genetic diagnoses. They will also yield insights into the pathophysiology of rare diseases, which could uncover therapeutic targets for these conditions.

Research into rare diseases can also reveal new information about the fundamental pathways governing human biology, which can subsequently improve our understanding of more common disorders (EURORDIS, 2010). For example, Gaucher's disease, a rare

metabolic condition caused by homozygous mutations in the glucocerebrosidase gene (*GBA*), causes deficiency of the β-glucocerebrosidase protein (Brady et al., 1966). Some heterozygous *GBA* variants have also been found to confer risk for the comparatively common neurodegenerative disorder, Parkinson's disease (Goker-Alpan et al., 2004). This genetic link between two clinically disparate diseases has exposed a role for β-glucocerebrosidase deficiency in some forms of Parkinson's disease (Wong and Krainc, 2016). As a result, Phase 2 clinical trials to test the efficacy of ambroxol, a pharmaceutical compound that restores the trafficking and enzymatic activity of β-glucocerebrosidase (Bendikov-Bar et al., 2013), are now underway in patients with Parkinson's disease and Parkinson's disease dementia (NCT02941822; NCT02914366).

1.2 Advantages of studying rare genetic diseases within consanguineous

In the context of medical genetics, a marriage is generally considered to be consanguineous if the couple are second cousins or more closely related (Bittles, 2008; Hamamy, 2012). Children born to consanguineous parents are at increased risk of developing autosomal recessive disorders compared with the general population. This is because they tend to inherit large portions of identical DNA from both of their parents, which makes them more likely to become homozygous for deleterious mutations (Woods et al., 2006). The association between consanguinity and rare inherited congenital disorders was previously explored as part of the 'Born in Bradford' study (Sheridan et al., 2013). The incidence of congenital abnormalities in Bradford is almost double that of the rest of the UK, and children born to parents of Pakistani origin were identified as being at greatest risk of developing these defects. This was attributed to high rates of consanguinity within the Pakistani community in Bradford, with babies born to first cousin parents reportedly being twice as likely to develop congenital abnormalities as those born to non-consanguineous parents (Sheridan et al., 2013).

The roles of many human protein-coding genes remain elusive (Wood et al., 2019). We can gather considerable information about gene function by studying the phenotypes of patients with genetic diseases (Gagliardi et al., 2018), but this approach is not possible for genes that are yet to be linked to human pathology. Consanguineous populations, such as the one in Bradford, offer unique opportunities to investigate the effects of loss-of-function variants that are unlikely to arise in outbred populations. This can provide valuable insights into the functions of these genes in both health and disease (Erzurumluoglu et al., 2016).

1.2.1 Insights into human biology from the study of novel rare disease-linked mutations in consanguineous pedigrees in Bradford

One example of a biological pathway that is now better understood as a result of functional investigations into rare genetic mutations arising in the Bradford population is the glycosylphosphatidylinositol (GPI)-anchored protein biosynthesis pathway. Novel autosomal recessive mutations in the phosphatidylinositol glycan anchor biosynthesis class G gene (*PIGG*) (Makrythanasis et al., 2016) and the glycosylphosphatidylinositol anchor attachment 1 gene (*GPAA1*) (Nguyen et al., 2017) were recently linked to rare congenital disorders in consanguineous pedigrees from Bradford. These genes encode proteins involved in the production of GPI-anchored proteins, which are tethered to the cell surface and play important roles in many biological processes (Nguyen et al., 2017). Patients with mutations in these genes presented with predominantly neurological phenotypes, featuring varying degrees of intellectual disability, cerebellar atrophy, seizures and hypotonia, with further involvement of the skeletal system in patients with *GPAA1* mutations. Additional variants in these genes were independently found to segregate with similar phenotypes in unrelated pedigrees, confirming the pathogenicity of the mutations (Makrythanasis et al., 2016; Nguyen et al., 2017).

The phenotypes of these patients were found to overlap considerably with those of patients with mutations in other components of the GPI-anchored protein biosynthesis pathway (Krawitz et al., 2012; Maydan et al., 2011; Nakashima et al., 2014; Nguyen et al., 2017). The clinical manifestations of most of these disorders are thought to arise from deficient production of, or structural defects in, GPI-anchored proteins (Chiyonobu et al., 2014; Ilkovski et al., 2015; Makrythanasis et al., 2016; Nakashima et al., 2014; Ng et al., 2012; Tarailo-Graovac et al., 2015). The enzyme encoded by *PIGG* is responsible for transiently attaching an ethanolamine phosphate molecule to the GPI anchor before it becomes tethered to its protein; however, the importance of this step of the pathway had previously remained elusive (Makrythanasis et al., 2016). Functional characterisation of the mutations identified in *PIGG* revealed that, unlike in other inherited GPI deficiencies, neither the levels of GPI-anchored proteins, nor their structures, are altered in *PIGG*-deficient cells (Makrythanasis et al., 2016). Thus, the study of these rare *PIGG* mutations has revealed not only that this transient *PIGG*-mediated modification of GPI is important for proper neurodevelopment, but also that the pathogenesis of this spectrum of disorders extends beyond deficient production of GPI-anchored proteins (Makrythanasis et al., 2016).

Contrastingly, the *GPAA1* mutations were found to result in reduced GPI-anchored protein levels (Nguyen et al., 2017). *GPAA1* encodes a subunit of the GPI transamidase complex, which is responsible for attaching GPI anchors to their proteins. Prior to the identification of these mutations, only one other subunit of the transamidase complex, phosphatidylinositol glycan anchor biosynthesis class T (*PIGT*), had been linked to inherited GPI deficiency (Nakashima et al., 2014; Nguyen et al., 2017). A prominent clinical feature shared by patients with mutations in these genes is progressive cerebellar atrophy, suggesting that proper function of the GPI transamidase complex is likely to be especially important for the health and development of the cerebellum (Nguyen et al., 2017). This is further supported by the more recent identification of patients who have mutations in phosphatidylinositol glycan anchor biosynthesis class U (*PIGU*) (another member of the

GPI transamidase complex) and also present with cerebellar abnormalities (Knaus et al., 2019). The identification of these novel rare *GPAA1* mutations has therefore presented a further opportunity to explore the precise contribution of this complex to cerebellar development.

1.3 A novel mutation in *TCP1* as the cause of a childhood-onset neurological disorder

The focus of this thesis is another novel genetic mutation that has been linked to a rare neurological disease within a consanguineous family in Bradford. A homozygous missense variant (cDNA level c.209C>T, protein level p.P70L) in the T-complex polypeptide 1 gene (*TCP1*) was identified by whole-exome sequencing in three siblings born to first cousin parents of Pakistani origin (unpublished findings from the Sheridan group, University of Leeds). These patients presented with mild childhood-onset motor and visual defects, underpinned by pathology of the cerebellum and retina, with some additional evidence of peripheral neuropathy (Table 1.2). The mutation segregates with the phenotype in this family; however, there are currently no published instances of *TCP1* mutations causing similar phenotypes, or any other diseases, in unrelated pedigrees. These patients therefore represent the first direct link between *TCP1* and human disease, and the discovery of this mutation points to a critical role for *TCP1* in the development of specific organs and tissues within the nervous system. This rare disorder therefore presents an opportunity for experimental research that could potentially reveal new information about the processes underpinning development in humans, as well as the pathophysiology of this rare disease.

Table 1.2. Clinical features of patients with the homozygous *TCP1*^{P70L} variant

Affected tissue	Clinical features
Cerebellum	Progressive atrophy of cerebellar vermis and hemispheres
	General clumsiness
	No evidence of typical cerebellar or long tract signs
Retina	Restriction of peripheral visual fields
	Colour vision deficit
	Retinal dystrophy
	Generalised electrophysiological defects of rod/cone photoreceptors
Peripheral nervous system	Pes cavus
	Sensory and motor neuropathy
	Reduced reflexes
	Reduced sensation in lower limbs
	No clear electrophysiological diagnosis

Although it is biologically interesting that this is the first mutation in *TCP1* to be linked to a human disorder, the lack of other published pedigrees with *TCP1* mutations means that the pathogenicity of the mutation cannot be confirmed in the same way as the *GPAA1* and *PIGG* mutations described earlier (Makrythanasis et al., 2016; Nguyen et al., 2017). As the patients with the *TCP1*^{P70L} mutation are very closely related, they are likely to share large homozygous regions of DNA, making it difficult to pinpoint the precise mutation responsible for their phenotypes. The *TCP1*^{P70L} variant has been identified as the most prominent candidate in these patients, since it is not known to exist in any healthy individuals, and computational analyses have predicted it to have deleterious effects upon protein structure and function (Table 1.3). Indeed, *TCP1* is predicted to be extremely intolerant of inactivating mutations according to the Genome Aggregation Database (Karczewski et al., 2019, gnomad.broadinstitute.org/gene/ ENSG00000120438).

However, these predictive measures cannot conclusively prove that the mutation is pathogenic, and we need further evidence to support these predictions.

Table 1.3. Computational predictions of the effects of the *TCP1*^{P70L} variant

Prediction tool	Reference	Score for the P70L mutation	Predicted impact of the P70L mutation
Combined Annotation Dependent Depletion (CADD)	(Rentzsch et al., 2019)	31 (>15 considered deleterious)	Deleterious
Sorting Intolerant from Tolerant (SIFT)	(Vaser et al., 2016)	0.00 (<0.05 considered damaging)	Damaging
Polymorphism Phenotyping v2 (PolyPhen-2)	(Adzhubei et al., 2010)	1.00 (>0.85 confidently predicted to be damaging)	Probably damaging
Screening for Non-Acceptable Polymorphisms v2 (SNAP2)	(Hecht et al., 2015)	77 (>50 considered highly likely to have effect)	Strong likelihood of effect on protein

1.4 Modelling rare genetic diseases

Where it is not possible to confirm the pathogenicity of a mutation by identifying additional, unrelated patients, experimental models of rare genetic diseases can provide convincing support of pathogenicity, reveal information about the functionality of candidate variants, and offer insights into pathophysiological mechanisms (Sunyaev, 2012).

1.4.1 *In vitro* and cell-based models

In vitro and cell-based disease models can be useful for exploring the functional effects of a candidate variant at the protein level. They can be used to investigate whether the mutation affects protein expression and localisation (Cnossen et al., 2014), which are often altered under disease conditions, or to measure the effect of a variant upon protein activity

(Heidari et al., 2015). However, it can be challenging to establish appropriate assays if the variant arises in a gene encoding a protein whose wild-type function is not well characterised. Moreover, experimental findings demonstrating that a novel variant has molecular consequences at the protein level, although supportive of causality, do not necessarily translate to pathogenicity at the whole organism level.

1.4.2 *In vivo* models

For many rare diseases, *in vivo* models are therefore required to confirm the pathogenicity of candidate mutations (Gui et al., 2017; Yuan et al., 2017; Zhang et al., 2014). This is especially important for neurological disorders, where pathologically relevant patient tissue is often inaccessible, and for conditions that manifest with phenotypes like those observed in the *TCP1* patients, involving multiple tissues and cell types. An important caveat is that some mutations may have species-specific effects, so the presence or lack of a phenotype in a model organism must be interpreted carefully. For example, several murine cystic fibrosis models fail to accurately recapitulate key respiratory features of the human phenotype, despite harbouring the pathogenic deletion mutation present in most patients (Colledge et al., 1995; Zeiher et al., 1995).

Besides allowing us to validate candidate mutations, *in vivo* models of rare diseases provide further opportunities to dissect disease mechanisms within a biologically relevant setting, and to explore the phenotypic consequences of therapeutic intervention. It is important that this can be done at scale, considering initiatives such as the 100,000 Genomes Project, which aim to reveal the genetic causes of rare diseases in thousands of patients (Turnbull et al., 2018).

1.4.2.1 Selecting an appropriate in vivo model organism

An *in vivo* model system for a rare genetic disease should have a fully sequenced genome that shares substantial homology with the human genome, and it must also be amenable

to genetic manipulation. Historically, the mouse (*Mus musculus*) has been considered a pre-eminent model for human genetic diseases, owing to its highly conserved mammalian genome and physiological characteristics which bear remarkable similarity to humans (Dow and Lowe, 2012). However, expensive husbandry and small litter sizes mean that the mouse is often not the most practical choice for validating novel candidate genes. This is particularly relevant in the context of large-scale rare disease gene discovery programmes (Table 1.1), which are likely to uncover huge numbers of novel candidate variants that need to be efficiently and cost-effectively validated. Furthermore, the slow *in utero* development of mammalian models often precludes experimental investigations into developmental processes. This can make it more challenging to investigate the pathophysiology of the substantial proportion of rare diseases that manifest during development (EURORDIS, 2007).

Invertebrate models, such as *Drosophila melanogaster* and *Caenorhabditis elegans*, are also commonly used to study human genetic diseases (Moulton and Letsou, 2016; Silverman et al., 2009). These models are far cheaper and more amenable to experimental manipulation, and they reproduce more rapidly than mice, in much greater numbers (Markaki and Tavernarakis, 2010; Pandey and Nichols, 2011). They are therefore better suited to the experimental validation of large numbers of candidate genes; however, because they are less evolutionarily related to humans, fundamental differences in their genetics and physiology can make them less biologically relevant for studying the pathophysiological mechanisms of human diseases.

1.5 The zebrafish as an emerging model system for rare genetic diseases

The zebrafish (*Danio rerio*) has recently entered the spotlight as an increasingly popular model organism for translational research into human genetic diseases. As a lower vertebrate, the zebrafish uniquely combines many of the genetic and physiological advantages of mammalian models with the high-throughput capabilities and experimental

manipulability associated with invertebrate models (Gama Sosa et al., 2012). This is reflected in the growing number of biomedical research publications featuring zebrafish (Figure 1.2). The next section of this chapter will highlight the key characteristics that make the zebrafish an attractive model system for the study of rare genetic diseases, with a focus on features that are particularly relevant to the *TCP1*-linked disorder.

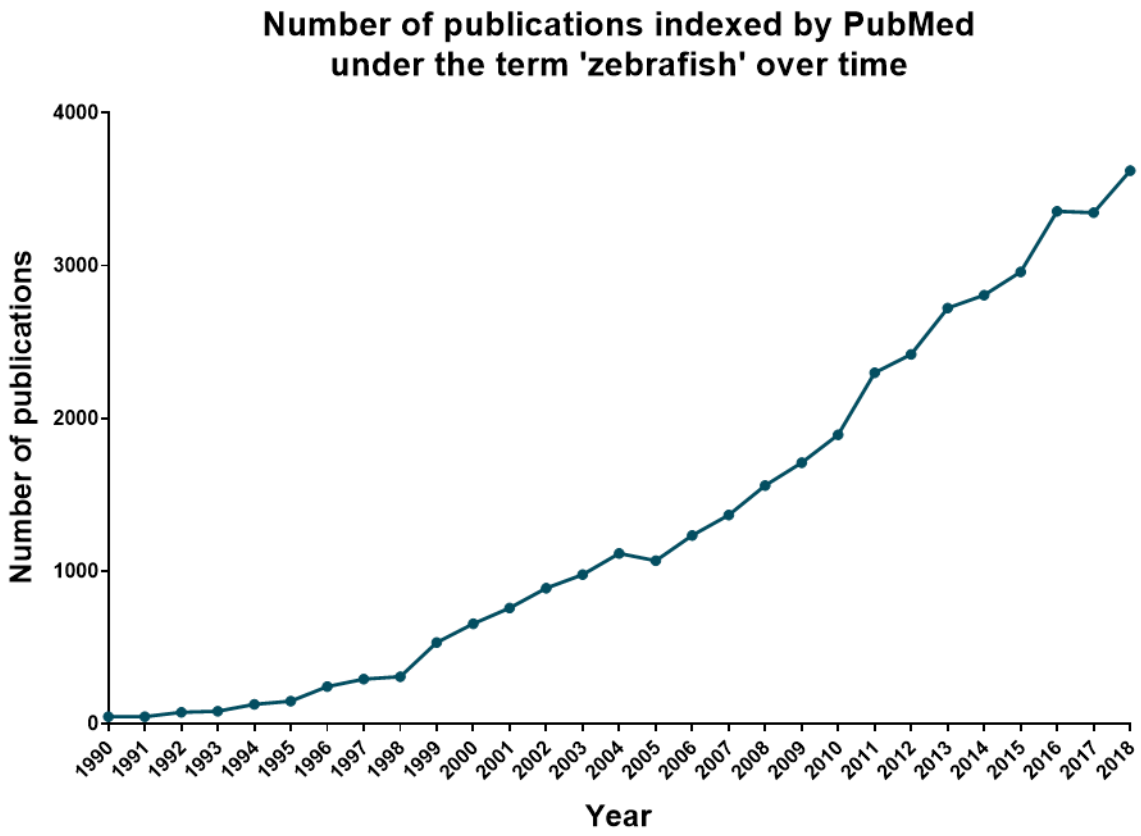

Figure 1.2. The use of zebrafish in biomedical research has been rising since the early 1990s. The line graph shows the number of publications indexed by PubMed under the term “zebrafish” each year between 1990 and 2018. Raw data obtained from Medline Trend (http://dan.corlan.net/medline-trend.html). Figure adapted from Adamson et al. (2018), under terms of the BMJ author licence.

1.5.1 Advantages of the zebrafish as a tool for studying developmental disorders

Prior to its use as a human disease model, the zebrafish gained popularity among developmental biologists as a model system for studying the genetics of vertebrate development (Driever et al., 1994). Zebrafish embryos develop rapidly and *ex utero*, with morphogenesis of most of their major organ systems complete within 48 hours of fertilisation (Kimmel et al., 1995) (Figure 1.3). These features, combined with their optical transparency as embryos, and the array of reporter lines and imaging techniques that are available for visualising developmental and physiological processes (Kamei et al., 2010; Langenau et al., 2004; Vacaru et al., 2014), make the zebrafish a powerful tool for investigating fundamental developmental processes. These features are also advantageous for rare disease research; three-quarters of rare diseases, including the disorder linked to the novel *TCP1* mutation, arise during childhood and 30% of rare disease patients do not survive past their fifth birthday (EURORDIS, 2007). Perturbed developmental processes are therefore likely to contribute to the pathogenesis of many of these conditions, and we can harness the utility of the zebrafish as a developmental model to study how these processes are affected by rare disease-linked mutations (Varga et al., 2018; Veldman and Lin, 2008).

1.5.2 Advantages of the zebrafish as a tool for studying genetic diseases

Although we are less evolutionarily related to the zebrafish than to mammalian models, the zebrafish genome still shares considerable homology with the human genome. Zebrafish orthologues have been identified for approximately 70% of human genes (Howe et al., 2013), providing scope for using the zebrafish to model human disorders linked to a huge number of genes.

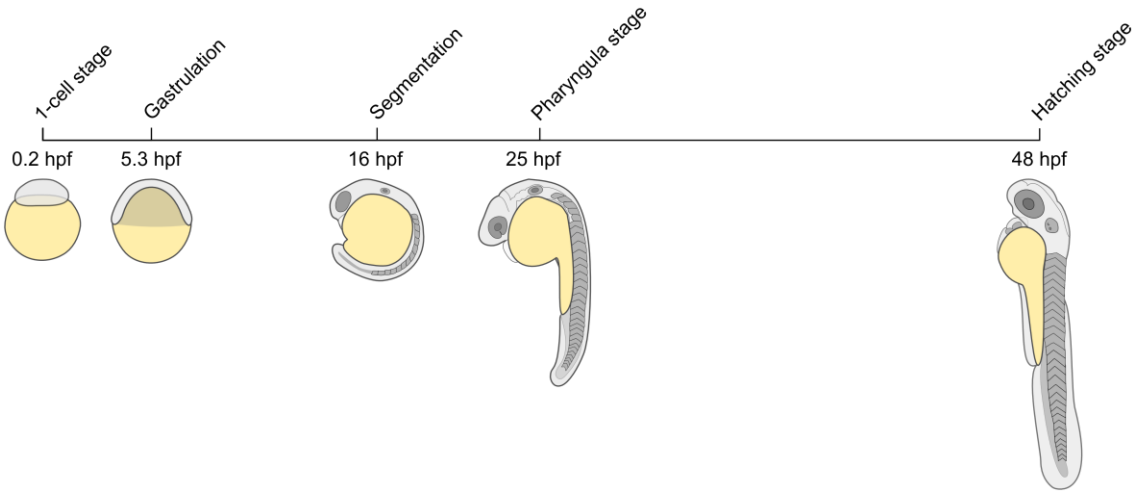

Figure 1.3. Developmental timeline of the embryonic zebrafish. Schematic illustration of the rapid embryonic development of a zebrafish embryo during the first 48 hours following fertilisation. Illustrations and developmental timeline based on Kimmel et al. (1995).

Still, it is important to consider the evolutionary relationship between specific human genes of interest and their zebrafish orthologues before using the zebrafish to model pathogenic human mutations. Almost half of human genes with a zebrafish orthologue have a 'one-to-one' relationship with their zebrafish counterpart, meaning that only one zebrafish orthologue is known to exist for these genes (Howe et al., 2013). However, after the teleost lineage diverged evolutionarily from other vertebrates, the zebrafish underwent a whole genome duplication event (Glasauer and Neuhauss, 2014). This means that for some human genes, multiple zebrafish orthologues exist (i.e. a 'one-to-many' relationship) (Howe et al., 2013). This can complicate the study of loss-of-function mutations, as paralogous genes that have retained similar or identical functions are sometimes able to compensate for these mutations and mask relevant phenotypes (She et al., 2019).

Provided that these limitations are taken into consideration, the zebrafish remains an excellent tool for modelling human genetic diseases (Santoriello and Zon, 2012). The utility of the zebrafish as a genetic model is further enhanced by its genetically tractability, which enables its genome to be manipulated to model human mutations of interest. Several tools are currently available to accomplish this; these are continuously being developed and optimised (Sassen and Köster, 2015), and are discussed in further detail later in this chapter.

1.5.3 Physiological conservation between humans and zebrafish

As well as considering the conservation of the gene of interest, it is also important to evaluate whether the tissues affected by a disease are sufficiently conserved in the zebrafish to allow phenotypic aspects of the human condition to be accurately recapitulated. The zebrafish is more distantly removed from humans in terms of its anatomy and physiology than mammalian models, and this can present challenges when investigating genetic diseases affecting anatomical structures that are absent in fish, such as the lungs (Santoriello and Zon, 2012). Even so, the basic vertebrate architecture of the

zebrafish enables the simplified study of disease in numerous organ systems and structures that are common to both zebrafish and humans. For example, the zebrafish has successfully been used to model genetic diseases affecting the human nervous (Chapman et al., 2013), visual (Zhang et al., 2016), cardiovascular (Smith et al., 2009), renal (Mangos et al., 2010) and muscular systems (Majczenko et al., 2012), among others.

1.5.3.1 General nervous system conservation between humans and zebrafish

In the context of the novel neurological disorder that we are investigating here, it is particularly important to consider the conservation of the nervous system. The organisation of the zebrafish nervous system broadly resembles that of other vertebrates, comprising a central nervous system, composed of a brain and spinal cord, which is connected to a network of peripheral nerves. These peripheral nerves relay information between the central nervous system and the rest of the body to control motor and sensory activities (Bally-Cuif and Vernier, 2010).

Many human brain regions have structural homologues in the zebrafish (Figure 1.4), although the zebrafish brain does lack some of the complexity of the human brain. This is most obvious within the telencephalon (Kozol et al., 2016), which underwent a significant expansion during evolution, giving rise to the elaborate mammalian neocortex involved in many higher order human brain functions (Briscoe and Ragsdale, 2019).

Nevertheless, many of the key neurotransmitter pathways (Chen et al., 2010; Panula et al., 2006) and neural circuits (Hashimoto and Hibi, 2012; Kozol et al., 2016) that underpin brain function in humans have been found to be conserved in zebrafish. Moreover, the reduced complexity of the zebrafish nervous system is advantageous for experimental applications, providing a simplified platform for studying how human disease-linked mutations affect conserved features of vertebrate neurodevelopment (Kozol et al., 2016).

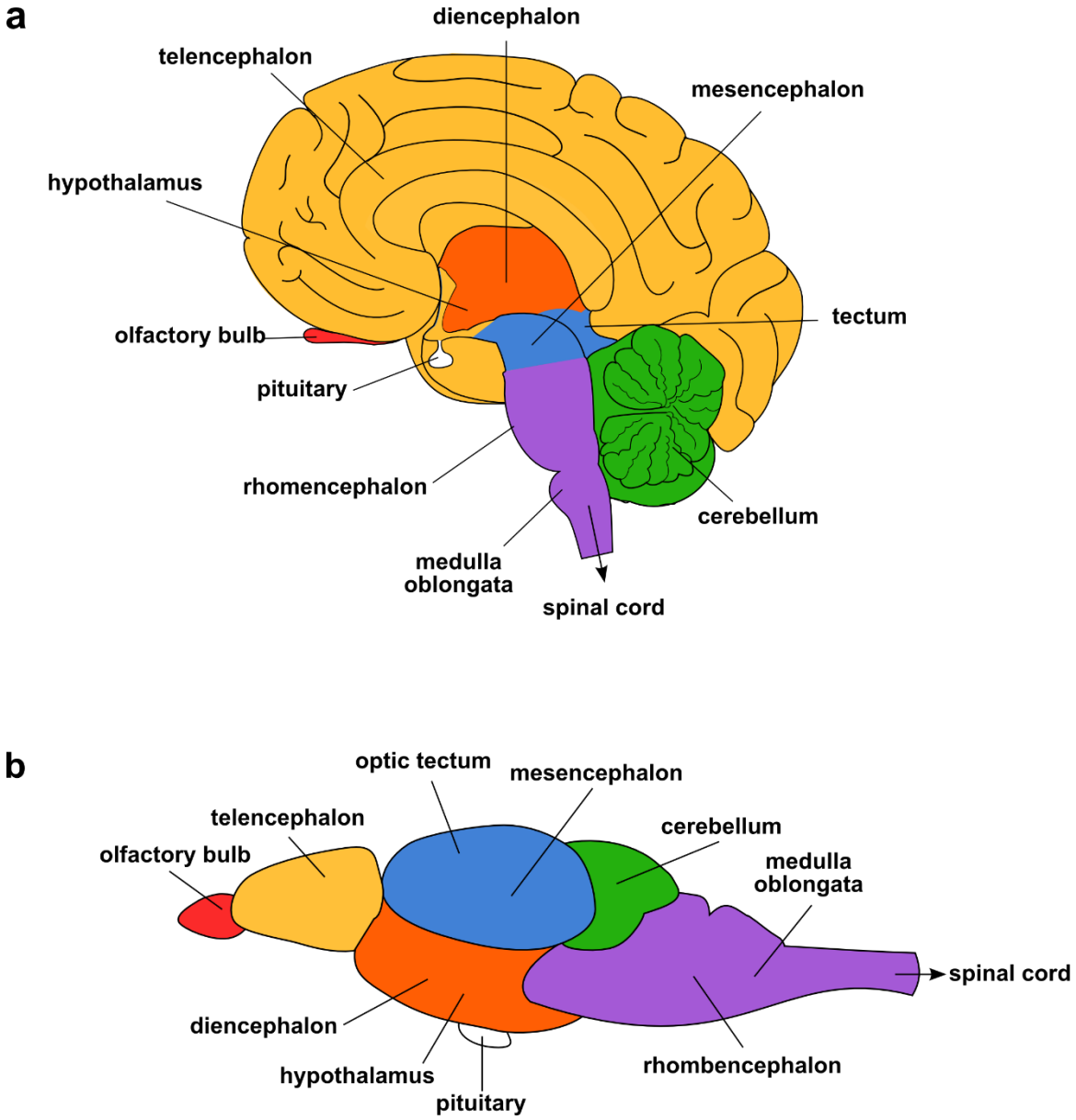

Figure 1.4. Structural homology between the human and zebrafish brain. Schematic representations of (**a**) the adult human brain and (**b**) the adult zebrafish brain (zebrafish brain structure based on Wullimann et al., (1996), colour-coded to highlight regions of homology between the two species (illustrations not to scale).

1.5.3.2 Conservation of the cerebellum between humans and zebrafish

One of the key phenotypic features of the human *TCP1*-linked disorder is cerebellar atrophy. The vertebrate cerebellum is responsible for integrating sensory and motor information to enable fine control over motor coordination and learning (Manto et al., 2012), and it also plays a role in cognition and processing of emotions (Schmahmann, 2019; Strata, 2015).

In mammals, the outer surface of the cerebellum has a distinctive appearance, with a highly folded cerebellar cortex formed of many individual structures called folia (Figure 1.5ai). These folia are arranged in groups, dividing the cerebellum more broadly into the anterior lobe, the posterior lobe and the flocculonodular lobe, which are distributed across two paired lateral hemispheres and an unpaired medial region called the vermis (Lai, 2010).

The zebrafish cerebellum is substantially less morphologically complex; it comprises the corpus cerebellum (or main body of the cerebellum) which extends anteriorly to form the valvula cerebelli, and the vestibulolateral lobe, located posteriorly to the corpus cerebellum. In contrast to the intricately folded cortex of the human cerebellum, the main body of the zebrafish cerebellum is formed of only a single, simple folium (Figure 1.5aii) (Bae et al., 2009).

Despite these gross structural differences, the cellular organisation within the cerebellum of humans and zebrafish remains extremely well conserved (Figure 1.5b) (Bae et al., 2009; Roostaei et al., 2014). Both share a characteristic, three-layered cortex, composed of an inner layer containing the granule cells, which are the most abundant neurons in the vertebrate brain; a middle layer containing the cell bodies of the Purkinje neurons; and an outer molecular layer, which is predominantly made up of granule cell axons and the dendritic arbours of Purkinje cells (Bae et al., 2009; Roostaei et al., 2014).

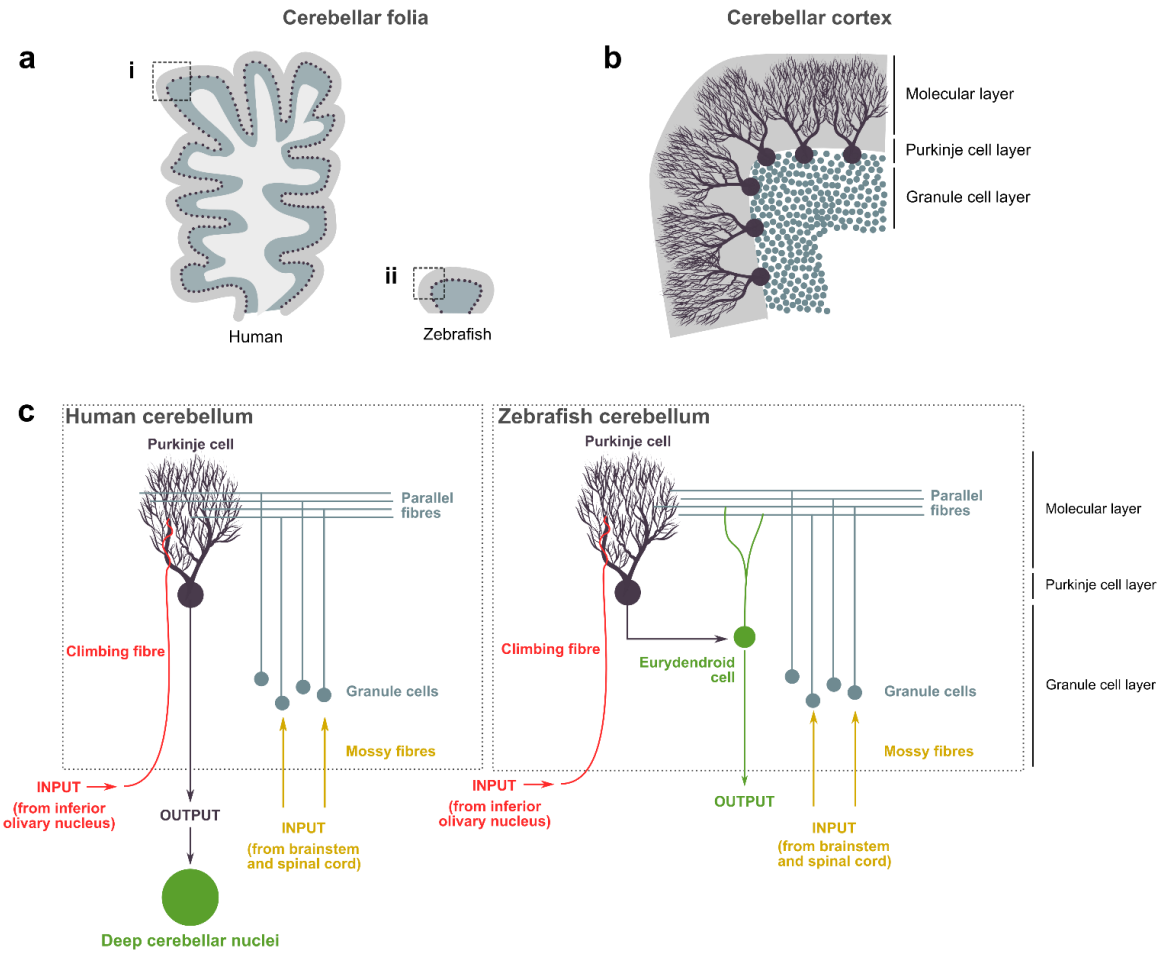

Figure 1.5. Comparative neuroanatomy and microcircuitry of the cerebellum in humans and zebrafish. (**a**) Schematic diagram of a sagittal cross-section through (**i**) a single human cerebellar folium and (**ii**) the zebrafish corpus cerebellum. (**b**) Schematic representation of the layered cellular organisation within the vertebrate cerebellar cortex (corresponding to regions outlined by black dashed boxes in **ai** and **aii**). (**c**) Simplified schematic overview of the cerebellar microcircuitry in humans and zebrafish.

In addition to this shared cellular organisation, much of the basic neuronal circuitry that underpins cerebellar function is also conserved between humans and zebrafish (Figure 1.5c) (Bae et al., 2009; Roostaei et al., 2014). Both receive their primary cerebellar inputs via the climbing fibres, which project from the inferior olivary nucleus to form excitatory synapses with Purkinje cell dendrites, and the mossy fibres, which project from the brainstem and spinal cord to form excitatory synapses with granule cells. The granule cells then transmit these signals to Purkinje cells by forming excitatory synapses via their parallel fibres. In humans, Purkinje cells form the sole output of the cerebellar cortex (Roostaei et al., 2014), sending inhibitory axonal projections to the deep cerebellar nuclei, where information is then passed to the rest of the motor system. Contrastingly, the zebrafish cerebellum does not contain deep cerebellar nuclei (Heap et al., 2013). Zebrafish Purkinje cell axons instead form local synapses with eurydendroid cells, which appear to be functionally homologous to the mammalian deep cerebellar nuclei and form the main output of the zebrafish cerebellum (Heap et al., 2013).

Human and zebrafish cerebella also differ slightly in their development. In both species, Purkinje cell precursors are specified at the ventricular zone by pancreas-associated transcription factor 1a (*PTF1A*) expression (Pascual et al., 2007), and granule cells are specified at the rhombic lip by transforming growth factor-beta (TGFβ)-induced expression of atonal basic helix-loop-helix transcription factor 1 (*ATOH1*) (Ben-Arie et al., 1997). However, during human cerebellar development, granule cell precursors subsequently migrate to form a structure known as the external germinal layer, where they undergo a round of sonic hedgehog (SHH)-dependent proliferation before migrating inwards, past the Purkinje cells, to form the granule cell layer (Haldipur et al., 2012). This SHH-dependent proliferation step is thought to regulate the larger size and complex foliation seen in the cerebella of humans and other amniotic species (Corrales et al., 2006).

In contrast, the zebrafish lacks an external germinal layer, and thus does not exhibit this second SHH-dependent proliferation step (Chaplin et al., 2010). This is worth considering

in the context of modelling human disease, as defects in SHH signalling in the external germinal layer have been proposed to play a role in the pathology of human disorders such as Joubert syndrome and Meckel syndrome (rare hereditary ciliopathies which manifest with defects in cerebellar development), and medulloblastoma (a type of paediatric brain cancer originating in the cerebellum) (Aguilar et al., 2012; Butts et al., 2014). For disorders such as these, it may be more appropriate to use mammalian models to investigate cerebellar pathophysiology.

Nevertheless, the conserved features of cerebellar anatomy, function and development between humans and zebrafish have already proved valuable for modelling aspects of several disorders affecting the human cerebellum (Akizu et al., 2015; Burns et al., 2018; Kasher et al., 2011; Namikawa et al., 2019).

1.5.3.3 Conservation of the retina between humans and zebrafish

Another prominent clinical feature of the *TCP1*-linked disorder is visual dysfunction, underpinned by retinal dystrophy and electrophysiological abnormalities. The vertebrate retina, though located in the eye, is an extension of the central nervous system (Purves et al., 2001). Its primary function is to transduce the light that enters the eye into electrochemical signals that are sent to visual centres in the brain for processing (Mannu, 2014).

The cellular organisation of the retina is highly conserved among vertebrates (Amini et al., 2018), with a laminar structure made up of three distinct nuclear layers, which contain the same neuronal cell types in both humans and zebrafish (Figure 1.6) (Angueyra and Kindt, 2018; Richardson et al., 2017). The most apical layer, the outer nuclear layer (ONL), is occupied by the cell bodies of the photoreceptors. These cells are directly responsible for phototransduction: the signalling cascade through which a photon is transformed into an electrical signal that can be transmitted to the brain. This specifically takes place in the photoreceptor outer segments. The outer segments are specialised sensory cilia that

contain light-absorbing G-protein coupled receptors (GPCRs), known as visual pigments, as well as other biochemical machinery involved in the phototransduction cascade (Khanna, 2015).

Following phototransduction, signals are passed to the inner nuclear layer (INL), which contains the cell bodies of three classes of retinal interneuron: the bipolar cells, the amacrine cells and the horizontal cells. Finally, the signals reach the ganglion cell layer and travel to the brain via the optic nerve, which is predominantly made up of ganglion cell axons. These three nuclear layers are spatially separated by the outer and inner plexiform layers (OPL and IPL), which contain the synapses between the photoreceptors and retinal interneurons, and the retinal interneurons and ganglion cells, respectively (Amini et al., 2018). In the zebrafish, the laminae of the retina are fully patterned by 3 days post-fertilisation (dpf) (Avanesov and Malicki, 2010), providing a platform for rapidly assessing the effects of mutations on vertebrate retinal development.

With regard to the defects associated with the *TCP1*-linked disorder, we are particularly interested in the conservation of photoreceptors between the two species. In both humans and zebrafish, the retina contains a single type of rod photoreceptor (Kefalov, 2011; Morris and Fadool, 2005); these cells are highly sensitive to light and are involved in discriminating light from dark and detecting form and movement, playing a particularly important role in peripheral and dim-light vision (Hoon et al., 2014).

The second major class of photoreceptor found in the vertebrate retina is the cone cell, which mediates colour vision (Kefalov, 2011; Meier et al., 2018). Humans and zebrafish both possess several cone subtypes. These are defined by the specific visual pigments that they express and their sensitivity to different wavelengths of light (Figure 1.7) (Meier et al., 2018; Zhang et al., 2019). Humans are capable of trichromatic vision, which is mediated by three distinct cone subtypes: S-, M- and L-cones. These subtypes are sensitive to short (blue), medium (green) and long (red) wavelengths, respectively (Zhang et al., 2019).

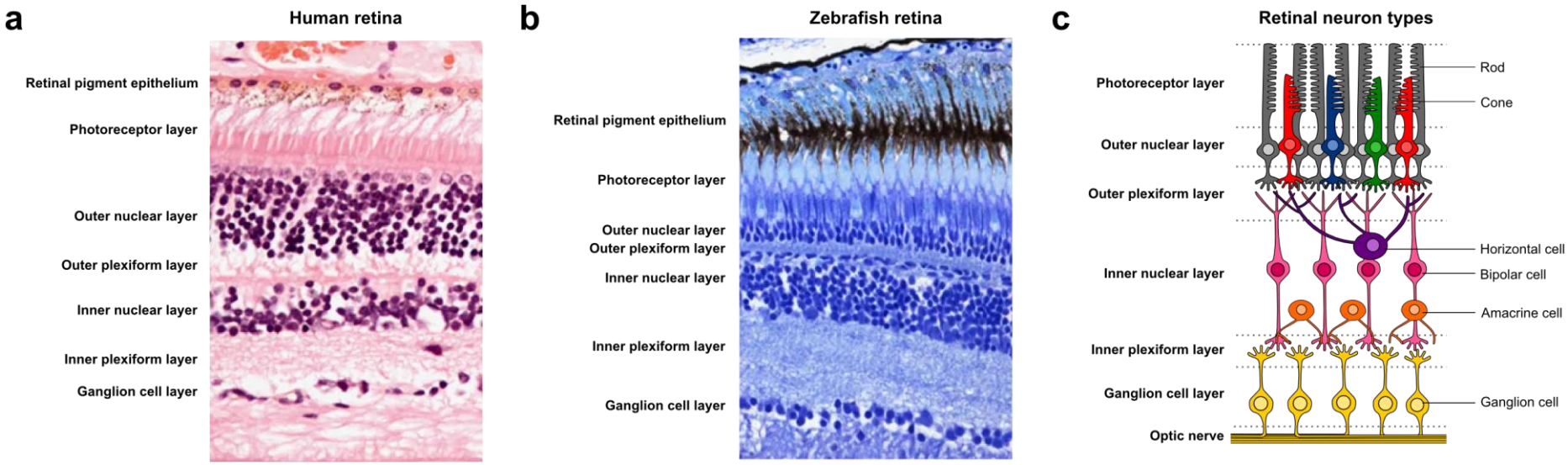

Figure 1.6. Conserved cellular organisation between the human retina and the zebrafish retina. (**a**) Histological section through the human retina. (**b**) Histological section through the zebrafish retina. (**c**) Schematic illustration of the organisation of individual cell types within the vertebrate retina. Images in (**a**) and (**b**) were adapted from Richardson et al. (2017), with permission from Springer Nature.

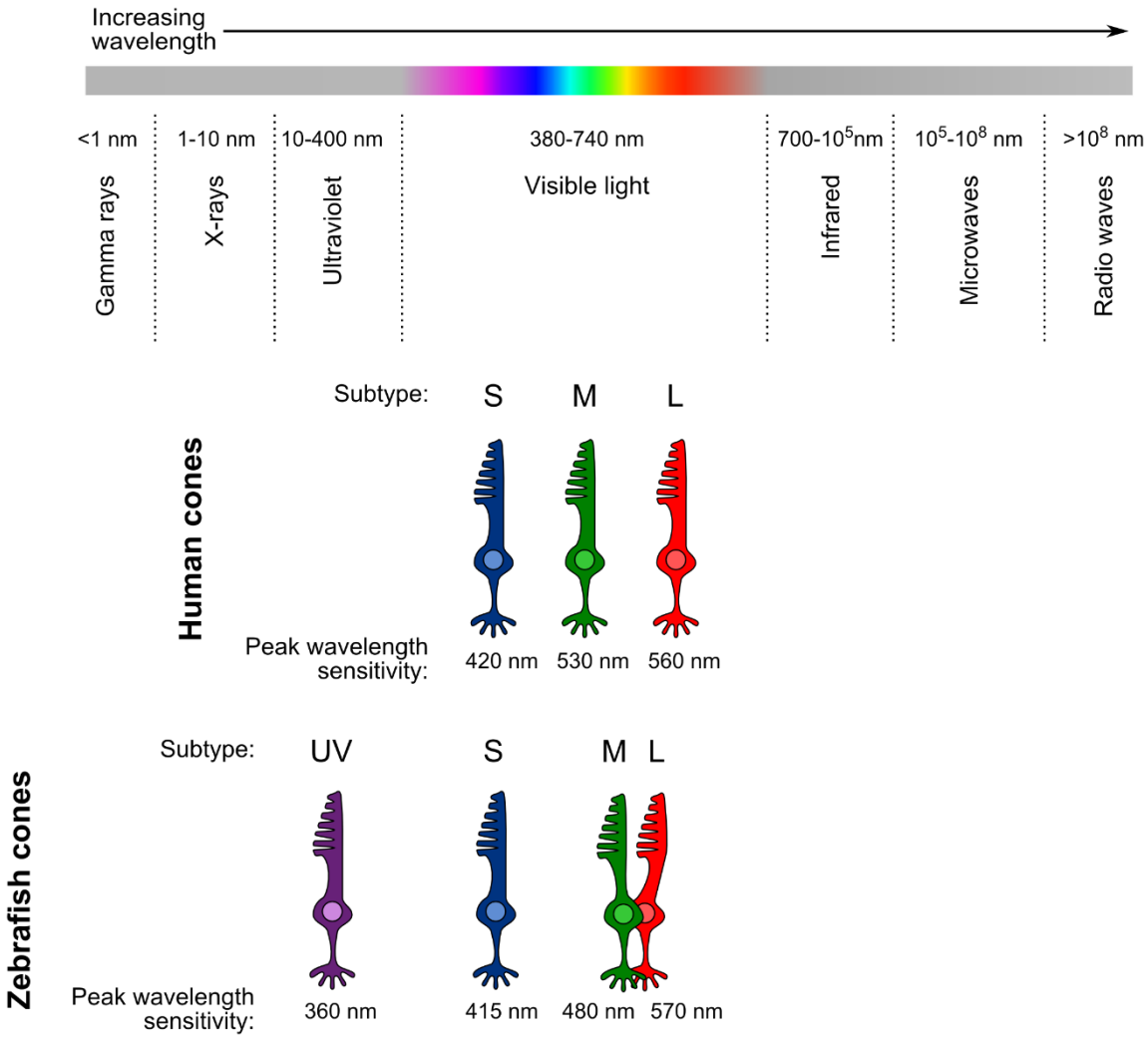

Figure 1.7. Comparison of cone photoreceptor subtypes in humans and zebrafish. Schematic representation of the electromagnetic spectrum, highlighting the peak wavelength sensitivities of the various subtypes of cone cell in the human and zebrafish retinae.

The zebrafish retina also contains S-, M- and L-cones with similar wavelength sensitivities to their human counterparts (Angueyra and Kindt, 2018); however, zebrafish are tetrachromats and possess a fourth cone subtype, which enables them to detect wavelengths in the ultraviolet (UV) range (Angueyra and Kindt, 2018). Notably, the green- and red- sensitive cones of the zebrafish retina are found in a paired configuration (Meier et al., 2018), consisting of a primary member (the L-cone) and an accessory member (the M-cone); however, the M- and L-cones of the human retina are not paired.

The relative abundance and arrangement of these photoreceptors within the retina also differs between zebrafish and humans (Kostic and Arsenijevic, 2016). The human retina is hugely rod-dominated, but contains a central region called the fovea, where most cone cells reside (Figure 1.8). The fovea is the most important component of the human retina for day-to-day visual tasks, enabling high-acuity central vision (Kostic and Arsenijevic, 2016).

Like humans, zebrafish are diurnal and perform most of their visual tasks during the day (Iribarne, 2019). However, the zebrafish retina is slightly cone-dominated, and their cones and rods are arranged in a regular mosaic pattern throughout the retina (Figure 1.8) (Avanesov and Malicki, 2010). This arrangement offers the zebrafish a unique advantage as an animal model of human disease, in that the overall composition of the zebrafish photoreceptors reflects the cone-rich fovea which is required for important visual tasks in humans (Iribarne, 2019). This contrasts with nocturnal species such as the mouse, which has a rod-dominated retina and performs most of its visual tasks at night, making it a less useful tool for studying cone-related human visual phenotypes (DuVal and Allison, 2017), such as the colour blindness observed in patients with the novel *TCP1* mutation.

These conserved features of the zebrafish retina, and the fact that it possesses counterparts for the full complement of photoreceptors that govern the most important aspects of visual function in humans, have already proved advantageous for studying the

pathophysiology of mutations linked to several human retinal disorders (Angueyra and Kindt, 2018; Dona et al., 2018; Jin et al., 2014; Lu et al., 2017; Oura et al., 2018).

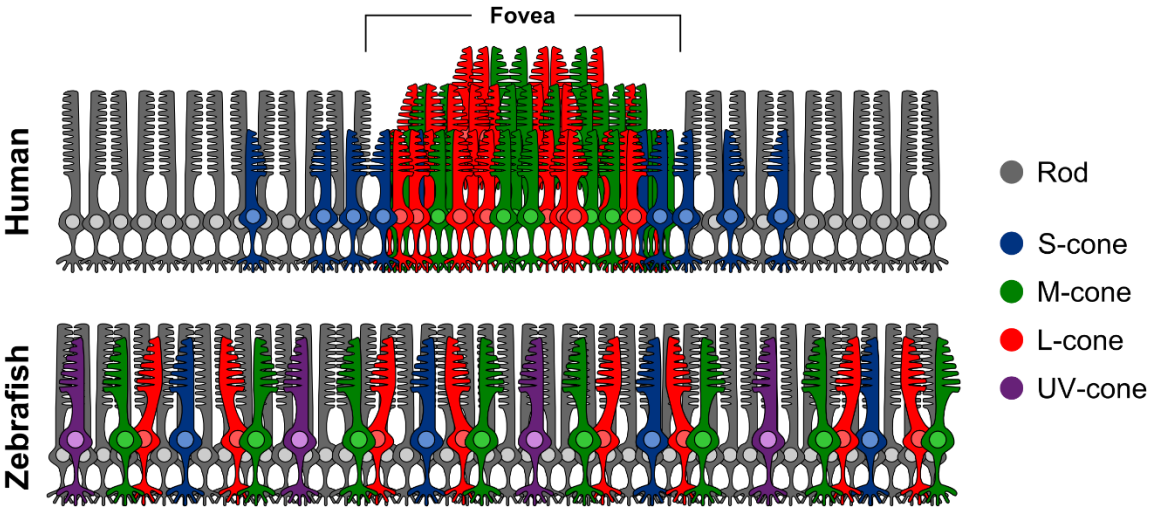

Figure 1.8. Comparison of the photoreceptor arrangement within the human retina and the zebrafish retina. Top: Schematic illustration of the photoreceptor layer within the central human retina, showing the rod-rich periphery, and the central fovea, which contains a high density of cone cells **Bottom:** Schematic illustration of the photoreceptor layer in the zebrafish retina, showing the regular arrangement of cone and rod cells across the retina. Schematic illustrations based on Kostic and Arsenijevic (2016).

1.5.4 Phenotypic analysis of zebrafish disease models

As well as assessing the physiological conservation of the tissues affected by the disorder of interest, it is also important to consider the availability of appropriate methods to measure disease-relevant phenotypes in the chosen model system. The zebrafish is particularly amenable to experimental analyses, and several tools exist to assess the phenotypic effects of pathogenic mutations on the development, morphology and function of various tissues in the fish (Angueyra and Kindt, 2018; Vaz et al., 2019). The following section will introduce some of the techniques that can be used for such investigations, focusing on those that are most relevant to the *TCP1*-linked disorder.

1.5.4.1 Approaches to characterise cerebellar and motor phenotypes in the zebrafish

One way in which we can investigate the effects of disease-linked mutations upon the cerebellum is by assessing cerebellar morphology (Bae et al., 2009). The transparency of the developing zebrafish is particularly useful here, as it allows brain development to be visualised in real time, and we can use transgenic lines to label cerebellar neurons specifically (Takeuchi et al., 2015; Weber et al., 2016) or to investigate more general markers of neurodevelopment (Vaz et al., 2019) and determine whether these are altered under disease conditions (Namikawa et al., 2019). It is also possible to use immunohistochemical approaches to investigate cerebellar morphology by using antibodies raised against specific markers of major cerebellar cell types (Bae et al., 2009). Alternatively, we can investigate early patterning defects that might impact on cerebellar development by using *in situ* hybridisation to analyse relevant gene expression patterns (Kasher et al., 2011).

As we described earlier, the main function of the cerebellum is to coordinate motor activity. Patients with the *TCP1*^{P70L} mutation display some motor dysfunction, which could be explained by their cerebellar atrophy, or by pathology in the peripheral nervous system.

Zebrafish exhibit many quantifiable motor behaviours, both as larvae and during adulthood, and these can be used to determine whether disease-linked mutations affect the function of the motor system (Vaz et al., 2019).

One example of a behaviour that can be used to assess motor function in zebrafish larvae is the touch-evoked escape response (Saint-Amant and Drapeau, 1998). This involves exposing larvae to a tactile stimulus, such as a light touch on the head or the trunk, and capturing their response using a high-speed camera (Sztal et al., 2016). From approximately 27 hpf, this type of stimulus typically induces a rapid escape response from a healthy fish (Saint-Amant and Drapeau, 1998), which can be absent or attenuated in larvae with motor dysfunction (Low et al., 2011, 2010a; Smith et al., 2013).

We can also use infrared tracking systems to assess motor activity in zebrafish larvae. This can either involve monitoring free swimming behaviour (Legradi et al., 2014; Pietri et al., 2013; Vaz et al., 2019) to determine whether mutant fish have reduced locomotor activity compared to healthy fish; measuring locomotor startle responses to stimuli such as noise or vibration (Legradi et al., 2014); or quantifying patterns of locomotor activity in response to visual cues such as light and dark (Basnet et al., 2019; Irons et al., 2010; MacPhail et al., 2009; Shaw et al., 2018).

In adult zebrafish, it is also possible to track free swimming to test for motor deficits (Panula et al., 2006). Furthermore, motor dysfunction has successfully been detected in adult zebrafish using the swim tunnel test, which provides a read-out of motor endurance (Chapman et al., 2013; Ramesh et al., 2010; Shaw et al., 2018).

One caveat associated with these assays is that locomotor behaviours are governed at various levels in the zebrafish, including by various neuronal circuits within and outside of the brain (Liu and Hale, 2017), as well as muscle function and neuromuscular junction integrity (Chapman et al., 2013; Sztal et al., 2016); therefore, further investigations are often required to determine the precise cause of an abnormal response. This could involve

using techniques such as calcium imaging (Muto and Kawakami, 2011; Ritter et al., 2001) or electrophysiology (Knogler et al., 2017; Roy and Ali, 2013) to assess the function of specific neuronal populations of interest.

1.5.4.2 Approaches to characterise retinal and visual phenotypes in the zebrafish

As for disorders of the cerebellum, it is also useful to assess morphological changes linked to mutations associated with human retinal diseases (Angueyra and Kindt, 2018). The overall organisation of the zebrafish retina can be evaluated through basic histological analysis (Berger et al., 2018; Lu et al., 2017), or specific cell types of interest can be visualised through the use of transgenic lines (Stearns et al., 2007), which are available for all major cells of the retina (Angueyra and Kindt, 2018; Raghupathy et al., 2013). An alternative approach is to perform immunohistochemical analysis, using antibodies that specifically recognise epitopes within retinal cells (Angueyra and Kindt, 2018; Messchaert et al., 2018; Wasfy et al., 2014).

It can also be useful to measure visual function in zebrafish models of human retinal disorders. One way in which retinal activity can be assessed in both humans and zebrafish is by generating electroretinogram (ERG) recordings to assess the electrical activity in the retina in response to a visual stimulus (Chrispell et al., 2015; Ebdali et al., 2018). This technique has been used to demonstrate retinal dysfunction in several zebrafish models of human visual disorders (Dona et al., 2018; Messchaert et al., 2018; Wasfy et al., 2014).

The zebrafish also possesses a wide repertoire of behaviours that are governed by vision and can be used to assess the effects of mutations on visual function (Angueyra and Kindt, 2018; Neuhauss, 2003). For example, we can measure the optokinetic response (Huang and Neuhauss, 2008; Neuhauss, 2003), in which larvae usually display a defined pattern of eye movements in response to a rotating stimulus of black and white stripes; or the optomotor response (Neuhauss, 2003; Stujenske et al., 2011), in which larval and adult

zebrafish naturally swim in the same direction as a moving visual stimulus of black and white stripes, to determine whether visual function is impaired.

It is also possible to assess visual function at low light levels to study phenotypes linked to night blindness in the zebrafish (Li and Dowling, 1997; Maaswinkel et al., 2005). One method involves placing the fish in an arena surrounded by a rotating white drum with a single black stripe. The black stripe acts as a threatening stimulus and evokes an escape response from the fish (Li and Dowling, 1997). By performing this assay under lighting conditions of varying intensity, the threshold intensity required for the fish to detect the stimulus can be measured. If this behavioural threshold is increased in a mutant fish, this can indicate visual dysfunction (Maaswinkel et al., 2005).

It is also possible to detect defects linked to colour blindness in zebrafish by performing a place preference test. Larval and adult zebrafish have been shown to exhibit innate colour preferences (Avdesh et al., 2012; Oliveira et al., 2015; Park et al., 2016), and this can be used as a behavioural paradigm to determine whether mutations affect the ability of mutants to detect certain colours. This generally involves placing fish into a T-maze or cross-maze composed of arms of different colours and quantifying the amount of time they spend in each coloured region (Park et al., 2016). If mutants are found to lack colour preference or show altered preferences compared to wild-type fish, this can be indicative of an impairment in colour processing (Park et al., 2016). A form of colour blindness was also demonstrated in mutant zebrafish using a modified version of the optokinetic response, in which mutant fish responded normally to the stimulus when the stripes were illuminated with white light, but failed to respond when the illumination was replaced with red light, indicating that they had a specific defect affecting their ability to detect red light (Brockerhoff et al., 1997).

Again, a drawback associated with these assessments of visual function is that multiple factors can impact on these behaviours; therefore, they are best employed in combination

with the other morphological and electrophysiological approaches described above (Maaswinkel et al., 2005; Messchaert et al., 2018).

1.6 Genetic tools for modelling rare diseases in zebrafish

Over time, various genetic tools have been used to model inherited human diseases in zebrafish. Summarised in Table 1.4, these encompass strategies for generating stable mutant lines by random mutagenesis or targeted gene editing (Doyon et al., 2008; Hwang et al., 2013b; Moens et al., 2008; Sander et al., 2011; Varshney et al., 2015), as well as methods for transiently interrogating of the effects of altered gene expression (Nasevicius et al., 2000; Nasevicius and Ekker, 2000; Rossi et al., 2015).

Table 1.4. Summary of methods for generating stable and transient zebrafish models of genetic human diseases

Technique	Mechanism	Required components	Advantages for modelling rare genetic diseases in zebrafish	Limitations for modelling rare genetic diseases in zebrafish
Stable models				
ENU-mediated mutagenesis	Random mutagenesis	Database of mutants that have already been generated by ENU-mediated random mutagenesis	If loss-of-function mutants for genes of interest are available, this abrogates need to generate a new model	Mutants for genes of interest are not always available. Outcrossing is often required to generate a stable model.
Retroviral-mediated insertional mutagenesis	Random mutagenesis	Database of mutants that have already been generated by retroviral-mediated insertional mutagenesis	If loss-of-function mutants for genes of interest are available, this abrogates need to generate a new model	Mutants for genes of interest are not always available. Outcrossing is often required to generate a stable model.
ZFNs + NHEJ-mediated repair	Creates double-stranded DNA break at target site, resulting in repair by NHEJ	Multiple DNA-binding zinc finger peptides (which each recognise 3bp of target DNA) fused to FokI nuclease domain	Enables targeted frameshift mutations to be introduced in candidate genes of interest	Tailored protein component needs to be generated for each genomic target. Outcrossing is often required to generate a stable model.

Table 1.4 (cont.)

TALENs + NHEJ-mediated repair	Creates double-stranded DNA break at target site, resulting in repair by NHEJ	Customisable DNA-binding domain (peptide-based) fused to FokI nuclease domain	Enables targeted frameshift mutations to be introduced in candidate genes of interest	Tailored protein component needs to be generated for each genomic target. Outcrossing is often required to generate a stable model.
CRISPR/Cas9 + NHEJ-mediated repair	Creates double-stranded DNA break at target site, resulting in repair by NHEJ	Specific 20nt gRNA complementary to target site + Cas9 endonuclease	Enables targeted frameshift mutations to be introduced in candidate genes of interest. gRNAs can easily be designed for different targets. Loss-of-function models can be efficiently generated through NHEJ-mediated repair.	Some off-target effects are possible but can be minimised through appropriate gRNA design. Outcrossing is often required to generate a stable model, though if mutagenesis is sufficiently efficient, phenotypes can be studied in F0 injected embryos.
ZFNs, TALENs or CRISPR/Cas9 + HDR-mediated repair	Creates double-stranded DNA break at target site. Simultaneous addition of DNA repair template results in HDR and incorporation of specific sequences or mutations of interest	Zinc finger peptides or customisable peptide-based DNA-binding domain fused to FokI nuclease domain, or specific ~20nt gRNA complementary to target site + Cas9 endonuclease (+ DNA repair template containing sequence of interest)	Allows knock-in of specific mutations of interest (most commonly via CRISPR/Cas9)	Currently less efficient than NHEJ-mediated loss-of-function model generation. Outcrossing is often required to generate a stable model.
CRISPR/Cas9-mediated base-editing	Deaminates cytidine or adenine bases at genomic target site, resulting in single-base-pair substitutions	Specific ~20nt gRNA complementary to target site + catalytically inactive Cas9 (dCas9), fused to cytidine or adenine deaminase enzyme	Allows introduction of disease-relevant missense mutations arising due to C-T or A-G base substitutions	Some base-pair substitutions cannot be modelled using this approach. Evidence of efficacy in zebrafish is limited. Specificity for target site needs to be established.

Table 1.4 (cont.)

Transient models				
Morpholino knockdown	Blocks mRNA translation or splicing (post-translational)	Modified 25bp oligonucleotide	Allows for rapid examination of loss-of-function phenotypes. Could be used to rapidly obtain evidence to support causality of loss-of-function candidate variants	Effects are short-lasting. May be associated with significant off-target effects. Cannot be used to model gain-of-function or patient-specific mutations.
CRISPR/dCas9 (CRISPR interference)	Blocks transcription (and can be coupled to transcriptional activators or repressors to further control gene dosage)	Specific ~20nt gRNA complementary to target site + dCas9 (which can be fused to a transcriptional activator or repressor)	Can be used to model both gain- and loss-of-function phenotypes. Has the potential to be used on a large scale	Currently not widely used in zebrafish. Specificity for target site needs to be established.

Abbreviations: Cas9 - CRISPR-associated protein 9, CRISPR - clustered regularly interspaced short palindromic repeats, dCas9 – catalytically inactive Cas9, ENU – *N*-ethyl-*N*-nitrosourea, HDR – homology-directed repair, NHEJ – non-homologous end joining, TALENs - transcription activation-like effector nucleases, ZFNs – zinc finger nucleases
(Table adapted from Adamson et al. (2018), under terms of the BMJ author licence.)

1.6.1 Generation of stable zebrafish disease models

1.6.1.1 Random mutagenesis

Traditionally, genetic manipulation of zebrafish has focused on random mutagenesis using chemical mutagens such as *N*-ethyl-*N*-nitrosourea (ENU), or retroviral-mediated insertional methods (Grunwald and Streisinger, 1992; Moens et al., 2008; Solnica-Krezel et al., 1994; Varshney et al., 2013). This approach was previously employed on a large scale to identify loss-of-function mutations responsible for various developmental phenotypes in the zebrafish, as exemplified in numerous publications in the December 1996 special issue of *Development* (Driever et al., 1996; Haffter et al., 1996). Moreover, reverse genetics approaches, such as TILLING (Targeting Induced Local Lesions in Genomes), have also been used to identify randomly mutagenised zebrafish carrying mutations in specific genes of interest (Moens et al., 2008). Huge libraries of frozen

gametes for stable zebrafish mutants that have been created using these methods are now available (Kettleborough et al., 2013). This can negate the need to generate a new model if a mutant for the affected gene has already been identified. Nevertheless, mutants are not available for all genes and this strategy does not allow specific disease-associated mutations to be modelled, limiting its utility for testing the pathogenicity of specific candidate variants.

1.6.1.2 Targeted gene-editing

More recently, powerful methods involving the use of engineered nucleases, including zinc finger nucleases (ZFNs), transcription activation-like effector nucleases (TALENs) and the clustered regularly interspaced short palindromic repeat (CRISPR)/CRISPR-associated protein 9 (Cas9) system have been employed to generate stable models of human disease, enabling targeted mutations to be created in specific zebrafish orthologues of interest (Doyon et al., 2008; Hwang et al., 2013b; Sander et al., 2011). Both ZFNs and TALENs require a tailored protein component to be generated for each target, which can be a costly and laborious process (Heintze et al., 2013). In contrast, the CRISPR/Cas9 system relies on recognition of the target site by a custom guide RNA (gRNA) molecule, and simply requires the design of a single oligonucleotide for each target site (Hwang et al., 2013a).

1.6.1.3 Using CRISPR/Cas9 technology to model rare genetic diseases in zebrafish

The CRISPR/Cas9 system has therefore become the tool of choice for generating stable models of human genetic diseases in recent years, as well as being used more generally to answer questions relating to developmental biology, through applications such as cell lineage tracing and large-scale gene knockout screens (Liu et al., 2019; Sun et al., 2020). A mechanistic overview of the classical CRISPR/Cas9 system in the context of disease modelling is shown in Figure 1.9. Most successes from CRISPR-mediated gene modification in zebrafish have arisen from the generation of null alleles through non-

homologous end joining (NHEJ)-mediated repair of CRISPR-induced DNA breaks (Gui et al., 2017; Perles et al., 2015; Zhang et al., 2017a). NHEJ is an error-prone process which often results in insertion or deletion of nucleotides at the break site. In two-thirds of cases, this will lead to a shift in the open reading frame, which may disrupt gene function (Li et al., 2016). This is useful for generating models of human disease caused by loss-of-function mutations, and continued optimisation of this strategy means that it is becoming increasingly efficient to generate zebrafish null mutants using CRISPR/Cas9 (Sun et al., 2020). In some cases, mutagenesis occurs efficiently enough to allow analysis of loss-of-function phenotypes directly in injected F0 embryos (crispants) (Hoshijima et al., 2019; Shankaran et al., 2017).

It may be desirable to introduce specific disease-associated mutations, particularly where complete loss-of-function alleles are lethal, or a variant is predicted to act through a gain-of-function mechanism. Specific mutations and exogenous DNA sequences have been knocked into the zebrafish genome by both homology-independent and homology-directed repair (HDR) (Armstrong et al., 2016; Auer et al., 2014; Boel et al., 2018; Hisano et al., 2015; Prykhozhij et al., 2018), but this approach is less efficient than generating loss-of-function alleles (Armstrong et al., 2016; Prykhozhij et al., 2018).

The prototypical Cas9 endonuclease, originating from *Streptococcus pyogenes*, requires the gRNA target sequence (or protospacer) to be located immediately 5' of a protospacer adjacent motif (PAM), which has the sequence 5'-NGG-3' (Cong et al., 2013). The efficiency of HDR-mediated knock-in of specific mutations appears to be influenced by the proximity of the desired mutation site to the PAM site (Boel et al., 2018), which limits the genomic sites that can feasibly be edited using this approach. However, several natural and engineered Cas variants that recognise alternative PAM sequences have now been shown to facilitate targeted mutagenesis in zebrafish (Feng et al., 2016; Fernandez et al., 2018; Kleinstiver et al., 2015; Liu et al., 2019; Moreno-Mateos et al., 2017), which could increase the potential for modelling specific mutations in the zebrafish genome by HDR.

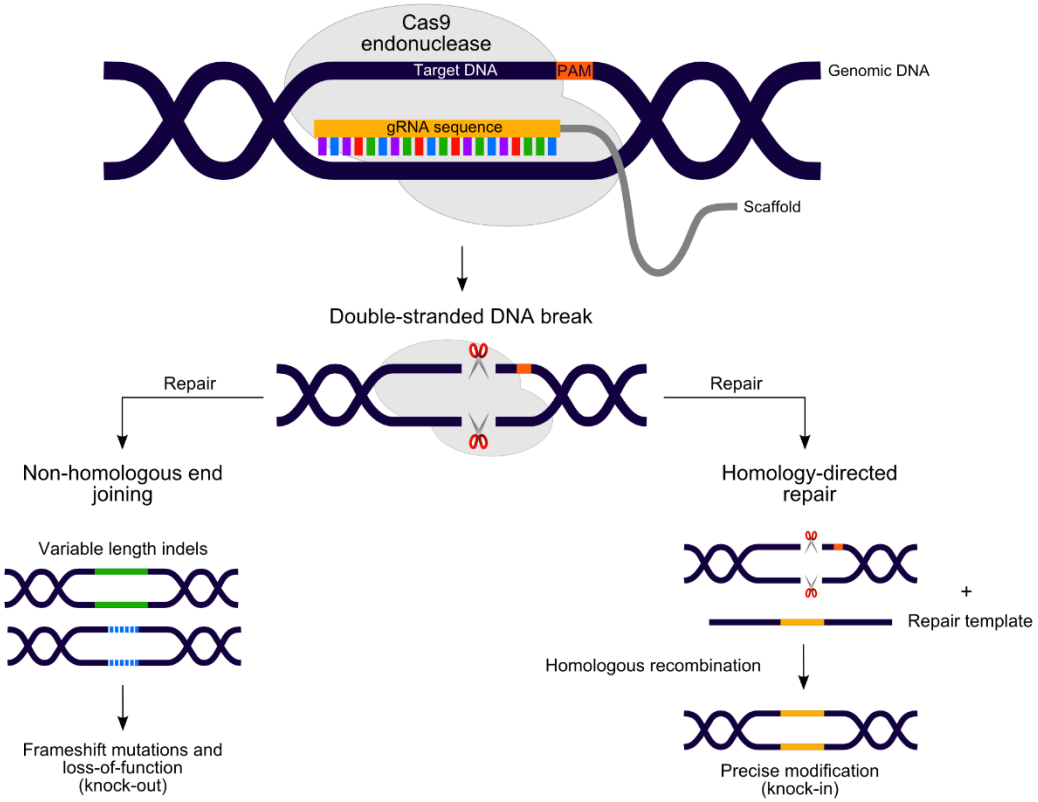

Figure 1.9. Overview of CRISPR/Cas9-mediated genome editing. A 20-nucleotide guide RNA (gRNA) directs Cas9 endonuclease to a chosen genomic target site (also known as the protospacer) immediately upstream of a protospacer-adjacent motif (PAM). On binding to the target site, Cas9 cleaves the genomic DNA to create a double-stranded DNA break 3–4 bp upstream of the PAM. Subsequent DNA repair via the non-homologous end joining (NHEJ) or homology-directed repair (HDR) pathways can be exploited to generate disease models through the creation of knockout alleles (to investigate loss-of-function of a gene of interest), or knock-in alleles (to study the consequences of a specific disease-associated mutation). For HDR approaches, a tailored repair template containing the variant of interest is also required. Figure reproduced from Adamson et al. (2018), under terms of the BMJ author licence.

Many genetic diseases are caused by missense mutations that arise from single base-pair substitutions. CRISPR/Cas9-derived gene editing tools, known as base editors (Gaudelli et al., 2017; Komor et al., 2016), have recently been developed, allowing targeted deaminase-mediated conversion of a single base-pair of interest to another without requiring DNA cleavage. Base editors are being assessed for their potential for modelling point mutations in various systems, including zebrafish (Gaudelli et al., 2017; K. Kim et al., 2017; Komor et al., 2016; Zhang et al., 2017b). A limitation of this approach is that only specific base-pair substitutions (C to T, T to C, A to G, G to A) are currently possible using this method, and the base-pair of interest must be located within an optimal window of proximity to the PAM (Y. B. Kim et al., 2017). However, efforts are currently underway to overcome this limitation through the development of Cas9 base-editing variants that recognise alternative PAM sequences (Y. B. Kim et al., 2017), which may increase the scope for modelling rare genetic diseases linked to point mutations.

1.6.2 Methods for transiently modelling genetic disease in zebrafish

Transient manipulation of the zebrafish genome can also be useful where complete loss-of-function of a gene of interest is undesirable. This is especially relevant considering the observation that deleterious loss-of-function zebrafish mutations, but not transient gene knockdowns, can sometimes cause relevant phenotypes to be masked due to genetic compensation mechanisms (Rossi et al., 2015). Transient gene knockdown in the zebrafish has traditionally been performed using antisense morpholino oligonucleotides to interfere with the expression of genes of interest at the level of splicing or translation (Nasevicius and Ekker, 2000). Concerns have been raised about the high risk for off-target effects when using morpholinos (Kok et al., 2015); however, provided that they are used cautiously, morpholinos can provide some useful insights into gene function (Stainier et al., 2017).

CRISPR interference (CRISPRi), another variation on the CRISPR/Cas9 system, can also be used to transiently interfere with gene expression at the transcriptional level (Larson et al., 2013). The basic CRISPRi mechanism involves the use of a catalytically inactive form of Cas9 (dCas9) which is targeted to a specific genomic site by a gRNA, as for the conventional CRISPR/Cas9 system. However, rather than creating a targeted DNA break, dCas9 acts to physically obstruct transcriptional elongation at the target site (Larson et al., 2013). CRISPRi machinery can also be coupled to transcriptional repressors or activators to alter levels of gene expression, allowing loss- or gain-of-function variants to be reversibly mimicked (Gilbert et al., 2013). Most examples of the use of this technology have come from cellular experiments (Heman-Ackah et al., 2016; Mandegar et al., 2016; Putri and Chen, 2018), although CRISPRi has successfully been used to silence gene expression *in vivo* in the zebrafish (Rossi et al., 2015). As CRISPRi continues to be developed, it may offer further possibilities for modelling human genetic diseases in zebrafish (Liu et al., 2016).

1.7 Functions of *TCP1*

1.7.1 TCP1 as a member of a eukaryotic chaperone complex

TCP1 is an essential gene which encodes T-complex polypeptide 1 (TCP1), a subunit of an essential type II eukaryotic chaperone complex known as the TCP1 Ring Complex or Chaperonin Containing TCP1 (TRiC/CCT). TRiC/CCT is a heteromeric, ATP-dependent complex, and is thought to assist with post-translationally folding around 10% of eukaryotic proteins to their native states (Yam et al., 2008). Many of these substrates contain WD40 repeat motifs, which assume β-propeller formations when folded (Willison, 2018).

TRiC/CCT is formed of two identical rings, each comprising eight structurally related subunits (Bigotti and Clarke, 2008; Hartl et al., 2011; Spiess et al., 2004) (Figure 1.10). These subunits all contain an apical substrate-binding domain, an equatorial ATP-binding domain, and an intermediate domain that connects the apical and equatorial domains

(Spiess et al., 2004). The ring shape of the complex forms a central cavity in which protein folding substrates are encapsulated by the ATP-dependent closure of a lid formed from flexible protrusions of the apical domains (Booth et al., 2008).

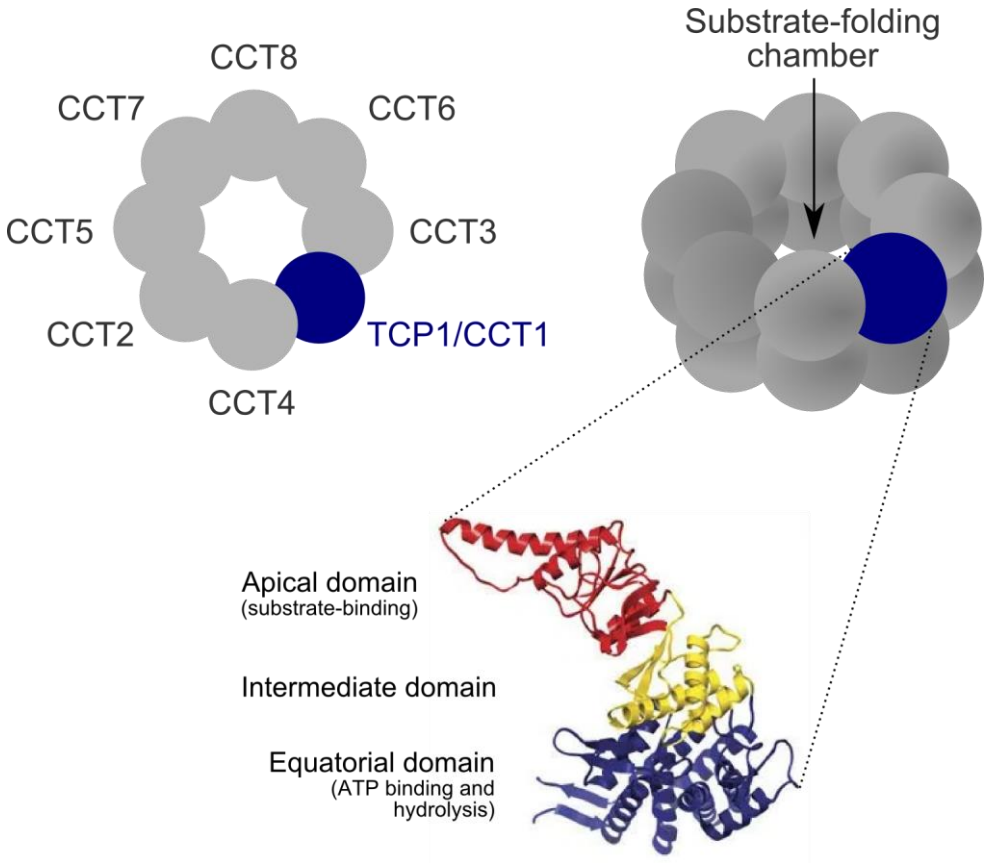

Figure 1.10. Schematic representation of subunit arrangement within TRiC/CCT. Two eight-membered rings, each composed of subunits CCT1-8, form the full TRiC/CCT complex and create a central substrate-folding chamber. The crystal structure of the bovine TCP1 subunit is shown, illustrating the three major domains found in all subunits of the complex. The image of the crystal structure was adapted from a figure by Booth et al. (2008), with permission from Springer Nature.

1.7.2 TRiC/CCT and neurological disease

The folding clients of TRiC/CCT represent a diverse collection of proteins which are involved in numerous biological pathways, including cytoskeletal organisation, cell cycle control, degradation pathways, and DNA maintenance mechanisms, among others (Yam et al., 2008). Combined with the ubiquitous expression of the complex, this raises the question of how a mutation in one of its constituent subunits could lead to a predominantly neurological phenotype, and how the cerebellum and retina might be selectively affected by such a mutation.

1.7.2.1 Direct links between TRiC/CCT dysfunction and neurological disease

While there have been no other pathogenic mutations reported in *TCP1* to date, there is some evidence linking other TRiC/CCT subunits to neurological disease. Specifically, a missense mutation in *CCT5* causes an autosomal recessive form of mutilating sensory neuropathy with spastic paraplegia (Bouhouche et al., 2006), and compound heterozygous *CCT2* mutations have been linked to Leber congenital amaurosis: a type of hereditary retinopathy (Minegishi et al., 2016). Moreover, a hereditary murine sensory neuropathy has been linked to a mutation in *Cct4* (Lee et al., 2003), and transcripts for some TRiC/CCT subunits were discovered to be differentially expressed in the brains of patients with Alzheimer's, Huntington's and Parkinson's diseases (Brehme et al., 2014).

Furthermore, experimental suppression of TRiC/CCT activity in the photoreceptors of mice induced rapid degeneration of the retina and affected several proteins that are critical for rod photoreceptor survival (Posokhova et al., 2011; Sinha et al., 2014), indicating that this complex is likely to be important for the health of retinal neurons. Correspondingly, phenotypic analyses of zebrafish harbouring insertional mutations in *tcp1*, *cct2*, *cct5* or *cct8* (Berger et al., 2018), chemically-induced frameshift or nonsense mutations in *cct3* (Berger et al., 2018; Matsuda and Mishina, 2004), or CRISPR-mediated mutations in *cct2* or *cct4* (Berger et al., 2018; Minegishi et al., 2018) have revealed severe retinal

degeneration phenotypes, along with cell death and neurite abnormalities within the optic tectum.

1.7.2.2 TRiC/CCT-linked pathways of relevance to neurological disease

Aside from this direct evidence linking dysregulation of TRiC/CCT to neurological defects, the chaperone complex, along with some of its interactors and protein folding clients, is associated with several pathways and processes that are implicated in the development, maintenance and function of the specific tissues affected in patients with the *TCP1* variant. These functions, which are discussed below, may offer mechanistic insights into the ways in which a mutation in *TCP1* could give rise to such phenotypes.

1.7.2.3 Cytoskeletal abnormalities

Actin and tubulin, two key cytoskeletal proteins, are major folding substrates of TRiC/CCT (Sternlicht et al., 1993) and cannot be folded by any other chaperone (Tian et al., 1995). TRiC/CCT dysfunction is therefore likely to result in cytoskeletal abnormalities. Indeed, knockdown of individual TRiC/CCT subunits has previously been shown to disrupt the filamentous actin (F-actin) cytoskeleton in HeLa cells (Pavel et al., 2016), *cct-1* knockdown produced microtubule-related defects in *C. elegans* (Lundin et al., 2008), and yeast *tcp1* mutant strains also display cytoskeletal dysfunction (Ursic et al., 1994).

Neurons, with their many polarised processes, and cytoskeleton-dependent intracellular transport machinery, are heavily reliant on an intricate cytoarchitecture to maintain a capacity for forming functional networks with other neurons, and to mediate proper neuronal migration during development (Dillon and Goda, 2005; Schaar and McConnell, 2005). The Purkinje cells of the cerebellum possess some of the most elaborately branched dendritic arbours in the brain and are therefore likely to be especially vulnerable to cytoskeletal irregularities.

The notion that cytoskeletal defects could lead to cerebellar disease is reinforced by the fact that patients with mutations in tubulin genes present with neurological disorders that often manifest with prominent cerebellar malformations (Tischfield et al., 2011). Moreover, mice with a mutation in the microtubule-associated protein 1a gene (*Map1a*), which encodes a protein involved in microtubule organisation, lose their Purkinje cells due to microtubule network alterations (Liu et al., 2015). The murine Purkinje cell degeneration (*pcd*) mutation, which affects a protein involved in post-translational processing of tubulin (Berezniuk et al., 2012), also causes Purkinje cells to degenerate, and additionally affects photoreceptor cells and the olfactory bulb (Mullen et al., 1976). Furthermore, deficiency of the Cordon-Bleu WH2 repeat protein (Cobl), which is involved in actin filament formation, has been shown to cause defects in the dendritic arbours of Purkinje cells in mice (Haag et al., 2012). Together, these findings suggest that faulty cytoskeletal organisation could contribute to cerebellar pathology.

Cytoskeletal abnormalities have also been shown to contribute to retinal disorders. As described above, photoreceptors degenerate in the *pcd* mutant mouse (Mullen et al., 1976). Moreover, the *ARAP1* (ArfGAP with RhoGAP domain, ankyrin repeat and PH domain 1) gene encodes a small GTPase belonging to the Arf family, members of which have been implicated in maintenance of the actin cytoskeleton (Myers and Casanova, 2008); and *Arap1*-deficient mice also display photoreceptor degeneration (Moshiri et al., 2017). Furthermore, a zebrafish model of a form of human retinitis pigmentosa caused by mutations in *EYS* (eyes shut homolog) (Arai et al., 2015), revealed disruption of the F-actin cytoskeleton in the retina (Lu et al., 2017), further linking cytoskeletal defects to photoreceptor dysfunction.

1.7.2.4 Primary ciliary defects

Disorders of the primary cilium, collectively termed ciliopathies, represent a genetically and clinically heterogeneous group of diseases. These manifest with a spectrum of phenotypes

featuring retinal degeneration, brain abnormalities and renal dysfunction, with additional involvement of other systems in some cases (Waters and Beales, 2011). Specific depletion of primary cilia in mouse granule cell precursors results in cerebellar hypoplasia due to reduced Shh-mediated proliferation of these cells (Spassky et al., 2008). Moreover, conditional knock-out of tau tubulin kinase 2 (*Ttbk2),* a gene critically involved in ciliogenesis, has revealed a crucial role for primary cilia in murine Purkinje cells (Bowie and Goetz, 2020). As these phenotypes associated with primary ciliary dysfunction partially overlap with those associated with the novel *TCP1* variant, it is possible that ciliary defects could play a pathogenic role in this disease.

An example of one of these ciliopathies is a genetically heterogeneous disorder called Bardet-Biedl syndrome (BBS) (Khan et al., 2016). The genes linked to BBS encode so-called BBS proteins, which regulate the structure and function of primary cilia. Seven of these proteins have been found to form a complex called the BBSome, which is required for proper ciliogenesis (Nachury et al., 2007). Three of the other BBS proteins, BBS6, BBS10 and BBS12, share sequence homology with TRiC/CCT subunits, and form a complex with some of these subunits to facilitate assembly of the BBSome (Seo et al., 2010). Accordingly, inhibition of TRiC/CCT activity in murine rod photoreceptors caused them to develop aberrantly as a result of defective ciliary biogenesis, which was linked to incomplete assembly of the BBSome (Sinha et al., 2014). Together, these findings point to a mechanism by which TRiC/CCT dysfunction could affect the biogenesis and function of primary cilia and contribute to the pathology seen in the *TCP1*-linked disorder.

1.7.2.5 Impaired protein homeostasis

The proteostasis network, comprising the chaperone-mediated protein-folding machinery and protein degradation pathways, such as the autophagolysosomal and ubiquitin-proteasome systems, is critical for maintaining neuronal health. Defective protein homeostasis has been connected to the pathogenesis of various neurodegenerative

diseases (Sweeney et al., 2017). Furthermore, conditional knockout of key genes involved in the autophagolysosomal degradation pathway, including autophagy-related 5 (*Atg5*), autophagy-related 7 (*Atg7*) and cathepsin D (*Ctsd*), causes Purkinje cell degeneration and ataxic phenotypes in mice (Koike et al., 2017; Nishiyama et al., 2007). This indicates that defective protein clearance mechanisms are sufficient to damage cerebellar neurons. Moreover, an overloading of the proteasome with misfolded proteins has also been proposed to contribute to the pathology of several forms of retinal degeneration (Lobanova et al., 2013).

TRiC/CCT functions within the proteostasis network at various levels; it folds newly translated proteins into their native states (Yam et al., 2008), it acts to prevent the formation of protein aggregates (Behrends et al., 2006; Pavel et al., 2016; Sot et al., 2017), and it intersects with other pathways involved in the cellular response to proteotoxic stress (Neef et al., 2014; Pavel et al., 2016; Tokumoto et al., 2000). Specifically, the complex has been found to interact directly with proteins containing expanded polyglutamine tracts, such as the mutant Huntingtin protein, to prevent their aggregation and toxicity (Behrends et al., 2006; Kitamura et al., 2006; Pavel et al., 2016; Tam et al., 2006), as well as preventing mutant α-synuclein from forming fibrillar aggregates (Sot et al., 2017).

TRiC/CCT has also been shown to regulate heat shock factor 1 (HSF1), the transcription factor responsible for inducing the heat shock response (Neef et al., 2014), and it interacts with the proteasome (Tokumoto et al., 2000), which is thought to facilitate the degradation of misfolded substrates (Guerrero et al., 2008). Moreover, some recent work suggests that TRiC/CCT has links with the autophagy machinery, with depletion of individual subunits of the complex resulting in defective autophagolysosomal degradation: a phenomenon which may arise through disruption of the actin cytoskeleton (Pavel et al., 2016). These findings highlight possible mechanisms by which TRiC/CCT dysfunction could give rise to defects in protein homeostasis, which may impact on neuronal health and function.

1.7.2.6 Transducin Gβ subunit folding

Transducin is a heterotrimeric G-protein which is expressed in photoreceptors and plays an important role in the phototransduction cascade by transducing signals generated by the visual pigment GPCRs (Asano et al., 2019).

Transducin, like other heterotrimeric G-proteins, is formed of three basic subunits: Gα, Gβ and Gγ. TRiC/CCT, along with its co-chaperone, phosducin-like protein 1 (PhLP1), has been shown to fold the Gβ subunits of heterotrimeric G-proteins, and mediate their compulsory dimerisation with Gγ subunits (Kubota et al., 2006; Lukov et al., 2006; Plimpton et al., 2015; Tracy et al., 2015), without which these subunits become unstable (Plimpton et al., 2015). The rod photoreceptors of mice lacking the Gγ transducin subunit produce large amounts of Gβ which does not properly fold without Gγ and becomes targeted for degradation by the proteasome (Lobanova et al., 2013). This causes the proteasome to become overloaded with misfolded Gβ, resulting in proteotoxic stress and photoreceptor death (Lobanova et al., 2013). The authors later showed that this can be rescued by overexpressing a component of the proteasome (Lobanova et al., 2018). Together, these findings point to a pathway through which TRiC/CCT dysfunction could result in misfolding of the Gβ transducin subunit, which could lead to photoreceptor degeneration.

1.7.2.7 DNA damage response and cell cycle control

There is also some evidence linking a defective DNA damage response to neurodegenerative phenotypes affecting the cerebellum. Ataxia telangiectasia, a disorder characterised primarily by cerebellar Purkinje cell degeneration, is caused by mutations in *ATM* (Savitsky et al., 1995), which encodes a key protein in the cellular response to DNA damage (Kitagawa and Kastan, 2005). Proteins encoded by genes implicated in other forms of cerebellar ataxia; for example, ataxin 3 (*ATXN3*) (Ward and La Spada, 2015) and polynucleotide kinase 3'-phosphatase (*PNKP*) (Bras et al., 2015), have also been found to

function within the DNA damage response pathway. This suggests a common mechanism whereby accumulation of DNA damage might contribute to selective neuronal loss in the cerebellum. DNA damage may also be relevant to retinal degeneration phenotypes, with increased basal levels of DNA damage having been observed in cells from age-related macular degeneration patients when compared with age-matched controls (Szaflik et al., 2009).

TRiC/CCT may play an indirect role in the DNA damage response; all eight subunits of the complex have been shown to interact with WD40-repeat protein 76 (WDR76) (Gallina et al., 2015), which is rapidly recruited to DNA in response to laser-induced damage (Gilmore et al., 2016). Moreover, several TRiC/CCT folding substrates, such as polo-like kinase 1 (Plk1) (Liu et al., 2005), cell division cycle protein 20 (Cdc20) (Camasses et al., 2003) and p53 (Trinidad et al., 2013) act within cell cycle control pathways, and TRiC/CCT itself may play a role in regulation of the mitotic checkpoint system (Kaisari et al., 2017). Since cell cycle control is an integral feature of the DNA damage response (Schmitt et al., 2007), it is possible that defects in key proteins involved in this process could contribute to pathology associated with TRiC/CCT dysfunction. Correspondingly, zebrafish with a mutation in *cct2* were found to have abnormalities in the cell cycle, which ultimately resulted in severe retinal degeneration (Minegishi et al., 2018).

1.8 Hypotheses and aims of this project

This thesis is centred on a novel missense mutation in *TCP1* (c.209C>T, p.P70L) which was linked to a neurological phenotype in three siblings born to consanguineous parents. To date, published pathogenic *TCP1* mutations have not been described in any other patients; therefore, we require further evidence to confirm that the *TCP1*^{P70L} mutation is responsible for these patients' phenotypes. Moreover, the identification of these patients suggests that *TCP1* plays an important role in the development and maintenance of

specific tissues within the nervous system; however, the precise nature of this role is yet to be investigated.

In line with this, the main hypotheses that we aimed to test were: a) that the *TCP1*^{P70L} mutation is responsible for the patients' phenotypes, and b) that *TCP1* plays an important role in the development and/or maintenance of the human cerebellum and retina (the primary tissues affected by the disease).

As we have discussed in this chapter, the zebrafish possesses many features that lend themselves well to the study of genetic and neurological disorders, as well as to the investigation of developmental processes. To test our hypotheses, we chose to take advantage of these features and use the zebrafish as a model system for assessing the pathogenicity of the *TCP1*^{P70L} mutation and exploring how this gene contributes to vertebrate development.

The first specific aim of the project, which we address in Chapter 3, was to generate our model systems by genetically engineering novel *tcp1* mutant zebrafish. We specifically aimed to use CRISPR/Cas9 and HDR to create a stable knock-in mutant zebrafish line harbouring a mutation equivalent to the human *TCP1*^{P70L} variant (*tcp1*^{P73L} in zebrafish). We reasoned that this model would best reflect the genetic status of the patients and would provide a platform in which we could test the hypothesis that the human *TCP1*^{P70L} mutation is pathogenic. To investigate whether *TCP1* is important for the development and maintenance of the tissues affected by the disease, we also aimed to generate a second stable mutant zebrafish line harbouring a frameshift mutation in *tcp1*, to create a platform for studying how loss of *tcp1* affects vertebrate development.

The second goal of the project, which we address in Chapters 4 and 5, was to harness the experimental manipulability of the zebrafish and characterise these mutant lines to determine a) whether the zebrafish *tcp1*^{P73L} mutation causes phenotypes that resemble those observed in patients, which would support the pathogenicity of the mutation; and b)

how loss of *tcp1* impacts on zebrafish development, focusing on the tissues implicated in the human disorder, which may provide us with novel insights into the developmental functions of this gene.

To achieve this, we aimed to use a combination of immunohistochemical approaches and fluorescent transgenic zebrafish lines to assess how zebrafish *tcp1* mutations affect the development and morphology of the cerebellum and retina. We then aimed to employ some of the behavioural assays that we have described in this chapter to explore whether functions of the motor or visual system are impaired in *tcp1* mutant zebrafish, as visual and motor defects have been identified as key phenotypic features of the human disease.

Chapter 2

Materials and methods

2.1 Materials

2.1.1 General reagents

Table 2.1. General laboratory reagents and suppliers

Reagent	Supplier
Acetic acid, glacial	VWR
Ammonium acetate	VWR
Ampicillin	Melford Laboratories Ltd.
Calcium chloride ($CaCl_2$)	Sigma-Aldrich
Chloroform	Fisher Scientific
Citric acid	VWR
Dimethyl sulfoxide (DMSO)	Sigma-Aldrich
Ethylenediaminetetraacetic acid (EDTA)	Thermo Fisher Scientific
Ethanol	VWR
Formamide	Sigma-Aldrich
Glycerol	Thermo Fisher Scientific
Hydrochloric acid (HCl), 37% (w/v)	VWR
Hydrogen peroxide (H_2O_2), 30% (w/w)	Sigma-Aldrich
Isopropanol	Fisher Scientific
LB Agar, Miller (Powder)	Fisher Scientific
LB Broth, Miller (Granulated)	Fisher Scientific
Lithium chloride (LiCl)	Sigma-Aldrich
Magnesium chloride ($MgCl_2$)	Sigma-Aldrich
Methanol	Fisher Scientific
Phenol red	Sigma-Aldrich
Potassium chloride (KCl)	Fisher Scientific
Potassium hydroxide (KOH)	Sigma-Aldrich
Potassium phosphate monobasic (KH_2PO_4)	Sigma-Aldrich
Sodium chloride (NaCl)	Fisher Scientific
Sodium citrate ($Na_3C_6H_5O_7$)	Fluka
Sodium phosphate dibasic (Na_2HPO_4)	Sigma-Aldrich
Sodium phosphate monobasic (NaH_2PO_4)	Sigma-Aldrich
Tris base	Melford Laboratories Ltd.
Triton X-100	Sigma-Aldrich
TRIzol®	Thermo Fisher Scientific
Trypsin	Invitrogen
Tween-20	Sigma-Aldrich

2.1.2 Oligonucleotides

2.1.2.1 Primer oligonucleotides

All primers were synthesised by Integrated DNA Technologies (IDT) or Sigma-Aldrich and were resuspended to 100 µM in distilled water (d.H_2O) before use. Unless otherwise stated, primers were designed in-house using the NCBI Primer-BLAST primer design tool (accessible at: ncbi.nlm.nih.gov/tools/primer-blast). M13 forward (M13F) primer tag sequences used for sequencing PCR products are underlined, where applicable.

Table 2.2. Zebrafish genomic DNA primer sequences

Primer name	Direction	Sequence (5' → 3')	Product length (bp)	Supplier
tcp1 gDNA sequencing primers	Forward	TGTAAAACGACGGCCAGTACCCAACCCTAGTGCTTGTCTTC	330	Sigma
	Reverse	CCGAGAGGGTTTCTGTATCCTG		
tcp1 gDNA TIDE sequencing primers	Forward	TGGTAAGGATAAAAAGGGAAACCT	667	IDT
	Reverse	TGTAAAACGACGGCCAGTTGTGCTCTCAACCTTGTGGA		
tcp1 HRM primers	Forward	CACCAATGACGGGGCCA	116	IDT
	Reverse	CTGATGTAGTGCCGTCTCCAA		
tcp1 left arm HDR AS-PCR primers	Forward	TGTTTCAGGACGTGACCA	80	IDT
	Reverse	CTTTAGCAGCCAGGTGCTCC		
tcp1 right arm HDR AS-PCR primers	Forward	CTGCTCGAGGTGGAGCACCT	151	IDT
	Reverse	ACGCAGCTCAGATGGATGGTA		

Table 2.3. gRNA oligonucleotide primer sequences

Primer name	Direction	Sequence (5' → 3')	Product length (bp)	Supplier
gRNA oligonucleotide primers*	Forward	GCGTAATACGACTCACTATAG	120	Sigma
	Reverse	AAAGCACCGACTCGGTGCCAC		

*Talbot and Amacher (2014)

Table 2.4. Zebrafish cDNA sequencing primers

Primer name	Direction	Sequence (5' → 3')	Product length (bp)	Supplier
tcp1 cDNA sequencing primers	Forward	TCCATTCTTCTCTCCAGTCCAA	779	IDT
	Reverse	TGTAAAACGACGGCCAGTGCCCAGCTTCATCT TGGTTT		

Table 2.5. *In situ* hybridisation probe synthesis primers

Primer name	Direction	Sequence (5' → 3')	Product length (bp)	Supplier
tcp1 ISH probe synthesis primers	Forward	AGATGACCTGGGCAGAGAGT	816	IDT
	Reverse	CCTCCTGGCACCACAGATTT		

Table 2.6. Zebrafish qPCR primers

Primer name	Direction	Sequence (5' → 3')	Working concentration (µM)	Product length (bp)	Supplier
tcp1 qPCR primers (exon 1-2)	Forward	TAGACAGTCCGTTAAG CGTGC	0.25	109	IDT
	Reverse	CCGAGAGAGCTCTTCA CGATG			
tcp1 qPCR primers (exon 5-6)	Forward	AGGAGGCTGTCCGCTA CATT	0.25	149	IDT
	Reverse	GGCGTCGACCACCATA TTAG			
eef1a qPCR primers	Forward	GGATTGCCACACGGCT CACATT	0.50	177	Sigma
	Reverse	GGTGGATAGTCTGAGA AGCTCTC			
hsp70.1 qPCR primers	Forward	TTCGCTCTATTTAAGA ATCTACTC	0.25	122	IDT
	Reverse	CTGAAACACCCCCACA CA			
hsp70l qPCR primers	Forward	TTCGCTCTATTTAAGA ATCTACTG	0.25	116	IDT
	Reverse	TCCATGCTGAAACACC CC			
actb1 qPCR primers*	Forward	CTCTTCCAGCCTTCCT TCCT	1.00	247	IDT
	Reverse	CACCGATCCAGACGGA GTAT			

Table 2.6 (cont.)

tuba1a qPCR primers+	Forward	CCTGCTGGGAACTGTATTGT	0.25	292	IDT
	Reverse	TCAATGAGTTCCTTGCCAAT			
gnb1b qPCR primers	Forward	TCCAGATGCGCACAAGAAGAA	0.25	108	IDT
	Reverse	GTTTTCCATCCTGGGAAGCACT			

*Sung et al. (2009) +McCurley and Callard (2008)

Table 2.7. Primers used to amplify FyntagRFP-T transgene

Primer name	Direction	Sequence (5' → 3')	Product length (bp)	Supplier
FyntagRFP-T primers	Forward	CCTGGCTACCAGCTTCATGT	105	IDT
	Reverse	CTCTCCCATGTGAAGCCCTC		

2.1.2.2 gRNA oligonucleotide template

The oligonucleotide used to synthesise *tcp1* gRNA was synthesised by IDT as a single-stranded Ultramer® DNA Oligo. The oligonucleotide was resuspended to 10 µM in TE buffer (10 mM Tris-HCl, pH 8.0, 1 mM ethylenediaminetetraacetic acid (EDTA), pH 8.0, and 100 mM NaCl) before use.

2.1.2.3 Single-stranded oligodeoxynucleotide (ssODN) HDR templates

Oligonucleotide templates used for HDR-mediated knock-in of desired mutations were synthesised by IDT as single-stranded Ultramer® DNA Oligos and resuspended 10 µM in d.H_2O before use.

2.1.3 Enzymes

2.1.3.1 Restriction endonucleases

Table 2.8. Restriction enzymes used for restriction fragment length analysis

Enzyme	Buffer	Digest temperature (°C)	Supplier	Catalogue number
*Alu*I	CutSmart®	37	NEB	R0137
*Bsl*I	CutSmart®	55	NEB	R0555
*Msp*I	CutSmart®	37	NEB	R0106
*Taq*I	Buffer E	65	NEB	R6151
*Spe*I	CutSmart	37	NEB	R0133
*Xho*I	CutSmart®	37	NEB	R0146

2.1.3.2 Cas9 endonuclease

Cas9 nuclease from *Streptococcus pyogenes* was obtained from New England Biolabs (NEB) (Cat. No. M0386) and was diluted 1:3 (to 6.7 µM) in Cas9 Nuclease Reaction buffer (NEB) prior to use.

2.1.3.3 Post-PCR clean-up (ExoSAP) enzymes

Exonuclease I was obtained from NEB (Cat. No. M0293) and Shrimp Alkaline Phosphatase was obtained from Affymetrix (Cat. No. 78390).

2.1.3.4 DNaseI

RNase-free DNaseI used to remove contaminating genomic DNA from RNA samples prior to cDNA synthesis was obtained from NEB (Cat. No. M0303) and was used in conjunction with NEB DNase buffer.

2.1.4 Kits

Table 2.9. Details of kits used in the project

Kit name	Application	Supplier	Catalogue number
GenElute™ Gel Extraction Kit	Gel purification of gRNA oligonucleotide template (as described on page 65)	Sigma-Aldrich	NA1111
MEGAShortScript™ T7 Transcription Kit	*In vitro* gRNA transcription (as described on page 66)	Thermo Fisher Scientific	AM1354
TOPO® TA Cloning® Kit	Cloning cDNA template for DIG-labelled probe synthesis (as described on page 74)	Invitrogen	4500030
NucleoSpin® Plasmid Kit	Plasmid DNA purification (as described on page 75)	Macherey-Nagel	740588

2.1.5 Antibodies

The following primary antibodies were used in this project: mouse 3A10 (anti-neurofilament associated antigen) (Developmental Studies Hybridoma Bank, deposited by Jessell TM, Dodd J and Brenner-Morton S), mouse anti-acetylated α-tubulin, clone 6-11B-1 (Sigma-Aldrich, Cat. No. T7451), rabbit anti-cleaved caspase 3 (BD Pharmigen, Cat. No. 559565), mouse zpr-3 (Zebrafish International Resource Center) and rabbit anti-rhodopsin (Abcam, Cat. No. ab3424).

The following fluorophore-conjugated secondary antibodies were used in this project: donkey anti-mouse Alexa Fluor™ 488 (Invitrogen, Cat. No. A-21202), donkey anti-rabbit Alexa Fluor™ 488 (Invitrogen, Cat. No. A-21206), donkey anti-mouse Alexa Fluor™ 647 (Invitrogen, Cat.No. A-31571), donkey anti-rabbit Alexa Fluor™ 647 (Invitrogen, Cat. No. A-31573).

2.2 Methods

2.2.1 Zebrafish maintenance and breeding

Zebrafish were housed in the Bateson Centre aquarium facility at the University of Sheffield. To obtain embryos for experiments, adult zebrafish were pair-mated or marbled in the evening and embryos were collected the following day. Embryos were then maintained at 28°C in E3 medium (5 mM NaCl, 0.17 mM KCl, 0.33 mM $CaCl_2$ and 0.0001% (v/v) methylene blue in d.H_2O) until the desired stage up to 5.2 dpf. For experiments conducted after 5.2 dpf, embryos were then transferred to tanks supplied with 28ºC water and raised to the desired stage. All zebrafish procedures were carried out in accordance with UK Home Office licensing regulations.

2.2.2 Transgenic zebrafish Purkinje cell reporter line

Transgenic zebrafish expressing FyntagRFP-T under the control of a Purkinje cell-specific regulatory element (Matsui et al., 2014) were obtained from the laboratory of Professor Reinhard Köster (Technical University of Braunschweig, Germany). For use in our experiments, heterozygous *tcp1*^{P73L} or *tcp1*^{I57fs} mutants were crossed onto these transgenic fish as summarised in Figure 2.1 and Figure 2.2. Briefly, zebrafish expressing one copy of the transgene were first crossed with heterozygous *tcp1*^{I57fs} or *tcp1*^{P73L} mutant zebrafish. Larval offspring were then selected for visible red fluorescent protein (RFP) expression and raised to adulthood. Fin biopsies from RFP-expressing adult zebrafish were then genotyped by PCR (page 67) and *Bsl*I or *Xho*I restriction fragment length analysis (page 68) to identify heterozygous *tcp1*^{I57fs} or *tcp1*^{P73L} mutants, and these were then crossed with *tcp1*^{I57fs} or *tcp1*^{P73L} heterozygotes that were not expressing the RFP transgene. For the *tcp1*^{P73L} line, offspring were then selected for imaging based on visible RFP expression and they were genotyped for the *tcp1*^{P73L} mutation after imaging. For the *tcp1*^{I57fs} line, offspring were first sorted according to whether they had a normal (*tcp1*$^{+/+}$ or *tcp1*$^{I57fs/+}$) or mutant (*tcp1*$^{I57fs/I57fs}$) phenotype, and larvae with normal phenotypes were

selected for imaging based on visible RFP expression. As RFP was not visible in homozygous *tcp1*^{I57fs} mutant larvae, transgenic status was determined after imaging, by extracting DNA and performing standard PCR (page 67) using primers designed against the FyntagRFP-T sequence (Table 2.7).

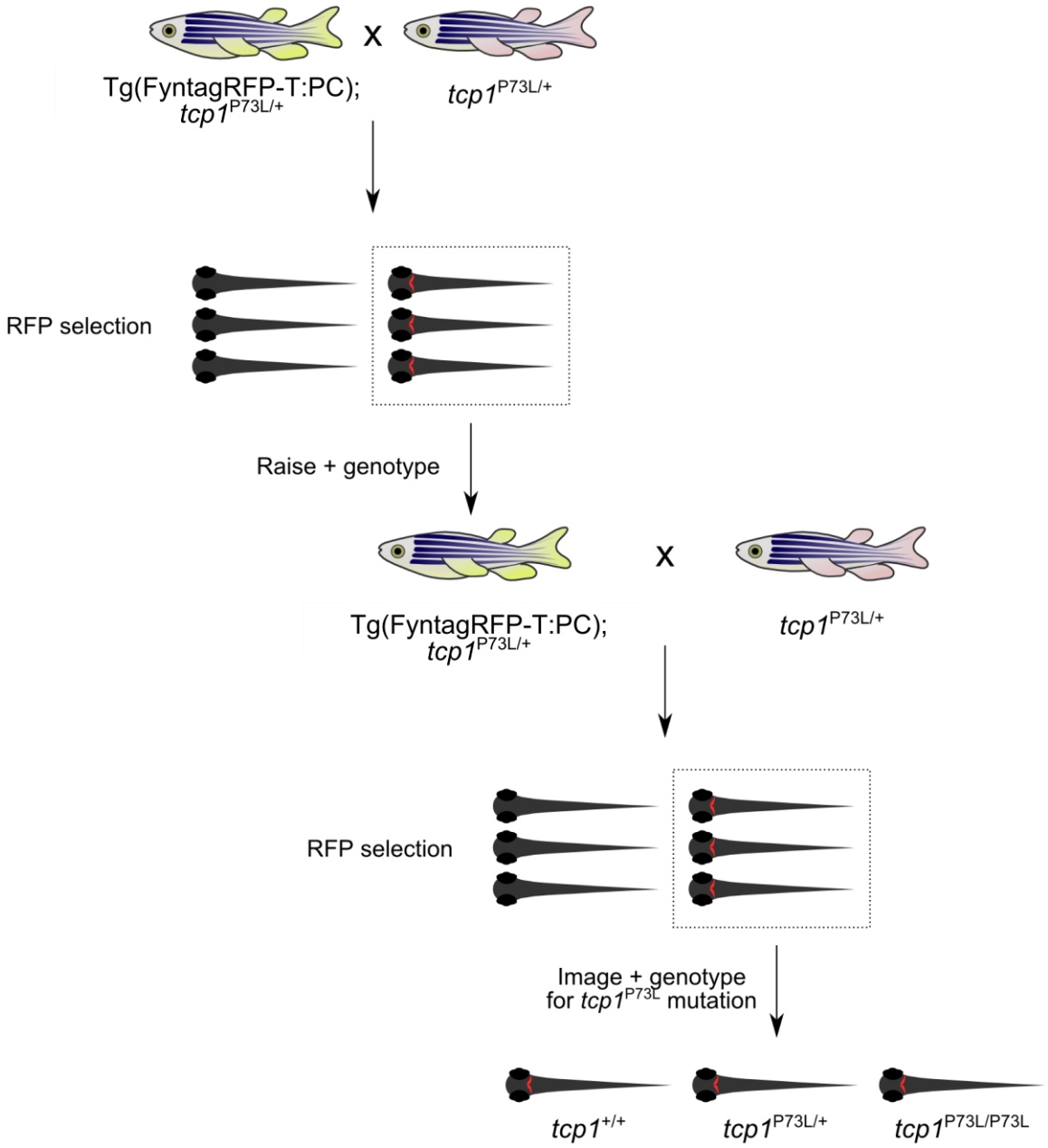

Figure 2.1. Summary of breeding process to obtain Tg(FyntagRFP-T:PC) *tcp1*^{P73L} larvae for characterisation of cerebellar Purkinje cells.

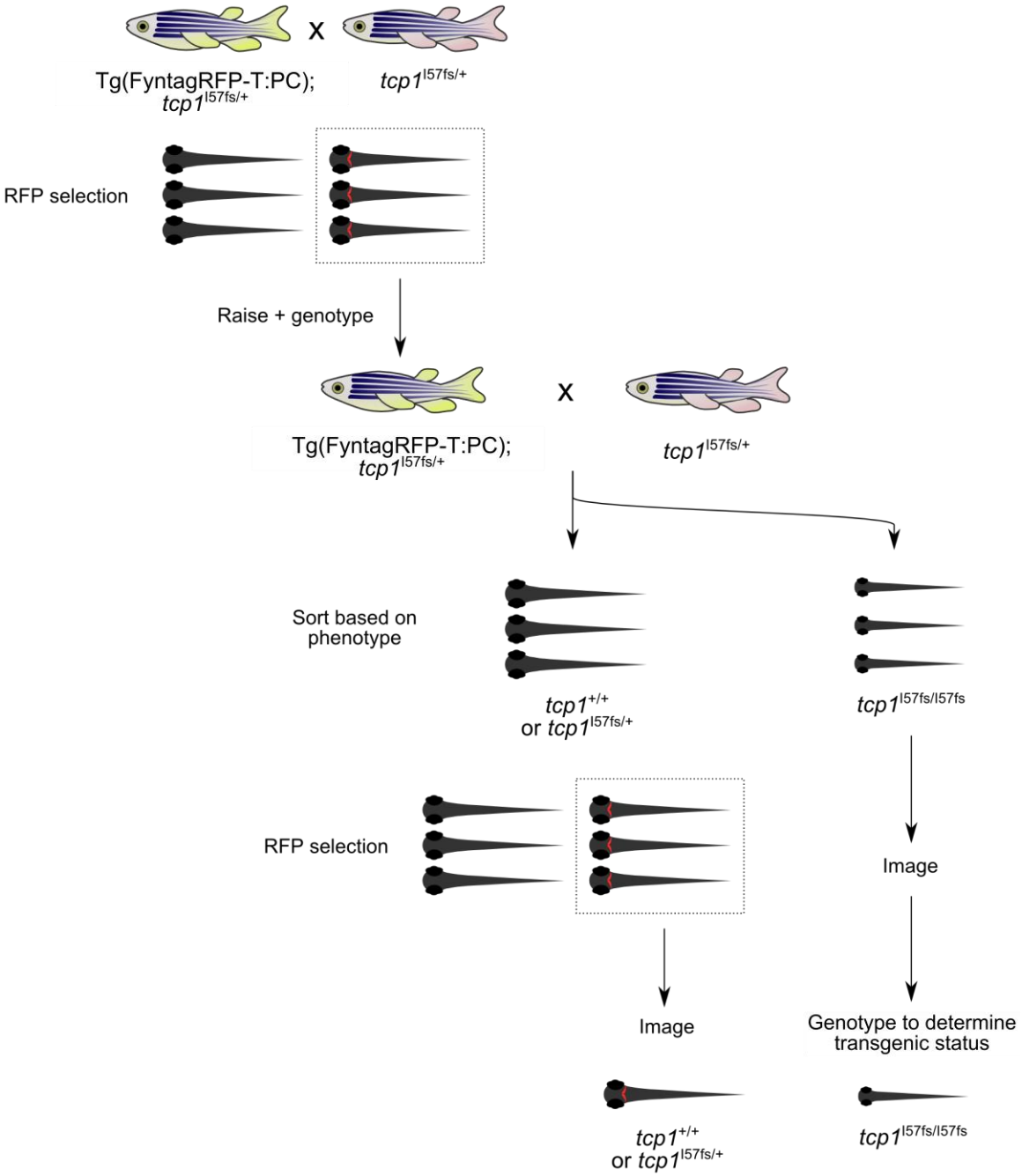

Figure 2.2. Summary of breeding process to obtain Tg(FyntagRFP-T:PC) *tcp1*^{l57fs} larvae for characterisation of cerebellar Purkinje cells.

2.2.3 Synthesis of *tcp1* gRNA

2.2.3.1 PCR amplification of tcp1 gRNA oligonucleotide template

A reaction mix was assembled to contain 1 x FIREPol ® Master Mix (Solis Biodyne), 5 µM forward primer and 5 µM reverse primer (as detailed in Table 2.3), 20 nM gRNA oligonucleotide template, and d.H_2O to give a final reaction volume of 100 µl. The template was then amplified using a G-Storm™ thermal cycler (Gene Technologies Ltd.) according to the parameters detailed in Table 2.10.

Table 2.10 Cycling parameters used to amplify *tcp1* gRNA oligonucleotide template

Programme name	Step		Temperature (ºC)	Duration (s)	Number of cycles
gRNA oligonucleotide PCR	Initial denaturation		95	60	-
	PCR	Denaturation	95	15	40
		Annealing	60	30	
		Elongation	72	30	
	Final elongation		72	300	-

2.2.3.2 Gel purification of tcp1 gRNA oligonucleotide template

The 100 µl PCR product (generated as described on page 65) was firstly separated on a 2% (w/v) agarose/TAE (40 mM Tris-acetate, 1 mM EDTA) gel and the 120 bp band was excised from the gel. DNA was then purified using the GenElute™ Gel Extraction Kit (Table 2.9), according to the manufacturer's protocol. Briefly, the excised gel fragment was weighed and then solubilised in 3 gel volumes of Gel Solubilisation Solution at 55°C. 1 gel volume of 100% isopropanol was then added to precipitate the DNA and the sample was centrifuged through a DNA binding column at 16,000 x g. The column was washed in Wash Solution and DNA was eluted in a total volume of 20 µl, then the DNA concentration was measured using a NanoDrop™ 1000 spectrophotometer (Thermo Fisher Scientific).

2.2.3.3 In vitro transcription of tcp1 gRNA

The MEGAShortScript™ T7 Transcription Kit (Table 2.9) was used to transcribe the purified *tcp1* gRNA oligonucleotide template generated as described on page 65. A 10 µl reaction was assembled to contain 1 µl T7 reaction buffer, 1 µl T7 enzyme mix, 1 µl each of 75 mM T7 ATP, CTP, GTP and UTP solutions and 358.4 ng purified *tcp1* gRNA oligonucleotide template. The reaction was then incubated at 37°C for 3 h to facilitate transcription, and the DNA template was subsequently removed from the reaction by the addition of 1 µl TURBO DNase. RNA was precipitated by the addition of 10 µl 7.5 M ammonium acetate and 250 µl 100% ethanol with overnight incubation at -20°C. The sample was then centrifuged at 12,000 x g for 15 min at 4°C to pellet RNA, the pellet was washed in 75% (v/v) ethanol in nuclease-free water, and RNA was resuspended in 20 µl nuclease-free water. Sample RNA concentration was then measured using a NanoDrop™ 1000 spectrophotometer.

2.2.4 Zebrafish DNA extraction

For DNA extraction from individual zebrafish, single embryos or tail fin biopsies were added to 20-30 µl QuickExtract™ DNA Extraction Solution (Epicentre Biotechnologies, Cat. No. QE09050), then incubated for 2 h at 65°C, followed by 2 min at 98°C. To extract DNA from pooled zebrafish embryos, the process was the same, but a volume of 10 µl QuickExtract™ per embryo was used. The wild-type DNA extracts used for the initial identification of polymorphisms in zebrafish *tcp1* had been previously prepared by an alternative method.

2.2.5 CRISPR microinjections

CRISPR injection mixes were prepared according to the recipes detailed in Table 2.11 and Table 2.12 for initial gRNA testing and co-injections of gRNA and ssODN HDR templates, respectively. For injections to create alternative frameshift alleles, the injection mix was

prepared using the 'gRNA + Cas9 only' recipe detailed in Table 2.12. Glass capillary needles were used to inject either 2 nl or 4 nl of these mixes directly into the yolk sac of 1-cell zebrafish embryos. DNA was then extracted at 33 hours post-fertilisation (hpf) for initial gRNA test injections, or 48 hpf for all other injections.

Table 2.11. Details of injection mix used to test *tcp1* gRNA

CRISPR mix	*tcp1* gRNA (µg)	Cas9 protein (µM)	Phenol red dye (µl)	Final mix volume (µl)
gRNA + Cas9 only	5.9	2.5	1	4.5

Table 2.12. Details of mixes used for injecting embryos to raise as founders

CRISPR mix	*tcp1* gRNA (µg)	Cas9 protein (µM)	ssODN HDR template (µM)	Phenol red dye (µl)	Final mix volume (µl)
gRNA + Cas9 only	4.3	1.2	-	1	5.6
gRNA + Cas9 + ssODN	4.3	1.2	2	1	5.6

2.2.6 Polymerase chain reaction (PCR) amplification of zebrafish DNA

2.2.6.1 Standard PCR

Zebrafish genomic DNA was amplified prior to restriction digest or sequencing analysis using a reaction mix containing 1 x FIREPol® Master Mix (Solis Biodyne), 1 µM forward primer, 1 µM reverse primer, 1 µl template DNA (1/5 dilution of crude DNA extract in d.H_2O) and d.H_2O to give a final reaction volume of 10 µl. Amplification was subsequently performed on a G-Storm™ thermal cycler (Gene Technologies Ltd.) according to the 'Standard 30 x touchdown PCR' described in Table 2.13.

2.2.6.2 HDR allele-specific PCR (AS-PCR)

To detect HDR alleles in injected F0 founders and F1 offspring, 10 µl reaction mixes were prepared in the same way as for standard PCRs using either the *tcp1* left arm

AS-PCR primer pair or the *tcp1* right arm AS-PCR primer pair. Genomic DNA was then amplified using the 'HDR allele-specific 30 x touchdown PCR' detailed in Table 2.13.

Table 2.13. Cycling parameters used for PCR amplification of zebrafish DNA

Programme name	Step		Temperature (°C)	Duration (s)	Number of cycles
Standard 30 x touchdown PCR	Initial denaturation		94	180	-
	Touchdown	Denaturation	94	45	15
		Annealing	65-50 (-1°C/cycle)	45	
		Elongation	72	90	
	PCR	Denaturation	94	30	30
		Annealing	58	45	
		Elongation	72	60	
	Final elongation		72	600	-
HDR allele-specific 30 x touchdown PCR	Initial denaturation		94	180	-
	Touchdown	Denaturation	94	45	15
		Annealing	65-60 (-1°C/cycle)	45	
		Elongation	72	90	
	PCR	Denaturation	94	30	30
		Annealing	58	5	
		Elongation	72	5	

2.2.7 Post-PCR restriction fragment length analysis

For restriction digest of PCR products, digest mixes contained 1 x enzyme buffer, 0.4 µl restriction enzyme, 10 µl post-amplification PCR product and d.H_2O to give a final volume of 20 µl per reaction. The reactions were then incubated at the appropriate temperature for 12-16 h and digest products were separated by agarose gel electrophoresis. Details of

the specific digest temperatures and reaction buffers used for each enzyme are listed in Table 2.8.

2.2.8 Post-PCR clean-up and sequencing analysis

Exonuclease I and Shrimp Alkaline Phosphatase (ExoSAP) were used to remove excess primers and dNTPs from PCR products prior to sequencing analysis. Individual ExoSAP reactions contained 5 µl post-amplification PCR product, 0.05 µl Exonuclease I, 1 µl shrimp alkaline phosphatase and d.H_2O to give a final reaction volume of 10 µl. Reactions were then incubated at 37°C for 45 min, followed by 80°C for 15 min. Samples were then sequenced at the University of Sheffield Core Genomic Facility using either an M13F primer (for PCR products amplified using primers containing an M13F tag sequence), or one of the specific primers used to amplify the PCR product.

2.2.9 High-resolution melt (HRM) analysis

A schematic overview of the HRM-based approach used to screen zebrafish DNA for CRISPR-induced mutations in *tcp1* is illustrated in Figure 2.3. HRM reaction mixes were assembled to contain 1 x HOT FIREPol® EvaGreen® HRM mix (Solis Biodyne), 1 µM forward and reverse *tcp1* HRM primers, 0.7 µl template DNA (crude DNA extract generated as on page 66, diluted 1/20 in d.H_2O), and d.H_2O to give a final volume of 5 µl per reaction. DNA was amplified and melted using the 'HRM analysis' programme detailed in Table 2.14 and melt profile data was extracted using the Bio-Rad CFX Manager™ software and plotted using GraphPad Prism version 8.0.0.

Table 2.14. Cycling parameters used for HRM analysis of zebrafish DNA

Programme name	Step		Temperature (°C)	Duration (s)	Number of cycles
HRM analysis	Initial denaturation		95	900	-
	PCR	Denaturation	95	15	40
		Annealing	60	30	
			PLATE-READ		
		Elongation	72	30	
			PLATE-READ		
	HRM		95	30	
			60 (Ramp 0.1°C/cycle)	60	
			65-95 (+0.2°C/cycle, Ramp 0.2°C/s)	10	
			PLATE-READ *(after each 0.2°C temperature increment)*		

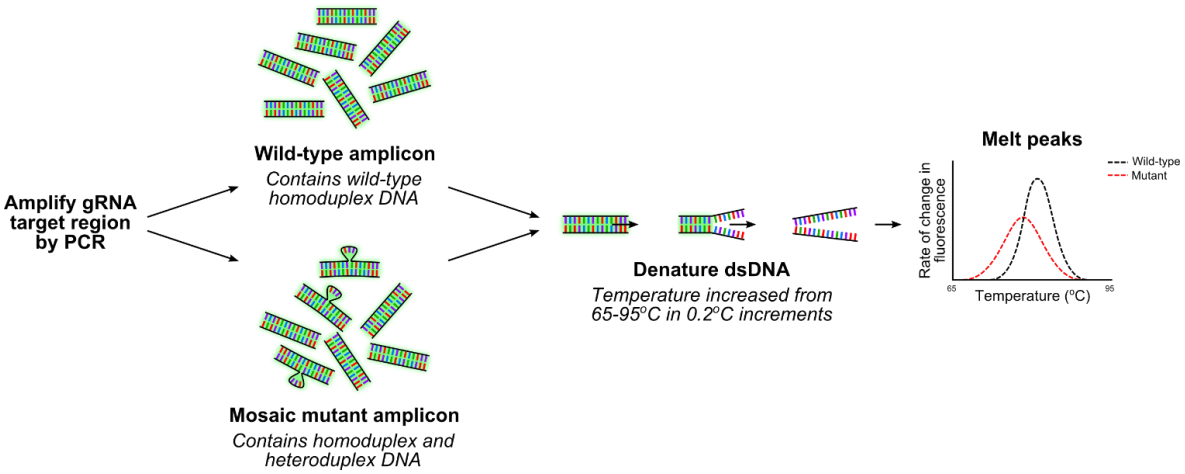

Figure 2.3 Overview of the HRM analysis strategy for detecting CRISPR-induced mutations. The gRNA target region is firstly amplified by PCR in the presence of EvaGreen® dye, which fluoresces when bound to double stranded DNA. PCR amplicons are then gradually denatured, resulting in decreasing fluorescence intensity as the DNA becomes single stranded. Due to the presence of heteroduplex DNA in amplicons from zebrafish harbouring mosaic CRISPR induced mutations, the melt profile of DNA from these fish will be shifted compared to wild-type homoduplex DNA from non-injected control zebrafish.

2.2.10 Generating *tcp1*^{H72fs} frameshift mutant zebrafish line

To generate stable *tcp1*^{H72fs} mutants, wild-type zebrafish embryos (AB strain) were injected with the 'gRNA + Cas9 only' mix detailed in Table 2.12 and raised to adulthood. Adult founders were then outcrossed to AB zebrafish and F1 offspring were screened by HRM analysis to identify offspring that had inherited CRISPR-induced mutations in *tcp1*. Sequencing analysis of these F1 offspring confirmed that one founder was transmitting a mutant *tcp1* allele (*tcp1*^{H72fs}) harbouring a 2 bp deletion, which shifts the reading frame and results in a premature stop codon (Figure 4.7). Heterozygous F1 offspring were outcrossed to wild-type fish for one further generation to generate F2 heterozygotes, which were incrossed to produce homozygous mutants for phenotypic analysis. As the small deletion in this line did not disrupt any restriction sites, offspring were genotyped by Sanger sequencing.

2.2.11 RNA extraction

2.2.11.1 RNA extraction from zebrafish larvae

Pools of up to 10 larvae per genotype were homogenised in 200 µl TRIzol® and 40 µl chloroform was added to each tube. Samples were shaken by hand for 15 s, incubated at room temperature for 2-3 min and centrifuged at 12,000 x g for 15 min at 4°C to allow phase separation. The aqueous phase was transferred to a new tube and 100 µl 100% isopropanol was added to precipitate RNA. Samples were then incubated at room temperature for 10 min and centrifuged at 12,000 x g for 10 min at 4°C to pellet RNA. RNA pellets were washed in 75% (v/v) ethanol before undergoing a final centrifugation step at 7,500 x g for 5 min at 4°C. Pellets were then resuspended in 9 µl nuclease-free water and RNA concentration was measured using a NanoDrop™ 1000 spectrophotometer.

2.2.12 Reverse transcription

To synthesise cDNA from zebrafish RNA extracts, contaminating genomic DNA was firstly removed by assembling a 10 µl reaction containing 1 µl DNaseI, 1 µl DNase buffer, and 1 µg RNA and incubating for 10 min at 37°C. The reaction was then terminated by adding 1 µl 25 mM EDTA, pH 8.0 to each sample and incubating for a further 10 min at 75°C. Samples were incubated on ice for 5 min, then 4 µl 5 x qScript cDNA SuperMix (Quantabio, Cat. No. 95048-025) was added to each sample, along with nuclease-free water to give a total reaction volume of 20 µl. Samples were incubated for 5 min at 25°C followed by 30 min at 42°C to facilitate reverse transcription, and the reverse transcriptase was inactivated with a final 5 min incubation at 85°C.

2.2.13 Quantitative real-time PCR (qPCR)

Reaction mixes were assembled to contain 1 x HOT FIREPol® EvaGreen® qPCR Supermix (Solis Biodyne), forward and reverse primers at concentrations detailed in Table 2.6, 1 µl cDNA template (diluted 1/25), and d.H_2O to give a final reaction volume of 20 µl. Reactions for each target gene primer pair and cDNA sample were performed in triplicate, and separate triplicate reactions for the reference gene (*eef1a* for all experiments) were performed on the same plate. DNA was amplified and melted using a CFX96 Touch Real-Time PCR Detection System (Bio-Rad), according to the 'qPCR programme' cycling parameters detailed in Table 2.15. Cycle threshold (Ct) values for each reaction were then extracted using the Bio-Rad CFX Manager™ software, and the relative mRNA expression for each target gene was calculated using the previously described $2^{-\Delta\Delta Ct}$ method (Schmittgen and Livak, 2008), according to the following formula:

where:

$\Delta Ct_{.sample}$ = difference in Ct value between target and reference genes for individual wild-type or mutant zebrafish cDNA samples

$\Delta Ct_{.control}$ = mean difference in Ct value between target and reference genes, averaged across three independent wild-type zebrafish cDNA samples

Table 2.15 Cycling parameters used for qPCR of zebrafish DNA

Programme name	Step		Temperature (°C)	Duration (s)	Number of cycles
qPCR programme	Initial denaturation		95	600	-
	PCR	Denaturation	95	30	39
		Annealing	60	60	
			PLATE-READ		
	Melting		95	60	
			65-95 (+0.5°C/cycle, Ramp 0.5°C/s)	5	
			PLATE-READ *(after each 0.5°C temperature increment)*		

2.2.14 Molecular cloning

2.2.14.1 TOPO-TA cloning

The TOPO® TA Cloning® Kit detailed in Table 2.9 was used to clone *Taq* polymerase-amplified PCR products generated by the 'Standard PCR' described on page 67. Briefly, a 6 µl ligation mix, containing 1 µl of PCR product, 1 µl Salt Solution, 3 µl d.H_2O and 1 µl pCR™4-TOPO® vector was gently mixed and incubated for 5 min at room temperature, before being transferred onto ice.

2.2.14.2 Bacterial transformation and antibiotic selection

Following ligation of the PCR product into the vector, plasmids were transformed into XL10-Gold® Ultracompetent *E. coli* cells (Agilent, Cat. No. 200314). Briefly, 25 µl cells were transferred into a pre-chilled Eppendorf on ice, and 2 µl of the ligation mix was added to the cells, along with 1 µl β-mercaptoethanol. The tube was gently flicked to mix the cells, before incubating on ice for 30 min. The cells were then heat shocked at 42°C for 30 s, before being incubated on ice for 2 min. Following heat shock, 250 µl LB broth (25 g LB broth powder in 1 L d.H_2O) was added to the cells and they were incubated for 1 h at 37°C on an orbital shaker. Cells were then plated onto LB agar (40 g LB agar powder in 1 L d.H_2O) plates containing ampicillin (100 µg/ml) for selection of resistant bacteria and incubated overnight at 37°C to allow colony formation. The following day, single colonies were picked and used to inoculate individual 5 ml LB broth cultures containing ampicillin (100 µg/ml). Cultures were then incubated overnight at 37°C on an orbital shaker to allow bacterial growth.

2.2.14.3 Plasmid DNA purification

LB broth cultures were centrifuged at 4°C for 10 min at 3,893 x g to pellet bacteria. The NucleoSpin® Plasmid Kit (detailed in Table 2.9) was then used to purify plasmid DNA, according to the manufacturer's protocol. Briefly, cells were lysed by sodium dodecyl sulphate (SDS)/alkaline lysis, and the lysates were clarified. Lysates were then centrifuged through a DNA binding column at 11,000 x g, the column was washed and dried, and plasmid DNA was eluted in 50 µl AE elution buffer. Sample DNA concentration was measured using a NanoDrop™ 1000 spectrophotometer.

2.2.15 Digoxigenin (DIG)-labelled *in situ* hybridisation probe synthesis

2.2.15.1 Template preparation

RNA was extracted and cDNA was synthesised from a pool of 3 dpf wild-type zebrafish larvae (as described on pages 72 and 73). An ~800 bp region of the *tcp1* cDNA sequence was then amplified by PCR (as described on page 67), using the *tcp1* ISH probe synthesis primers detailed in Table 2.5. The PCR product was then TA-cloned into the pCR™4-TOPO® vector (as described on page 74), and plasmid DNA was transformed and purified (as described on page 75).

TA cloning allows bidirectional ligation of the PCR product into the pCR™4-TOPO® vector. Because the T7 promoter required for transcription of the RNA probe is located downstream of the insert site, an insert oriented in the forward direction will be transcribed as an antisense probe (which can be used for detection of sense transcripts) and an insert oriented in the reverse direction will be transcribed as sense probe (which can be used for detection of antisense transcripts). We therefore determined the orientation of the inserts in our purified plasmids by PCR, using an M13 reverse primer and either the forward or reverse primer used to generate the insert, and then selected appropriate plasmids to generate our sense and antisense *tcp1* probes.

Plasmid DNA was subsequently linearised by digestion with *Spe*I, then an equal volume of phenol:chloroform:isoamyl alcohol (25:24:1) (Sigma, Cat. No. P3803) was added and samples were centrifuged at 15,800 x g for 30 s to allow phase separation. The aqueous phase was then transferred to a fresh tube and DNA was precipitated in 0.5 x volumes of 7.5 M ammonium acetate and 2.5 x volumes of 95% (v/v) ethanol for 1 h at -20°C. Samples were centrifuged at 15,800 x g for 10 min at 4°C and DNA pellets were washed in 70% (v/v) ethanol in nuclease-free water. The

pellets were then dried at room temperature for 5-10 min and resuspended in 20 µl nuclease-free water.

2.2.15.2 In vitro transcription

A transcription reaction was assembled to contain 1 µg purified linear plasmid DNA, 2 µl 10 x transcription buffer (Roche), 2 µl 10 x DIG RNA Labelling mix (Roche), 2 µl T7 RNA polymerase (Roche), and nuclease-free water to give a final reaction volume of 20 µl. The reaction was then incubated at 37°C for 2 h to allow transcription to take place.

2.2.15.3 Probe purification

Following transcription, template DNA was removed by adding 2.5 µl DNaseI and 2.5 µl DNase buffer and incubating at 37°C for 30 min. Probe RNA was then precipitated overnight at -80°C in 1.3 µl 7.5 M lithium chloride and 75 µl 100% ethanol. Samples were centrifuged at 15,870 x g for 20 min at 4°C to pellet RNA, pellets were washed in 100 µl 70% (v/v) ethanol, and then samples were centrifuged for a further 15 min at 15,870 x g. Pellets were then air-dried at room temperature for 5 min, resuspended in 50 µl nuclease-free water, and rehydrated on ice for 15 min. 50 µl formamide was then added to each sample and probes were stored at -20°C.

2.2.16 Whole-mount *in situ* hybridisation

Embryos for *in situ* hybridisation experiments were generated by incrossing F2 heterozygous *tcp1*^{P73L} or *tcp1*^{I57fs} mutant fish. Following overnight fixation in 4% (w/v) paraformaldehyde (PFA) and storage at -20°C in 100% methanol, embryos were washed once in 50% (v/v) methanol/phosphate-buffered saline (PBS) (137 mM NaCl, 2.7 mM KCl, 4.3 mM Na_2HPO_4,1.4 mM KH_2PO_4 in nuclease-free water), then four times (5 min per

wash) in PTW (PBS + 0.1% (v/v) Tween-20) on a benchtop rocker. Embryos were then permeabilised by incubating for 10 min in 10 µg/ml proteinase K in PTW. After proteinase K treatment, embryos were re-fixed in fish fix solution (20 mM NaH_2PO_4, 80 mM Na_2HPO_4, 4% (w/v) PFA and 4% (w/v) sucrose in nuclease-free water) for 20 min at room temperature and washed a further five times in PTW (5 min per wash). Embryos were rinsed in 300 µl cheap hybridisation buffer (50% (v/v) formamide, 5 x saline-sodium citrate (SSC) buffer (from a 20 x SSC stock solution containing 3 M NaCl and 341.8 mM $Na_3C_6H_5O_7$), 0.1% (v/v) Tween-20 and 9.2 mM citric acid, made up in nuclease-free water), before undergoing prehybridisation in 300 µl full hybridisation buffer (50% (v/v) formamide, 5 x SSC buffer, 0.1% (v/v) Tween-20, 9.2 mM citric acid, 0.5 mg/ml yeast tRNA (Sigma) and 50 µg/ml porcine heparin sodium salt (Sigma), made up in nuclease-free water) for 2-3 h at 68°C. Sense and antisense DIG-labelled *tcp1* probes were diluted 1/200 in full hybridisation buffer and pre-heated to 68°C, and embryos were incubated with 300 µl probe mix overnight at 68°C.

The following day, embryos were washed for 20 min at 68°C in a mix containing equal volumes of cheap hybridisation buffer and 2 x SSC, followed by a further 20 min in 2 x SSC, then twice in 0.2 x SSC (1 h per wash), with all buffers being preheated to 68°C before use. Embryos were then washed on a benchtop rocker at room temperature for 10 min in a mix containing equal volumes of 0.2 x SSC and blocking buffer (0.1% (v/v) Tween-20, 2% (v/v) sheep serum (Sigma) and 0.2% (w/v) bovine serum albumin (BSA; Sigma) in PBS), then for a further 10 min in blocking buffer only, before being incubated in blocking buffer for 2-3 h. Embryos were then incubated at 4°C overnight with alkaline phosphatase-conjugated anti-DIG Fab antibody fragments (Roche), diluted 1/2000 in blocking buffer.

Following antibody incubation, six 20 min washes in PTW were performed at room temperature on a benchtop rocker. Embryos were then washed four times (10 min per wash) in staining buffer (100 mM Tris-HCl pH 9.5, 50 mM $MgCl_2$, 100 mM NaCl and 0.1% (v/v) Tween-20 in nuclease-free water), then transferred to a 12-well plate with 1 ml of

staining buffer containing 3.5 µl 5-bromo-4-chloro-3-indolyl-phosphate (BCIP; Roche) and 4.5 µl 4-nitro blue tetrazolium chloride (NBT; Roche). Embryos were incubated for approximately 30 min in the dark to allow the stain to develop, then washed three times (5 min per wash) in PTW. Embryos were then re-fixed overnight in fish fix solution at 4°C and transferred through a glycerol series (10% → 25% → 50% → 75% (v/v) glycerol in PBS), allowing embryos to sink to the bottom of the tube before transferring to the next solution, before being mounted onto glass microscope slides for imaging, with heads oriented dorsally and tails oriented laterally. Bright field images were then captured with a 10x objective on an Olympus BX51 microscope, using a MicroPublisher 6™ CCD Camera (QImaging).

2.2.17 Gross morphological quantification

Larvae used for gross morphological analyses were generated by incrossing F2 heterozygous *tcp1*^{P73L}, *tcp1*^{I57fs} or *tcp1*^{H72fs} mutants. To quantify larval gross morphology, 4 dpf zebrafish larvae were anaesthetised and placed under a dissecting microscope. Images of individual laterally oriented larvae were then captured using an Apex Minigrab camera. NIH ImageJ (Rashband, NIMH, Bethesda, MD) was used to quantify the size of the eyes and head, and the total body length, of each fish by drawing regions of interest as illustrated in Figure 2.4. Data were then plotted and statistically analysed using GraphPad Prism version 7.0.3.

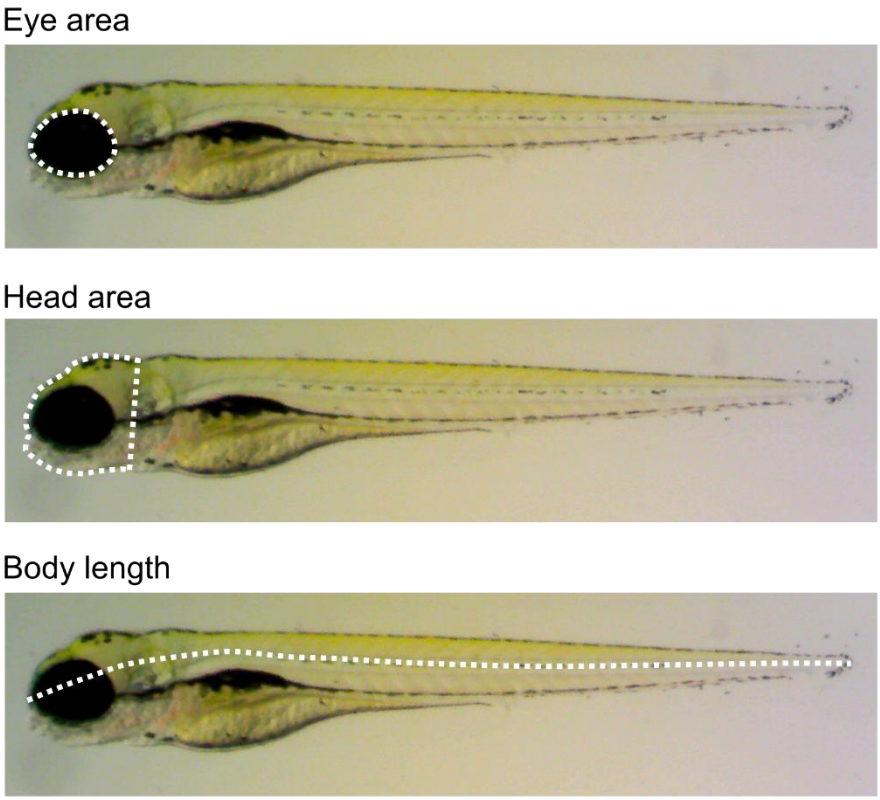

Figure 2.4. Representative images showing regions of interest used to quantify eye size, head size and total body length of zebrafish larvae. To quantify eye size, a region of interest was drawn around the perimeter of the eye and the area of the region was measured. To quantify head size, a region of interest was drawn around the perimeter of the region of the head located anterior to the heart and the area of the region was measured. To quantify body length, the line selection tool was used to draw a line along the anterior-posterior axis of the larva, following the body curvature, and the length of the line was measured.

2.2.18 Whole-mount antibody and phalloidin staining

2.2.18.1 Whole-mount immunofluorescence

Larvae for whole-mount immunofluorescence experiments were generated by incrossing F2 heterozygous *tcp1*^{P73L} or *tcp1*^{I57fs} mutant fish. Larvae were firstly fixed in 4% (w/v) PFA overnight at 4°C and were then washed three times in PBS (5 min per wash). For pigmented larvae, a solution containing 3% (v/v) H_2O_2 and 0.5% (w/v) KOH in PBS was used to bleach larvae before washing for a further 5 min in PBS. Larvae were then washed five times in 1% (v/v) Triton X-100 in PBS (PBST) and permeabilised at room temperature in 0.25% (v/v) trypsin for 15 min (3 dpf larvae) or 25 min (5 dpf larvae).

Trypsin activity was quenched at the appropriate time point by adding an equal volume of 1% (v/v) goat serum in PBST to each tube and larvae were then washed five times in PBST (5 min per wash). Larvae were blocked in a solution containing 10% (v/v) goat serum, 1% (w/v) BSA and 1% (v/v) DMSO in PBST for 1-3 h at room temperature to prevent non-specific antibody binding. Primary antibodies were then diluted in an antibody dilution buffer containing 5% (v/v) goat serum, 1% (w/v) BSA and 1% (v/v) DMSO in PBS, as detailed in Table 2.16, and larvae were incubated with antibodies overnight at 4°C.

Table 2.16 Primary antibody dilutions used for whole-mount immunofluorescence

Antibody	Dilution
rabbit anti-cleaved caspase 3	1/1000
mouse anti-acetylated tubulin	1/1000
mouse 3A10	1/800

*Supplier details for all antibodies can be found on page 60

Following primary antibody incubation, larvae were washed for a minimum of 3 h at room temperature in PBST, with at least 5 changes of PBST. Fluorophore-

conjugated secondary antibodies (details on page 60) were then diluted to 1/1000 in antibody dilution buffer, and larvae were incubated with secondary antibodies overnight at 4°C in the dark. The following day, larvae were washed for a minimum of 3 h at room temperature in PBST, with at least 5 changes of PBST. Nuclei were then counterstained by incubating larvae at 4°C for 1-2 days in 2 µg/ml 4′,6-diamidino-2-phenylindole (DAPI) in PBS. Larvae were then washed three times in PBS and transferred through a glycerol series (25% → 50% → 75% (v/v) glycerol in PBS), allowing larvae to sink to the bottom of the tube before transferring to the next solution. Larvae were then mounted onto glass slides for confocal imaging (page 84), with heads oriented dorsally for 3A10, caspase and acetylated α-tubulin staining, and tails oriented laterally for acetylated α-tubulin staining.

2.2.18.2 Whole-mount phalloidin staining

Larvae for whole-mount phalloidin staining were generated by incrossing F2 heterozygous *tcp1*^{P73L} or *tcp1*^{I57fs} mutant fish. Larvae were fixed and bleached as described for whole-mount immunofluorescence (page 81) and then permeabilised for 2 h in 2% (v/v) Triton X-100 in PBS at room temperature. Larvae were then incubated for 2 h at 4°C with Alexa Fluor™ 647- or Alexa Fluor™ 555-conjugated Phalloidin (Invitrogen, Cat. No. A22287/A34055) diluted 1/20 in 2% (v/v) Triton X-100 in PBS. Larvae were then washed times in PBS (5 min per wash), before being transferred through a glycerol series as described for whole-mount immunofluorescence. Tails were then mounted laterally on glass slides for confocal imaging.

2.2.19 Immunostaining retinal cryosections

2.2.19.1 Cryosectioning

Larvae for cryosectioning were generated by incrossing F2 heterozygous *tcp1*^{P73L} or *tcp1*^{I57fs} mutant fish. Larvae were fixed overnight in 4% (w/v) PFA and then cryoprotected in a solution of 30% (w/v) sucrose in PBS overnight at 4°C. Larvae were then embedded in optimal cutting temperature (OCT) embedding matrix (CellPath) and frozen at -80°C. Serial 14 µm transverse sections were then taken through the eyes of the larvae using a Leica CM1860 cryostat, set to -18°C, and sections were transferred to SuperFrost Plus™ Adhesion slides (Thermo Fisher Scientific). Slides were left to dry at room temperature for a minimum of 1 h, before being stored at -20°C

2.2.19.2 Immunostaining

Slides were removed from the freezer and briefly washed in PBS to remove OCT. Antigen retrieval was then performed in 150 mM Tris-HCl, pH 9.5, using an antigen access unit set to 120°C. Slides were then washed once in PBS, and sections were blocked for 1 h at RT in blocking solution (1% (w/v) BSA, 10% (v/v) goat serum, 0.1% (v/v) Tween-20 and 0.4% (v/v) Triton X-100 in PBS). Sections were then incubated overnight at 4°C in primary antibodies diluted in blocking solution, as detailed in Table 2.17.

Table 2.17 Primary antibody dilutions used for immunofluorescence on retinal cryosections

Antibody	Dilution
mouse zpr-3	1/100
rabbit anti-cleaved caspase 3	1/100
rabbit anti-rhodopsin	1/100

*Supplier codes for all antibodies can be found on page 60

The following day, slides were washed three times in PBS (20 min per wash), before being incubated in fluorophore-conjugated secondary antibodies (as detailed on page 60) diluted 1/1000 in blocking solution for 1.5 h at room temperature. Slides were then washed a further three times in PBS (20 min per wash), with the addition of 10 µl DAPI in the final wash to counterstain nuclei. Coverslips were then mounted onto the slides using fluorescence mounting medium (Dako) and slides were stored at 4°C prior to imaging.

2.2.20 Confocal microscopy

All fluorescently-stained samples were imaged with a Leica SP5 confocal microscope, using a 20x air objective unless otherwise stated. To image larvae immunostained with 3A10 antibody, z-stacks (5 µm slices) were taken through the entire depth of the Mauthner neurons and maximum intensity z-projections were assembled in ImageJ. For the brains of larvae immunostained with anti-acetylated α-tubulin antibody, images were captured through a single focal plane within the optic tectum. To image the motor axons of larvae immunostained with anti-acetylated α-tubulin antibody, z-stacks (5 µm slices) were taken through one side of the trunk and maximum intensity z-projections were assembled in ImageJ. For the brains of transgenic larvae expressing FyntagRFP-T in Purkinje cells, z-stacks (10 µm slices) were taken through the cerebellum and maximum intensity z-projections were assembled in ImageJ. For brains of larvae immunostained with anti-cleaved caspase 3 antibody, z-stacks (10 µm slices) were taken through the optic tectum and maximum intensity z-projections were assembled in ImageJ. To image phalloidin-stained skeletal muscle fibres, images were captured through a single focal plane in the lateral region of the trunk, immediately posterior to the end of the yolk sac extension. To image fluorescently-stained retinal cryosections, z-stacks (1.5 µm slices) were taken through the samples and maximum intensity z-projections were assembled in ImageJ. To obtain higher magnification DAPI-stained images of the brain, z-stacks (10 µm slices) were

taken through the optic tectum using a 40x oil immersion objective, and maximum intensity z-projections were assembled in ImageJ.

2.2.21 Larval locomotor function assays

To test the larval locomotor response to alternating light and dark stimuli, larvae were arrayed into wells of a 96-, 24-, or 12-well plate at 5, 8 or 12 dpf, respectively, and spontaneous swimming was recorded using the ZebraLab system (ViewPoint Behavior Technology). Before motion tracking commenced, larvae underwent 30 min habituation to the soundproof ZebraBox apparatus with the light turned on, then spontaneous swimming was tracked over three consecutive light/dark cycles (1 cycle = 5 min dark, 5 min light). For all experiments, speed (x) thresholds for swimming were set as follows: $x < 5$ mm/s = no movement, 5 mm/s ≤ $x < 10$ mm/s = slow movement, $x \leq 10$ mm/s = fast movement). An R script was generated to calculate the total swimming distance (distance swum during slow movement + distance swum during fast movement), total active duration (duration of slow movement + duration of fast movement) or average duration of fast or slow swimming for individual fish across each 5 min period from the output files generated by the ZebraLab software. Data were then combined across experimental repeats, grouped by genotype, and plotted in GraphPad Prism version 8.3.1.

To capture slow-motion videos of larval touch-evoked escape responses, individual 3 dpf control or *tcp1*^{I57fs} mutant larvae were firstly placed into the centre of a petri dish containing E3 medium under a dissecting microscope. A slow-motion video (240 frames per second (fps)) of larval response to a light touch on the tail with a teasing needle was then generated using an iPhone 7 mounted to the microscope eyepiece. Every 24th frame was then extracted from the video as an image (equivalent to one image every 100 ms in real time) using VLC Media Player, starting from the point at which the needle made contact with the tail.

2.2.22 Adult locomotor function assay

To test adult locomotor function, fish were generated by incrossing F2 heterozygous *tcp1*^{P73L} mutants. Swimming endurance tests were conducted using a swim tunnel, as previously described (Chapman et al., 2013). Individual wild-type or mutant zebrafish were placed into the tunnel and water was flowed through the tunnel at an initial speed of 6.57 cm/s. The speed was increased by a further 6.57 cm/s every 5 min until the fish reached exhaustion and could no longer swim against the flow. Total body length was recorded for each fish following the swimming test. Time to exhaustion was used to calculate the critical swimming velocity (Ucrit) for each fish according to the formula:

$$Ucrit = \frac{Ui + \left(\frac{UiiTi}{Tii}\right)}{B}$$

where:

Ucrit = critical swimming velocity (body lengths/s)
Ui = the highest velocity maintained for a full 5 min period (cm/s)
Uii = the velocity increment (6.57 cm/s)
Ti = the time to exhaustion (s)
Tii = the time interval (5 min)
B = body length (cm)

2.2.23 Larval colour preference assay

Larval colour preference was measured using an acrylic cross maze formed of four transparent arms surrounded by removable transparent coloured sleeves (red, green, blue or yellow), which was constructed by Dr Paweł Łysyganicz based on the maze described by (Park et al., 2016). A schematic illustration of the cross maze is shown in Figure 2.5. Wild-type or mutant zebrafish larvae (n = 6-8 per genotype, per experimental replicate) were placed into the maze with E3 medium lacking methylene blue. The maze was placed into the ViewPoint ZebraBox apparatus and larval activity was filmed from above the maze for 15 min. To quantify larval colour preference, the number of larvae located in each arm of the maze was counted every 10 s for the final 10 min of each video. This was used to

calculate the mean proportion of the group occupying each coloured arm across the 10 min. To mitigate the possibility of any non-colour-related bias toward specific arms, the arrangement of the coloured sleeves around the maze was altered between experiments.

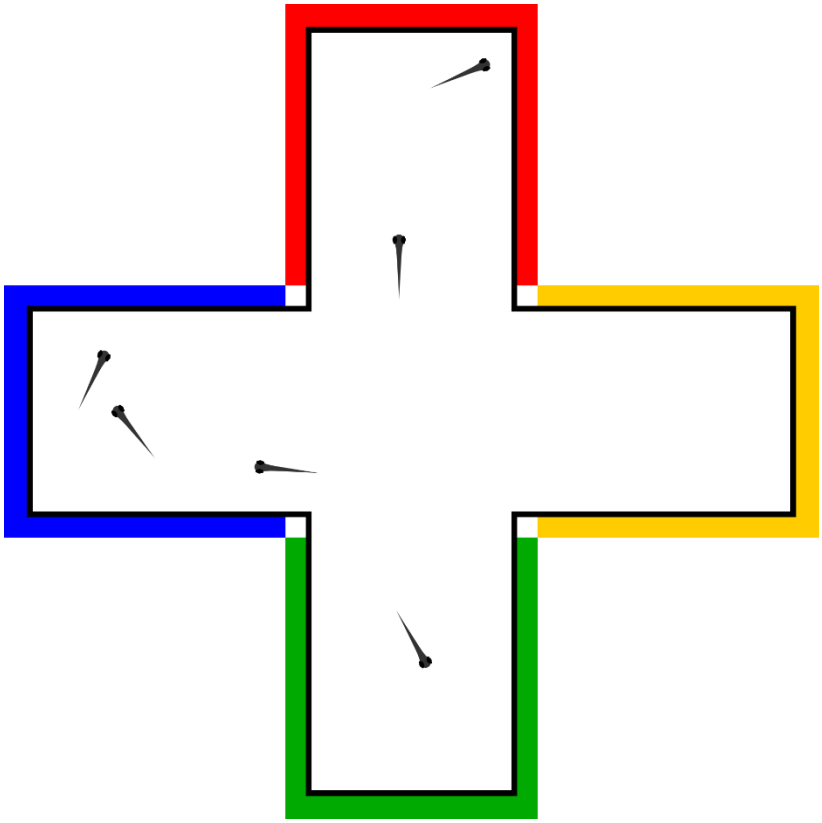

Figure 2.5 Schematic illustration of the cross maze used to assay larval colour vision.

Chapter 3

Generating new mutant zebrafish lines to genetically model *TCP1*-related disease

3.1 Introduction

As we outlined in Chapter 1, the *TCP1*^{P70L} variant has only been reported in three patients from a single family to date, and we do not currently know of any other *TCP1* mutations that have been linked to human disease. We therefore devised two hypotheses: a) that the *TCP1*^{P70L} mutation is the cause of the patients' phenotypes and b) that *TCP1* plays an important role in the tissues implicated in the disease. To test these hypotheses, our goal was to experimentally model the disease, using the zebrafish as a model system.

Although *in vitro* and cell-based disease models can provide helpful insights into the molecular and biochemical functionality of novel genetic variants, it is often more informative to study the consequences of these mutations in the context of a whole organism. This is especially important when studying disorders in which multiple cell types and tissues may be affected by the mutation. The zebrafish is especially well-suited to such investigations; it has a fully sequenced and highly conserved vertebrate genome, and its fast-developing and optically transparent larvae allow the developmental effects of genetic mutations to be visualised in real time. Of relevance to the phenotypes associated with this disease, the zebrafish possesses a vertebrate nervous system which shares significant homology with the human nervous system. Zebrafish are also genetically manipulatable, and the scope for modelling genetic diseases in this system has been revolutionised by the field of CRISPR/Cas9 gene-editing technology. We therefore chose to generate a zebrafish model of *TCP1*-related disease, with a view to using the CRISPR/Cas9 system to precisely recapitulate the human *TCP1*^{P70L} variant in the zebrafish.

In this chapter, we describe the process of assessing the genetic suitability of the zebrafish for modelling *TCP1* mutations. We then describe the steps we took to design and test a CRISPR/Cas9-based approach for introducing the patients' mutation into the zebrafish

genome by HDR, and we present a screening strategy that allowed us to identify founders that were stably transmitting the mutation of interest to their offspring.

An additional rationale for studying novel rare disease-linked mutations is that they provide opportunities to gain insight into the normal functions of the affected gene. In the final part of this chapter, we describe how we generated a second mutant zebrafish line harbouring a frameshift mutation in *tcp1*, as a model for investigating the effects of loss of *tcp1* during vertebrate development.

3.2 Evaluating the genetic suitability of the zebrafish for modelling human *TCP1*-related disease

3.2.1 *TCP1* encodes an evolutionarily highly conserved protein

Orthologues for *TCP1* have been identified in over 130 species. We initially assessed the evolutionary conservation of the proteins encoded by these genes, focusing on the proline residue mutated in human patients (P70 of the human sequence) and key residues implicated in ATPase activity (Reissmann et al., 2012). The residues that are required for ATP binding and hydrolysis are fully conserved across diverse eukaryotic species (Figure 3.1a), indicating that ATP-dependent functions of TCP1 have been evolutionarily maintained. P70 is also highly conserved, pointing to a key role for this residue in the structure and/or function of the protein.

Similar conservation exists between TCP1 and other members of the TRiC/CCT chaperone complex (Figure 3.1b). All subunits possess the catalytic aspartic acid residue involved in ATP hydrolysis, and the ATP-binding ‘GDGTT’ motif is conserved across every subunit apart from CCT8. P70 is also conserved across seven of the eight subunits, further supporting the importance of this residue to TRiC/CCT function.

3.2.2 Zebrafish and human *TCP1* are highly conserved

To evaluate the suitability of zebrafish for genetically modelling human *TCP1*-related disease, we next examined the relationship between the zebrafish and human *TCP1* genes in further detail. We performed a BLAST search for the human TCP1 protein sequence against the zebrafish genome, revealing a single zebrafish orthologue for *TCP1* (*tcp1*) which shares 72% cDNA and 86% protein identity with the human sequence. The extensive homology between the two proteins is illustrated in Figure 3.2. Notably, the zebrafish sequence contains the key motifs required for ATP binding and hydrolysis, as well as the P70 residue (P73 in zebrafish) which is mutated in patients.

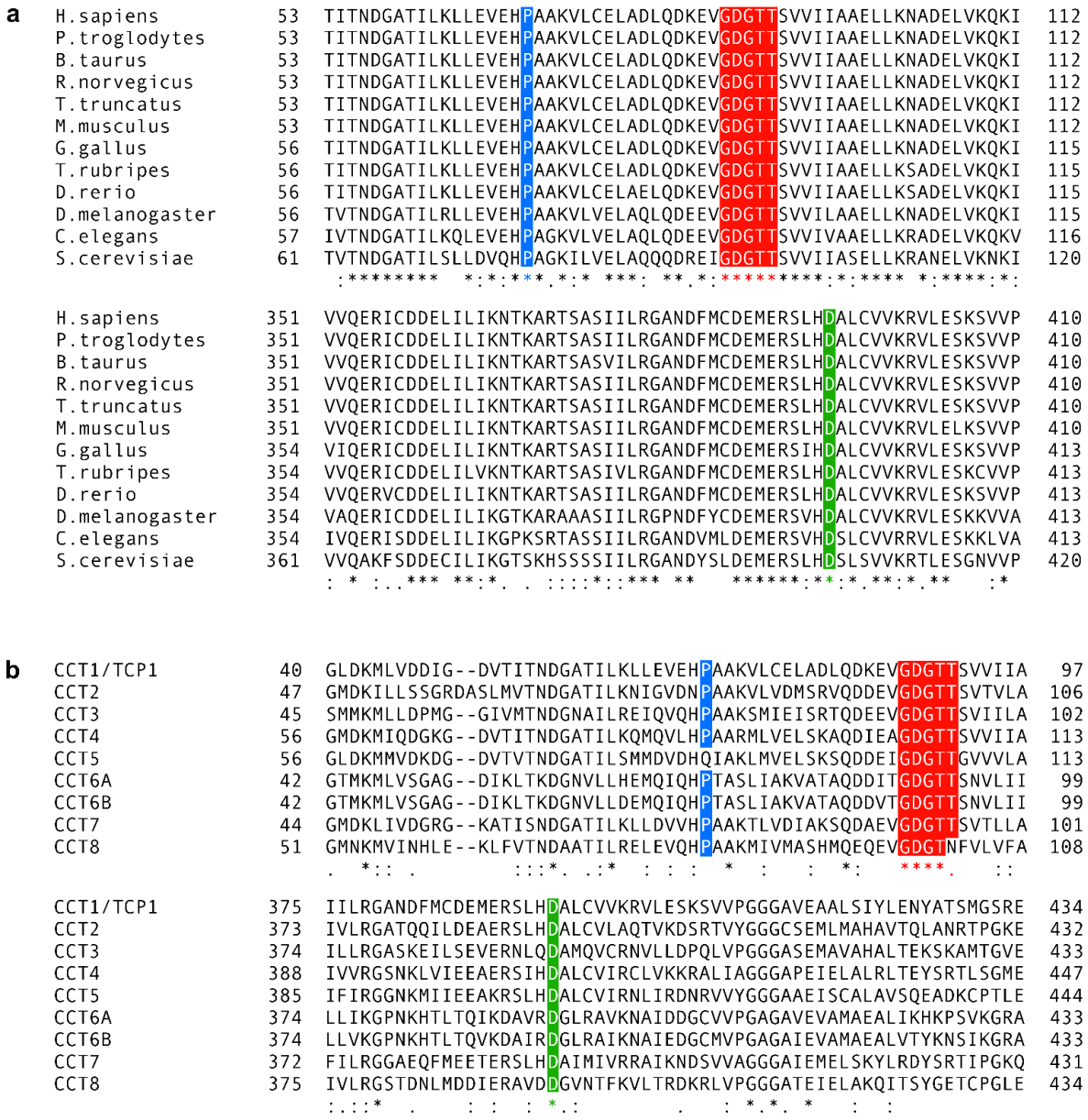

Figure 3.1. Protein sequence alignment of TCP1 reveals conservation of key residues across evolutionarily diverse species and TRiC/CCT subunits. (**a**) Multiple sequence alignment of TCP1 across species and (**b**) multiple sequence alignment of human TRiC/CCT subunits. The proline residue mutated in the human patients is highlighted in blue and key ATP binding and hydrolysis residues are highlighted in red and green, respectively. Sequences were aligned using the Clustal Omega Multiple Sequence Alignment tool (European Bioinformatics Institute). ***** denotes full conservation of a single residue across all sequences, **:** indicates conservation between residues sharing strongly similar properties and **.** denotes conservation between residues sharing weakly similar properties.

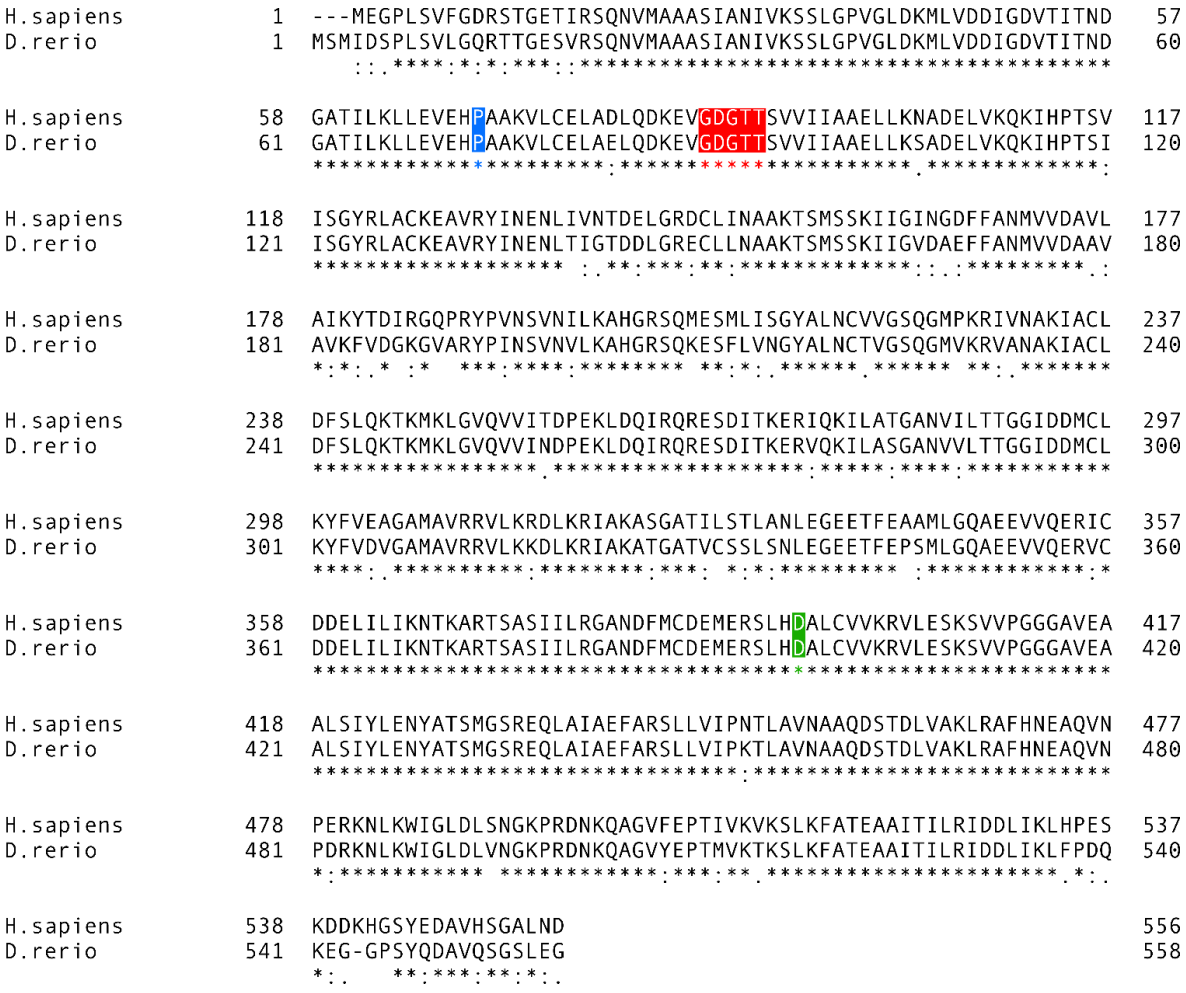

Figure 3.2. Alignment of the full protein sequences of human and zebrafish TCP1 reveals extensive sequence homology. The proline residue mutated in human patients (human P70/zebrafish P73) is highlighted in blue and key residues involved in ATP binding and hydrolysis are highlighted in red and green, respectively. Sequences were aligned using the Clustal Omega Multiple Sequence Alignment tool (European Bioinformatics Institute). ***** denotes full conservation of a single residue across all sequences, **:** indicates conservation between residues sharing strongly similar properties and **.** denotes conservation between residues sharing weakly similar properties.

3.3 Generating a *tcp1* knock-in mutant zebrafish line

3.3.1 Identifying polymorphisms in zebrafish *tcp1*

Before attempting to use CRISPR/Cas9 to generate a novel *tcp1* mutant zebrafish line to genetically model human *TCP1*-related disease, we determined whether there were any polymorphisms in exon 3 (containing the codon for P73) of zebrafish *tcp1.* Such polymorphisms could interfere with gRNA choice and downstream identification and genotyping of mutants.

We amplified the target region by PCR, using template DNA from three strains of wild-type zebrafish (16 embryos obtained from a total of 4 sets of parents for each strain), and sequenced the products. We identified two single nucleotide polymorphisms (SNPs) in intron 2-3 and one synonymous SNP in exon 3 (Figure 3.3). The only polymorphism we detected in the AB strain was the intronic SNP furthest from the codon for P73, so we chose to target AB strain zebrafish for mutagenesis.

a

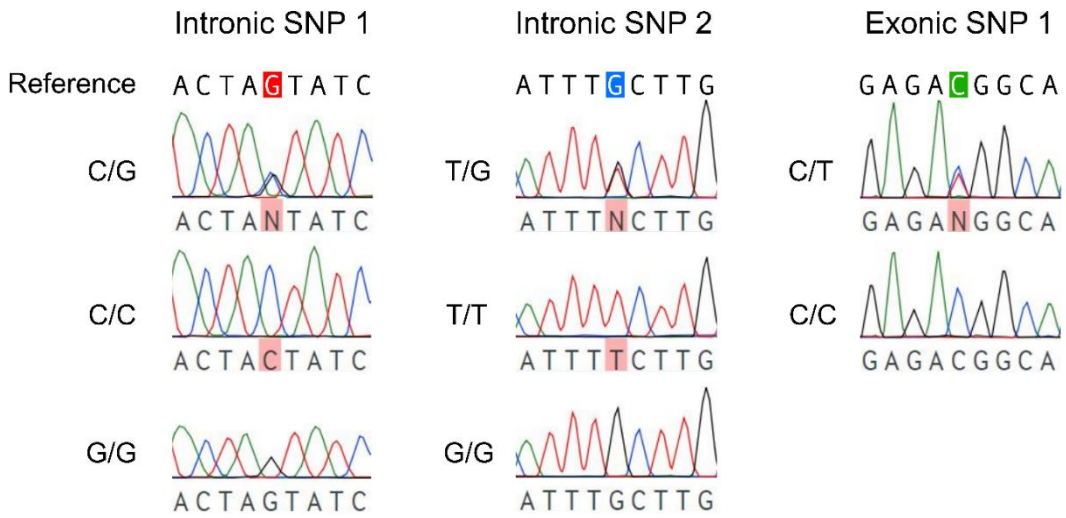

b

Intronic SNP 1

Genotype	Frequency (%)		
	AB	TL	WIK
C/G	43.7	100.0	50.0
C/C	0.0	0.0	25.0
G/G	56.3	0.0	25.0

Intronic SNP 2

Genotype	Frequency (%)		
	AB	TL	WIK
T/G	100.0	6.7	100.0
T/T	0.0	33.3	0.0
G/G	0.0	60.0	0.0

Exonic SNP 1

Genotype	Frequency (%)		
	AB	TL	WIK
C/T	0.0	20.0	0.0
C/C	100.0	80.0	100.0
T/T	0.0	0.0	0.0

c

acccaaccctagtgcttgtcttcacccgttggagtaactagtatccaagttttaagaccatt
tgcttgtgtgtttcag**GACGTGACCATCACCAATGACGGGGCCACCATCCTGAAGCTGCTGGA**
GGTCGAACACCCGGCTGCTAAAGTCCTCTGTGAGCTGGCAGAGCTGCAGGACAAGGAGGTTGG
AGACGGCACTACATCAGTGgtgagctgaagctgtgcattagcagattttcctgttatagtacc
atccatctgagctgcgtcggtgtgtgtggctatgctaacaggatacagaaaccctctcgg

Figure 3.3. Identification of three single-nucleotide polymorphisms (SNPs) in the target region of zebrafish *tcp1*. (**a**) Representative sequencing chromatograms illustrating each of the SNPs identified in *tcp1*. (**b**) Frequencies of each SNP in wild-type AB, TL and WIK zebrafish strains (n = 16 embryos per strain). (**c**) Locations of intronic SNP 1 (red), intronic SNP 2 (blue) and exonic SNP 1 (green) relative to exon 3 (bold) and the codon for proline 73 (yellow). Exon 3 is shown in uppercase, flanking introns are shown in lowercase, and binding sites for primers used to amplify the target region are underlined.

3.3.2 Designing a gRNA to target zebrafish *tcp1*

We used the Deskgen CRISPR gRNA design tool (deskgen.com/landing/#/cloud) to identify gRNA target sequences near the codon for P73. The ten gRNAs with target sequences closest to this codon are listed in Table 3.1 and illustrated in Figure 3.4a. We selected gRNA 6 due to the proximity of its Cas9 cleavage site to the codon for P73 (Figure 3.4a) and its high target and off-target scores compared with other gRNAs (Table 3.1). Deskgen returned a single predicted off-target hit for this gRNA, located within the apoptotic protease activating factor 1 gene (*apaf1*) on chromosome 4. However, the off-target sequence contains three mismatches with respect to the *tcp1* target sequence, so off-target activity is unlikely to arise at this locus. As an additional measure, we also conducted a BLAST search of the target sequence against the entire zebrafish genome, but we found no other loci where off-target activity is likely to arise.

Table 3.1. Details of *tcp1* gRNAs identified by Deskgen

Guide number	Target sequence	PAM	Exon	Activity score*	Off-target
1	CTCCAGCAGCTTCAGGATGG	TGG	3	55	89
2	GACCTCCAGCAGCTTCAGGA	TGG	3	60	90
3	GTTCGACCTCCAGCAGCTTC	AGG	3	36	89
4	GGCCACCATCCTGAAGCTGC	TGG	3	42	98
5	CACCATCCTGAAGCTGCTGG	AGG	3	59	95
6	GCTGCTGGAGGTCGAACACC	CGG	3	60	99
7	CACAGAGGACTTTAGCAGCC	GGG	3	52	97
8	TCACAGAGGACTTTAGCAGC	CGG	3	52	94
9	GCAGCTCTGCCAGCTCACAG	AGG	3	64	94
10	TGCTAAAGTCCTCTGTGAGC	TGG	3	49	97

*Higher activity score indicates greater predicted target activity.

#Higher off-target score indicates less predicted off-target activity.

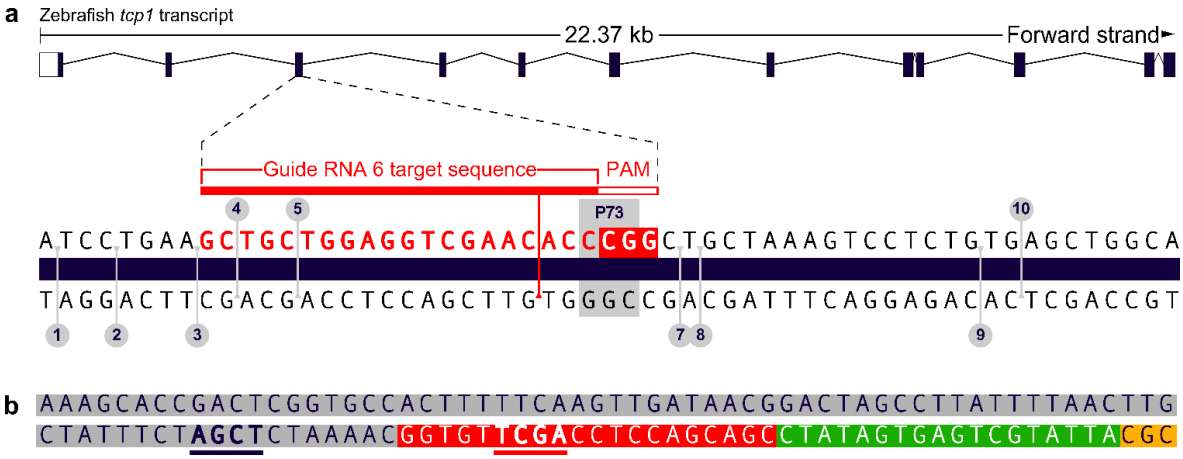

Figure 3.4. Designing a gRNA to target exon 3 of zebrafish *tcp1*. (**a**) Schematic diagram modified from Deskgen output showing a partial sequence of exon 3, annotated with the Cas9 cleavage sites for *tcp1* gRNAs 1-10, relative to the codon for P73 (highlighted in grey). The target sequence, PAM and Cas9 cleavage site for gRNA 6 are shown in red. (**b**) Sequence of the oligonucleotide template used to synthesise gRNA 6, highlighting the Cas9 scaffold sequence (grey), the target sequence of gRNA 6 in antisense orientation (red), the T7 promoter sequence (green) and the clamp sequence (yellow). *Alu*I and *Taq*I restriction sites (located within the Cas9 scaffold sequence and the gRNA target sequence, respectively) are shown in bold underline.

3.3.3 Synthesising *tcp1* gRNA

We designed an oligonucleotide template for *in vitro* gRNA synthesis (Figure 3.4b). First, we amplified the template by PCR to ensure that no impurities would be carried over from the oligonucleotide synthesis to the *in vitro* transcription reaction, but we detected a product in the negative control reaction (Figure 3.5a) which we were unable to eliminate by repeating the PCR using fresh reagents (data not shown).

The primers for this template bind within the regions of the template encoding the Cas9 scaffold and T7 promoter, so they can amplify from any gRNA template containing these generic sequences. To exclude the possibility that the PCR might have been contaminated by another gRNA template that we had used in the lab, we performed diagnostic restriction fragment length analysis using *Alu*I, which only cuts within the generic scaffold sequence, and *Taq*I, which only cuts within the specific *tcp1* gRNA target sequence (Figure 3.4b, Figure 3.5b).

The amplicon from the negative control reaction was digested by *Alu*I, but not *Taq*I (Figure 3.5c), suggesting that the contaminant is likely to be another gRNA oligonucleotide template. However, in the *TCP1* gRNA template-containing reactions, we detected restriction fragments of the expected lengths, with no residual undigested product after incubation with either enzyme (Figure 3.5b,c). The contaminant is therefore likely to be present at a low level, becoming outcompeted by the *TCP1* gRNA template in the template-containing reaction. On this basis, we concluded that the PCR product generated from the *TCP1* gRNA template was unlikely to be contaminated by another gRNA template and proceeded to gel purify the product and perform *in vitro* transcription to synthesise the *tcp1* gRNA.

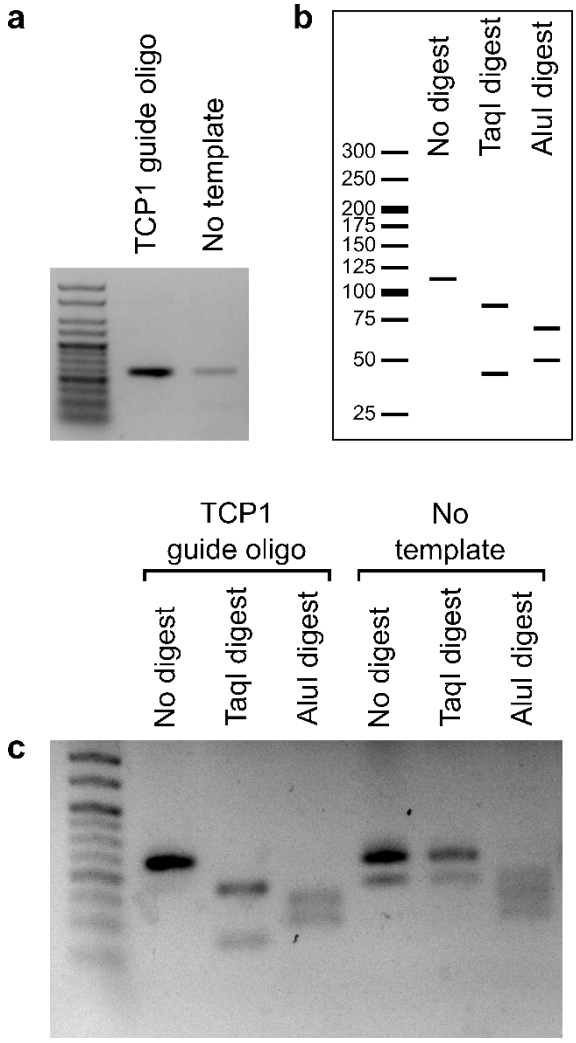

Figure 3.5. PCR amplification of the *tcp1* gRNA oligonucleotide template. (**a**) Gel electrophoresis of the PCR-amplified *tcp1* gRNA oligonucleotide template. (**b**) Schematic view of expected product sizes for undigested, *Taq*I-digested and *Alu*I-digested PCR-amplified *tcp1* gRNA oligonucleotide. (**c**) Gel electrophoresis of *Taq*I- and *Alu*I-digested PCR-amplified *tcp1* gRNA oligonucleotide. Gels: 2.5% agarose, markers: Hyperladder V (Bioline).

3.3.4 Mosaic mutations can be detected at the target site in zebrafish embryos injected with Cas9 and *tcp1* gRNA

Once we had synthesised the *tcp1* gRNA, we then assessed its *in vivo* activity by testing whether it could induce mutagenesis at the target site in zebrafish embryos. We microinjected wild-type embryos with a mix containing Cas9 protein and *tcp1* gRNA, before extracting DNA at 30 hpf. Typically, we would raise embryos to 48 hpf before extracting DNA, but on this occasion, we observed considerable toxicity in the *tcp1* gRNA-injected embryos and therefore extracted DNA at an earlier time point.

Following DNA extraction, we screened for CRISPR-induced mutagenesis by high-resolution melt (HRM) analysis of a short (116 bp) PCR product spanning the target site (Figure 3.6a). The melt profile of this amplicon was shifted in several of the injected fish compared to the non-injected controls (Figure 3.6b). For clarity, only embryos that displayed shifted melt profiles are shown in Figure 3.6b, though we also identified some embryos for which the melt profile of the amplicon was not shifted. The shifted melt profiles indicate that heteroduplexes of wild-type and mutant DNA were present in these samples, and we confirmed that we had successfully introduced mosaic mutations at the target site by Sanger sequencing analysis (Figure 3.6c). Both 2 nl and 4 nl injections produced sequencing results with additional peaks in the electropherogram, indicating that indels had been introduced following misrepair of the Cas9 cleavage site.

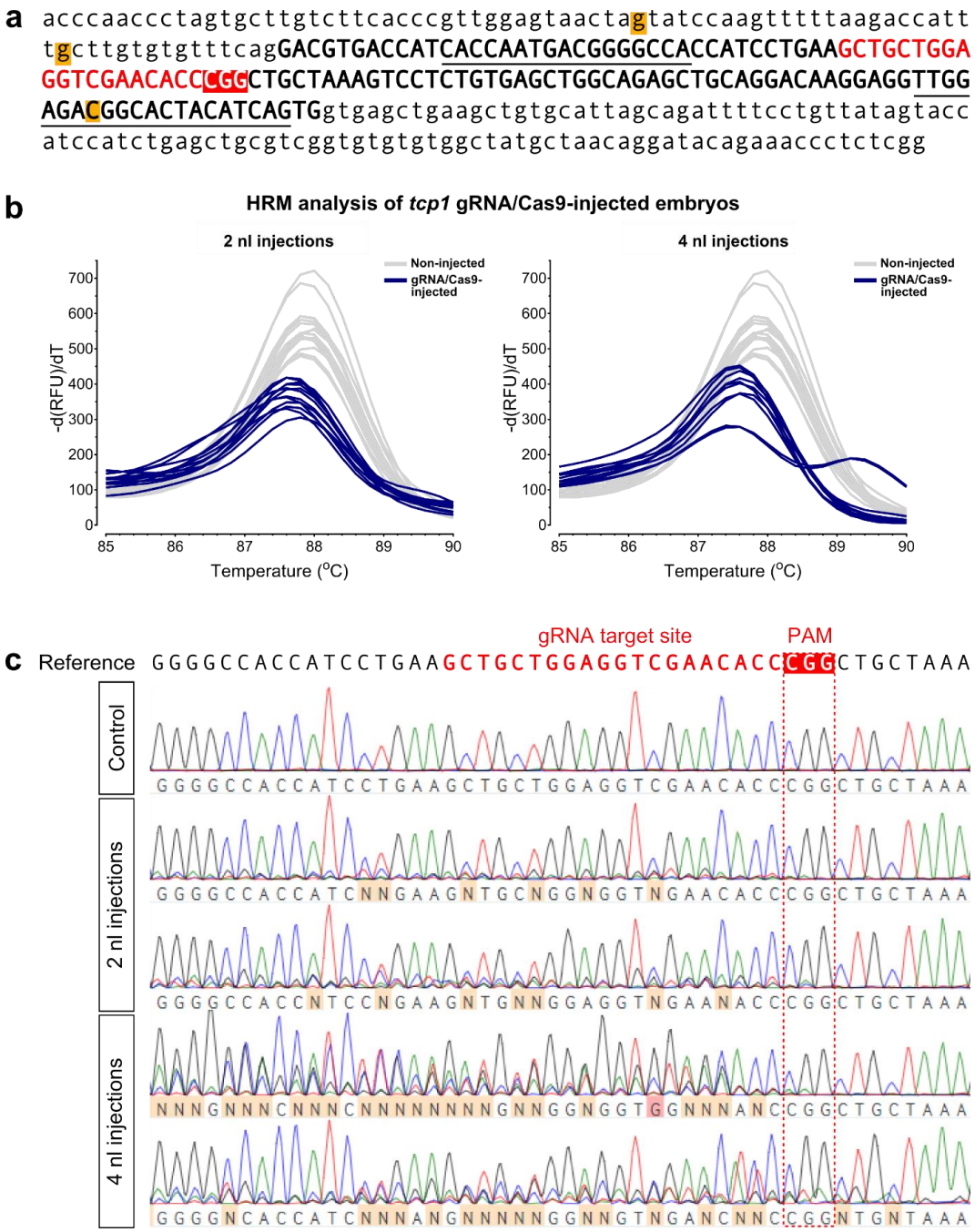

Figure 3.6. High-resolution melt (HRM) analysis and Sanger sequencing revealed successful mutagenesis of the target site in embryos injected with Cas9 and *tcp1* gRNA. (**a**) Binding sites for primers used to generate amplicons for HRM analysis (underlined), relative to the gRNA target sequence (red) and SNPs previously identified in the region (yellow). Exon 3 is shown in uppercase and flanking introns are shown in lowercase. (**b**) Melt peak graphs depicting shifts in the melt profiles of target site amplicons from gRNA/Cas9-injected embryos vs. non-injected controls. Each plot represents the melt profile for an individual HRM reaction and reactions were performed in duplicate for each DNA sample (n = 8 non-injected embryos, n = 5 injected embryos). (**c**) Representative Sanger sequencing chromatograms illustrating the presence of mosaic mutations at the target site in injected embryos.

3.3.5 Designing an oligonucleotide template to introduce the disease-linked missense mutation by HDR

Prior to generating our knock-in model, short single-stranded oligonucleotide repair templates, between 23 and 100 nt in length, had previously been used to successfully introduce pathogenic point mutations into the zebrafish *tardbp* and *fus* genes by HDR (Armstrong et al., 2016). We therefore designed a 65-nt single-stranded oligonucleotide to serve as a repair template for HDR and generate our *tcp1* P73L knock-in zebrafish line (Figure 3.7a). This template contains a point mutation encoding the P73L missense variant, as well as three synonymous point mutations located within the gRNA target sequence; these have no impact at the protein level but should prevent further gRNA binding and Cas9 cleavage following successful HDR. Where possible, we codon-optimised these mutations for efficient expression in zebrafish. Through introducing the mutations, we also created a novel *Xho*I restriction site and disrupted an existing *Msp*I restriction site (Figure 3.7b) to allow HDR mutant zebrafish to be identified by restriction fragment length analysis. It is worth noting, however, that the *Msp*I site can also be disrupted by NHEJ-mediated repair if indels are introduced into the target site. Finally, the mutated region of the template is flanked by two short (25-nt) homology arms to facilitate recombination with the genomic DNA.

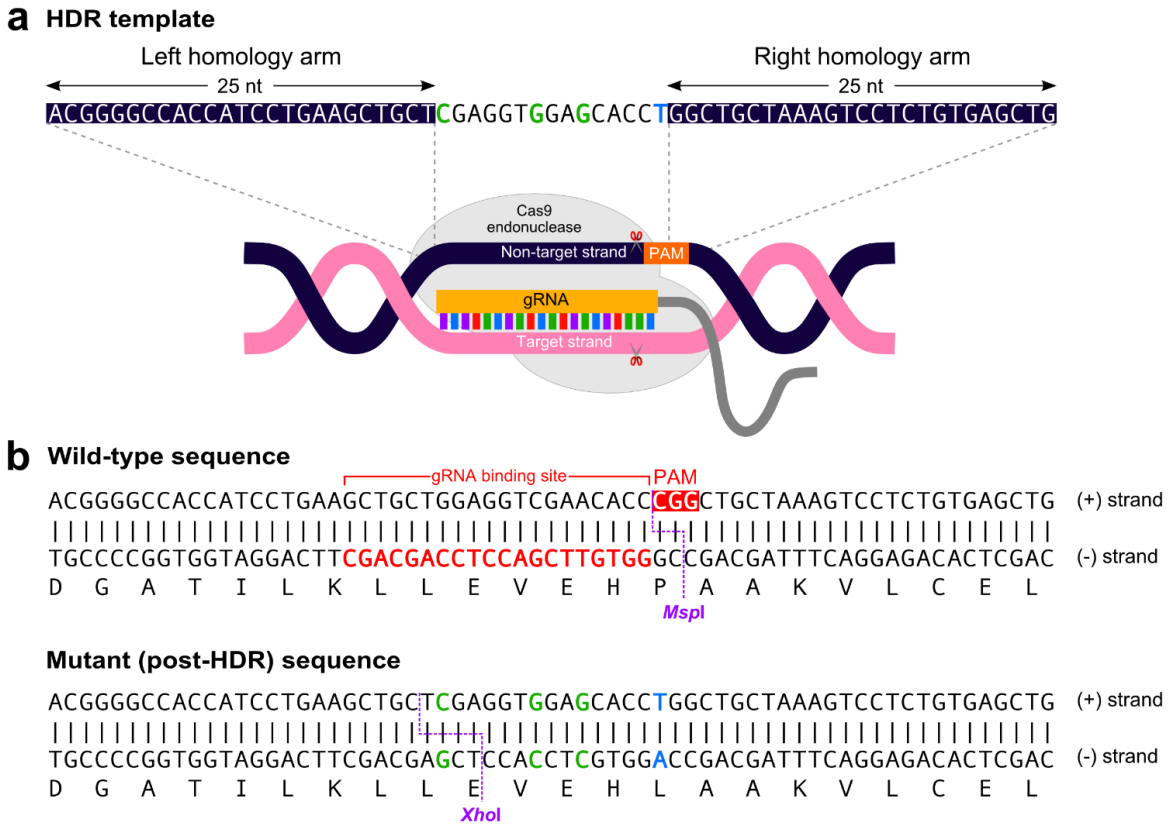

Figure 3.7. Sequence of the HDR template designed to generate *tcp1* knock-in mutant zebrafish. (**a**) HDR template sequence, highlighting the single-nucleotide substitution encoding the P73L mutation (blue), the synonymous gRNA target site mutations (green) and the 25-nt homology arms, which share their sequence with the PAM-containing strand of the genomic DNA. (**b**) DNA and protein sequences for the wild-type target site vs. the expected outcome following successful HDR. Restriction recognition sites for *Msp*I (wild-type sequence) and *Xho*I (mutant sequence) are highlighted in purple.

3.3.6 HDR events can be detected in zebrafish embryos co-injected with *tcp1* gRNA, Cas9 protein and the HDR template

To test our repair template, we microinjected wild-type zebrafish embryos with a mix containing Cas9 protein, *tcp1* gRNA and the repair template. Given the toxic effects we had previously observed after injection of gRNA and Cas9, we decided to use both at lower concentrations on this occasion. We saw much less toxicity under the new conditions, and we were able to raise embryos to 48 hpf before extracting their DNA. We initially used HRM analysis to screen embryos that had only been injected with gRNA and Cas9 to confirm that we were still able to achieve mutagenesis at the target site with these lower concentrations. As before, we detected shifted melt profiles in the amplicons from injected embryos compared to the non-injected controls (Figure 3.8), consistent with the presence of mutations at the target site.

We then screened embryos that had also been injected with our repair template to assess whether HDR had taken place. Initially, we amplified the target exon by PCR and performed restriction fragment length analysis using *Msp*I or *Xho*I (Figure 3.9). Following incubation with *Msp*I, we detected some undigested PCR product in samples from embryos injected with gRNA and Cas9 alone or in addition to the repair template, but not in non-injected controls. This is consistent with loss of the *Msp*I site in some cells of the injected embryos, which could be a consequence of either successful HDR or creation of indels. After incubation with *Xho*I, there were no digested fragments in the non-injected control samples or in embryos that were only injected with gRNA and Cas9, but we detected a very small amount of *Xho*I-digested product in several embryos that had been co-injected with the repair template. This is consistent with integration of the repair template into the target site in some cells of these embryos, though we noted that some of the digested fragments were not of the anticipated size, suggesting that the repair may not have been completely accurate in these embryos.

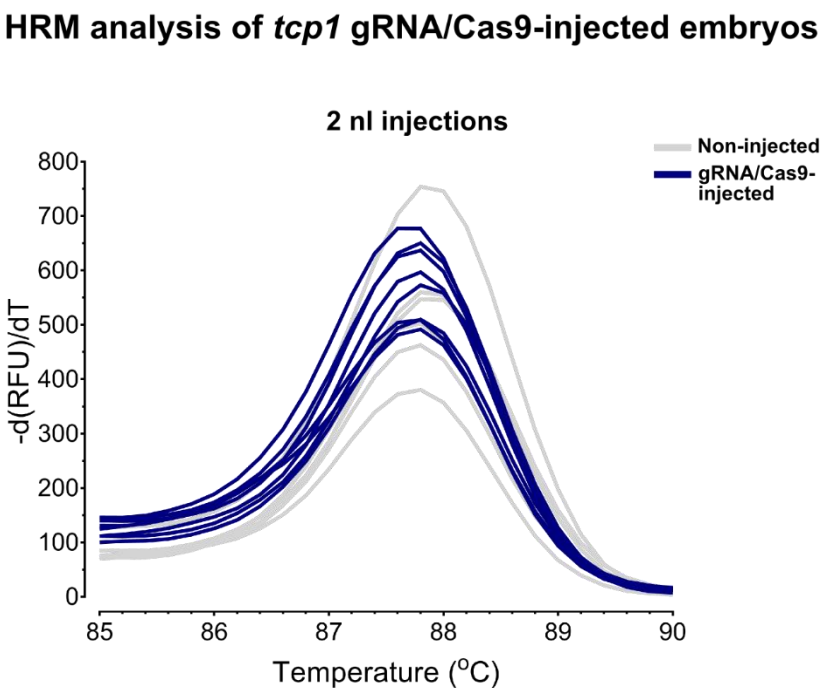

Figure 3.8. HRM analysis revealed shifted melt peak profiles for embryos injected with lower concentrations of *tcp1* gRNA and Cas9. Melt peak graphs depicting shifts in the melt profiles of target site amplicons from gRNA/Cas9-injected embryos vs. non-injected controls. Each plot represents the melt profile for an individual HRM reaction and reactions were performed in duplicate for each DNA sample (n = 3 non-injected embryos, n = 4 injected embryos).

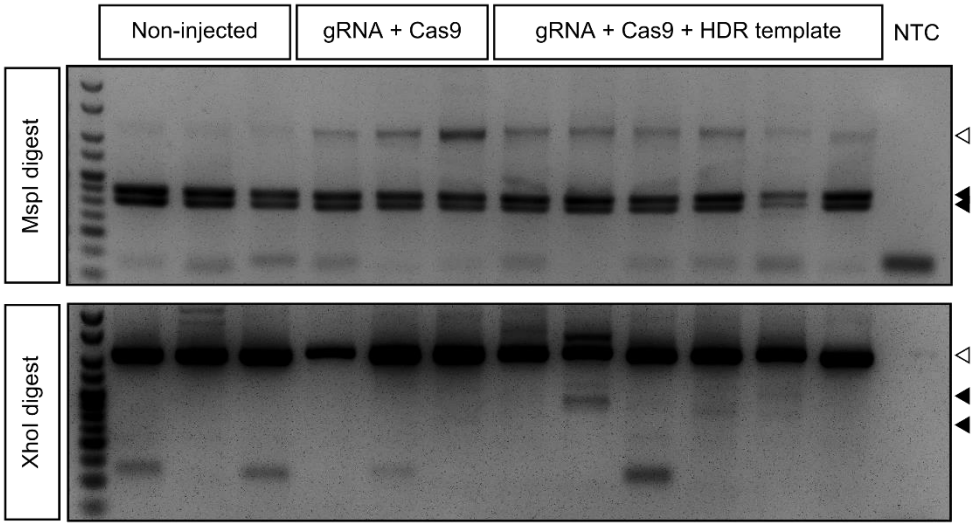

Figure 3.9. Restriction fragment length analysis of DNA from zebrafish embryos demonstrated partial loss of the *Msp*I restriction site and partial gain of the *Xho*I restriction site in embryos injected with *tcp1* gRNA, Cas9 and HDR template. Restriction fragments generated from PCR products spanning the target region in individual injected embryos or non-injected controls were separated on a 3% agarose gel. Open arrowheads indicate expected band sizes for full-length PCR products and black arrowheads indicate expected sizes for restriction fragments. Marker: Hyperladder V (Bioline). NTC: no template control.

Although these findings are consistent with HDR having occurred within some cells of the injected fish, they are not necessarily specific to HDR. This screening method also lacks sensitivity, as HDR is likely to arise in only a small proportion of cells in the injected embryos. We therefore developed a second, allele-specific PCR (AS-PCR)-based screening strategy to enable us to more selectively and sensitively detect HDR events in the injected fish.

For this assay, we designed two pairs of primers (Figure 3.10a,b), each comprised of one primer that binds outside (upstream or downstream) of the repair template sequence and a second primer that binds within the mutated region of the repair template sequence. We specifically ensured that the second primer of each pair contained a mismatch with the wild-type sequence on its 3'-most base, thereby promoting specific amplification of the mutant allele.

We then screened template DNA from injected and non-injected embryos by AS-PCR (Figure 3.10c). As expected, we did not detect any products of the expected sizes for either PCR from the non-injected control embryos or embryos that were only injected with gRNA and Cas9. In several embryos that had been co-injected with the repair template, we were able to detect products of the expected sizes, consistent with successful HDR having taken place in these embryos. Notably, both primer pairs also yielded some products that were larger than anticipated, suggesting that some erroneous repair may also have taken place in these embryos.

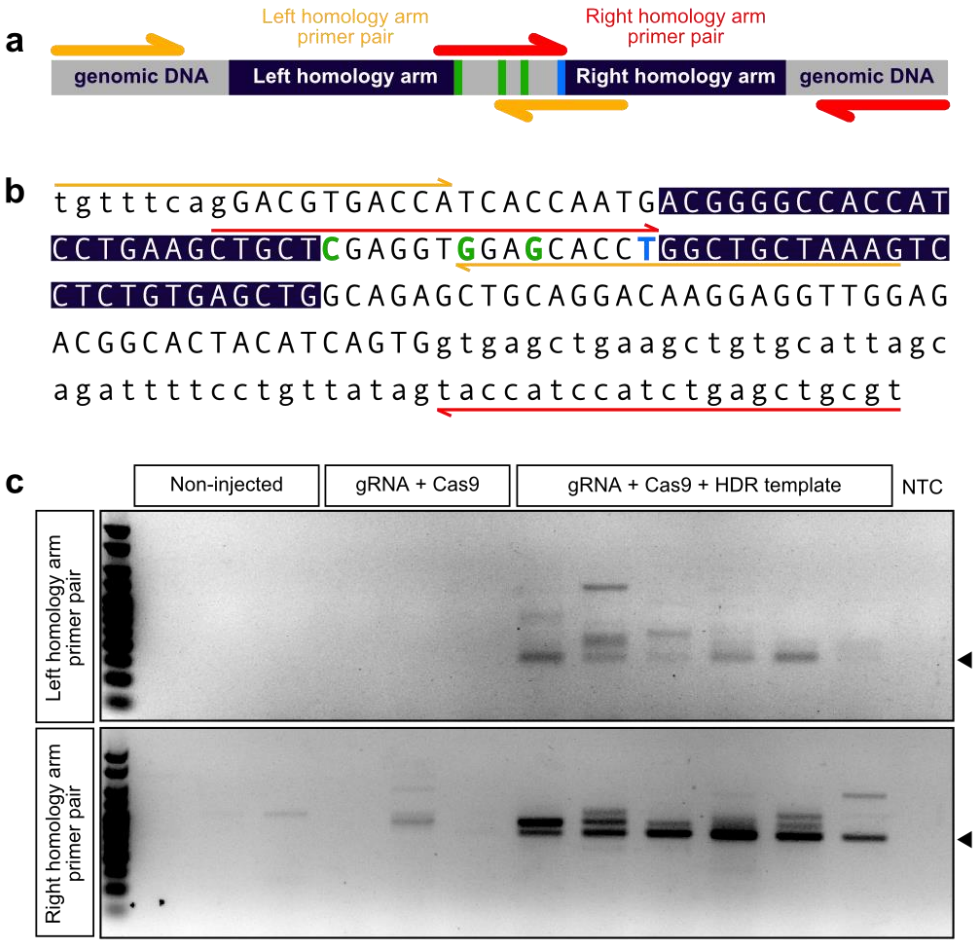

Figure 3.10. PCR-based screening of zebrafish embryos revealed evidence of HDR allele amplification in embryos injected with *tcp1* gRNA, Cas9 and HDR template. (**a**,**b**) Schematic representations of HDR allele-specific primer binding sites. (**c**) AS-PCR products generated from individual injected embryos and non-injected controls were separated on a 3% agarose gel. Arrowheads indicate expected sizes for HDR-specific PCR products. Marker: Hyperladder V (Bioline). NTC: no template control.

3.3.7 HDR events can also be detected in zebrafish embryos co-injected with a repair template complementary to the gRNA non-target strand

The homology arms of our initial repair template share their sequence with the PAM-containing DNA strand (the gRNA non-target strand) and are therefore complementary to the strand of genomic DNA to which the gRNA binds (the gRNA target strand). However, Richardson et al. (2016) postulated that double-stranded DNA strands dissociate from Cas9 in an asymmetric fashion following cleavage, with the 3' end of the non-target strand being released before the other strands (Figure 3.11a). By using repair templates with homology arms complementary to this non-target strand, they were able to increase the efficiency of HDR-mediated knock-in of precise mutations in human cells.

On this basis, we therefore designed a second repair template (the target strand, or "T", template) with the complementary sequence to our original template (the non-target strand, or "NT", template) (Figure 3.11b) to test whether this approach would also increase the efficiency of HDR-mediated knock-in in our zebrafish. As with embryos injected with the NT repair template, we saw incomplete digest of DNA from embryos injected with the T repair template after incubation with *Msp*I, and we observed a small amount of *Xho*I-digested product (Figure 3.12a). We also performed AS-PCR using DNA from these embryos, and both primer pairs yielded products of the anticipated sizes, as well as some larger products similar to those that we observed in embryos injected with the NT template (Figure 3.12b). These results are therefore consistent with successful HDR having been achieved in embryos injected with either T or NT templates.

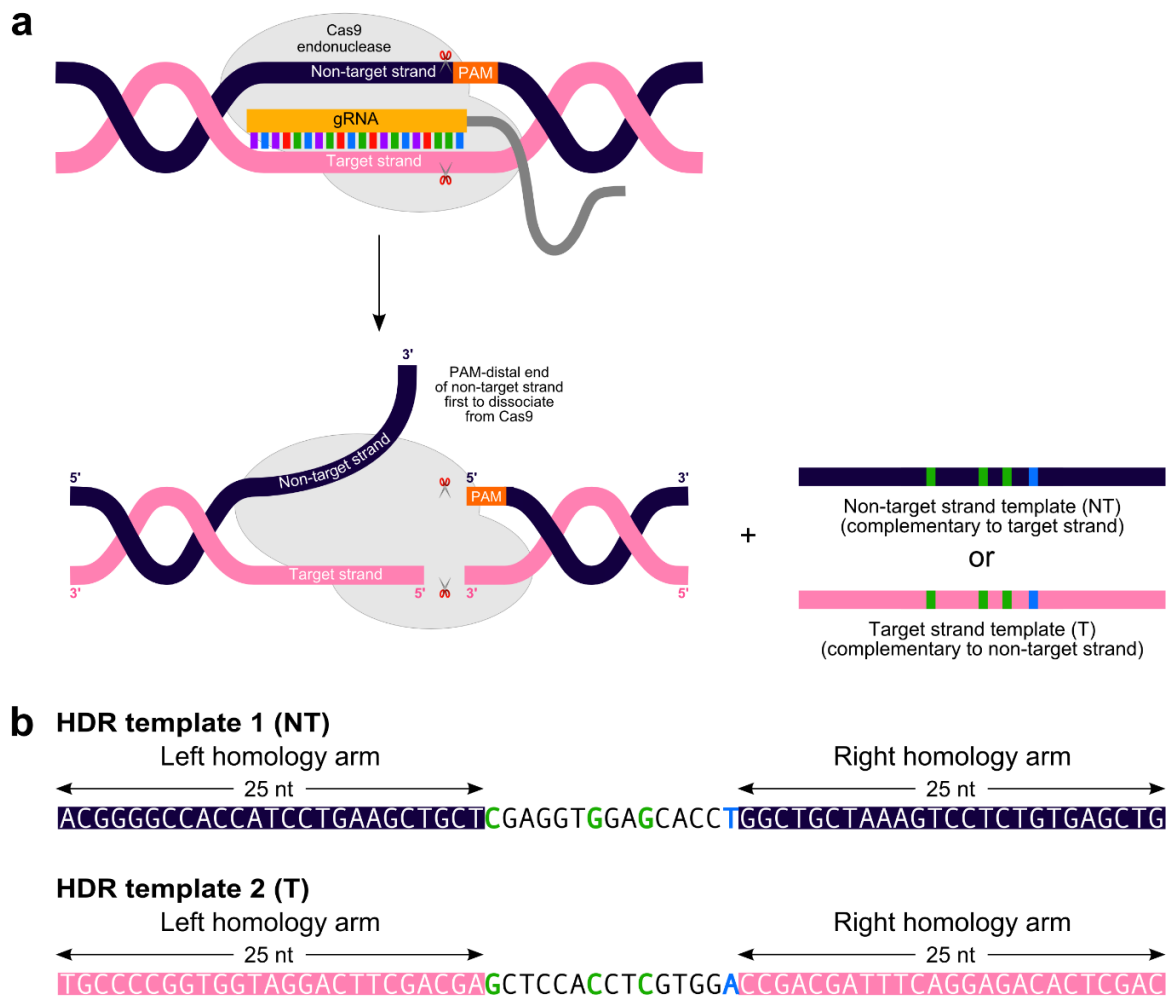

Figure 3.11. Sequence of the alternative repair template designed to generate *tcp1* knock-in mutant zebrafish. (**a**) Schematic diagram illustrating the initial process of DNA dissociation from Cas9 following double-stranded cleavage (according to Richardson et al., 2016). The PAM distal portion of DNA on the non-target strand is first to be released from the complex, thereby becoming available for recombination with a complementary repair template (i.e. one that shares homology with the target strand). (**b**) Sequence of the original (NT) repair template vs. the new (T) repair template sequence. For both templates, the single-nucleotide substitution encoding the P73L mutation is highlighted in blue, the synonymous gRNA target site mutations are highlighted in green, and the 25-nt homology arms are shown in blue (NT template) or pink (T template).

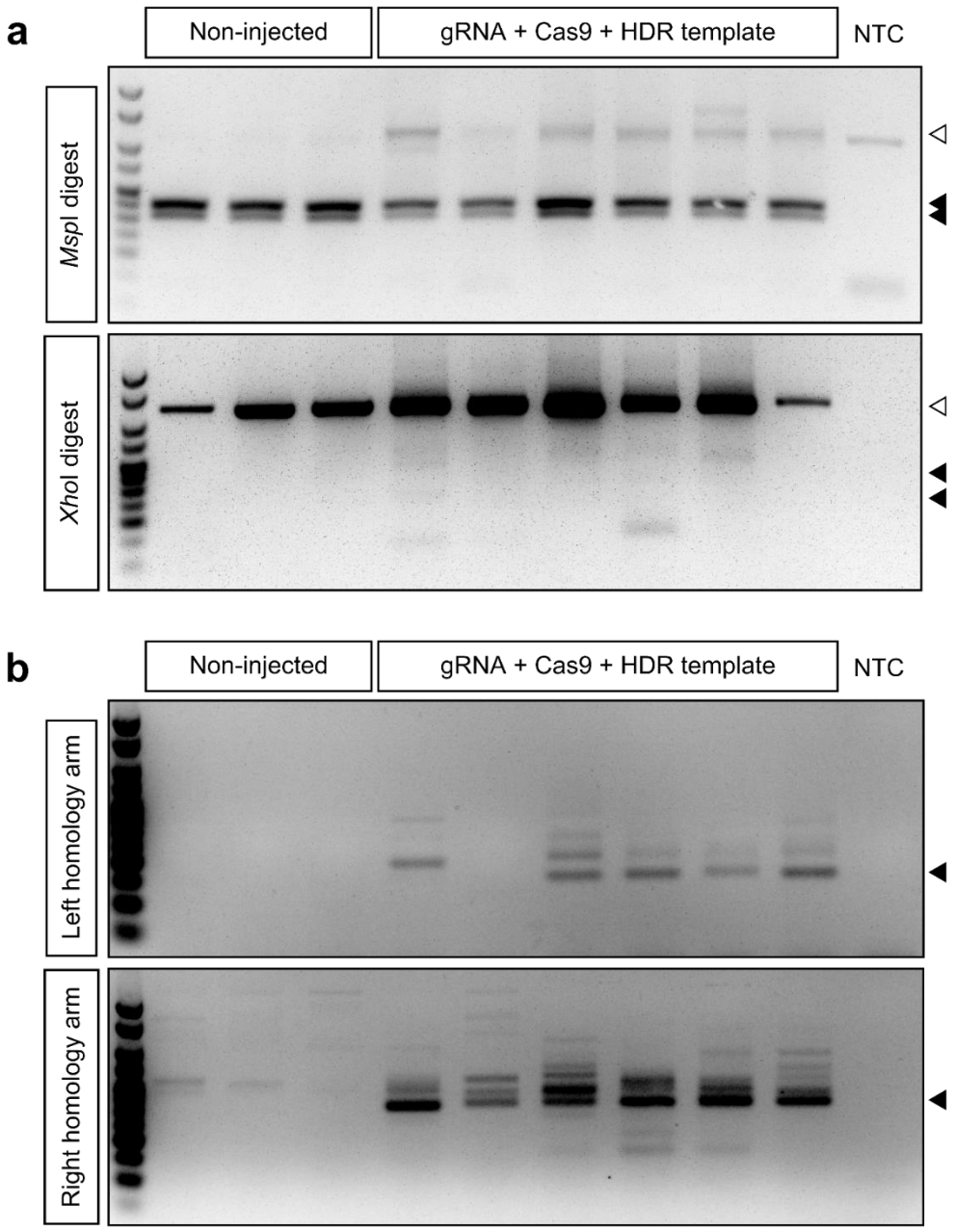

Figure 3.12. Restriction fragment length analysis and PCR-based screening of zebrafish embryos revealed evidence of successful HDR in embryos injected with *tcp1* gRNA, Cas9 and the T HDR template. (**a**) Restriction fragments generated from *Msp*I- or *Xho*I-digested PCR products spanning the target region in individual injected embryos or non-injected controls were separated on a 3% agarose gel. Open arrowheads indicate expected band sizes for full-length PCR products and black arrowheads indicate expected sizes for restriction fragments. (**b**) AS-PCR products generated from individual injected embryos and non-injected controls were separated on a 3% agarose gel. Arrowheads indicate expected sizes for HDR-specific PCR products. Marker: Hyperladder V (Bioline). NTC: no template control.

3.3.8 Identification of founders transmitting the correctly repaired HDR allele through the germline

Since we had detected evidence of successful HDR in embryos injected with the *tcp1* gRNA and HDR templates, we then raised injected founders to adulthood and began screening them for stable transmission of the correctly repaired HDR allele to F1 offspring. Our initial screening approach (Figure 3.13) involved outcrossing each founder with a wild-type fish, before performing *Msp*I restriction fragment length analysis on DNA extracts from individual F1 offspring. We were specifically interested in whether we could detect 50% loss of the restriction site, which would be consistent with heterozygosity for the HDR allele. However, this method proved laborious and, having screened several founders without identifying any F1 offspring with partial *Msp*I site loss, we decided to establish a more efficient screening approach.

The first phase of our optimised screening method involved using our HDR AS-PCR primers to amplify DNA from pools of up to 50 F1 embryos from individual founders (Figure 3.14). This enabled us to efficiently distinguish the vast majority of founders that were not transmitting the HDR allele (i.e. where DNA from the F1 pool either did not amplify with either AS-PCR primer pair, or only amplified with one of the pairs) from the few that might be transmitting the HDR allele (i.e. where both AS-PCR primer pairs yielded products of the expected size from the F1 pool), without the need to individually assay 50 F1 embryos for every founder (Figure 3.15a,c).

For founders that produced a positive result at this stage, we then proceeded to a second screening phase (Figure 3.14), in which we performed AS-PCR on individual F1 embryos to identify specific embryos yielding products of the expected size with both primer pairs. We then sequenced the entire target region in these embryos (Figure 3.15b). At this stage, we observed germline transmission of the correctly repaired *tcp1*^{P73L} allele from Founder A, which had been injected with the NT repair template and Founder B, which had been

injected with the T repair template. In both cases, the transmission frequency of the mutant allele to F1 offspring was approximately 14.5% (7/48 F1 heterozygotes). Of note, we also identified some founders (e.g. Founders C and D) which, despite having given positive results in the AS-PCR screen, were excluded following sequencing analysis, as they were transmitting alleles that contained indels alongside some of the specific mutations in the HDR template (Figure 3.15b,c).

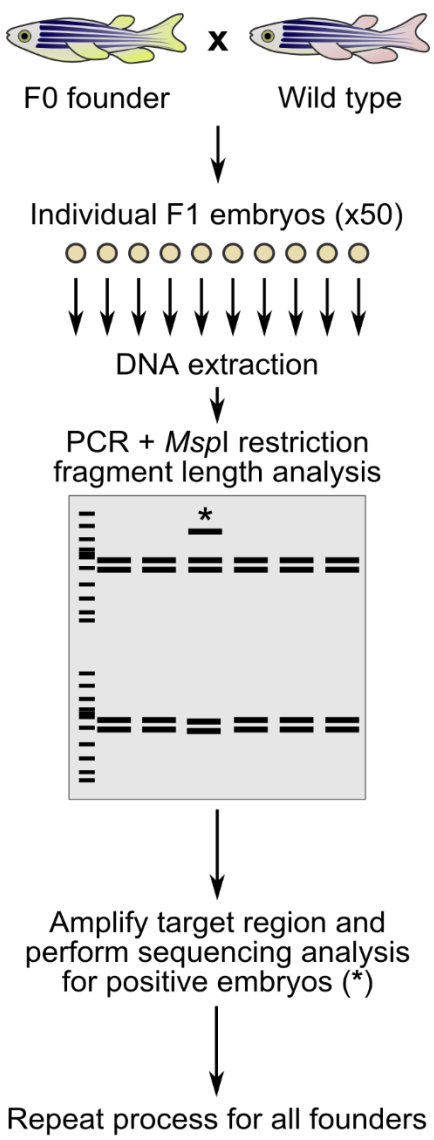

Figure 3.13. Schematic overview of the initial approach used to screen injected founders for germline transmission of the *tcp1*^{P73L} HDR allele. Injected founders are first outcrossed to AB zebrafish, then DNA is extracted from ~50 individual F1 offspring for *Msp*I restriction fragment length analysis. The target region is then sequenced for any F1 offspring showing 50% loss of the *Msp*I site (e.g. sample denoted by the asterisk in the schematic gel electrophoresis results) to determine whether they carry the *tcp1*^{P73L} allele.

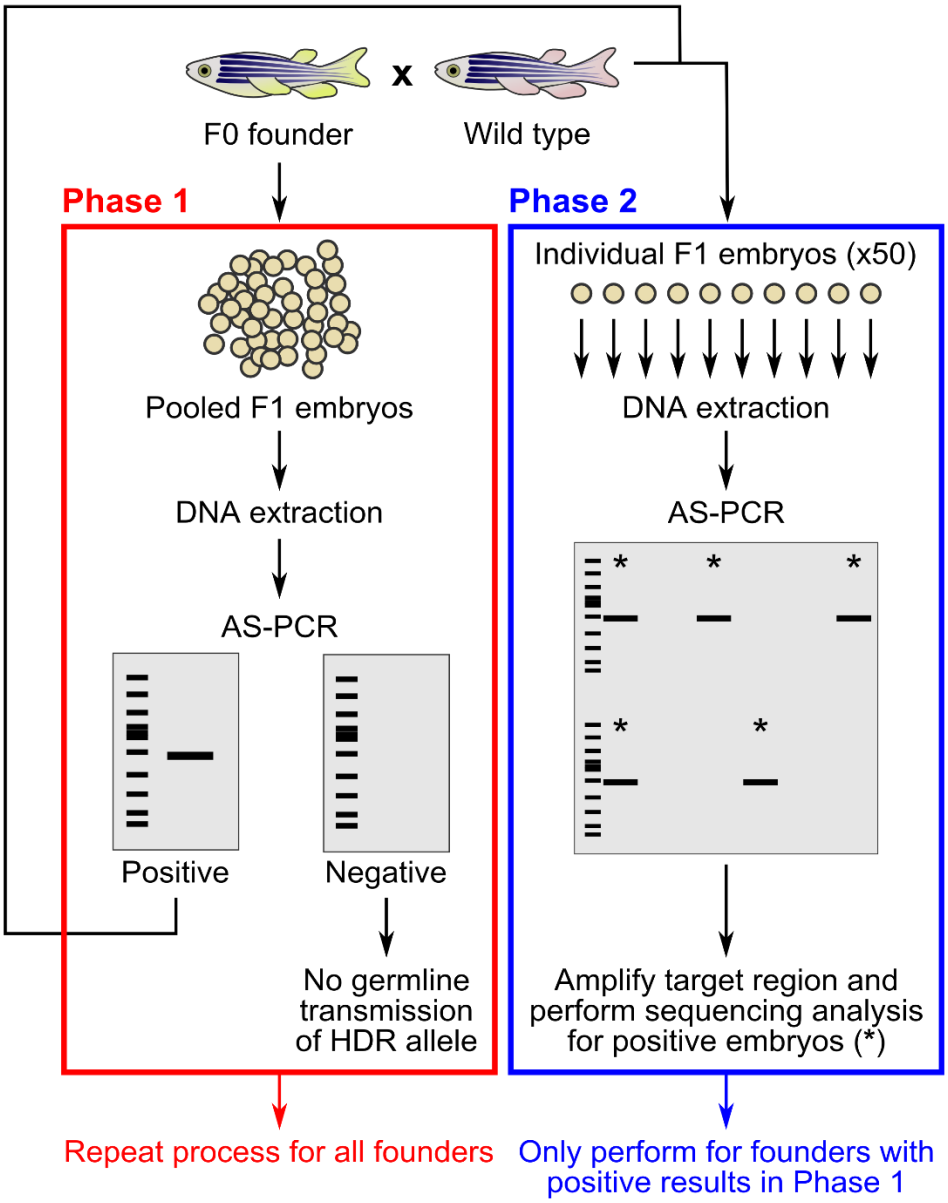

Figure 3.14. Schematic overview of the streamlined method used to screen injected founders for germline transmission of the *tcp1*^{P73L} HDR allele. Injected founders are first outcrossed to AB zebrafish, then DNA is extracted from pools of up to 50 F1 offspring for analysis by AS-PCR. If a positive result is detected in this pool by AS-PCR, a second outcross is then performed so that individual F1 embryos can be screened. The target region is then sequenced in any F1 embryos amplifying AS-PCR products of the expected sizes to determine whether they are carrying the *tcp1*^{P73L} allele.

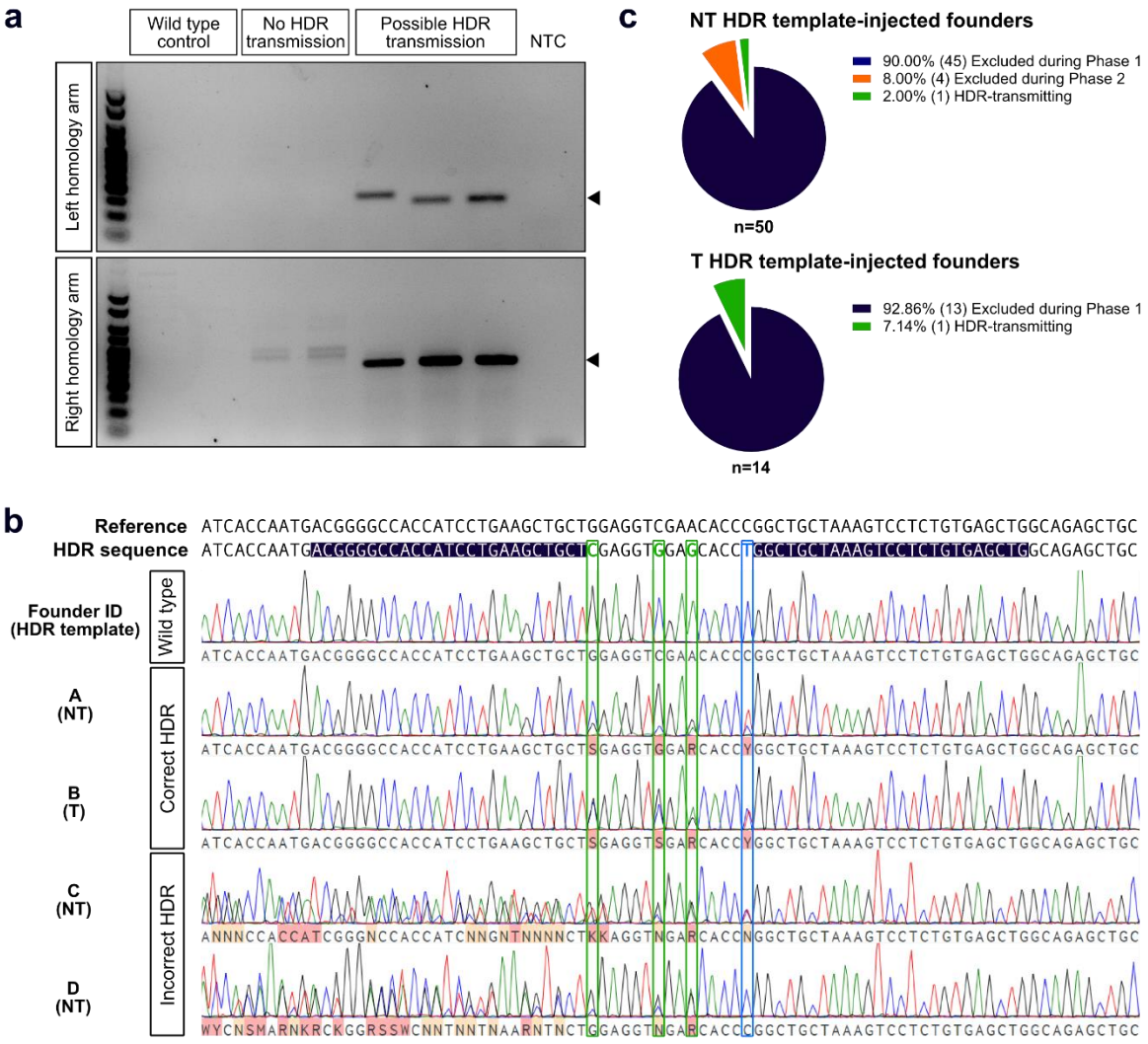

Figure 3.15. Identification of founders transmitting the *tcp1*^{P73L} allele to F1 offspring. (**a**) Gel electrophoretic analysis of AS-PCR products from pooled F1 embryos, showing representative results obtained from the progeny of non-transmitting founders and founders that may be transmitting the *tcp1*^{P73L} allele. Arrowheads indicate expected sizes for HDR-specific PCR products. Marker = Hyperladder V (Bioline), NTC = no template control. (**b**) Sequencing analysis of F1 offspring from two founders (A and B) that were transmitting the correctly repaired *tcp1*^{P73L} allele and two founders (C and D) that were transmitting incorrectly repaired alleles. (**c**) Pie charts summarising the screening outcomes for all template-injected founders for both repair templates (n = 50 F1 embryos screened for each founder). Numbers of founders for each outcome are in brackets. Total number of founders screened for each template is indicated below each pie chart.

3.3.9 Raising stable mutant zebrafish carrying the *tcp1*^{P73L} HDR allele

Once we had confirmed that Founders A and B were transmitting the *tcp1*^{P73L} allele through the germline, the next step was to raise their offspring to generate stable heterozygous mutants that we could then breed to obtain homozygotes for phenotypic analysis. We were unfortunately unable to obtain any further offspring from Founder B at this point, so subsequent investigations were limited to the progeny of Founder A.

Although the off-target analysis for our *tcp1* gRNA suggested that it was unlikely to induce off-target mutagenesis, we cannot be certain that we did not introduce any unintended mutations elsewhere in the genome. To minimise the risk that any phenotypes we observe in our mutant fish might be attributed to an off-target mutation, we outcrossed Founder A to a wild-type (AB) strain for two successive generations and selected for carriers of the *tcp1*^{P73L} allele at each stage by AS-PCR (Figure 3.16).

We then incrossed F2 carriers and genotyped F3 progeny by *Xho*I restriction fragment length analysis at 10 dpf to confirm that wild-type and mutant genotypes were present at approximately Mendelian frequencies within the clutch (Figure 3.17a,b). We also synthesised cDNA from pools of these F3 larvae and sequenced a ~800 bp product spanning the mutation site to verify that the expected sequences were present in each of the three genotypes (Figure 3.17c).

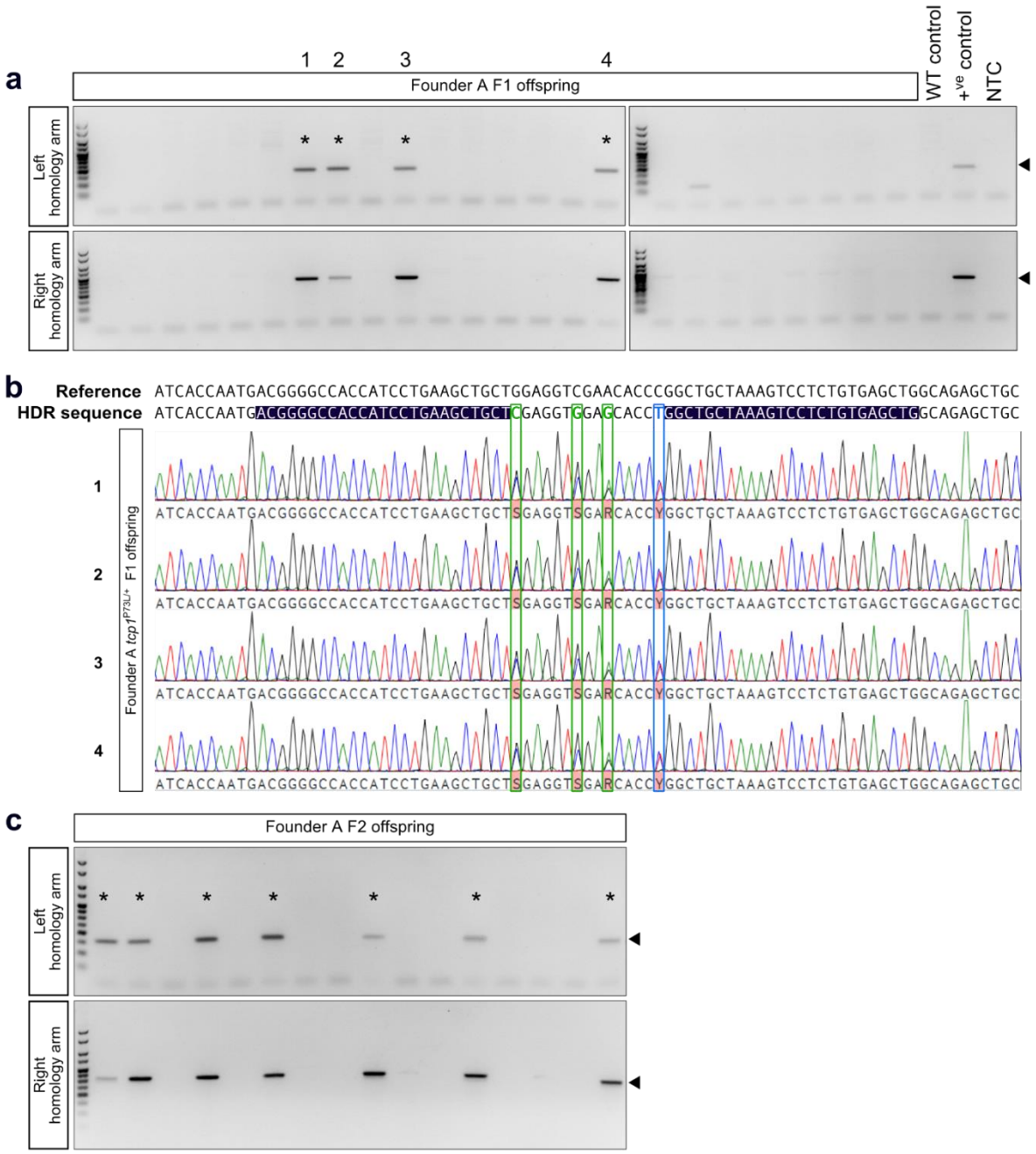

Figure 3.16. Identification of adult F1 and F2 offspring carrying the *tcp1*^{P73L} allele. (**a**) Gel electrophoretic analysis of AS-PCR products generated from fin biopsies taken from F1 offspring. Samples for which products of the expected size amplified with both primer pairs (i.e. *tcp1*^{P73L} carriers) are denoted by asterisks. Marker = Hyperladder V (Bioline), NTC = no template control. Positive control = heterozygous F1 embryo from Founder A. (**b**) Sequencing analysis confirmed that these fish were heterozygous for the *tcp1*^{P73L} allele. (**c**) Gel electrophoretic analysis of AS-PCR products generated from fin biopsies taken from F2 offspring (from the same F1 parent). Samples for which products of the expected size amplified with both primer pairs (i.e. *tcp1*^{P73L} carriers) are denoted by asterisks. Marker = Hyperladder V (Bioline).

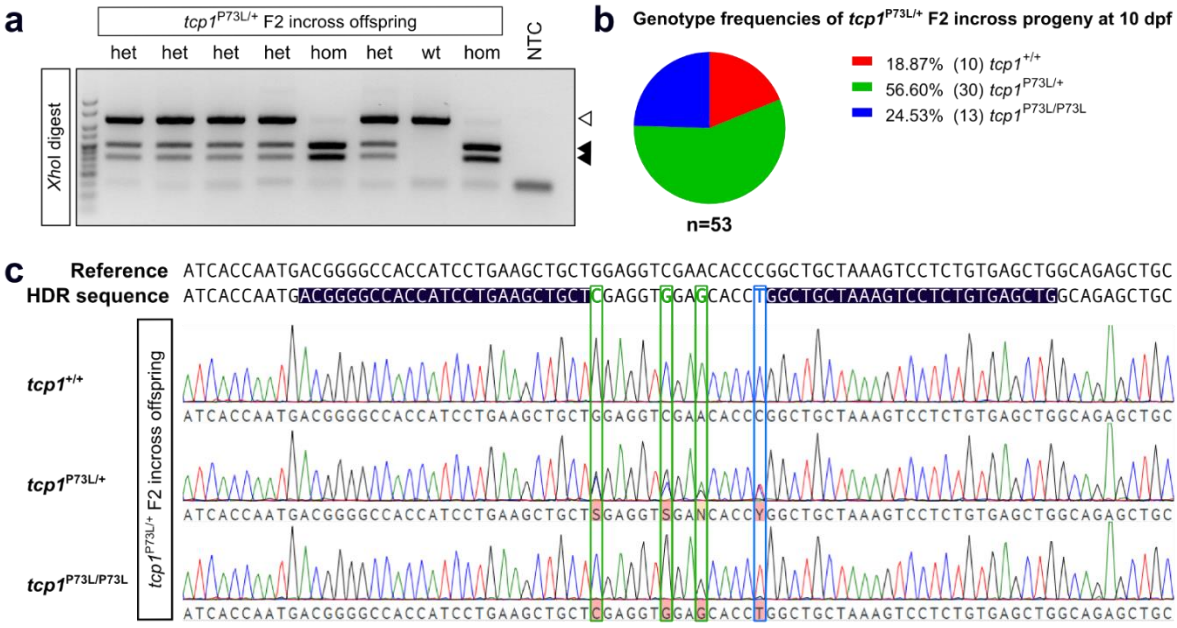

Figure 3.17. *Xho*I restriction fragment length analysis enables genotyping of F2 incross offspring. (**a**) Gel electrophoresis of PCR products generated from DNA of individual F3 larvae, following incubation with *Xho*I. Open arrowhead indicates the size of the full-length PCR product (corresponding to the wild-type allele) and black arrowheads indicate the expected sizes of *Xho*I restriction fragments (corresponding to the *tcp1*^{P73L} allele). Marker = Hyperladder V (Bioline). (**b**) Wild-type, heterozygous and homozygous mutant larvae were present at approximately Mendelian frequencies within a clutch of F3 offspring at 10 dpf (**c**) Sequencing analysis of a ~800 bp region of cDNA spanning the target site in pools of F3 progeny confirmed that the correct allele sequences were present in all genotypes (n = 10 larvae per pool).

3.4 Generating a *tcp1* frameshift mutant zebrafish line

3.4.1 Identification of a founder transmitting a frameshift mutation in *tcp1*

The primary purpose of generating our *tcp1*^{P73L} mutant line was to recapitulate the genotype of the human patients as accurately as possible, so that we could use our zebrafish as a tool to validate the pathogenicity of the *TCP1*^{P70L} variant and to investigate potential mechanisms of disease.

Another motive for studying novel rare disease mutations is that they offer opportunities to uncover new information about the functions of genes that are relevant to human biology. This disease specifically points to a previously undiscovered direct relationship between *TCP1* function and the health and development of the human nervous system; however, the precise details of this link are yet to be explored.

We may gain some insight into how *tcp1* contributes to neurological development from our *tcp1*^{P73L} mutant zebrafish line; however, we reasoned that a *tcp1*-null mutant zebrafish line would provide a more comprehensive overview of potential neurodevelopmental functions. Given that *TCP1* has been shown to be essential for survival in several other model systems (Iijima et al., 1998; Kim and Choi, 2019; Seixas et al., 2010; Ursic et al., 1994), we expected that loss of *tcp1* in zebrafish would likely also display severe defects and early lethality; however, because zebrafish development can be visualised immediately following fertilisation, we anticipated that this model may provide a window of opportunity for exploring the effects of loss of *tcp1* upon development. Moreover, as the *TCP1*^{P70L} variant is recessively inherited and therefore likely to act through at least a partial loss-of-function mechanism, a *tcp1*-null mutant may provide additional information about pathophysiological processes that could be relevant to the human disease.

In the process of screening our previously injected founders for germline transmission of the *tcp1*^{P73L} allele using our restriction digest-based screening approach (Figure 3.13), we noted that one of the F1 offspring from Founder E generated a product that was much

smaller than the expected sizes for either the full-length PCR product or the *Msp*I-digested restriction fragments (Figure 3.18a). To determine whether this smaller product corresponded to a mutant allele containing a deletion in *tcp1*, we sequenced the target region in this embryo. Indeed, this embryo was carrying a 46 bp deletion in *tcp1*; this mutation shifts the reading frame to give rise to a premature stop codon at the start of exon 4, which we expect to result in nonsense-mediated decay of the transcript (Figure 3.18b,c).

We therefore generated our stable frameshift mutant line by outcrossing Founder E to a wild-type strain for two generations and selecting for heterozygous F1 and F2 mutants by screening for 50% loss of a *Bsl*I restriction recognition site which is destroyed by the deletion (Figure 3.18c, Figure 3.19). This ultimately gave rise to F2 offspring carrying the mutant allele (*tcp1*^{I57fs}) which we then planned to incross to generate homozygous mutants for phenotypic analysis.

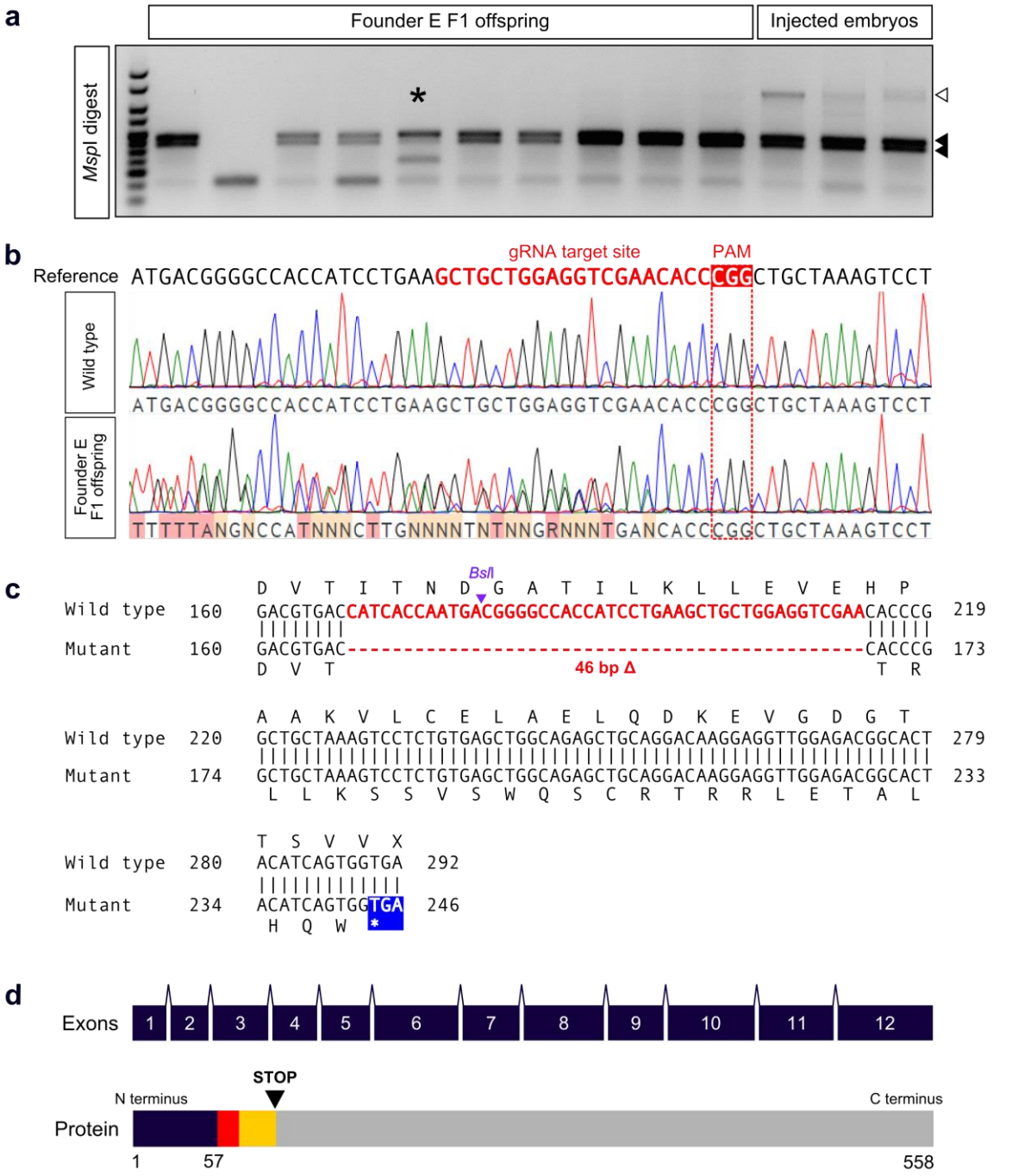

Figure 3.18. Identification of a founder transmitting a frameshift deletion in *tcp1*. (**a**) Gel electrophoresis of PCR products generated from DNA of individual F1 offspring from Founder E, following incubation with *Msp*I. Black arrowheads indicate the expected sizes for *Msp*I restriction fragments (as expected for the wild-type allele) and the open arrowhead indicates the size of the full-length PCR product (corresponding to mutant alleles in which the *Msp*I site has been disrupted, as detected in embryos injected with *tcp1* gRNA, Cas9 and repair template). A small product that does not correspond to any of the expected sizes was observed one F1 embryo (denoted by the asterisk). Marker = Hyperladder V (Bioline). (**b**) Sequencing analysis revealed that Founder E was transmitting an allele with a frameshift (46 bp) deletion in *tcp1* (*tcp1*^{l57fs}). (**c**) Sequence alignment of the wild-type and mutant alleles, showing that the shifted reading frame introduces a premature stop codon (blue) downstream of the deletion (red). The mutation also disrupts a *Bsl*I restriction site, indicated by the purple arrowhead. (**d**) Schematic diagram illustrating the location of the mutation in the context of the whole tcp1 protein sequence. The site of the deletion is highlighted in red, the frame shift downstream of the deletion is highlighted in yellow, and site of the premature stop codon is marked by the black arrowhead.

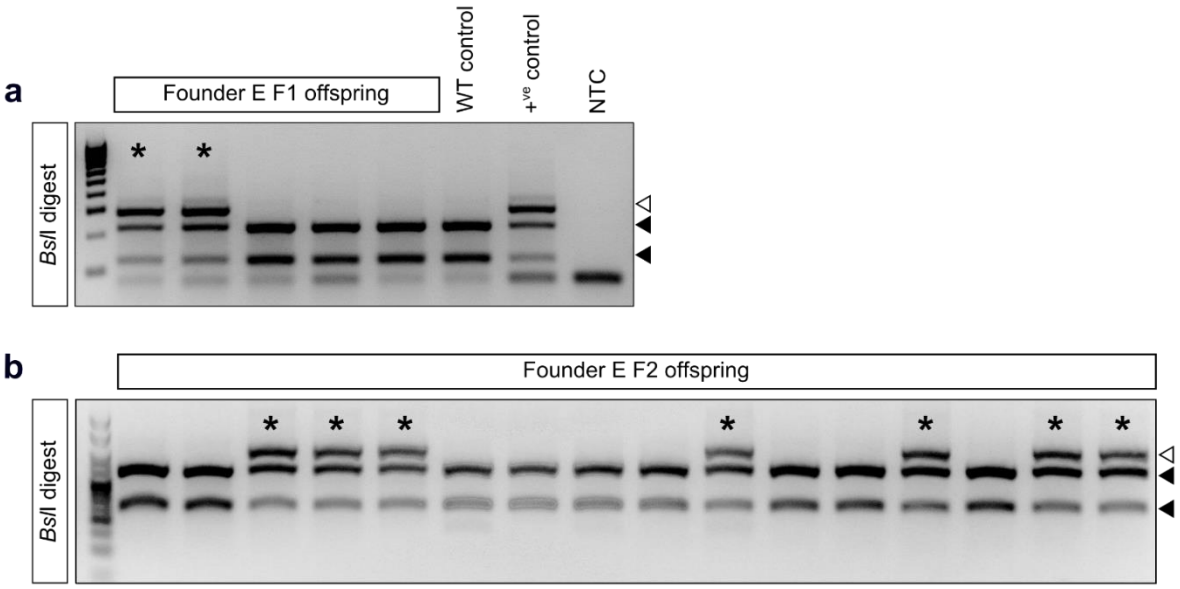

Figure 3.19. *Bsl*I restriction fragment length analysis enables identification of F1 and F2 offspring carrying the *tcp1*^{l57fs} allele. (**a**,**b**) Gel electrophoresis of PCR products generated from fin biopsies of F1 and F2 offspring following incubation with *Bsl*I. Black arrows indicate the expected sizes for *Bsl*I restriction fragments (as expected for the wild-type allele) and open arrows indicate the expected size of the full-length PCR product (corresponding to the mutant allele). Asterisks denote fish identified as heterozygous *tcp1*^{l57fs} carriers. Markers = (**a**) Hyperladder IV, (**b**) Hyperladder V (Bioline), NTC = no template control.

3.5 Discussion

The initial goal of this project was to genetically engineer new zebrafish models that we could use to test our hypotheses relating to the pathogenicity of the *TCP1*^{P70L} variant and the role of *TCP1* during development. Specifically, we aimed to use CRISPR/Cas9 to precisely model the human mutation in the zebrafish genome and additionally to generate a *tcp1* frameshift mutant zebrafish that we can use to explore how loss of *tcp1* affects development of the nervous system.

3.5.1 Genetic suitability of the zebrafish for modelling this disorder

When developing *in vivo* models for genetic diseases, it is critical to ensure the genetic suitability of the chosen model system. This is particularly important for zebrafish models; although zebrafish orthologues exist for most human genes (Howe et al., 2013), the zebrafish genome is notorious for harbouring duplicate copies of many of these genes (Howe et al., 2013). Under some circumstances, these paralogues may be able to compensate for genetically engineered mutant alleles of interest, potentially masking disease-relevant phenotypes (She et al., 2019). Here, we confirmed that the zebrafish genome has only one orthologue for human *TCP1*, precluding the possibility that a direct paralogue of *tcp1* might compensate for our mutant alleles.

We also noted that the zebrafish and human TCP1 proteins have high levels of sequence conservation, as is the case for *TCP1* orthologues that have been identified in many other eukaryotic species. Importantly, the proline residue mutated in patients has also been highly conserved through evolution. These findings point to an evolutionarily preserved structure and function for the TCP1 protein and provide reassurance that any functional consequences we observe upon introduction of an equivalent mutation at this residue in the zebrafish protein are also likely to be relevant to the mutant human protein.

3.5.2 Strategy for knocking in the *tcp1*^{P73L} mutation

To generate our knock-in mutant zebrafish line, we chose to use the CRISPR/Cas9 system to introduce the patient-specific variant into the zebrafish genome by HDR. Although CRISPR/Cas9 technology is now widely used as an efficient method to generate null alleles for zebrafish genes, there has been limited success in creating alleles containing precise genetic modifications. This is a continuously evolving field, and there is no universal consensus on the best strategy for efficiently generating precise mutations; however, some factors that are likely to influence efficiency of HDR-mediated knock-in have been identified. For example, the distance between the Cas9 cleavage site and the intended mutation has been shown to inversely correlate with knock-in efficiency by HDR both in human cells and in zebrafish (Liang et al., 2017; Paquet et al., 2016; Prykhozhij et al., 2018). This can present problems if there are no PAM sites situated near the site to be mutated, but we were fortunate enough to identify a suitable gRNA for which the site of our intended mutation is located within the PAM.

Optimal repair template design has also been a focus for improving the efficiency and accuracy of HDR-mediated CRISPR knock-in. Before we began generating our knock-in line, short single-stranded oligonucleotide templates of up to 100-nt in length had successfully been used to introduce single-base edits into zebrafish genes by HDR (Armstrong et al., 2016). We chose to use a similar approach by designing a 65-nt, single-stranded template encoding our disease-linked missense mutation. Previous work had shown that CRISPR-blocking mutations are effective in increasing the accuracy of HDR in human cells (Paquet et al., 2016), so we also introduced three silent blocking mutations into our template within the gRNA target sequence. It is worth noting that this approach was more effective in cells when the blocking mutations affected one of the guanine residues in the PAM instead of affecting the gRNA target site (Paquet et al., 2016); however, we were unable to introduce a blocking mutation into the PAM for the *tcp1* gRNA without introducing nonsynonymous mutations.

Before we began creating our knock-in model, repair templates with sequences complementary to the non-gRNA-binding strand had previously been proposed to increase HDR-mediated knock-in efficiency in cells (Richardson et al., 2016). On this basis, we designed and tested a second (T) repair template with a sequence complementary to our original (NT) template. Our findings appear to be consistent with those of Richardson et al. (2016), in that we observed a higher germline transmission frequency for the correctly repaired HDR allele from founders injected with the T template than from those injected with the NT template. Furthermore, we did not identify any founders injected with the T template that were transmitting 'false positive' alleles (e.g. Founders C and D, Figure 3.15b); that is, where the DNA of F1 embryos amplified products of the expected size using the AS-PCR primers but the sequencing results showed erroneous repair at the target site. This is consistent with the repair having been more accurate with the T template; however, the total number of founders we screened was notably lower for the T repair template than for the NT template. We therefore do not know whether the germline transmission frequency would remain higher, or whether we would identify founders transmitting incorrectly repaired alleles, if we were to screen a larger number of founders that were injected with the T repair template.

Some studies have used NGS to directly measure HDR frequencies in injected embryos to compare the knock-in efficiency when using various repair template designs (Boel et al., 2018; Prykhozhij et al., 2018). Contrastingly, our only read-out of efficiency is the proportion of founders that we found to be transmitting the correctly-repaired mutation to their offspring. We therefore cannot draw direct comparisons between the knock-in efficiencies we observed using the two templates and the efficiencies that have previously been reported for similar templates. Furthermore, because we were primarily interested in identifying founders transmitting our mutation of interest and did not set out to uncover every allele that might have been introduced into the injected embryos, we also cannot draw any robust conclusions about the accuracy of repair and frequency of erroneously

repaired alleles using either of our templates. To gain a more quantitative insight into the efficiency and accuracy of our knock-in approach, we could have analysed DNA from injected embryos by NGS to determine the proportion of cells carrying correctly repaired alleles (Boel et al., 2018; Prykhozhij et al., 2018).

3.5.3 Screening approaches for detecting successful HDR

Given the currently limited efficiency of HDR-mediated knock-in in zebrafish, it is critical to devise effective screening strategies to identify zebrafish carrying successfully repaired alleles. We firstly required a method to detect evidence of successful HDR in embryos that had been injected with the repair templates. We initially tested a restriction digest-based approach in which we screened injected embryos for gain or loss of restriction sites that we had either introduced or disrupted in our repair template. We noted that our screening approach based on loss of the *Msp*I site was not specific to HDR and could also detect alleles containing insertions or deletions that had disrupted this site through NHEJ. Consistent with this, we also observed incomplete *Msp*I digest in embryos that had only been injected with Cas9 and *tcp1* gRNA. When we screened injected embryos for introduction of the novel *Xho*I site in our repair template, we observed some digested products in a few embryos injected with our repair templates; however, these bands were extremely weak and difficult to detect. This is consistent with findings from Prykhozhij et al. (2018), where restriction digest-based screening methods were unable to detect HDR knock-in alleles in injected embryos. The authors attributed this to low knock-in efficiency and speculated that this could be compounded at the PCR stage if heteroduplexes form, resulting in only a fraction of total PCR products being comprised of two complementary strands containing the novel restriction site.

In contrast to the restriction digest-based screening method, the AS-PCR assay offered much greater sensitivity and we were able to detect amplification of products of the expected sizes in most of our injected embryos but not in non-injected controls. For most

injected embryos, we also observed additional amplified products that were larger than expected. These are also consistent with results from Prykhozhij et al. (2018) and likely correspond either to alleles where indels have been introduced into the target site alongside our intended mutations, or to alleles where the repair template has integrated elsewhere in the genome.

A limitation of the AS-PCR approach is that it provides little information about knock-in efficiency, as amplification will likely occur even if only a very small number of cells within the embryo contain the knock-in sequence. Moreover, though this approach likely offers greater specificity for detecting knock-in events than restriction fragment length analysis-based approaches, it is not completely specific for alleles that have been repaired with 100% accuracy, as we later identified some incorrectly repaired sequences which were amplified by both pairs of our AS-PCR primers.

3.5.4 Screening approaches for identifying founders transmitting the *tcp1*^{P73L} mutation through the germline

As well as establishing a method to detect evidence of successful HDR in injected embryos, we also required a strategy to identify injected founders that were transmitting the correctly repaired allele through the germline, so that we could ultimately create a stable mutant line. Considering that our screening of injected embryos by *Xho*I restriction fragment length analysis indicated that the knock-in efficiency in the injected embryos was very low, we anticipated that the rate of germline transmission from the injected founders to their F1 progeny would also be low, and that we may need to screen a large number of founders to identify one transmitting our mutation of interest.

To streamline our screening approach for detecting germline transmission of the correct mutation, we employed AS-PCR and devised a strategy that allowed us to identify founders transmitting the correctly repaired allele while minimising the amount of time required to exclude non-transmitting founders. A drawback of our approach is that we

uncovered several ‘false positive’ founders at this stage, whose F1 embryos gave positive results at the AS-PCR screening stage but were later revealed to be carrying incorrectly repaired alleles. Several of these incorrectly repaired alleles appeared to contain fragments of the repair template sequence (e.g. Founder C and D, Figure 3.15b). Similar integration of repair template fragments at the target site was illustrated by Boel et al. (2018) to be a common phenomenon when using ssODNs to create specific mutations. Detection of erroneously repaired alleles by AS-PCR was also observed by Prykhozhij et al. (2018), and likely represents a limitation of AS-PCR-based screening approaches. Nevertheless, AS-PCR-based screening appears to present an efficient strategy for rapidly and efficiently eliminating the majority of non-transmitting founders, and any ‘false positive’ founders can be excluded following subsequent restriction digest-based screening and/or sequencing analysis.

3.5.5 Conclusion

To conclude, we aimed to generate novel zebrafish models that we can use to establish the pathogenicity of the human *TCP1*^{P70L} mutation and its contribution to pathogenesis, and to explore the role of *TCP1* during vertebrate neurodevelopment. In this chapter, we have demonstrated the genetic suitability of the zebrafish for modelling the human *TCP1*^{P70L} mutation, and we tested approaches to precisely introduce this mutation into the zebrafish genome, ultimately leading to the successful generation of a stable *tcp1*^{P73L} knock-in mutant line. As we have discussed above, several of the strategies that we employed to generate and identify our knock-in line are in keeping with those used by other groups to introduce precise mutations into the zebrafish genome.

Alongside the *tcp1*^{P73L} mutant line, we also created a second mutant line, harbouring a frameshift mutation in *tcp1*. We reasoned that this line would provide us with an *in vivo* platform for exploring the consequences of *tcp1* loss of function. The next goal of the project was to characterise these mutant lines to determine whether they recapitulate any

of the phenotypes associated with the human disease, so that we can determine whether the *TCP1*^{P70L} mutation is likely to be responsible for the patients' phenotypes, and whether this gene is important for the development and maintenance of the tissues affected by the disease.

Chapter 4

Characterising the developmental effects of zebrafish *tcp1* mutations on tissues implicated in human *TCP1*-related disease

4.1 Introduction

In Chapter 3, we described how we genetically engineered novel *tcp1* mutant zebrafish models to create experimental platforms for testing our hypotheses: a) that the *TCP1*^{P70L} mutation is responsible for the patients' phenotypes, and b) that *TCP1* plays an important role in development and maintenance of the human cerebellum and retina

Our next goal was to begin to test these hypotheses using our zebrafish models, by characterising how the disease-linked missense mutation, or the frameshift mutation that we introduced into zebrafish *tcp1*, affect the morphology and development of the tissues that are implicated in the human disease.

In the following chapter, we first aimed to verify that the frameshift mutation that we introduced into *tcp1* results in nonsense-mediated decay of the transcript and thus represents an allele that we can use to investigate the consequences of loss of *tcp1*. We then sought to investigate the effects of the *tcp1* mutations in zebrafish at the gross morphological level, to determine whether they cause obvious developmental defects that might be relevant to the pathology of the human disease. Subsequently, we focused more specifically on how these mutations affect development of the cerebellum and retina (i.e. the main tissues affected in patients) to determine whether any specific defects arise in these tissues, using a combination of fluorescent cell-specific reporter lines and immunohistochemistry to investigate the morphology of these tissues.

4.2 Zebrafish *tcp1*^{l57fs} mutant mRNA undergoes nonsense-mediated degradation

As a platform in which to explore developmental roles for *tcp1*, we created the *tcp1*^{l57fs} mutant zebrafish line, which harbours a frameshift mutation in *tcp1*. As we described in Chapter 3, the frame shift introduced by this mutation gives rise to a premature stop codon. We would predict this to result in nonsense-mediated decay of the mutant transcript, thus

allowing us to investigate the phenotypic consequences of loss of *tcp1*. However, it has previously been shown that mutant zebrafish transcripts containing premature stop codons can be aberrantly processed and evade nonsense-mediated degradation (Anderson et al., 2017), which may result in masking of mutant phenotypes.

To confirm that the *tcp1*^{I57fs} frameshift mutation results in nonsense-mediated decay of mutant *tcp1* mRNA and that our model would reflect a loss of *tcp1*, we synthesised RNA probes against zebrafish *tcp1* and performed whole-mount *in situ* hybridisation to compare *tcp1* transcript expression in wild-type, heterozygous and homozygous *tcp1*^{I57fs} mutant embryos (Figure 4.1a).

In wild-type embryos, we saw that *tcp1* mRNA was ubiquitously expressed at 24 hpf, but was particularly highly expressed in the eyes, midbrain and somites. The spatial expression pattern of *tcp1* mRNA in heterozygous mutants was comparable to that of wild-type embryos, but the staining intensity in the heterozygous mutants was reduced, consistent with a decrease in *tcp1* transcript expression. In the homozygous mutants, we were unable to detect *tcp1* mRNA by *in situ* hybridisation, consistent with the mutant transcript being subject to nonsense-mediated degradation.

To validate these findings, we synthesised cDNA from pools of wild-type and *tcp1*^{I57fs} mutant larvae at 5 dpf and performed qPCR analysis, using two independent pairs of primers to quantify the relative levels of *tcp1* transcript expression in mutant larvae (Figure 4.1b). One of the primer pairs we designed binds upstream of the exon containing the mutation and the other pair binds downstream of the mutation. We used the eukaryotic translation elongation factor 1 alpha gene (*eef1a*) as an internal reference for these qPCRs (see later for justification of this). In keeping with our *in situ* hybridisation data, we saw that *tcp1* mRNA expression was significantly reduced in the homozygous mutants (by approximately 90%) compared to wild-type larvae. We also observed a significant reduction in *tcp1* expression (by approximately 25-35%) in heterozygous mutants, which is consistent with the mutant transcript being degraded.

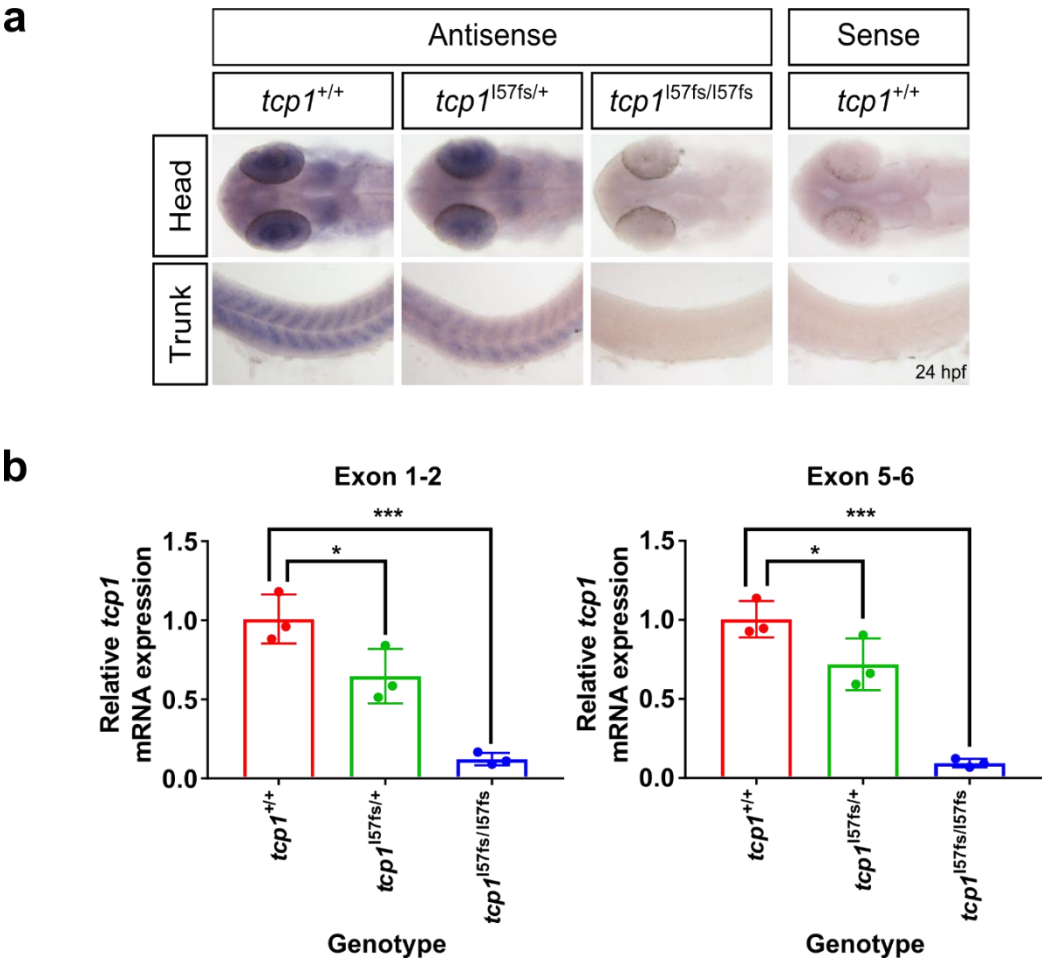

Figure 4.1. Whole-mount *in situ* hybridisation and qPCR analysis demonstrates nonsense-mediated decay of *tcp1* transcript in *tcp1*^{l57fs} mutant zebrafish embryos. (**a**) Bright field images of heads (dorsal view) and trunks (lateral view) of wild-type and *tcp1* frameshift mutant embryos at 24 hpf, stained with antisense or sense RNA probes against *tcp1*. (**b**) Bar graphs of qPCR results, showing mean fold change in *tcp1* transcript expression in *tcp1* frameshift mutant zebrafish larvae at 5 dpf. Two independent primer pairs were designed to generate products spanning the boundary between exon 1 and exon 2 or the boundary between exon 5 and exon 6. Expression of *tcp1* was normalised to the internal reference gene, *eef1a*. Three independent experimental replicates (indicated by individual points on the graph) were performed, using cDNA generated from pools of 4-6 larvae per genotype, per experiment. Error bars represent standard deviations of results from the three experiments, and statistical significance was determined using GraphPad Prism 7.03, by performing ordinary one-way analysis of variance (ANOVA) followed by Dunnett's multiple comparisons tests between wild-type and mutant samples.

4.3 Zebrafish *tcp1*^{P73L} mutant mRNA is not degraded

To genetically model the human *TCP1*-linked disorder, we precisely engineered the missense mutation associated with the human disease into the zebrafish genome. Since none of the single-nucleotide substitutions that we introduced into this line result in a premature stop codon, we did not expect to see any loss of *tcp1* transcript expression in our *tcp1*^{P73L} mutant zebrafish.

In line with this, whole-mount *in situ* hybridisation analysis of these mutants revealed that *tcp1* mRNA expression levels were comparable across all three genotypes; however, the heterozygous *tcp1*^{P73L} mutant embryos did not appear to display the same pattern of strong *tcp1* expression in the brain that we observed in the wild-type embryos, indicating that the spatial expression of the *tcp1* transcript may be altered in these mutants. Moreover, when we performed qPCR analysis to quantitatively measure *tcp1* transcript levels in the *tcp1*^{P73L} line at 5 dpf (Figure 4.2b), we observed an unexpected significant increase in mRNA expression in the heterozygous mutants compared to wild-type larvae (by approximately 60%). This effect was observed with both primer pairs. We also detected a slight (approximately 20-35%) increase in *tcp1* mRNA expression in the homozygous mutants, though this only reached statistical significance with one of the two primer pairs that we designed to amplify *tcp1* cDNA.

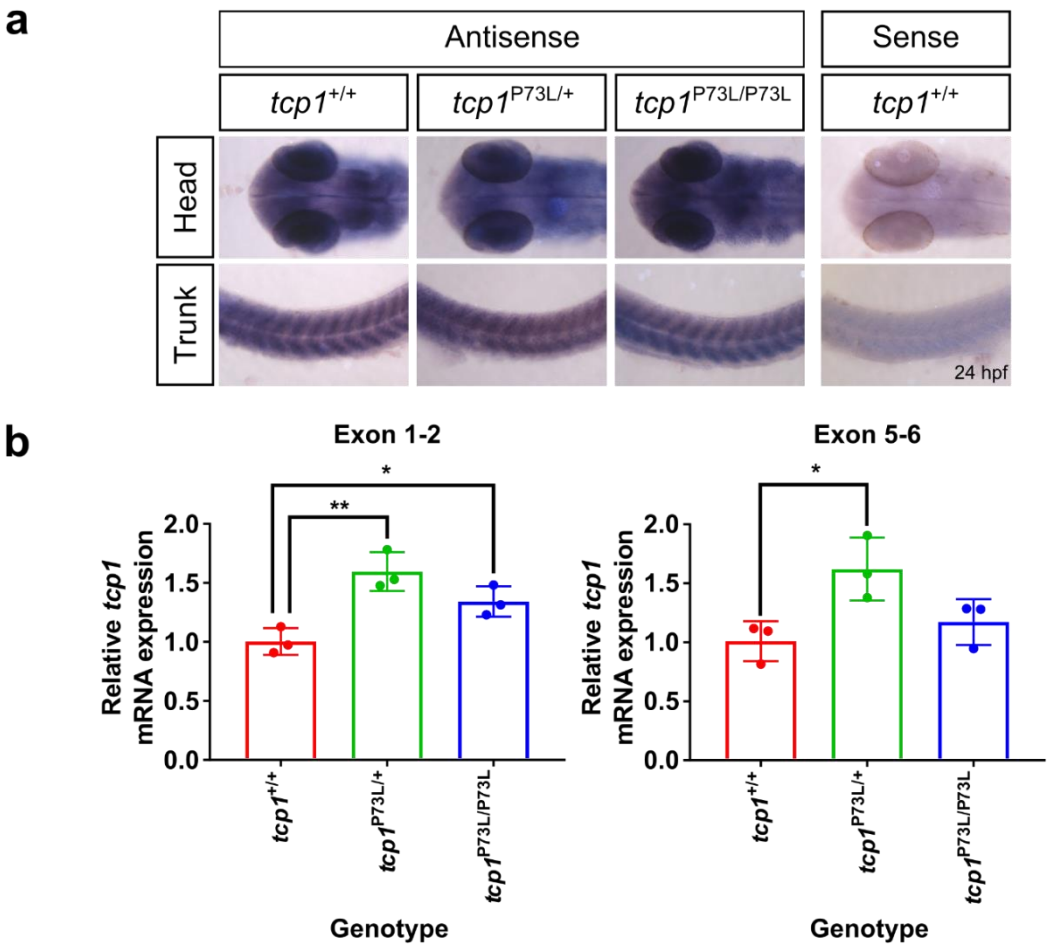

Figure 4.2. Whole-mount *in situ* hybridisation and qPCR analysis confirms that *tcp1* transcript does not undergo nonsense-mediated decay in *tcp1*^{P73L} mutant zebrafish embryos. (**a**) Bright field images of heads (dorsal view) and trunks (lateral view) of wild-type and *tcp1*^{P73L} mutant embryos at 24 hpf, stained with antisense or sense RNA probes against *tcp1*. (**b**) Bar graphs of qPCR results, showing mean fold change in *tcp1* transcript expression in *tcp1*^{P73L} mutant zebrafish larvae at 5 dpf. Two independent primer pairs were designed to generate products spanning the boundary between exon 1 and exon 2 or the boundary between exon 5 and exon 6. Three independent experimental replicates (indicated by individual points on the graph) were performed, using cDNA generated from pools of 4-6 larvae per genotype, per experiment. Error bars represent standard deviations of results from the three experiments, and statistical significance was determined using GraphPad Prism 7.03, by performing ordinary one-way ANOVA followed by Dunnett's multiple comparisons tests between wild-type and mutant samples.

4.4 Transcripts for TRiC/CCT folding substrates are differentially expressed in *tcp1*^{l57fs}, but not *tcp1*^{P73L}, mutant zebrafish larvae

As we discussed in Chapter 1, the functions of *TCP1* and its substrates are wide-ranging and have been linked to numerous cellular pathways. Before we conducted the qPCR experiments presented in Figure 4.1 and Figure 4.2, we were concerned that the mutations we had introduced into *tcp1* might indirectly lead to changes in the expression levels of genes that we typically use as internal reference controls for qPCR, which could influence the outcome of the experiments. As a precautionary measure, we initially tested primers designed against two independent internal reference genes, *eef1a* and beta-actin (*actb1*), to determine whether their expression was altered in *tcp1* mutant larvae.

As shown in Figure 4.3a, the raw qPCR cycle threshold (Ct) values for *eef1a* were not significantly different between wild-type and mutant larvae, indicating that *eef1a* expression is not affected by either of our *tcp1* mutations. We therefore used *eef1a* as the internal reference gene to calculate the relative *tcp1* transcript levels shown in Figure 4.1 and Figure 4.2.

Contrastingly, we noted that the Ct values for *actb1* were significantly lower in the homozygous *tcp1*^{l57fs} mutants than in the wild-type larvae (Figure 4.3bi), indicating that *actb1* mRNA levels are increased at 5 dpf in homozygous *tcp1*^{l57fs} mutants. Accordingly, when we calculated the relative fold change in *actb1* transcript expression using *eef1a* as the internal reference control, we found that levels of *actb1* mRNA were approximately three times higher in homozygous *tcp1*^{l57fs} mutants than in wild-type larvae (Figure 4.4ai). We did not, however, observe any significant difference in *actb1* expression in homozygous *tcp1*^{P73L} mutants (Figure 4.3bii, Figure 4.4aii).

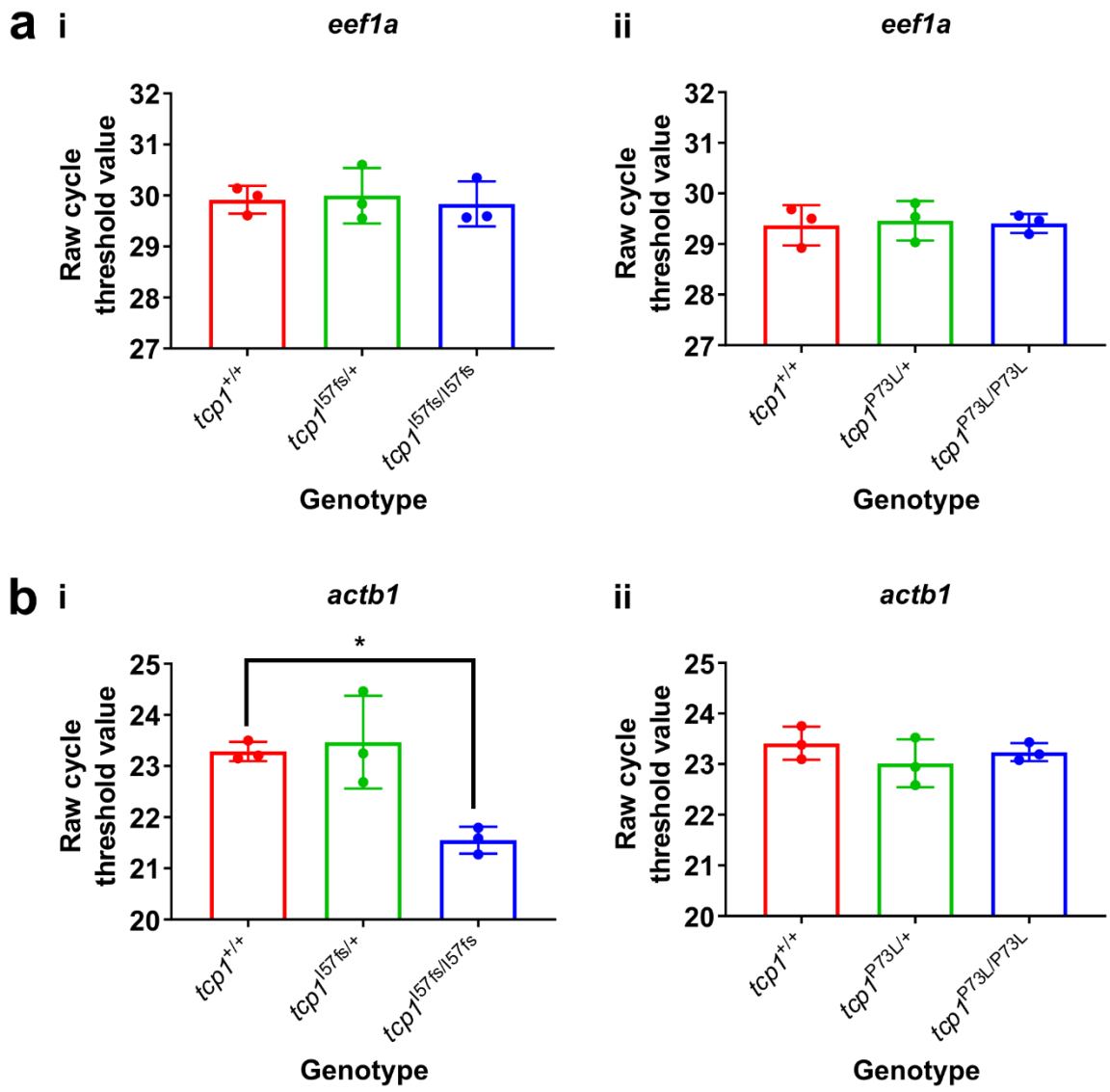

Figure 4.3. Effect of zebrafish *tcp1* mutations on raw Ct values for internal qPCR reference genes. Bar graphs of mean raw Ct values for (**a**) *eef1a* and (**b**) *actb1* in wild-type or mutant larvae from (**i**) the *tcp1*^{I57fs} line and (**ii**) the *tcp1*^{P73L} line at 5 dpf. Three independent experimental replicates were performed, using cDNA generated from pools of 4-6 larvae per genotype, per experiment. Error bars represent standard deviations of results from the three experiments, and statistical significance was determined using GraphPad Prism 8.3.1, by performing ordinary one-way ANOVA followed by Dunnett's multiple comparisons tests between wild-type and mutant samples.

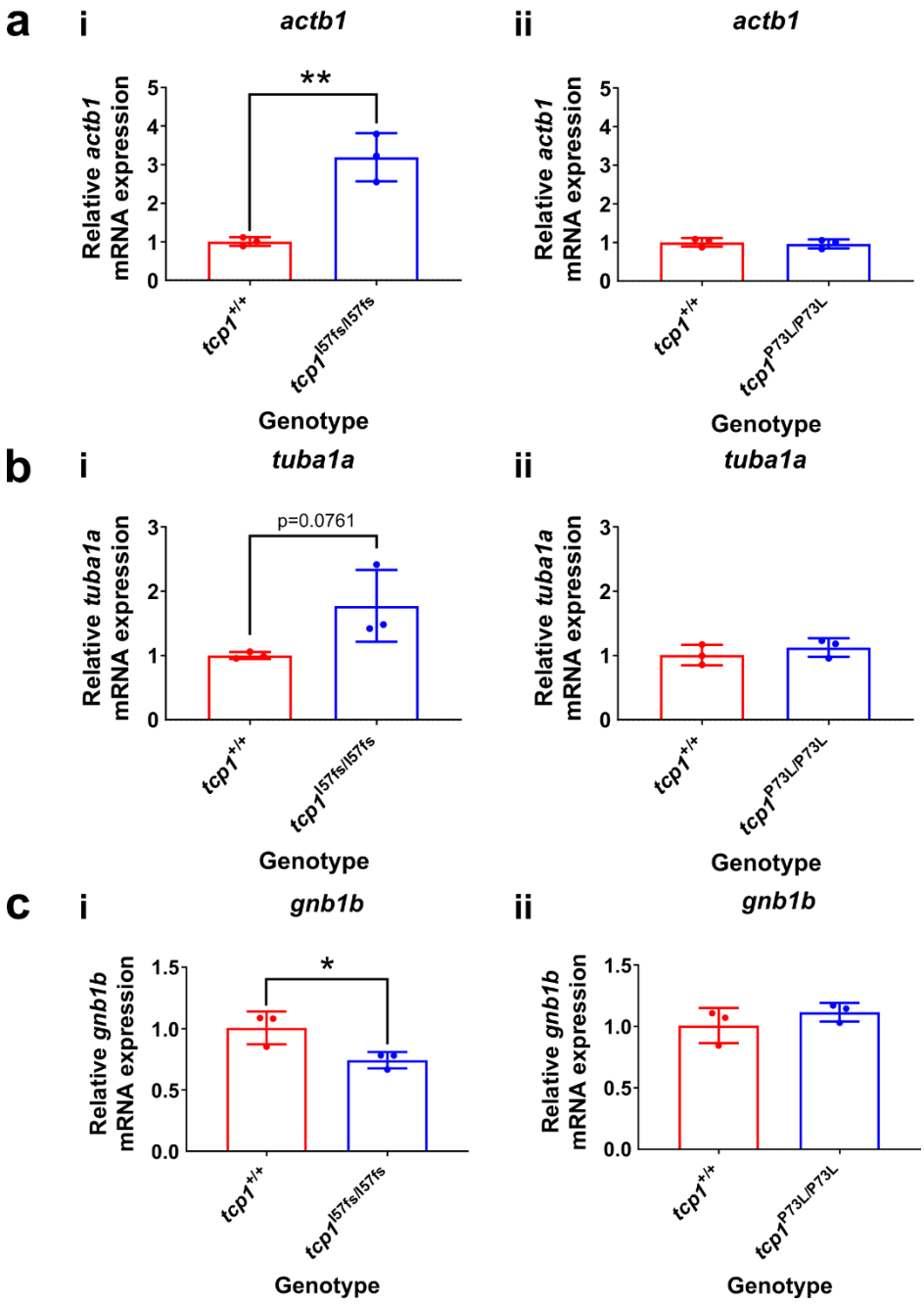

Figure 4.4. qPCR analysis demonstrates differential expression of TRiC/CCT substrate-encoding mRNA in *tcp1*^{l57fs}, but not *tcp1*^{P73L}, mutant zebrafish larvae. Bar graphs of qPCR results, showing mean fold changes in transcript expression for (**a**) *actb1*, (**b**) *tuba1a* and (**c**) *gnb1b* in (**i**) homozygous *tcp1*^{l57fs} and (**ii**) homozygous *tcp1*^{P73L} mutant zebrafish larvae at 5 dpf. Three independent experimental replicates (indicated by individual points on the graph) were performed for each target, using cDNA generated from pools of 4-6 larvae per genotype, per experiment. Error bars represent standard deviations of results from the three experiments, and statistical significance was determined using GraphPad Prism 7.03, by performing unpaired t tests between wild-type and mutant samples.

The zebrafish *actb1* gene encodes β-actin, which is one of the best-characterised folding substrates of TRiC/CCT (Sternlicht et al., 1993). We therefore theorised that the upregulation of *actb1* transcripts in *tcp1*^{I57fs} mutant zebrafish may reflect a failure of TRiC/CCT to properly fold β-actin, provoking a compensatory increase in the expression of *actb1* mRNA to offset insufficient production of functional β-actin protein.

We hypothesised that, if this were the case for *actb1*, we might also expect to see altered transcript expression for other TRiC/CCT folding substrates in *tcp1*^{I57fs} larvae. We therefore analysed expression levels of genes encoding two other well-characterised TRiC/CCT substrates: *tuba1a* (encoding α-tubulin) and *gnb1b* (encoding a rod cell-specific Gβ subunit of transducin).

Consistent with our hypothesis, we observed an approximately two-fold increase in *tuba1a* expression in homozygous *tcp1*^{I57fs} mutants compared with wild-type larvae (Figure 4.4bi), though this failed to reach statistical significance. Contrastingly, the levels of *gnb1b* mRNA were significantly reduced (by approximately 25%) in the *tcp1*^{I57fs} mutants (Figure 4.4ci). As for *actb1*, the mRNA levels for *tuba1a* and *gnb1b* remained unchanged in homozygous *tcp1*^{P73L} mutants compared to wild-type larvae (Figure 4.4bii,cii).

4.5 Loss of zebrafish *tcp1* results in induction of the heat shock response

To further probe the evidence for TRiC/CCT dysfunction in our *tcp1*^{I57fs} zebrafish model, we also investigated whether loss of *tcp1* results in induction of the heat shock response. The heat shock response is involved in maintaining proteostasis and is triggered in response to cellular stresses, such as the accumulation of misfolded proteins (Vabulas et al., 2010). We would predict TRiC/CCT dysfunction to impact on the heat shock response at two levels: firstly, by causing misfolded TRiC/CCT substrates to accumulate in the cytoplasm, resulting in proteostatic stress; and secondly, by disrupting the suppressive effect of TRiC/CCT upon HSF1, which is the primary transcription factor responsible for mediating the heat shock response (Neef et al., 2014).

To assess whether the heat shock response is induced in our *tcp1* mutant zebrafish, we measured the transcript levels for *hsp70.1* and *hsp70l*, which encode heat shock chaperone proteins and are well-characterised downstream targets of zebrafish hsf1 (Rupik et al., 2011). We observed an approximately 5-fold increase in the expression of both genes in homozygous *tcp1*^{I57fs} larvae compared to wild-type controls (Figure 4.5ai,bi), consistent with induction of the heat shock response. In contrast, we did not observe induction of these genes in homozygous *tcp1*^{P73L} mutant larvae (Figure 4.5aii,bii), indicating that the heat shock response is unlikely to be activated as a result of the *tcp1*^{P73L} mutation.

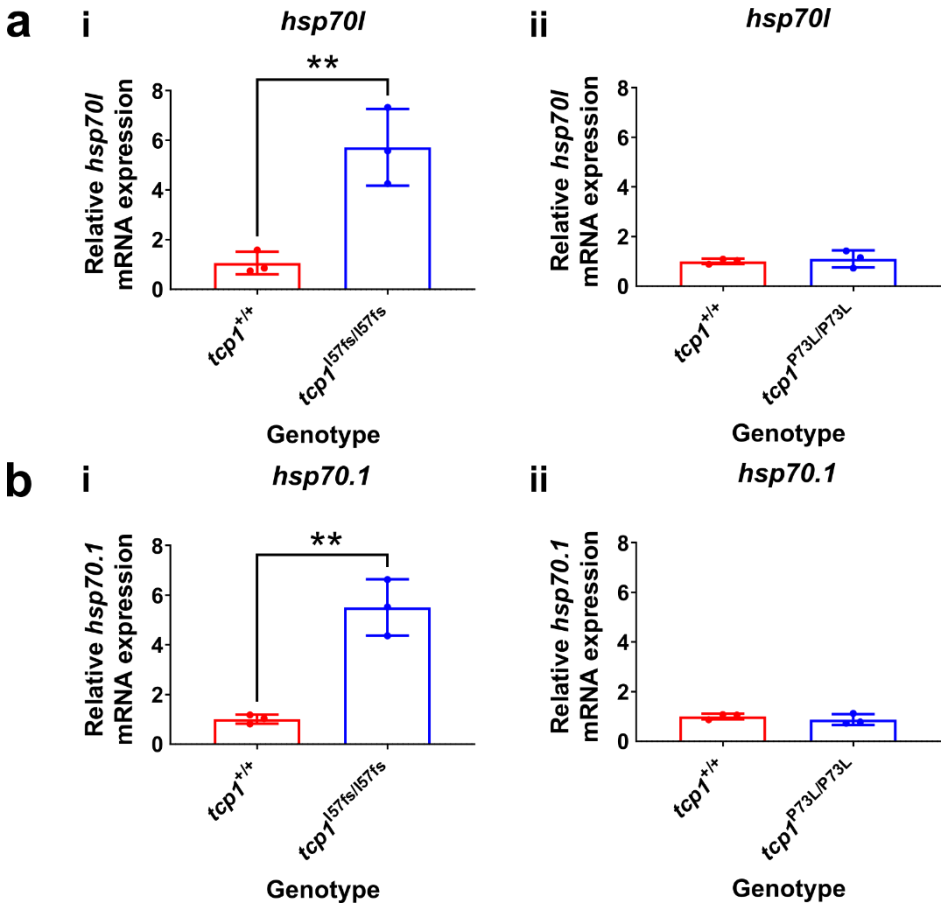

Figure 4.5. qPCR analysis demonstrates upregulation of *hsp70.1* and *hsp70l* mRNA expression in *tcp1*^{I57fs}, but not *tcp1*^{P73L}, mutant zebrafish larvae. Bar graphs of qPCR results, showing mean fold change in transcript expression for (**a**) *hsp70l* and (**b**) *hsp70.1* in (**i**) *tcp1*^{I57fs} and (**ii**) *tcp1*^{P73L} mutant zebrafish larvae at 5 dpf. Three independent experimental replicates (indicated by individual points on the graph) were performed for both targets, using cDNA generated from pools of 4-6 larvae per genotype, per experiment. Error bars represent standard deviations of results from the three experiments, and statistical significance was determined using GraphPad Prism 7.03, by performing unpaired t tests between wild-type and mutant samples.

4.6 Loss of zebrafish *tcp1* results in severe morphological defects during development

Once we had established that our *tcp1*^{I57fs} mutant zebrafish reflects a loss of *tcp1*, we proceeded to characterise the gross morphological effects of our *tcp1* mutations upon zebrafish development so that we could test our hypotheses relating to the pathogenicity of the *TCP1*^{P70L} mutation and developmental roles for *TCP1*. We were primarily interested in determining whether either mutant line would exhibit obvious defects that might be relevant to the pathology of the human disorder.

By 4 dpf, homozygous *tcp1*^{I57fs} mutant larvae exhibited several severe malformations and were developmentally delayed (Figure 4.6a), with significantly reduced body length, prominent pericardial oedema, and delayed yolk sac absorption. Interestingly, in the context of the retinal and cerebellar defects associated with the human *TCP1*-linked disorder, the homozygous mutants had significantly smaller eyes and heads than their siblings (Figure 4.6b-d).

In the interests of welfare, we did not attempt to raise these mutants past the point at which they would become legally protected (5.2 dpf); therefore, we did not formally quantify their survival. However, by 5 dpf, some embryos were no longer viable, and the phenotype of the mutants that were still alive was so severe that we did not expect them to be viable beyond this point.

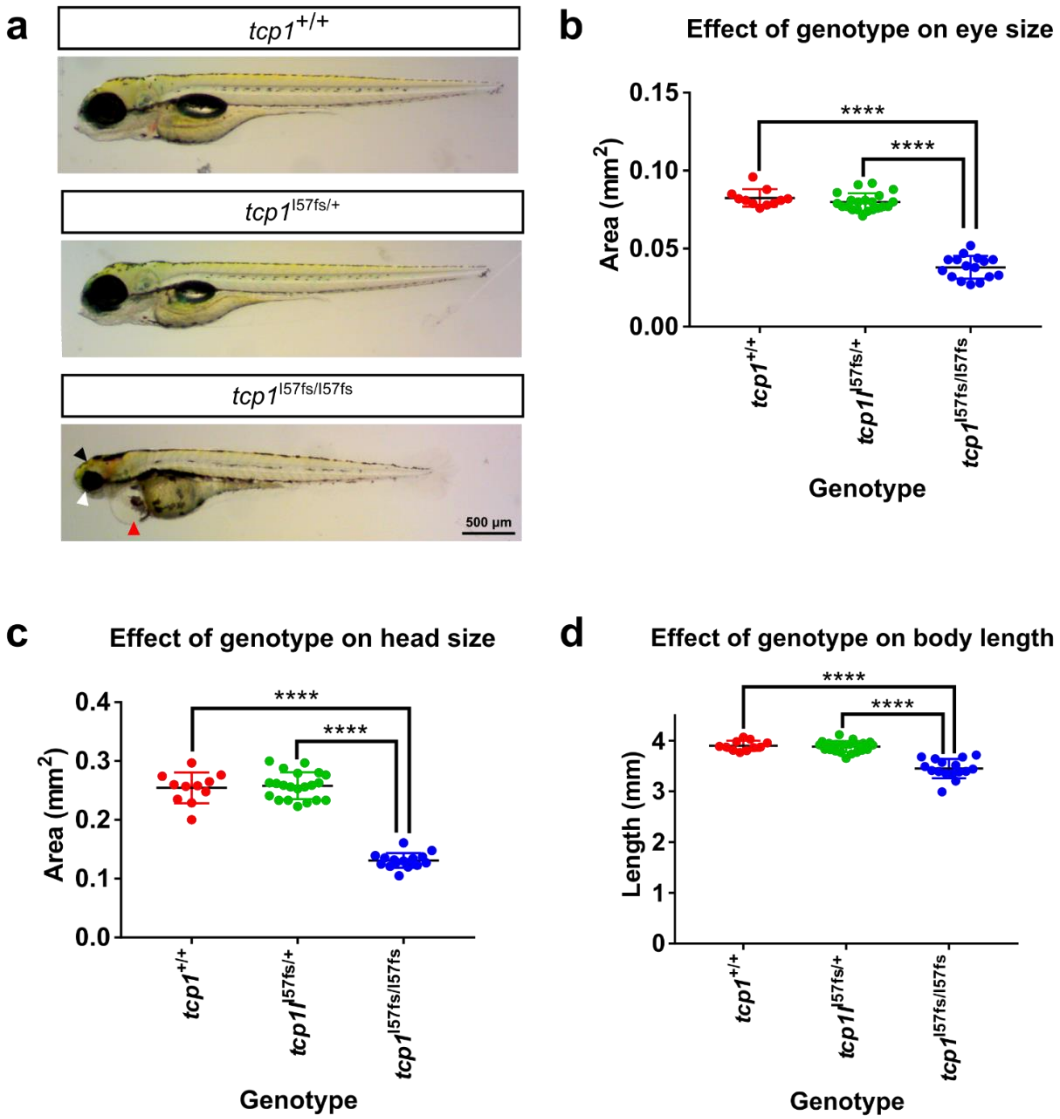

Figure 4.6. Loss of *tcp1* results in severe developmental defects in zebrafish larvae. (**a**) Representative photomicrographs of wild-type, heterozygous and homozygous *tcp1*^{l57fs} mutant zebrafish (lateral view) at 4 dpf, highlighting the smaller eyes (white arrowhead), smaller head (black arrowhead) and pericardial oedema (red arrowhead) observed in homozygous mutants. All images shown to scale. Graphs showing quantification of (**b**) mean eye size, (**c**) mean head size and (**d**) mean body length in wild-type and mutant larvae at 4 dpf, measured as described in Chapter 2. Error bars represent standard deviations of measurements from n = 11 wild-type, n = 21 heterozygous mutants and n = 16 homozygous mutant larvae (represented by individual data points), from two separate clutches. Statistical significance was determined using GraphPad Prism 7.03, by performing ordinary one-way ANOVA followed by Tukey's multiple comparisons between wild-type, heterozygous and homozygous mutant samples.

As we only outcrossed our founders through two generations before we began incrossing heterozygous mutants for phenotypic analysis, there is a small possibility that any off-target mutations that were unintentionally introduced by the CRISPR could have persisted through these outcrosses.

To confirm that the phenotypes we had observed in our *tcp1*^{I57fs} mutants could be attributed to the *tcp1*^{I57fs} mutation, and not an off-target mutation elsewhere in the genome, we generated a second, independent frameshift mutant line (*tcp1*^{H72fs}), as described in Chapter 2. This second mutant line carries a 2 bp deletion in *tcp1*; this results in a premature stop codon in a different reading frame to that of the *tcp1*^{I57fs} line (Figure 4.7).

When we incrossed this second frameshift mutant line, we observed severe phenotypes in the homozygous mutants that closely recapitulate those exhibited by homozygous *tcp1*^{I57fs} mutants (Figure 4.8a). However, we also detected some spinal curvature in the homozygous *tcp1*^{H72fs} mutants which we had not seen in homozygous *tcp1*^{I57fs} mutants. Furthermore, when we crossed both frameshift mutant lines with each other and examined compound heterozygotes carrying both mutant alleles, we observed the same phenotypes as in the homozygous *tcp1*^{I57fs} mutants, without the spinal curvature that we saw in the homozygous *tcp1*^{H72fs} mutants (Figure 4.8b).

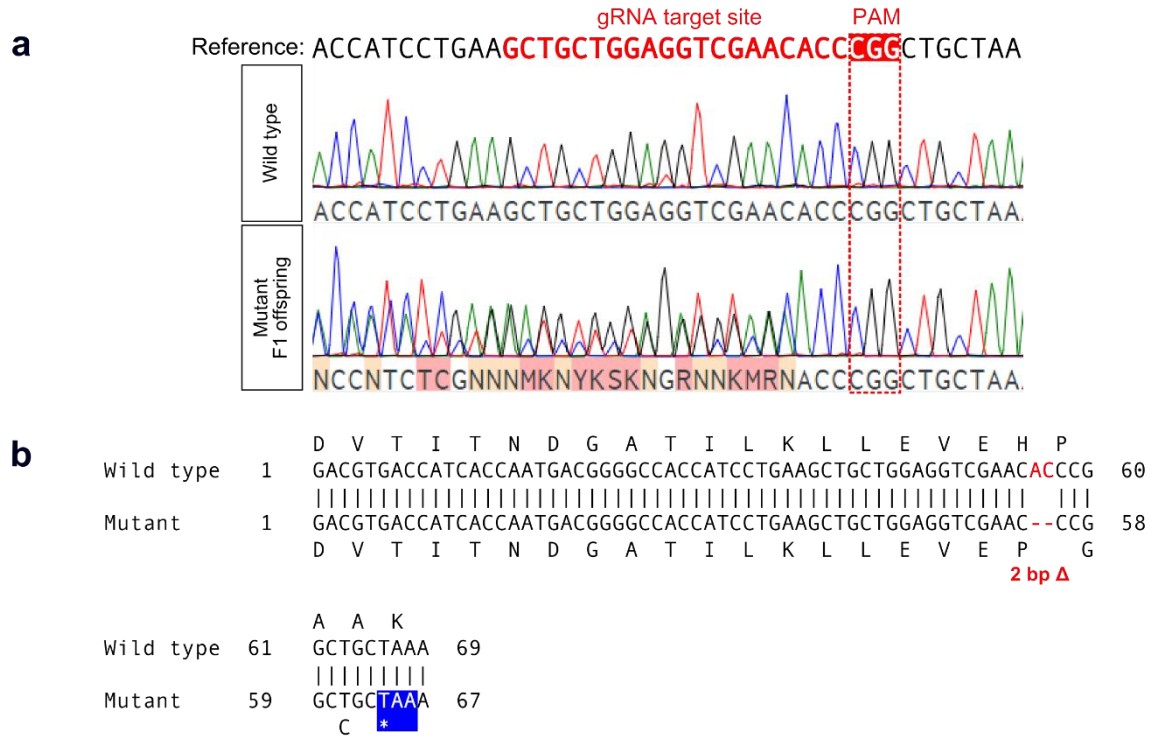

Figure 4.7. Identification of a founder transmitting an alternative frameshift mutation in *tcp1*. (**a**) Sequencing analysis of heterozygous F1 offspring carrying the *tcp1*^{H72fs} mutant allele. (**b**) Sequence alignment of the wild-type and mutant alleles, showing that the shifted reading frame introduces a premature stop codon (**blue**) downstream of the deletion (**red**).

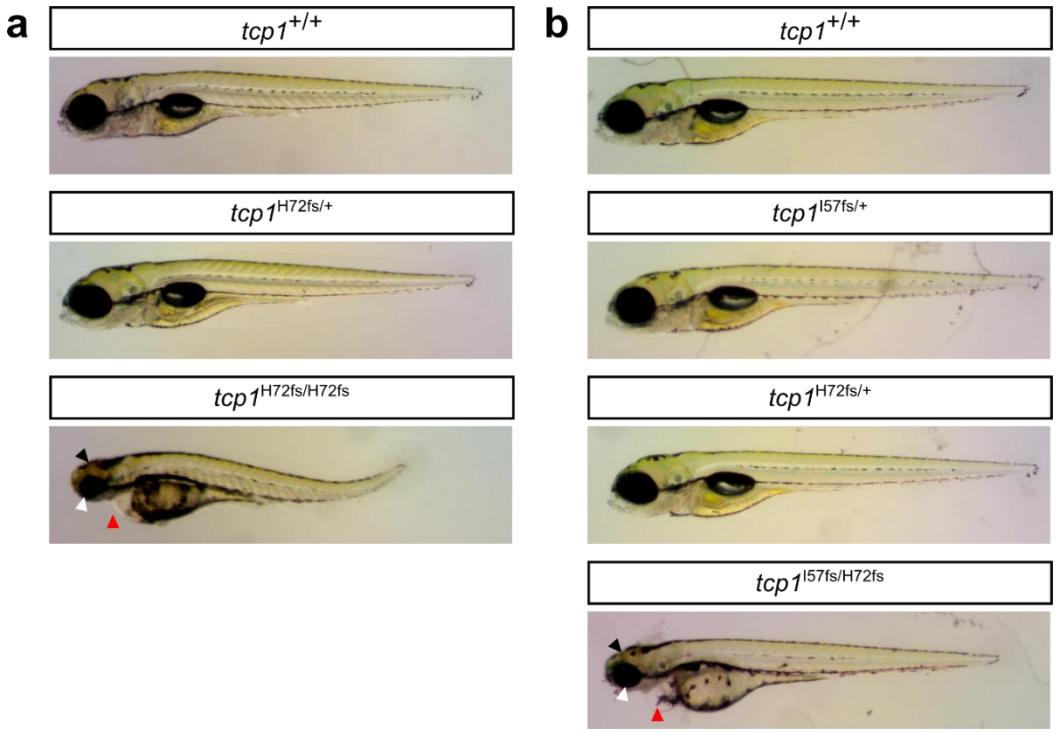

Figure 4.8. Developmental defects associated with loss of *tcp1* are recapitulated in an independent *tcp1* frameshift mutant line. (**a**) Representative photomicrographs of wild-type, heterozygous and homozygous *tcp1*^{H72fs} mutant zebrafish (lateral view) at 4 dpf, highlighting the smaller eyes (white arrowhead), smaller head (black arrowhead) and pericardial oedema (red arrowhead) observed in homozygous mutants. (**b**) Photomicrographs of wild-type, heterozygous (*tcp1*$^{H72fs/+}$ and *tcp1*$^{I57fs/+}$) and compound heterozygous (*tcp1*$^{I57fs/H72fs}$) mutant zebrafish (lateral view) at 4 dpf, highlighting the smaller eyes (white arrowhead), smaller head (black arrowhead) and pericardial oedema (red arrowhead) observed in compound heterozygous mutants. All images shown to scale.

4.7 The *tcp1*^{P73L} mutation does not alter the gross morphology of larval or adult zebrafish

In contrast to the severe developmental defects that we observed in homozygous *tcp1* frameshift mutant larvae, we did not detect any obvious gross morphological abnormalities in homozygous *tcp1*^{P73L} mutant larvae (Figure 4.9a), and we saw no significant difference in their body length, head size or eye size compared to their wild-type and heterozygous siblings (Figure 4.9b-d). We also saw no discernible difference in the gross morphology of these mutants compared with their wild-type siblings once they reached adulthood (Figure 4.10).

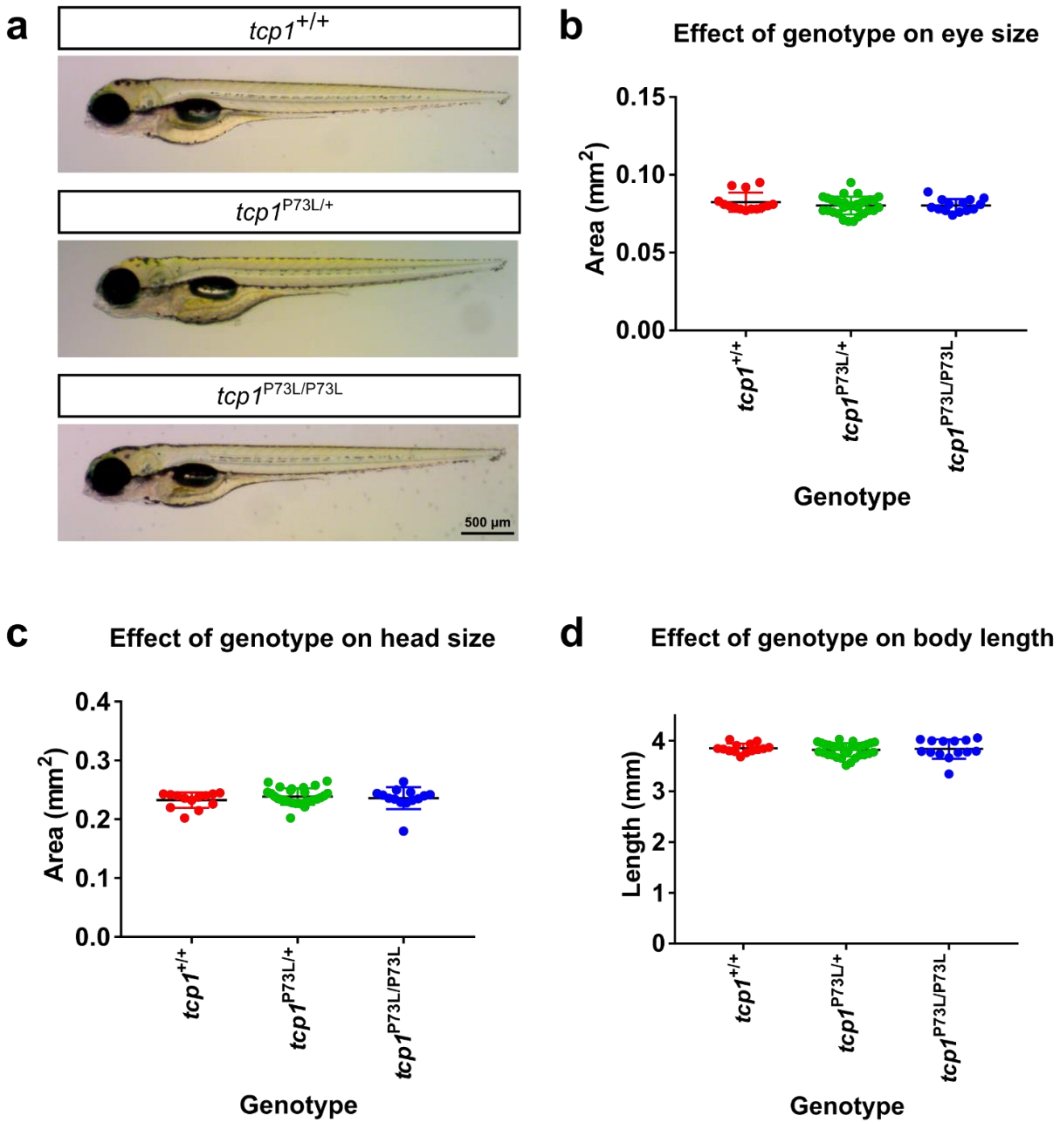

Figure 4.9. The *tcp1*^{P73L} mutation does not cause any gross morphological defects in zebrafish larvae. (**a**) Representative photomicrographs of wild-type, heterozygous and homozygous *tcp1*^{P73L} mutant zebrafish (lateral view) at 4 dpf. All images shown to scale. Graphs showing quantification of (**b**) mean eye size, (**c**) mean head size and (**d**) mean body length in wild-type and mutant larvae at 4 dpf, measured as described in Chapter 2. Error bars represent standard deviations of measurements from n = 14 wild-type, n = 31 heterozygous mutants and n = 14 homozygous mutant larvae (represented by individual data points), from two separate clutches. Statistical analysis was performed in GraphPad Prism 7.03 by ordinary one-way ANOVA.

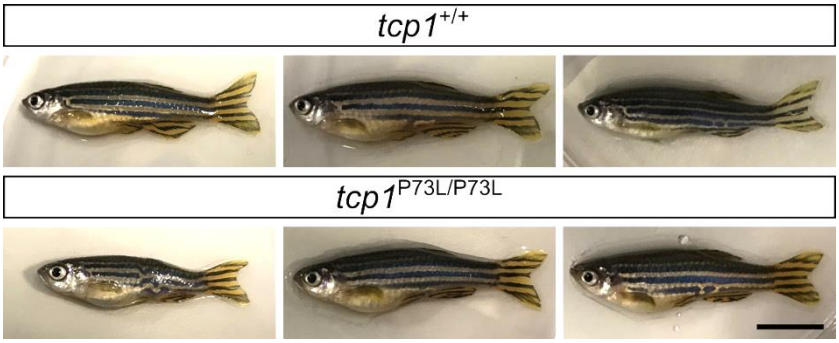

Figure 4.10. The *tcp1*^{P73L} mutation does not cause any gross morphological defects in adult zebrafish. Representative photographs of three wild-type (top) and three homozygous *tcp1*^{P73L} mutant (bottom) zebrafish (lateral view) at 14 months post-fertilisation (mpf). All images shown to scale; scale bar = 1 cm.

4.8 *tcp1* is required for proper cerebellar development in zebrafish

Once we had assessed the effects of *tcp1* mutations on zebrafish development at the gross morphological level, we then proceeded to investigate how they affect the development of the specific tissues associated with the human disease, starting with the cerebellum.

To investigate cerebellar development in our *tcp1* mutant zebrafish, we crossed heterozygous *tcp1*^{I57fs} or *tcp1*^{P73L} mutants onto a transgenic line (FyntagRFP-T:PC) which specifically expresses the red fluorescent protein, FyntagRFP-T, in cerebellar Purkinje cells (Matsui et al., 2014). We then crossed heterozygous *tcp1* mutants that were expressing RFP with non-transgenic heterozygous *tcp1* mutants to obtain homozygous *tcp1* mutants carrying a single copy of the RFP transgene for phenotypic analysis.

When we examined the brains of *tcp1*^{I57fs} zebrafish at 5 dpf, we were unable to detect any RFP-positive Purkinje cells (Figure 4.11). We reasoned that the lack of RFP expression in the *tcp1*^{I57fs} larvae at this stage could be explained either by a complete failure of Purkinje cells to develop, or by a degenerative loss of Purkinje cells following their initial development.

To gain further insight into which of these possibilities was more likely, we explored whether Purkinje cells are present in the brains of *tcp1*^{I57fs} mutant larvae at an earlier stage (3 dpf). However, we were still unable to detect RFP-positive Purkinje cells in *tcp1*^{I57fs} mutants (Figure 4.12), supporting the notion that *tcp1* may be important for Purkinje cell development.

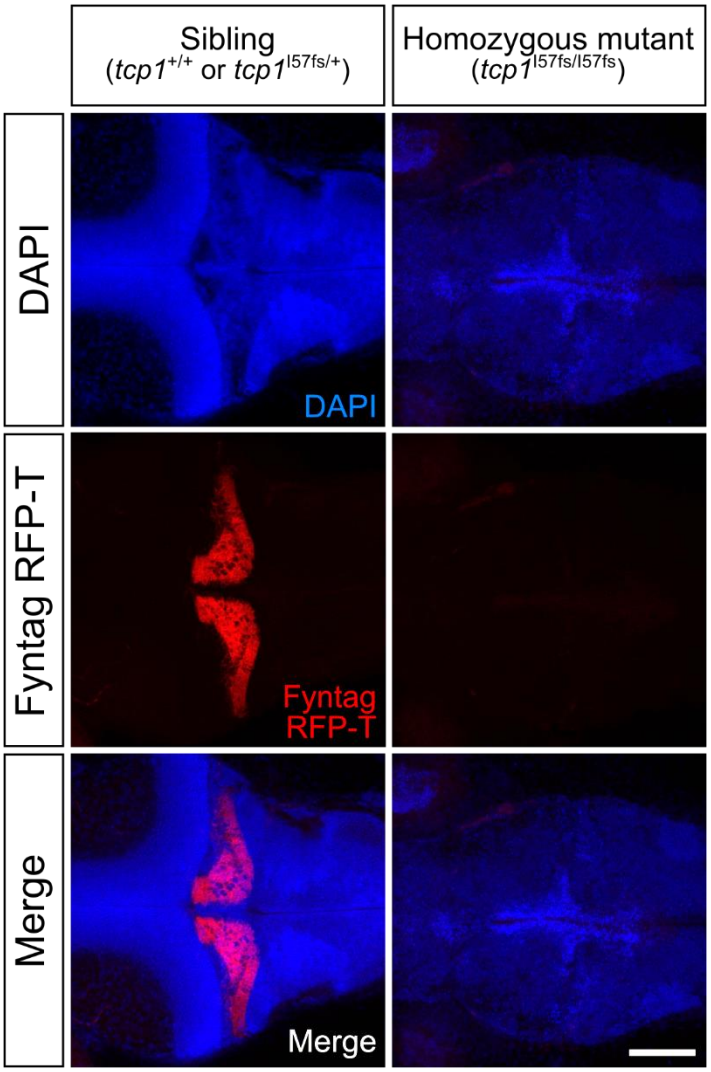

Figure 4.11. *tcp1*^{l57fs} zebrafish larvae lack cerebellar Purkinje cells at 5 dpf. Representative confocal micrographs (maximum intensity z-stack projections) of the brains (dorsal view) of one *tcp1*^{l57fs} mutant larva and one sibling, at 5 dpf. Larvae expressed FyntagRFP-T (**red**) under the control of a Purkinje cell-specific regulatory element and nuclei were counterstained with DAPI (**blue**). Images are representative of n = 15 homozygous mutants and n = 10 control siblings, obtained from at least three independent clutches. All images shown to scale; scale bar = 100 µm.

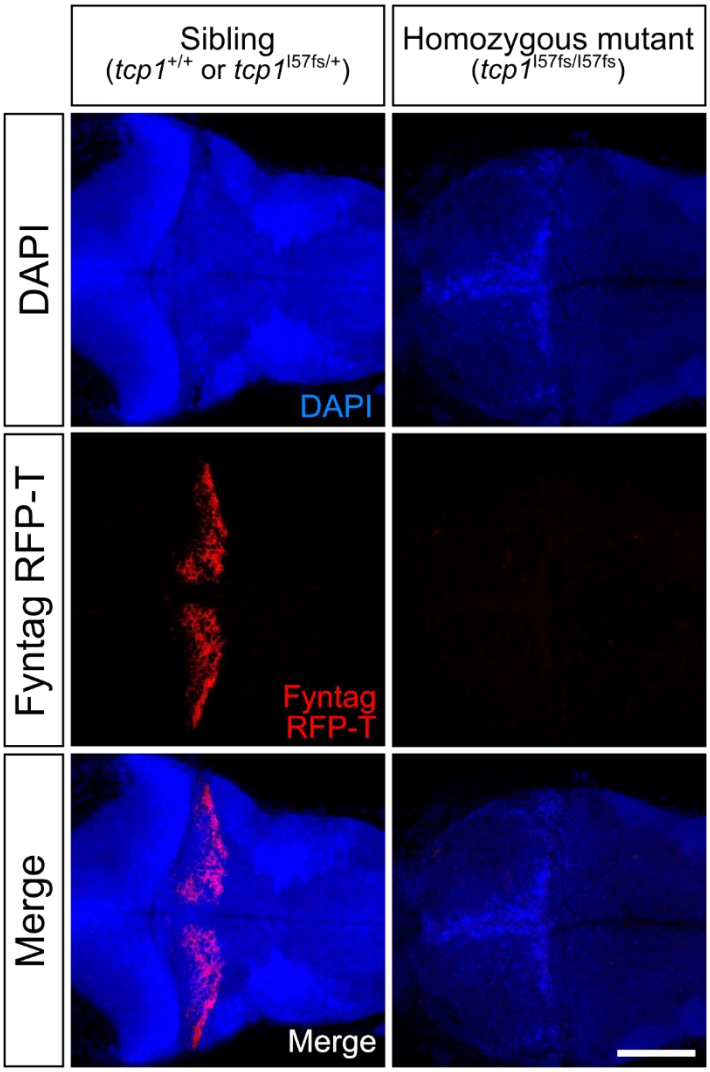

Figure 4.12. *tcp1*^{l57fs} zebrafish larvae lack cerebellar Purkinje cells at 3 dpf. Representative confocal micrographs (maximum intensity z-stack projections) of the brains (dorsal view) of one *tcp1*^{l57fs} mutant larva and one sibling, at 3 dpf. Larvae expressed FyntagRFP-T (**red**) under the control of a Purkinje cell-specific regulatory element and nuclei were counterstained with DAPI (**blue**). Images are representative of n = 12 homozygous mutants and n = 6 control siblings, obtained from at least three independent clutches. All images shown to scale; scale bar = 100 μm.

4.9 The *tcp1*^{P73L} mutation does not affect cerebellar Purkinje cell development

We then investigated whether Purkinje cell development is affected by the specific mutation associated with the human *TCP1*-linked disorder. In contrast to their absence in the *tcp1*^{I57fs} mutant larvae, neither the development of Purkinje cells, nor the overall morphology of the cerebellum, appeared to be compromised in homozygous *tcp1*^{P73L} mutants (Figure 4.13).

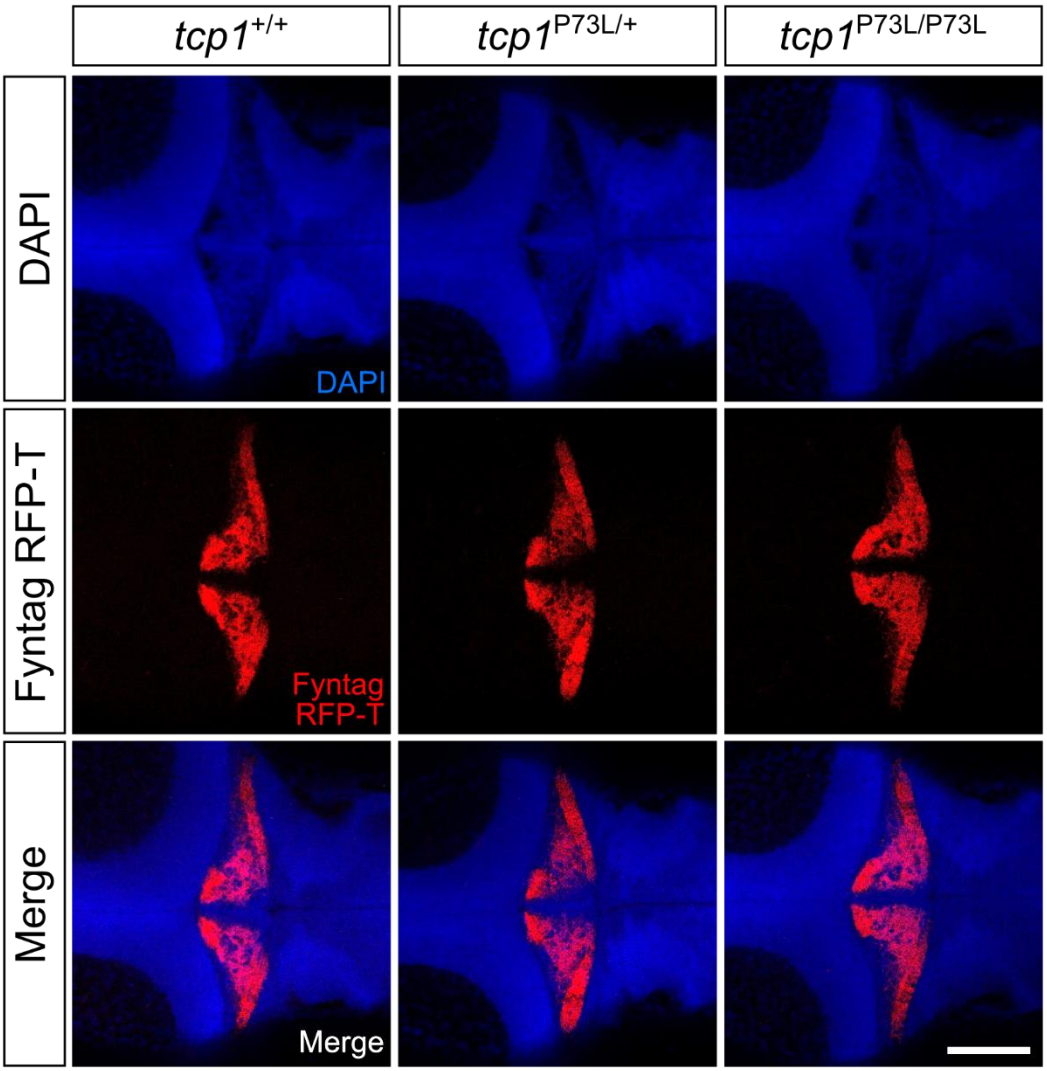

Figure 4.13. Cerebellar Purkinje cell development does not appear to be affected in *tcp1*^{P73L} mutant larvae. Representative confocal micrographs (maximum intensity z-stack projections) of the brains (dorsal view) of one wild-type, one heterozygous and one homozygous *tcp1*^{P73L} mutant larva, at 5 dpf. Larvae expressed FyntagRFP-T (**red**) under the control of a Purkinje cell-specific regulatory element and nuclei were counterstained with DAPI (**blue**). Images are representative of n = 6 wild-type larvae, n = 13 heterozygous mutants and n = 7 homozygous mutants. All images shown to scale; scale bar = 100 μm.

4.10 Loss of zebrafish *tcp1* results in irregularities in the optic tectum

When we investigated cerebellar development in the *tcp1*^{I57fs} mutant larvae, we noted that, not only did the mutants lack Purkinje cells, but their overall brain morphology was also grossly abnormal. Unsurprisingly, given the significantly smaller head size of these mutants (Figure 4.6c), their brains were substantially smaller than those of their siblings (Figure 4.11,Figure 4.12), and DAPI staining highlighted a large number of cells with condensed nuclei, which were present in large numbers throughout the optic tectum (Figure 4.14), indicative of widespread cell death in this region. Moreover, we also detected some condensed nuclear staining posterior to the optic tectum, indicating that the hindbrain may also be affected (Figure 4.14).

To further investigate cell death in the *tcp1*^{I57fs} mutant brain, we performed immunohistochemical analysis of cleaved caspase 3 expression to detect cells undergoing apoptosis. Consistent with the DAPI staining, this revealed large populations of caspase-positive cells, which were predominantly clustered within the optic tectum (Figure 4.15). Correspondingly, when we immunostained larvae for the axonal marker, acetylated α-tubulin, we noted that the axons within the optic tectum also appeared grossly abnormal in the *tcp1*^{I57fs} mutants (Figure 4.16).

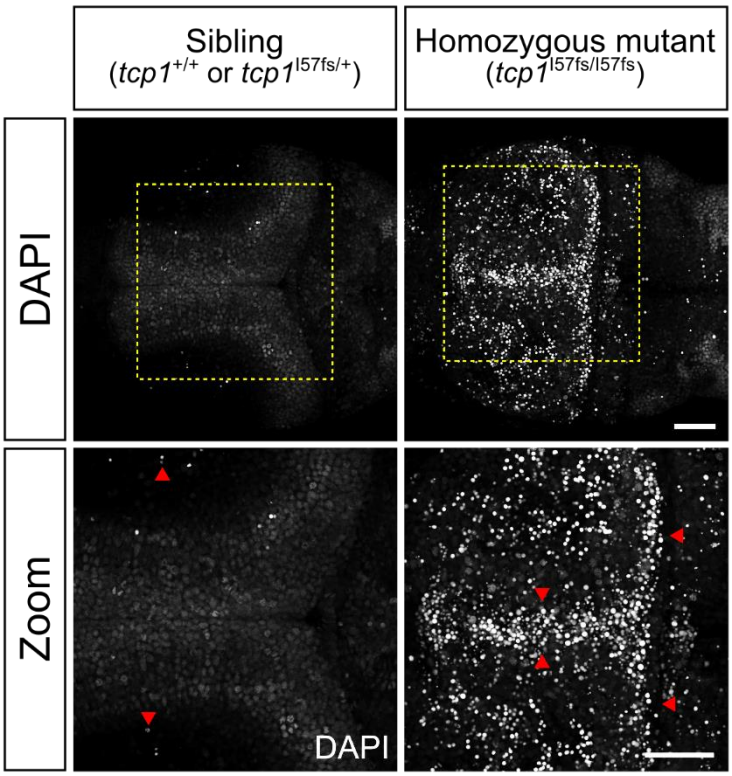

Figure 4.14. DAPI staining highlighted large numbers of cells with condensed nuclei in the optic tectum of *tcp1*^{l57fs} mutant larvae. Representative confocal micrographs (maximum intensity z-stack projections) of the brains (dorsal view) of one *tcp1*^{l57fs} mutant larva and one sibling, at 3 dpf. Nuclei were stained with DAPI (**grey**). All images and zoomed panels shown to scale; scale bars = 50 µm. Red arrowheads indicate examples of condensed nuclear staining. Zoomed panels correspond to regions highlighted by dashed yellow boxes.

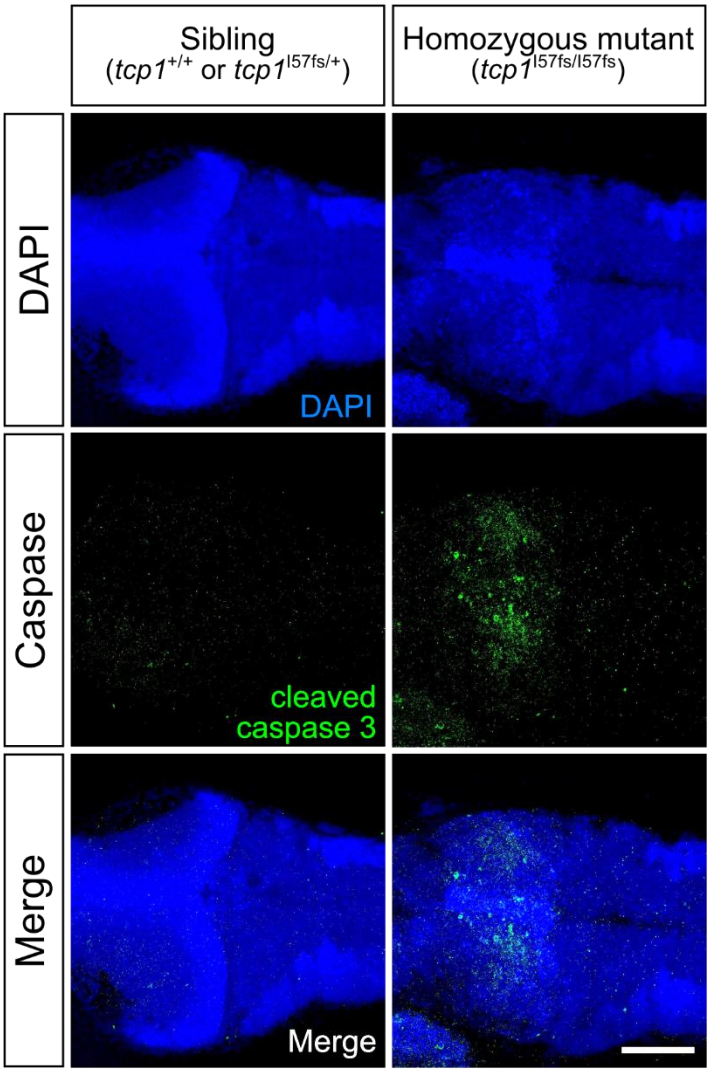

Figure 4.15. Apoptotic cells are prevalent in the optic tectum of *tcp1*^{l57fs} zebrafish larvae. Representative confocal micrographs (maximum intensity z-stack projections) of the brains (dorsal view) of one *tcp1*^{l57fs} mutant larva and one sibling, at 3 dpf. Whole-mount immunostaining was performed to detect cleaved caspase 3 (**green**) and nuclei were counterstained with DAPI (**blue**). Images are representative of n = 20 homozygous mutants and n = 6 control siblings. Larvae were obtained from at least three independent clutches in total and were stained across three separate experiments. All images shown to scale; scale bar = 100 μm.

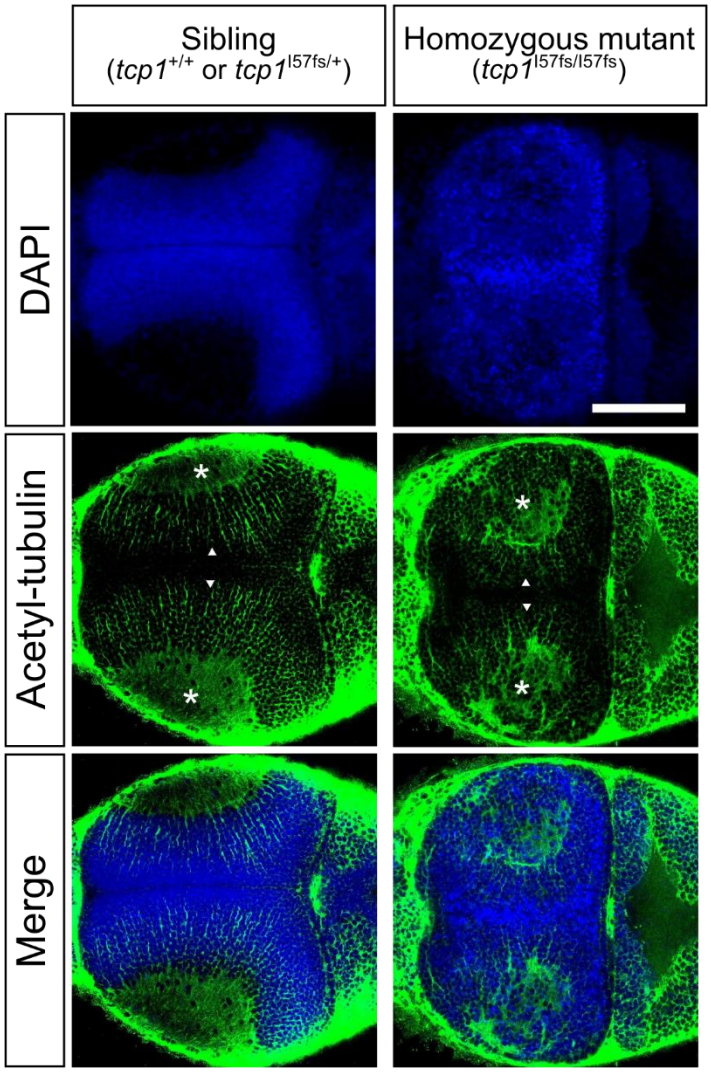

Figure 4.16. Axonal abnormalities are apparent in the optic tectum of *tcp1*^{l57fs} zebrafish larvae. Representative confocal micrographs (single z-slices) of the brains (dorsal view) of one *tcp1*^{l57fs} mutant larva and one sibling, at 3 dpf. Whole-mount immunostaining was performed to detect acetylated α-tubulin (**green**) and nuclei were counterstained with DAPI (**blue**). The tectal neuropil is marked by white asterisks and white arrowheads point to axonal projections. Images are representative of n = 13 homozygous mutants and n = 7 control siblings. Larvae were obtained from at least three independent clutches in total and were stained across three separate experiments. All images shown to scale; scale bar = 100 μm.

4.11 Loss of *tcp1*, but not the *tcp1*^{P73L} mutation, results in retinal abnormalities in zebrafish larvae

When we analysed the gross morphology of our *tcp1* mutant larvae, we saw that loss of *tcp1*, but not the human disease-associated *tcp1*^{P73L} mutation, resulted in a significant decrease in overall eye size. We therefore planned to more specifically investigate the morphology of the retina to determine: a) whether the smaller eye size of the *tcp1*^{I57fs} mutants is underpinned by abnormalities in the retina, and b) whether we can detect any morphological defects in the *tcp1*^{P73L} mutant retina that might reflect the pathology of the human disorder. Given that the clinical features of patients suggest that the pathology primarily involves photoreceptors, we were particularly interested in whether photoreceptor development is altered in *tcp1*-mutant zebrafish.

To investigate retinal morphology in our mutant lines, we performed immunohistochemistry using antibodies to specifically detect photoreceptors. To do this, we took cryosections from the retinae of wild-type and *tcp1* mutant larvae at 5 dpf. By this stage, the constituent layers of the retina have been established and the photoreceptors have differentiated into their main subtypes (Schmitt and Dowling, 1999; Suzuki et al., 2013).

We did not detect any obvious differences in retinal morphology in homozygous *tcp1*^{P73L} mutants compared to wild-type larvae (Figure 4.17). The nuclear organisation within the retinae of these mutants suggests that retinal lamination is not impaired by the mutation, and the overall pattern of photoreceptor staining in the *tcp1*^{P73L} mutants was also comparable to that of the wild-type larvae.

In contrast, the morphology of the *tcp1*^{I57fs} mutant retina was grossly abnormal, with evidence of disrupted lamination. We also performed immunohistochemistry against cleaved caspase 3 to detect cells undergoing apoptosis and found that apoptotic cells were prevalent throughout the *tcp1*^{I57fs} mutant retina, especially in the retinal ganglion cell layer (Figure 4.17, Figure 4.18). We were still able to find cells that were stained positively for

photoreceptor markers in the *tcp1*^{l57fs} mutant retina (Figure 4.17); however, the organisation of these cells was abnormal, and we saw that they were often clustered and occupying a more vitread position within the retina, rather than being restricted to a distinct photoreceptor layer as in the wild-type larvae.

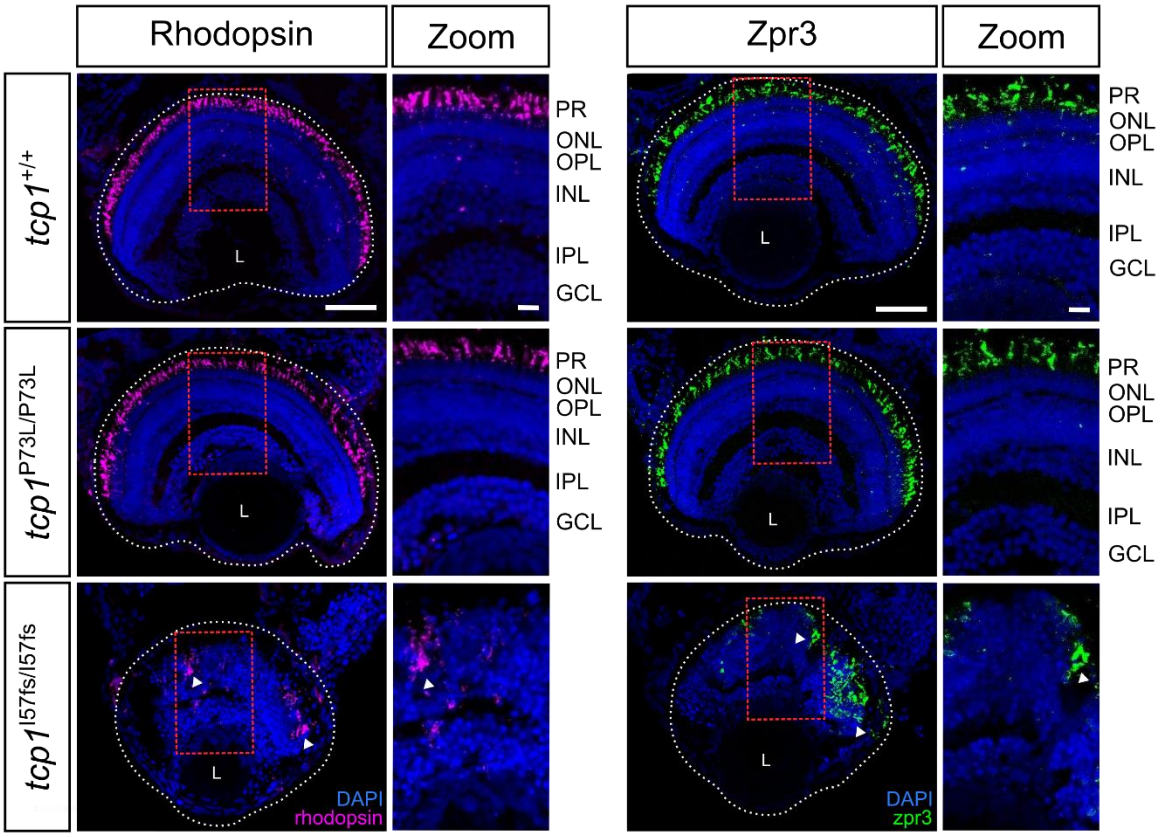

Figure 4.17. Retinal morphology is disrupted in *tcp1*^{I57fs}, but not *tcp1*^{P73L}, mutant zebrafish larvae. Representative confocal micrographs (maximum intensity z-stack projections) of retinal cryosections taken from wild-type, *tcp1*^{I57fs} mutant and homozygous *tcp1*^{P73L} mutant zebrafish larvae at 5 dpf. Sections were immunostained with rhodopsin (**magenta**) or zpr-3 (**green**) antibodies to label photoreceptors, and nuclei were counterstained with DAPI (**blue**). In each image, the perimeter of the eye is marked by a white dashed line, and regions corresponding to the areas shown in the higher magnification panels are marked by red dashed boxes. Images are representative of n = 3 individual fish of each genotype, stained across three separate experiments in total. All images and zoomed panels shown to scale; scale bars = 50 μm (whole retina), 10 μm (zoomed images). L = lens, PR = photoreceptor layer, ONL = outer nuclear layer, OPL = outer plexiform layer, INL = inner nuclear layer, IPL = inner plexiform layer, GCL = ganglion cell layer.

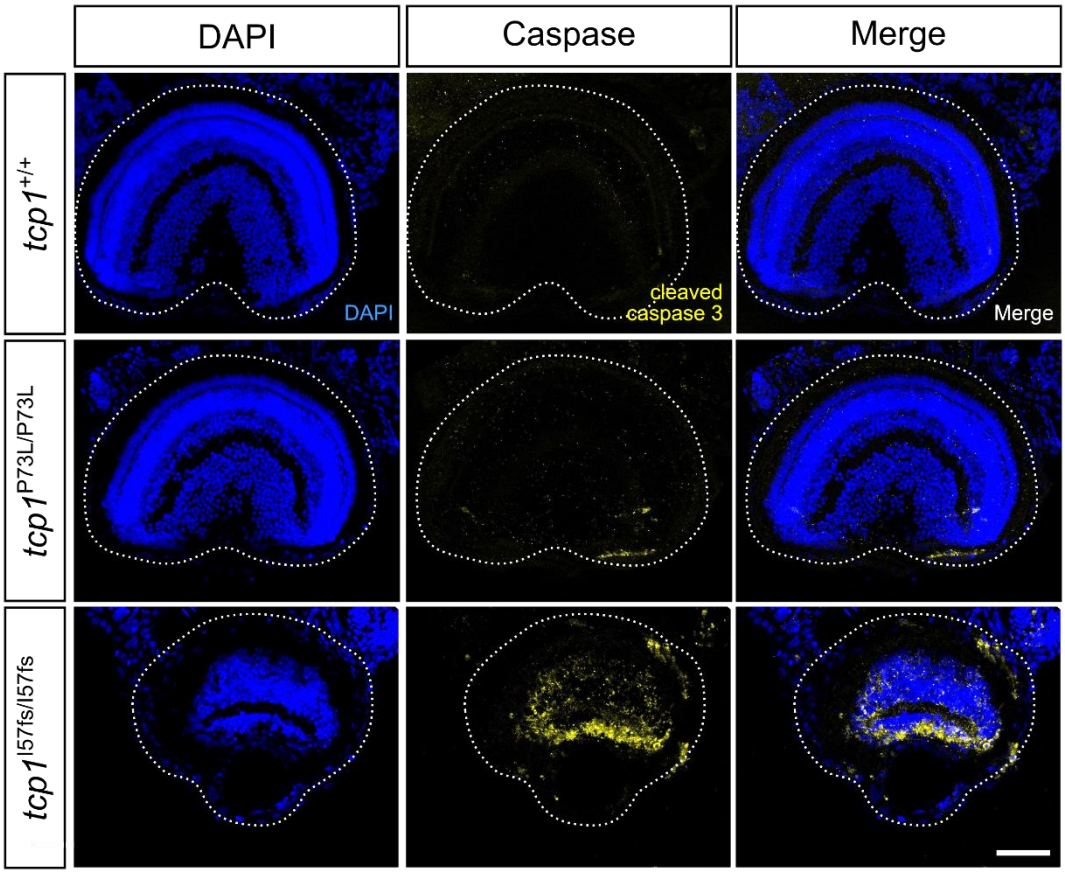

Figure 4.18. Apoptotic cells are prevalent in the retinae of *tcp1*^{I57fs}, but not *tcp1*^{P73L}, mutant zebrafish larvae. Representative confocal micrographs (maximum intensity z-stack projections) of retinal cryosections taken from wild-type, *tcp1*^{I57fs} mutant and homozygous *tcp1*^{P73L} mutant zebrafish larvae at 5 dpf. Sections were immunostained with an antibody against cleaved caspase 3 (**yellow**, to detect apoptotic cell death) and nuclei were counterstained with DAPI (**blue**). In each image, the perimeter of the eye is marked by a white dashed line. Images are representative of n = 3 individual fish of each genotype, stained across three separate experiments in total. All images shown to scale; scale bar = 50 μm.

4.12 Discussion

In this chapter, we began to use our novel mutant zebrafish lines to address the hypotheses that: a) the *TCP1*^{P70L} mutation is responsible for the patients' phenotypes, and b) *TCP1* plays an important role in development and maintenance of the cerebellum and retina.

To do this, we primarily sought to examine how the mutations we introduced into *tcp1* affect gross zebrafish morphology and, more specifically, the morphology and development of the cerebellum and retina. Our investigations did not reveal any gross morphological abnormalities, or cerebellar or retinal malformations, in homozygous *tcp1*^{P73L} mutant zebrafish. However, we observed severe developmental defects in *tcp1*^{I57fs} mutant larvae, along with considerable pathology affecting the brain and retina.

4.12.1 Effect of zebrafish *tcp1* mutations on *tcp1* transcript expression

Before we began to morphologically characterise our novel mutant zebrafish, we first examined the expression of *tcp1* in these lines. It has previously been reported that *tcp1* is ubiquitously expressed in wild-type zebrafish (Thisse and Thisse, 2004, data submitted to ZFIN), consistent with the TRiC/CCT chaperone playing a critical role in numerous pathways that are important for many cell and tissue types. In line with this, our whole-mount *in situ* hybridisation analysis also revealed ubiquitous *tcp1* expression in wild-type zebrafish at 24 hpf.

Notably, the expression was particularly strong in the eye, midbrain and somites, consistent with *tcp1* being particularly important in these regions during development. This is in line with previous findings showing that the *cct3* subunit of TRiC/CCT is similarly highly expressed in these regions (Matsuda and Mishina, 2004). The importance of TRiC/CCT in these tissues is further corroborated by our observation that loss of *tcp1* in

the zebrafish results in abnormalities of the retina and optic tectum, which were also identified as prominent phenotypic features of *cct3* mutants (Matsuda and Mishina, 2004).

We were unable to detect *tcp1* mRNA in homozygous *tcp1*^{I57fs} larvae by *in situ* hybridisation, and qPCR analysis revealed that transcript levels were reduced to approximately 10% of wild-type levels in these mutants. This indicates that the mutant mRNA undergoes nonsense-mediated decay, which will likely result in depletion of the tcp1 protein. We were unable to specifically confirm effects on the protein due to the lack of available antibodies to detect zebrafish tcp1, so we cannot be absolutely certain that no protein is produced in these mutants.

Conversely, our *in situ* hybridisation analysis did not expose any obvious differences in *tcp1* expression levels in *tcp1*^{P73L} mutants compared with wild-type fish; however, we observed qualitatively weaker expression in the brains of heterozygous *tcp1*^{P73L} mutants than in the wild-type embryos. We would need to analyse transcript expression in further detail by performing *in situ* hybridisation on tissue sections to confirm whether the spatial distribution of *tcp1* mRNA is indeed altered in these mutants. We also performed qPCR analysis, which revealed an unexpected increase in *tcp1* expression in both heterozygous and homozygous *tcp1*^{P73L} mutant larvae. The magnitude of this effect was relatively small (~1.5-fold increase in heterozygous mutants and ~1.25-fold increase in homozygous mutants); however, it was statistically significant, and we observed the same effect with both primer pairs that we designed against *tcp1*, indicating that this is unlikely to be an artefact that can be explained by our choice of primers.

There are several possibilities that may offer an explanation as to why we observed this increase in transcript expression (though it remains unclear how these would result in a greater effect in heterozygous mutants than in homozygous mutants). Firstly, it may be that the P73L mutation itself somehow influences gene expression. Another possibility is that the silent point mutations that we introduced into the repair template somehow affect the stability of the transcript. Notably, we codon-optimised most of these mutations and

codon optimisation has been shown to impact on mRNA stability in yeast and human cells (Presnyak et al., 2015; Wu et al., 2019). It is also possible that genetically-linked variants are present in the regulatory elements for the *tcp1* gene; we did not sequence these regions, so we cannot rule out the possibility of the CRISPR having introduced unexpected off-target mutations here.

To investigate whether the P73L mutation itself might be responsible for the effect on transcript expression, or whether off-target mutagenesis is likely to have contributed to the effect, it would be beneficial to validate the results by measuring mRNA levels in an independently-generated *tcp1*^{P73L} mutant line, or by investigating the effects on *tcp1* transcript expression when P73L mutant *tcp1* is overexpressed in wild-type zebrafish. It would also be useful to assess transcript levels in a *tcp1*^{P73L} line in which the silent mutations introduced into the gRNA target site do not result in optimal codons, to investigate whether codon optimisation could be increasing the stability of the mutant transcript. We could also sequence the promoter and untranslated regions for *tcp1* in the *tcp1*^{P73L} mutants to ensure that we have not inadvertently introduced any mutations into these regions. Moreover, because it is unclear whether the upregulation we observed is due to an increase in the rate of transcription or an increase in the stability of the mRNA, it would be informative to assess mRNA levels in the mutants following treatment with a transcription inhibitor (e.g. actinomycin D) (Matsui et al., 2012). We could also perform allele-specific qPCR using primers to specifically amplify the wild-type or mutant transcript to determine whether the effect is specific to the mutant allele.

4.12.2 Gross developmental effects of zebrafish *tcp1* mutations

We observed severe developmental defects and reduced survival in homozygous *tcp1*^{I57fs} mutants; this was as we expected, considering that *tcp1* has been shown to be essential for survival in several other model systems (Iijima et al., 1998; Kim and Choi, 2019; Seixas et al., 2010; Ursic et al., 1994). Though we saw substantially reduced viability in these

mutants, they still survived up to 5 dpf, highlighting an advantage of the zebrafish as a model for studying genes that are essential during development, as this mutant provides a window in which we can experimentally investigate how loss of *tcp1* affects developmental processes in a living vertebrate.

Notably, the *tcp1*^{I57fs} mutants had considerably smaller eyes and heads than their siblings, consistent with them having pathology in tissues relevant to the *TCP1*-linked human disease. However, we also detected substantial evidence of gross developmental abnormalities (pericardial oedema, reduced body length, reduced yolk sac absorption) in these larvae, indicating that loss of zebrafish *tcp1* causes defects that are more widespread and severe than those observed in patients with the *TCP1*^{P70L} mutation. These phenotypes were recapitulated in an additional frameshift (*tcp1*^{H72fs}) mutant line; however, we observed spinal curvature in homozygous *tcp1*^{H72fs} mutants, which was not a feature of the *tcp1*^{I57fs} phenotype. As this curvature did not arise in compound heterozygotes carrying one *tcp1*^{I57fs} allele and one *tcp1*^{H72fs} allele, this is likely to be an effect of an unrelated mutation that is only present in the *tcp1*^{H72fs} line. However, as we have not characterised the expression of *tcp1* in the *tcp1*^{H72fs} mutants to determine whether this transcript is subject to nonsense-mediated decay in the same way as the *tcp1*^{I57fs} mutant transcript, we cannot rule out the possibility that this allele results in production of a truncated or dysfunctional protein that may have additional phenotypic consequences.

In contrast to the severe morphological defects that we identified in *tcp1* frameshift mutants, we saw no overt phenotype in homozygous *tcp1*^{P73L} mutants at either the larval or the adult stage; however, this was expected, given that the clinical features of the human phenotype are relatively mild.

4.12.3 Effects of zebrafish *tcp1* mutations on cerebellar development

When we moved on to specifically characterise tissues implicated in the human disease, we discovered that *tcp1*^{I57fs} mutant larvae completely lacked cerebellar Purkinje cells at

both 3 dpf and 5 dpf. Zebrafish Purkinje cells normally differentiate just before 3 dpf (Hamling et al., 2015), so our observation that no differentiated Purkinje cells are present at 3 dpf suggests that these cells may have failed to develop. Such a developmental defect could arise due to aberrant brain region patterning or specification of Purkinje progenitor cells. Another possibility is that, rather than being required for the development of Purkinje cells, *tcp1* is important for the maintenance of these cells, and the absence of *tcp1* causes them to degenerate soon after they have differentiated. We would need to perform further experiments to identify the precise nature of the requirement for *tcp1* in these cells. For example, we could perform *in situ* hybridisation analysis at various developmental stages in *tcp1*^{I57fs} mutant embryos to assess whether they exhibit early patterning defects that might affect processes known to be important for cerebellar development. This could include investigating the formation of the midbrain-hindbrain boundary (Gibbs et al., 2017; Kimmel, 1993) or specification of Purkinje cell progenitors at the ventricular zone (Kani et al., 2010). If the patterning and specification of the cerebellum and Purkinje cells are unaffected in the mutants, it would then be useful to perform live imaging experiments using the FyntagRFP-T:PC transgenic line, so that we can follow Purkinje cells after they are born, to determine if and when they begin to degenerate. The fact that some of the condensed nuclei we observed in these mutants were located posteriorly to the optic tectum, where we would expect the cerebellum to form, may be consistent with degeneration of cerebellar neurons and/or their precursors following specification; however, we would need to determine whether the condensed nuclei belong to cerebellar cells before we can draw this conclusion. We could further investigate this by combining DAPI staining with *in situ* hybridisation to detect markers of cerebellar neurons and progenitor cells (Bae et al., 2009; Kani et al., 2010; Takeuchi et al., 2017).

Conversely, we did not detect any obvious defects in the development of Purkinje cells in the *tcp1*^{P73L} mutant larvae. One possible explanation for this is that the *tcp1*^{P73L} mutation does not affect cerebellar development; however, we cannot draw this conclusion solely

based on the data we have gathered so far. Another possibility is that this mutation causes subtle defects (e.g. affecting the number or morphology of Purkinje cells) that we would not have detected with the approach that we used here. We could address this by performing more detailed morphological analysis of Purkinje cells to investigate whether the formation of their dendritic arbours or axons is impaired, or by quantifying the number of Purkinje cells present in the mutant brain compared with wild-type fish at various developmental stages.

Notably, we have not yet assessed whether other major cell types within the cerebellum, such as the granule cells, are affected by the mutation; and we also have not investigated whether the *tcp1*^{P73L} mutants develop degenerative pathology in the cerebellum as they become older. This may be relevant to the human disorder; although onset of disease was during childhood for all affected patients, the progressive nature of their cerebellar atrophy implies that degenerative processes may play a pathogenic role in the condition. We could further investigate this in our model by assessing how the size and morphology of the *tcp1*^{P73L} mutant cerebellum compares with wild-type fish as they develop through juvenile and adult stages.

4.12.4 Effects of zebrafish *tcp1* mutations on retinal development

When we investigated how *tcp1* mutations affect the zebrafish retina, we observed severe morphological disruption of the retina in homozygous *tcp1*^{I57fs} mutant larvae, along with reduced numbers of photoreceptors and widespread cell death. These findings support an important role for *tcp1* in the retina, though we can infer that *tcp1* is probably not required for specification of the photoreceptors, as we were still able to detect some of these cells in the *tcp1*^{I57fs} mutant retina. The fact that the photoreceptors appeared to be mislocalised within the retina could mean that *tcp1* is required for proper patterning of the retinal layers; or *tcp1* may be required for the maintenance of retinal cells, in which case the cellular disorganisation we observed may be due to retinal degeneration. The fact that we

observed particularly strong immunoreactivity against cleaved caspase 3 in the retinal ganglion cell layer indicates that these cells may be particularly affected by loss of tcp1. This would be in line with findings from the *cct2* mutant zebrafish model of Leber congenital amaurosis, in which impaired retinal ganglion cell differentiation, underpinned by cell cycle defects, was shown to contribute to the observed retinal degeneration phenotype (Minegishi et al., 2018).

These findings also relate to the cell death and reduction of neurites that we observed in the optic tectum, which is where many retinal ganglion axons terminate (Robles et al., 2014). Abnormalities of the retina and optic tectum have also been observed in zebrafish with insertional mutations in *tcp1*, *cct2*, *cct5* or *cct8* (Berger et al., 2018), frameshift or nonsense mutations in *cct3* (Berger et al., 2018; Matsuda and Mishina, 2004), and CRISPR-induced mutations in *cct2* or *cct4* (Berger et al., 2018; Minegishi et al., 2018).

More detailed characterisation of one of the *cct3* mutant lines revealed that the early developmental patterning of the retina did not appear to be affected by the mutation, but retinal degeneration was later observed. The authors found that the degeneration was preceded by optic tectum abnormalities (Matsuda and Mishina, 2004). These defects were linked to impaired retinal ganglion cell differentiation (Matsuda and Mishina, 2004). It would be interesting to investigate retinal ganglion cell differentiation and early retinal patterning in the *tcp1*^{I57fs} mutant zebrafish to determine whether the retinal abnormalities in these mutants arise through a similar mechanism. It would also be informative to more specifically investigate the effects of loss of *tcp1* on the health of photoreceptors. Although the photoreceptors do not appear to have been characterised in detail in any of the other TRiC/CCT zebrafish mutants, TRiC/CCT function has previously been shown to be important in the formation and survival of rod photoreceptors in the mouse (Posokhova et al., 2011; Sinha et al., 2014).

In contrast to the striking retinal pathology that we saw in the *tcp1*^{I57fs} mutants, we did not observe any abnormalities in either the gross morphology of the retina, or in the

development and localisation of photoreceptors, in *tcp1*^{P73L} mutant larvae. However, it is worth noting that the antibodies we used to stain the photoreceptors are only likely to have revealed rod and red-/green-sensitive double cone cells (Yin et al., 2012); therefore we cannot currently exclude any possible defects linked to blue- or UV-sensitive photoreceptors. We also have not looked in detail at the morphology of individual photoreceptors, and we do not know if or how the mutation will affect the cells of the retina over time. It would therefore be beneficial to extend our investigations to gain more detailed insight into photoreceptor morphology; for example, by conducting higher resolution imaging of these cells in paraffin-embedded sections, and by performing histological analyses in the retinae of older *tcp1*^{P73L} mutants to determine whether pathology arises at a later stage.

4.12.5 Effects of *tcp1* mutations on transcript levels for TRiC/CCT substrates

We found that mRNAs encoding β-actin, and possibly α-tubulin, were upregulated in *tcp1*^{I57fs} mutant larvae, but not in *tcp1*^{P73L} larvae (though the effect was not statistically significant for *tuba1a*). This indicates that the loss of *tcp1* expression may give rise to a compensatory or feedback mechanism, which might result from misfolding of these substrates.

Previous studies have demonstrated that misfolding of tubulin (Hari et al., 2003) or actin (Vang et al., 2005) can affect cytoskeletal dynamics. In turn, altered cytoskeletal dynamics can elicit changes in mRNA expression. For example, perturbed microtubule dynamics have been shown to affect tubulin mRNA stability (Gasic et al., 2019). Specifically, paclitaxel (a microtubule-stabilising poison) treatment resulted in increased expression of several tubulin mRNA isoforms in an immortalised human retinal epithelial cell line (Gasic et al., 2019). Moreover, *Actb1* mRNA was upregulated in murine cells when they were treated with cytochalasin D (a drug known to disrupt F-actin microfilaments) (Sympson et al., 1993).

When we measured the levels of *gnb1b* mRNA, which encodes the Gβ1 subunit of transducin, we found that expression was slightly reduced in *tcp1*^{I57fs}, but not *tcp1*^{P73L} mutant larvae. This is consistent with earlier findings from *cct2* mutant zebrafish, which were found to exhibit retinal degeneration and had reduced levels of Gβ1 protein in the retina (Minegishi et al., 2018). Decreased Gβ1 levels were also observed in the retinae of mice with impaired TRiC/CCT function in their rod photoreceptors (Posokhova et al., 2011).

An overloading of the proteasome with misfolded Gβ1 was previously shown to lead to photoreceptor degeneration in mice (Lobanova et al., 2013). Considering this, one possible explanation for the decreased *gnb1b* transcript levels we observed in *tcp1*^{I57fs} zebrafish is that Gβ1 may fail to be properly folded in these mutants, instead becoming targeted for degradation by the proteasome. This may trigger an attempt to reduce the amount of Gβ1 protein being produced and alleviate the burden on the proteasome through downregulation of *gnb1b* mRNA expression. However, because the Gβ1 protein is specifically expressed in photoreceptors, it is also possible that this reduced transcript expression reflects the fact that these mutants also have fewer photoreceptors than wild-type larvae. We could explore this further by performing *in situ* hybridisation to examine the spatial expression of *gnb1b* mRNA.

4.12.6 Induction of the heat shock response in *tcp1* mutant zebrafish

As well as these effects on the expression of TRiC/CCT substrates, we also saw a huge upregulation of the heat shock genes, *hsp70.1* and *hsp70l*, in *tcp1*^{I57fs} mutant larvae, which is consistent with activation of the heat shock response in these mutants. It may be that the loss of *tcp1* in these mutant larvae results in an accumulation of misfolded proteins due to TRiC/CCT dysfunction. Such an accumulation could cause proteotoxic stress and ultimately trigger the heat shock response. However, because TRiC/CCT has also been shown to directly regulate HSF1 (Neef et al., 2014), which is the key transcription factor

responsible for mediating the heat shock response, it is possible that the upregulation of *hsp70.1* and *hsp70l* arises due to loss of this repressive interaction between TRiC/CCT and HSF1 in the *tcp1*^{I57fs} mutant larvae.

Although the results of these qPCR experiments are consistent with the loss of zebrafish *tcp1* causing TRiC/CCT dysfunction and affecting the folding of its client proteins, we would need to conduct further experiments to test whether the mutation does indeed cause defects in TRiC/CCT function or substrate folding. For example, it would be useful to perform assays to measure how *tcp1* mutations affect the folding kinetics of TRiC/CCT substrates, though this might be better addressed using cell-based or *in vitro* systems. It would also be informative to assess the levels of TRiC/CCT substrates in the *tcp1*^{I57fs} mutant larvae at the protein level; although the lack of suitable antibodies for many zebrafish proteins may mean that we cannot use this approach for some substrates. Given the links between TRiC/CCT and the proteasomal (Tokumoto et al., 2000) and autophagolysosomal (Pavel et al., 2016) degradation pathways, we could also investigate how the *tcp1*^{I57fs} mutation affects folding of TRiC/CCT substrates by employing biochemical approaches to assess whether the amount of misfolded protein being targeted for degradation via these pathways is increased in the mutant larvae.

Contrary to our observations in the *tcp1*^{I57fs} mutant larvae, we saw no effect on the expression of TRiC/CCT substrate mRNAs, and no evidence for activation of the heat shock response, in *tcp1*^{P73L} mutant larvae. This does not, however, preclude the possibility that this mutation causes dysfunction of the chaperone. It is possible that any substrate misfolding in these mutants occurs on a much smaller scale, or only affects certain substrates or arises in particular cell types, which may not be sufficient to induce detectable compensatory effects at the transcriptional level. We could investigate this further by performing *in situ* hybridisation to assess whether the expression of these transcripts is altered in tissues or cell types that are relevant to the human disease. Defects in substrate folding in the *tcp1*^{P73L} mutant zebrafish also may not become apparent

until later stages; therefore, it would be useful to assess whether there is any evidence to support TRiC/CCT dysfunction in adult *tcp1*^{P73L} mutant zebrafish.

4.12.7 Conclusions

To summarise the findings presented in this chapter, we discovered severe morphological defects in homozygous *tcp1*^{I57fs} mutant larvae, in relation to both their gross development and the tissues implicated in the human *TCP1*-linked disorder. This supports the notion that *tcp1* is important for the development and/or maintenance of these tissues. We also uncovered evidence to suggest that TRiC/CCT function may be impaired by the loss of *tcp1* in these mutants, which may have implications for the folding of TRiC/CCT substrates.

Conversely, we did not detect any obvious morphological defects affecting disease-relevant tissues in *tcp1*^{P73L} mutant larvae. However, we would need to conduct further investigations to determine whether these mutants exhibit subtle defects that we have so far been unable to detect, or whether they develop pathology of relevance to the human disease as they become older. Moreover, although these mutants appear morphologically healthy, this does not preclude the possibility of functional defects that might be relevant to the human disorder.

Chapter 5

Characterising the effects of zebrafish *tcp1* mutations on motor and visual function

5.1 Introduction

In the previous chapter, we began to use our zebrafish models to test the hypotheses that a) the human *TCP1*^{P70L} mutation is the cause of the patients' neurological phenotypes and b) *TCP1* is important for the development and maintenance of the specific tissues affected by the disease. To do this, we initially explored the broad consequences of *tcp1* mutations on zebrafish development, and then we specifically investigated how these mutations affect the morphology and development of the tissues implicated in the human disease.

As we described in Chapter 1, the zebrafish is amenable to phenotypic analyses not only at a morphological level, but also at a functional level. In the following chapter, we therefore aimed to further test the above hypotheses by investigating whether zebrafish *tcp1* mutations impact on the functions that are relevant to the *TCP1*-linked disorder.

The clinical phenotypes of patients with the *TCP1*^{P70L} mutation primarily manifest as motor and visual dysfunction. We therefore specifically planned to test our hypotheses by employing some of the behavioural approaches described in Chapter 1 to characterise the effects of *tcp1* mutations on aspects of locomotor and visual function in zebrafish.

5.2 Zebrafish *tcp1*$^{\mathbf{I57fs}}$ mutants exhibit an impaired touch-evoked escape response

We began by examining the effects of *tcp1* mutations on locomotor activity in zebrafish larvae. While we were characterising the gross morphological phenotypes of the homozygous *tcp1*^{I57fs} mutant larvae, we noted that their motor function was severely compromised. To investigate this defect, we monitored the touch-evoked escape response of homozygous *tcp1*^{I57fs} mutants and their siblings at 3 dpf (Figure 5.1). In this assay, control siblings responded to a light touch to the trunk by initiating a rapid escape response accompanied by smooth tail movements. Contrastingly, the *tcp1*^{I57fs} mutants failed to execute a full escape response; they instead responded to the stimulus with uncoordinated tail contractions (Figure 5.1).

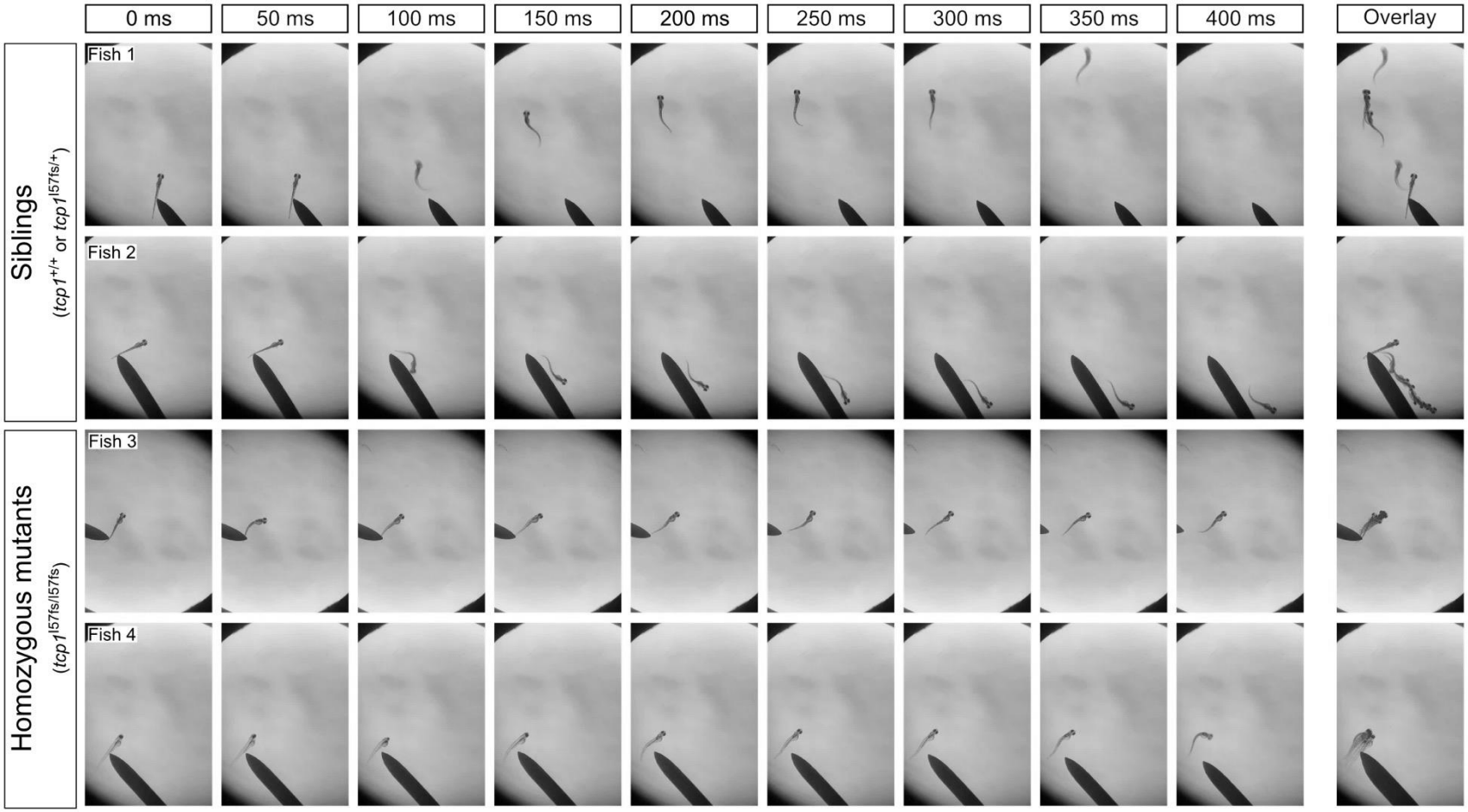

Figure 5.1. Loss of *tcp1* results in abnormal touch-evoked escape response in zebrafish larvae. Sequential photomicrographs showing the touch-evoked escape response of two control siblings (*tcp1*$^{+/+}$ or *tcp1*$^{l57fs/+}$, top panels) and two homozygous mutant larvae (*tcp1*$^{l57fs/l57fs}$, bottom panels) at 3 dpf.

5.3 Homozygous *tcp1*^{l57fs} mutants display abnormalities in components of the neural circuitry governing the touch-evoked escape response

In zebrafish larvae, the touch-evoked escape response is mediated at a basic level by a simple neuronal circuit (Figure 5.2), comprising mechanosensory Rohon-Beard neurons which fire in response to tactile stimuli, the Mauthner neurons (a pair of large reticulospinal neurons located in the hindbrain), and the spinal motor neurons, which innervate skeletal muscle to induce muscle contractions in the trunk (Liu and Hale, 2017; Low et al., 2010b, 2010a). The touch-evoked escape response can be impaired by dysfunction in any of these components (Bercier et al., 2019; Liu and Fetcho, 1999; Low et al., 2011; Sztal et al., 2016).

To explore possible explanations for the aberrant escape response in the homozygous *tcp1*^{l57fs} mutants, we investigated some of the components of this circuit to determine whether we could identify any obvious sources of dysfunction. We began by performing whole-mount immunohistochemistry against acetylated α-tubulin to assess whether the spinal motor neurons were affected. However, we did not observe any obvious morphological abnormalities in the motor neurons of the homozygous mutants at 3 dpf compared with their wild-type and heterozygous siblings (Figure 5.3).

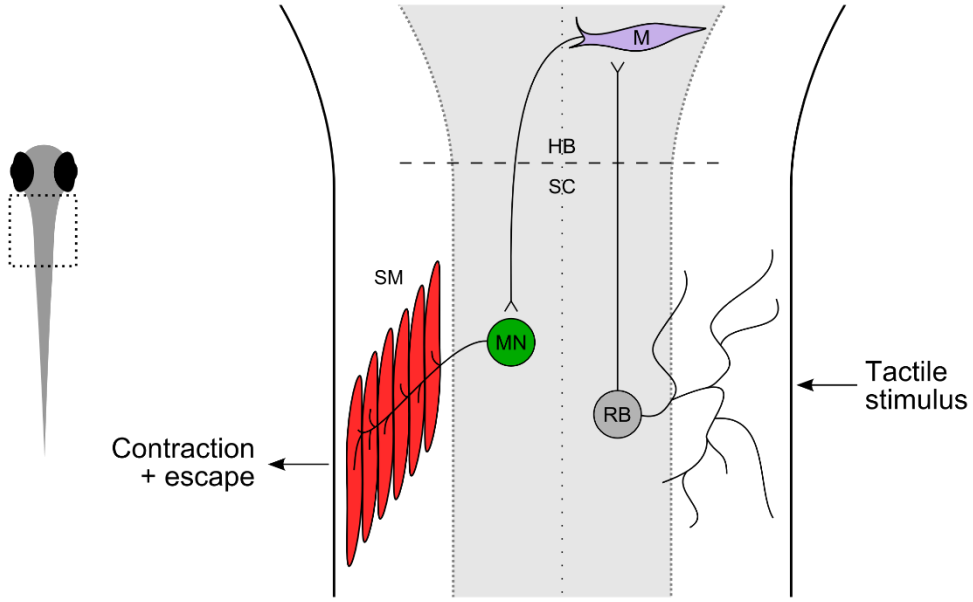

Figure 5.2. Schematic overview of a simple neural circuit governing the touch-evoked escape response. A tactile stimulus activates the mechanosensory Rohon-Beard (RB) neurons, which project to the reticulospinal Mauthner (M) cells located in the hindbrain. Mauthner cell axons cross the midline of the hindbrain and pass these signals contralaterally to spinal motor neurons (MN) which innervate skeletal muscle (SM) fibres in the trunk, mediating their contraction. HB = hindbrain, SC = spinal cord. Schematic based on (Low et al. 2010b). For simplicity, only one of the pair of Mauthner cells is shown in the diagram.

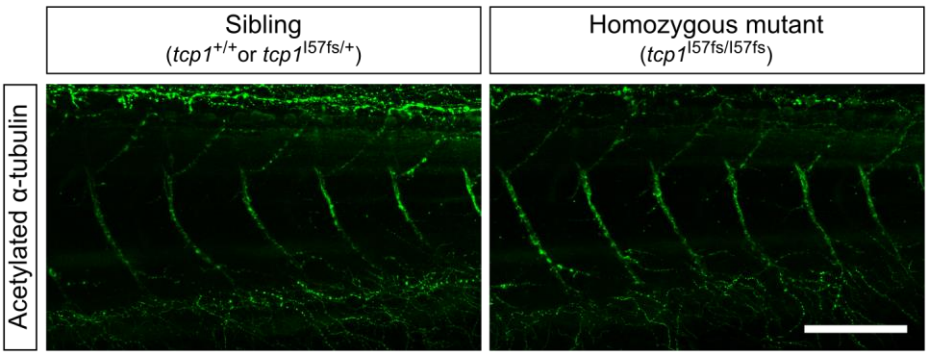

Figure 5.3. Motor neurons appear morphologically normal in *tcp1*^{l57fs} mutant zebrafish larvae. Representative confocal micrographs (maximum intensity z-stack projections) of the motor neurons (lateral view) of one homozygous *tcp1*^{l57fs} mutant larva and one sibling, at 3 dpf. Whole-mount immunostaining was performed to detect acetylated α-tubulin (**green**). Images are representative of n = 12 homozygous mutants and n = 12 control siblings, obtained from at least three independent clutches and stained across three separate experiments. Images shown to scale; scale bar = 100 μm.

Next, we performed immunohistochemistry using the 3A10 antibody, which labels a subset of hindbrain reticulospinal neurons, including the Mauthner cells (Almeida and Lyons, 2016; Kastenhuber et al., 2009; Roy et al., 2015). At 3 dpf, these cells consistently appeared abnormal in homozygous *tcp1*^{I57fs} mutants compared to their siblings, but the precise nature of these abnormalities varied among mutant larvae (Figure 5.4).

In all homozygous *tcp1*^{I57fs} mutants that we examined, the antibody staining within the Mauthner cell bodies and proximal axons appeared substantially more intense than in the distal axons (white arrowheads in Figure 5.4). This contrasts with the staining pattern that we observed in wild-type and heterozygous siblings, which generally appeared more uniform or slightly brighter in the distal axon than in the cell body. However, we were unable to quantify these subjective findings, because the difference in 3A10 staining intensity between mutants and siblings was such that we could not use the same gain and offset settings for all larvae when we imaged them by confocal microscopy. We therefore cannot directly compare the staining intensities between different fish.

We also found that, in some homozygous mutants, the staining intensity for one of the Mauthner cell bodies was much weaker than the other cell body (red arrowhead in Figure 5.4), whereas the staining intensity for control siblings was roughly equal in both cell bodies. Furthermore, we identified one homozygous mutant in which the axons of the Mauthner cells appeared to cross the midline twice (green arrowhead in Figure 5.4), resulting in their axons descending ipsilaterally through the spinal cord.

We then investigated skeletal muscle morphology by performing whole-mount phalloidin staining to label F-actin in the skeletal muscle fibres of the trunk. This revealed that the trunk muscles of homozygous *tcp1*^{I57fs} mutants contained considerably fewer myofibrils than those of their siblings at 3 dpf (Figure 5.5).

In summary, we have observed defects in the circuitry governing the touch-evoked escape response in *tcp1*^{I57fs} mutants at the level of the Mauthner neurons and the skeletal muscle.

Contrastingly, we have not observed any obvious defects in the spinal motor neurons of these mutants, though this does not rule out the possibility of motor neuron dysfunction.

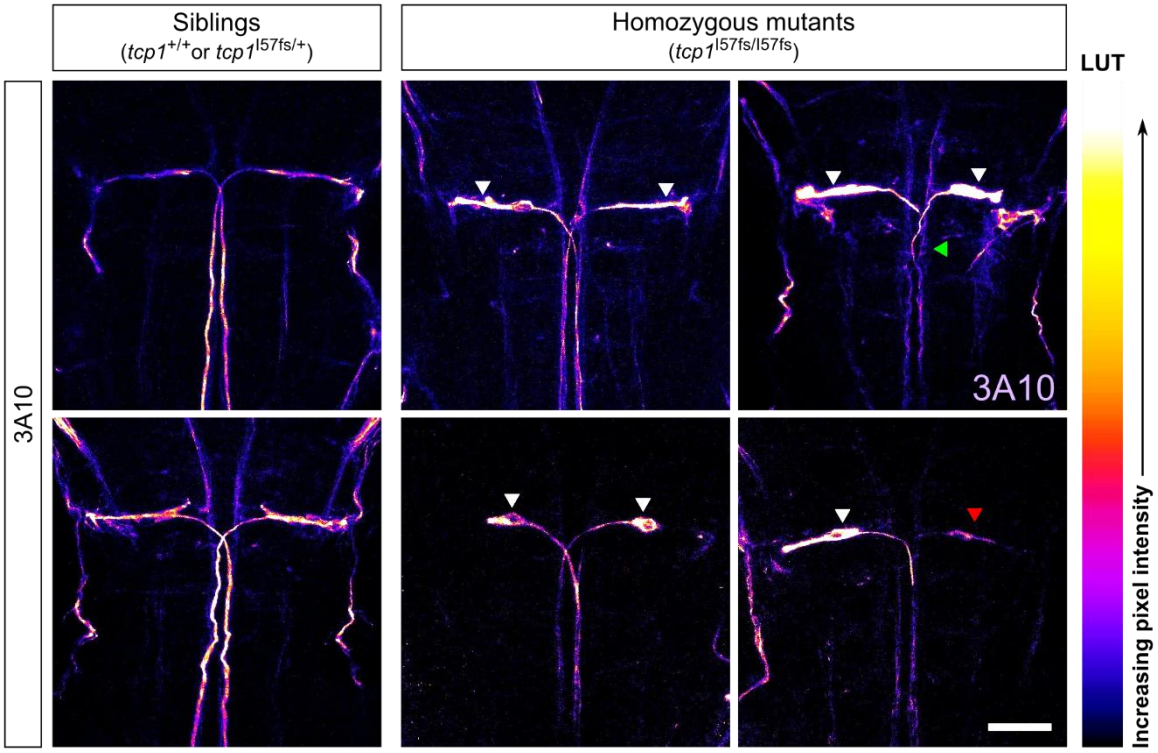

Figure 5.4. Loss of *tcp1* results in Mauthner cell abnormalities in zebrafish larvae. Representative confocal micrographs (maximum intensity z-stack projections) of the Mauthner cells (lateral view) of four homozygous *tcp1*^{l57fs} mutant larvae and two control siblings, at 3 dpf. Whole-mount immunostaining was performed using 3A10 antibody to label Mauthner cells. Examples of abnormalities identified in homozygous mutants are indicated by arrowheads: white arrowheads indicate Mauthner cell bodies in which antibody staining was relatively more intense than in the distal axon (seen in 12/12 homozygous mutant larvae), green arrowhead indicates Mauthner cell axons that appear to cross the midline twice (seen in 1/12 homozygous mutant larvae), red arrowhead indicates Mauthner cell body in which staining intensity was relatively much weaker than for the other Mauthner cell body in the same fish (seen in 3/12 homozygous mutant larvae). Images are representative of n = 12 homozygous mutants and n = 12 control siblings in total, obtained from at least three independent clutches and stained across three separate experiments. All images shown to scale; scale bar = 50 µm. Because of the substantial differences in 3A10 staining intensity between mutants and siblings, images were captured using different gain settings for each fish and are shown with different brightness and contrast settings; therefore, intensities cannot be directly compared between fish. Relatively pixel intensities for each image are colour-coded according to the graded LUT scale shown on the right-hand side of the figure, to illustrate the difference in signal intensity between the cell bodies and axons of the Mauthner cells within individual larvae.

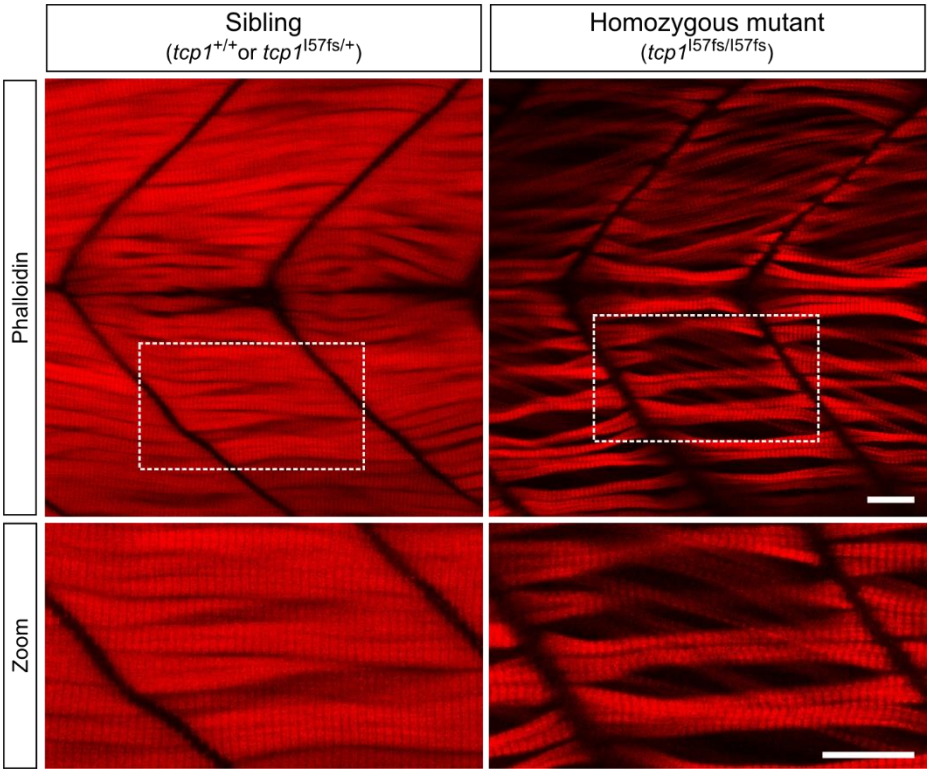

Figure 5.5. Loss of *tcp1* results in skeletal muscle abnormalities in zebrafish larvae. Representative confocal micrographs (single z-slice) of skeletal muscle in the trunk (lateral view) of one homozygous *tcp1*^{l57fs} mutant larva and one control sibling, at 3 dpf. Whole-mount staining was performed using Phalloidin to label F-actin (**red**). Images are representative of n = 7 homozygous mutants and n = 7 control siblings in total. Larvae were obtained from at least two independent clutches and were stained across two separate experiments. Images and higher magnification panels shown to scale; scale bars = 20 μm.

5.4 The *tcp1*^{P73L} mutation does not result in reduced spontaneous larval locomotor activity in response to alternating dark/light periods

In contrast to the profound motor dysfunction exhibited by homozygous *tcp1*^{I57fs} mutant larvae, we did not observe any obvious motor defects in homozygous *tcp1*^{P73L} larvae. To investigate whether *tcp1*^{P73L} mutants displayed more subtle motor impairment, we performed tracking experiments to quantify their spontaneous locomotor activity in response to alternating light and dark stimuli.

Zebrafish larvae have been reported to exhibit a distinct pattern of spontaneous locomotor activity in response to short alternating periods of light and dark by 4 dpf, manifesting as increased locomotion during dark periods and decreased locomotion during light periods (Basnet et al., 2019; Irons et al., 2010; MacPhail et al., 2009). We therefore reasoned that we could use this as a behavioural paradigm to test whether larval motor function is impaired as a result of the *tcp1*^{P73L} mutation. Given the visual stimulus associated with this response, we speculated that this assay may also provide a crude read-out of visual function in the *tcp1*^{P73L} mutant larvae, by revealing whether they are able to discriminate light from dark.

We used this assay to measure locomotion at 5 dpf (Figure 5.6), 8 dpf (Figure 5.7) and 12 dpf (Figure 5.8) in larvae obtained from incrosses of heterozygous F2 *tcp1*^{P73L} mutants. To quantify the response, we tracked the swimming of wild-type and *tcp1*^{P73L} mutant larvae across three repeated cycles of alternating 5-minute dark and 5-minute light periods, and we calculated the total swimming distance and total active duration for each fish across each 5-minute period.

When we statistically analysed the data from these experiments, we observed no significant interacting effects between genotype and lighting condition on total swimming distance or total active duration at any of the developmental stages we tested (Figure 5.6b, Figure 5.7b, Figure 5.8b, Appendix 1). As expected, there was a significant effect of lighting condition upon both measures of locomotor activity at every stage, though this effect

became much smaller over time (see “% of total variation” values, Appendix 1). However, we observed no effect of genotype on locomotion at any stage (Appendix 1). Together, these results indicate that, at all three stages, larvae respond to the alternating light and dark stimuli as expected (increased locomotion in the dark, decreased locomotion in the light), though this response becomes attenuated with age; and that neither the response to the stimulus, nor total locomotor activity, is impaired as a result of the *tcp1*^{P73L} mutation.

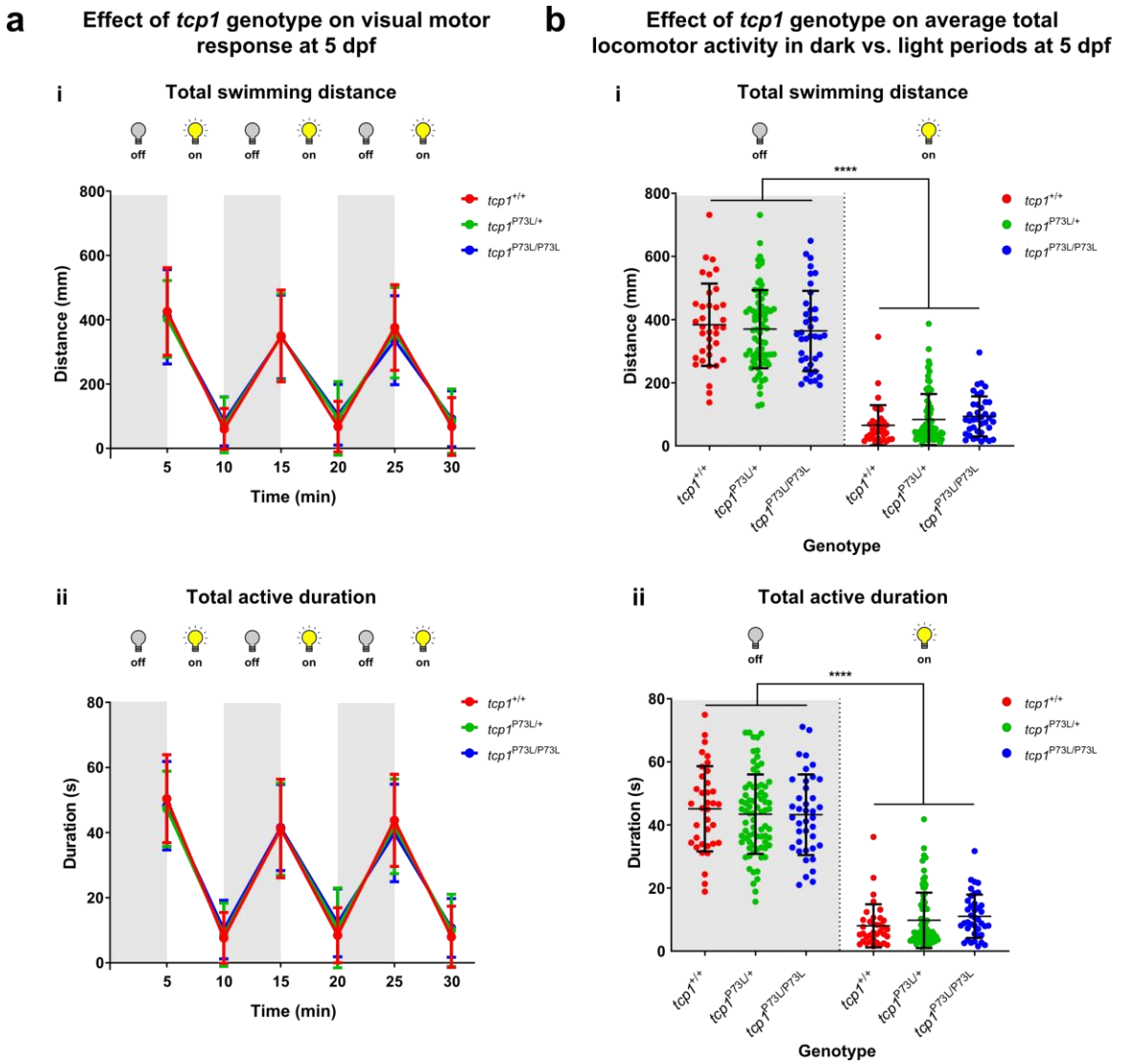

Figure 5.6. Zygotic *tcp1*^{P73L} mutant zebrafish larvae do not exhibit impaired locomotion in response to light and dark stimuli at 5 dpf. (**a**) Graphs illustrating the effects of alternating dark/light cycles on (**i**) total swimming distance and (**ii**) total active duration of wild-type and *tcp1*^{P73L} mutant larvae at 5 dpf. (**b**) Graphs showing (**i**) total swimming distance and (**ii**) total active duration of wild-type and *tcp1*^{P73L} mutant larvae at 5 dpf, averaged across all three dark periods and all three light periods. For all graphs, error bars represent standard deviations for n = 36 wild-type, n = 76 heterozygous mutant and n = 39 homozygous mutant larvae from four independent experimental replicates (individual larvae are represented by individual points in (**bi**) and (**bii**). Statistical significance of the effects of genotype and lighting condition on locomotion were determined in GraphPad Prism 8.3.1, by performing two-way repeated measures ANOVA. Significant effects of lighting condition on locomotion are indicated by asterisks (**** = $p < 0.0001$). See Appendix 1 for a summary of ANOVA results.

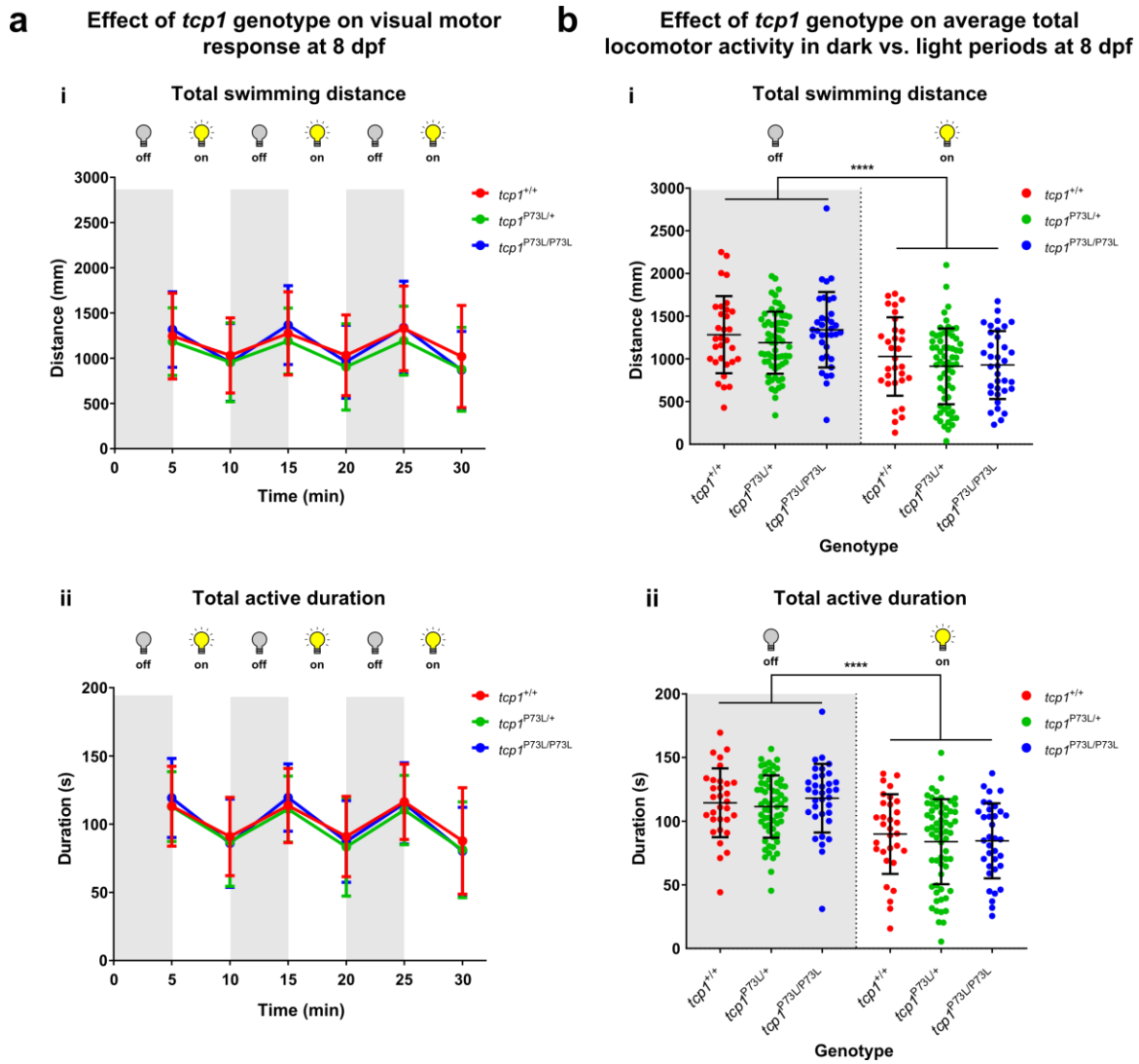

Figure 5.7. Zygotic *tcp1*^{P73L} mutant zebrafish larvae do not exhibit impaired locomotion in response to light and dark stimuli at 8 dpf. (**a**) Graphs illustrating the effects of alternating dark/light cycles on (**i**) total swimming distance and (**ii**) total active duration of wild-type and *tcp1*^{P73L} mutant larvae at 8 dpf. (**b**) Graphs showing (**i**) total swimming distance and (**ii**) total active duration of wild-type and *tcp1*^{P73L} mutant larvae at 8 dpf, averaged across all three dark periods and all three light periods. For all graphs, error bars represent standard deviations for n = 31 wild-type, n = 63 heterozygous mutant and n = 35 homozygous mutant larvae from three independent experimental replicates (individual larvae are represented by individual points in (**bi**) and (**bii**). Statistical significance of the effects of genotype and lighting condition on locomotion were determined in GraphPad Prism 8.3.1, by performing two-way repeated measures ANOVA. Significant effects of lighting condition on locomotion are indicated by asterisks (**** = $p < 0.0001$). See Appendix 1 for a summary of ANOVA results.

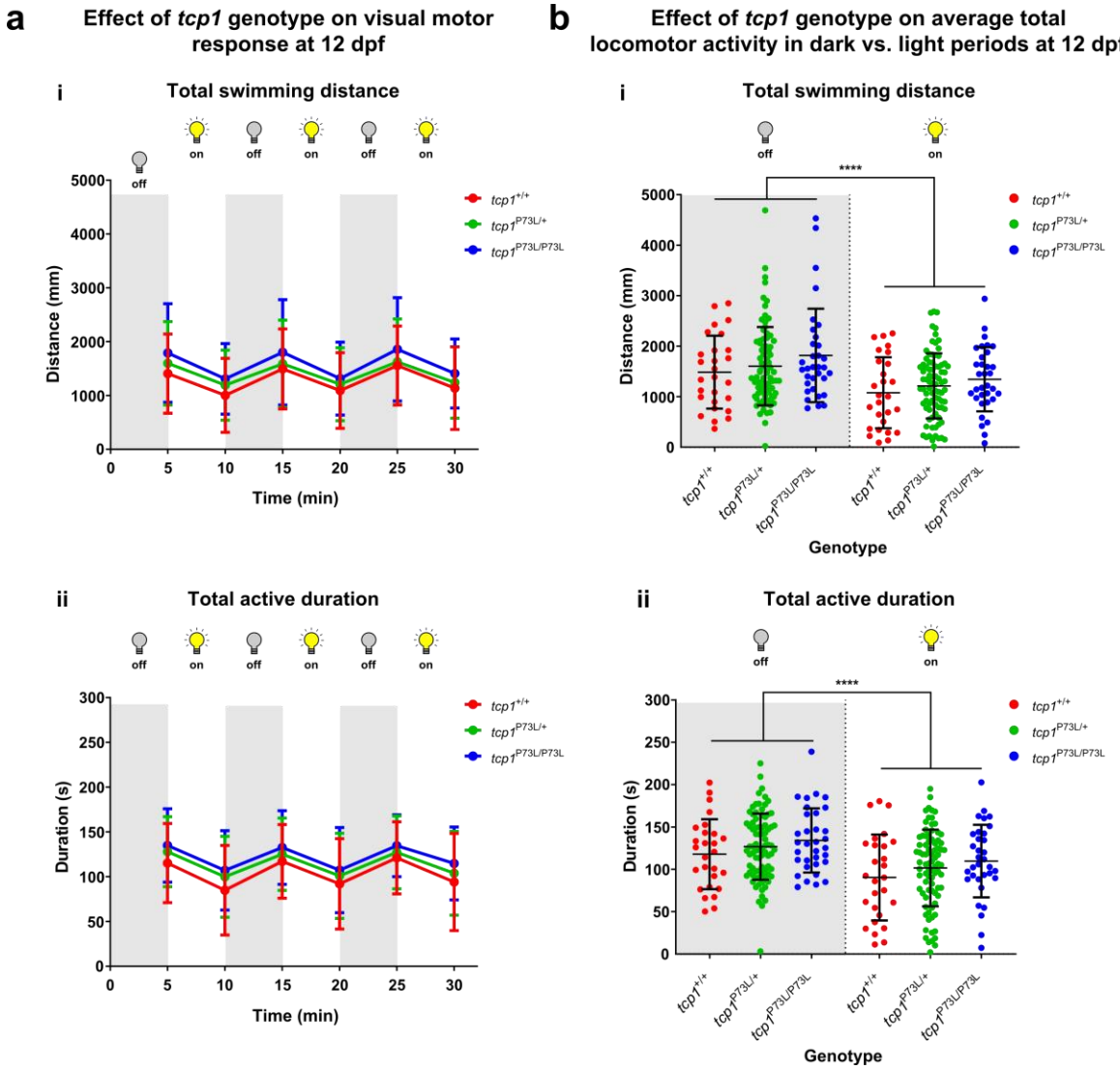

Figure 5.8. Zygotic *tcp1*^{P73L} mutant zebrafish larvae do not exhibit impaired locomotion in response to light and dark stimuli at 12 dpf. (**a**) Graphs illustrating the effects of alternating dark/light cycles on (**i**) total swimming distance and (**ii**) total active duration of wild-type and *tcp1*^{P73L} mutant larvae at 12 dpf. (**b**) Graphs showing (**i**) total swimming distance and (**ii**) total active duration of wild-type and *tcp1*^{P73L} mutant larvae at 12 dpf, averaged across all three dark periods and all three light periods. For all graphs, error bars represent standard deviations for n = 27 wild-type, n = 83 heterozygous mutant and n = 33 homozygous mutant larvae from three independent experimental replicates (individual larvae are represented by individual points in (**bi**) and (**bii**). Statistical significance of the effects of genotype and lighting condition on locomotion were determined in GraphPad Prism 8.3.1, by performing two-way repeated measures ANOVA. Significant effects of lighting condition on locomotion are indicated by asterisks (**** = $p < 0.0001$). See Appendix 1 for a summary of ANOVA results.

For the above experiments, we obtained larvae from incrosses of F2 heterozygous *tcp1*^{P73L} mutant zebrafish. We hypothesised that one possible explanation for the apparent lack of motor dysfunction in the homozygous *tcp1*^{P73L} mutants is that maternal wild-type *tcp1* transcripts could have been present at early developmental stages in these larvae. This may have resulted in production of wild-type tcp1 protein, which could potentially have led to a later motor phenotype becoming masked.

To test this hypothesis, we performed the same experiment in larvae obtained from incrosses of wild-type or homozygous *tcp1*^{P73L} mutant zebrafish from the F3 generation. Because both parents of the homozygous *tcp1*^{P73L} mutants in this experiment are also homozygous *tcp1*^{P73L} mutants, there is no possibility of wild-type tcp1 protein being produced during development in these larvae.

In this experiment, we observed a significant interacting effect ($p = 0.0398$) between lighting condition and genotype on total swimming distance, but not total active duration, at 12 dpf (Figure 5.11b, Table 8.11, Appendix 2), suggesting that the response of homozygous *tcp1*^{P73L} mutant larvae to light and dark stimuli is attenuated compared with the response of wild-type larvae at this stage. However, although the interaction was statistically significant, it accounted for less than 0.5% of the total variation among the data (Table 8.11, Appendix 2). Moreover, post-hoc analyses showed that there was no significant difference in swimming distance between wild-type and *tcp1*^{P73L} mutant larvae in either the light or the dark periods (Table 8.12, Appendix 2), indicating that motor function is not impaired in the *tcp1*^{P73L} mutants.

As in the previous experiment, we noted a significant effect of lighting condition on locomotion at all stages (Figure 5.9b, Figure 5.10b, Figure 5.11b, Appendix 2), demonstrating that, irrespective of genotype, the larvae exhibited the expected pattern of increased locomotor activity in the dark periods and decreased locomotor activity in the light periods. We also observed a significant effect ($p = 0.04$) of genotype on total swimming distance at 8 dpf (Figure 5.10biii, Table 8.9, Appendix 2), suggesting that

locomotion is increased in homozygous *tcp1*^{P73L} mutants at this stage, irrespective of lighting condition (13% increase in mean total swimming distance vs wild-type, 95% CI 6-26%).

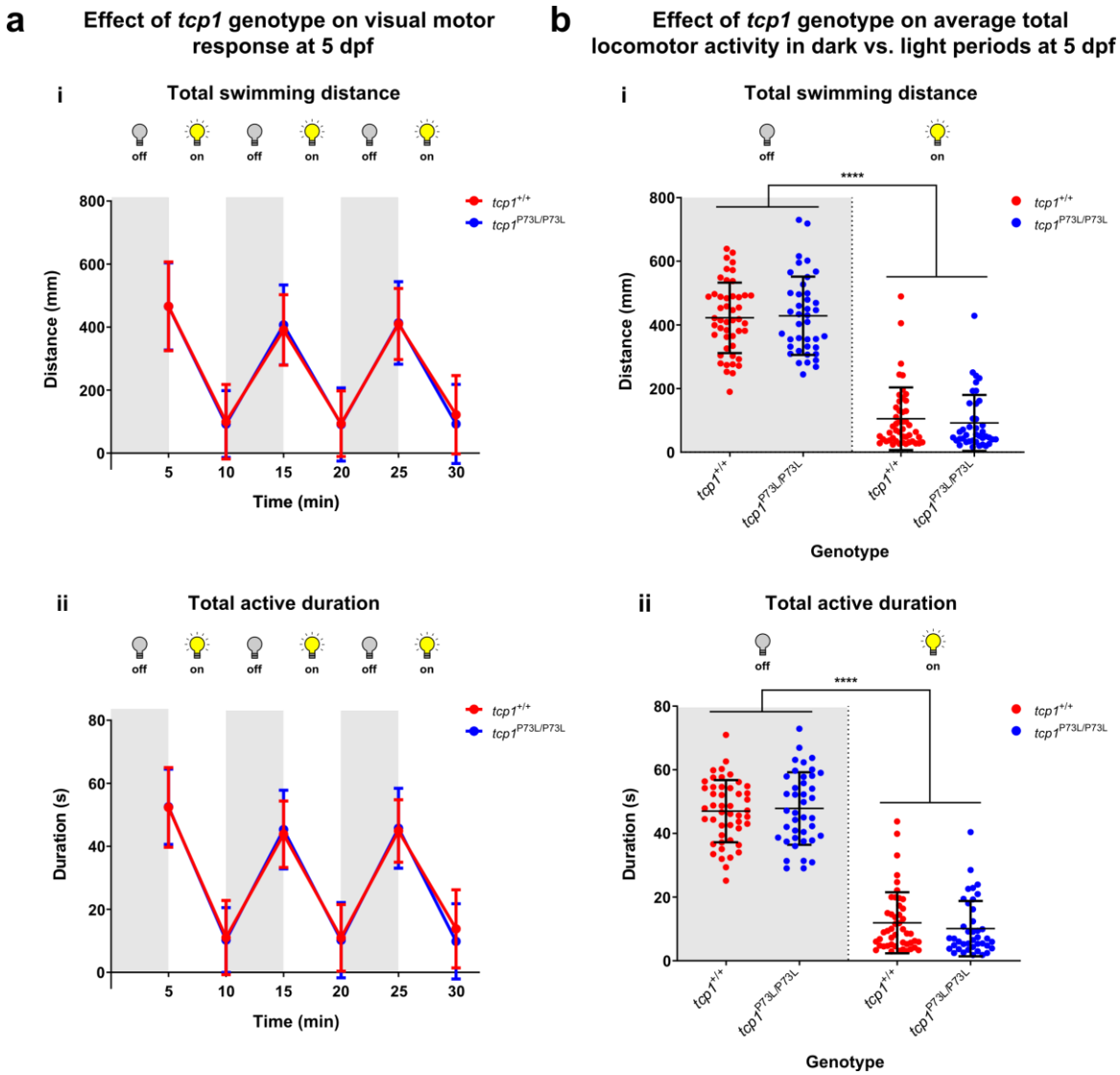

Figure 5.9. Maternal zygotic *tcp1*^{P73L} mutant zebrafish larvae do not exhibit impaired locomotion in response to light and dark stimuli at 5 dpf. (**a**) Graphs illustrating the effects of alternating dark/light cycles on (**i**) total swimming distance and (**ii**) total active duration of wild-type and *tcp1*^{P73L} mutant larvae at 5 dpf. (**b**) Graphs showing (**i**) total swimming distance and (**ii**) total active duration of wild-type and *tcp1*^{P73L} mutant larvae at 5 dpf, averaged across all three dark periods and all three light periods. For all graphs, error bars represent standard deviations for n = 47 wild-type and n = 40 homozygous mutant larvae from three independent experimental replicates (individual larvae are represented by individual points in (**bi**) and (**bii**). Statistical significance of the effects of genotype and lighting condition on locomotion were determined in GraphPad Prism 8.3.1, by performing two-way repeated measures ANOVA. Significant effects of lighting condition on locomotion are indicated by asterisks (**** = $p < 0.0001$). See Appendix 2 for a summary of ANOVA results.

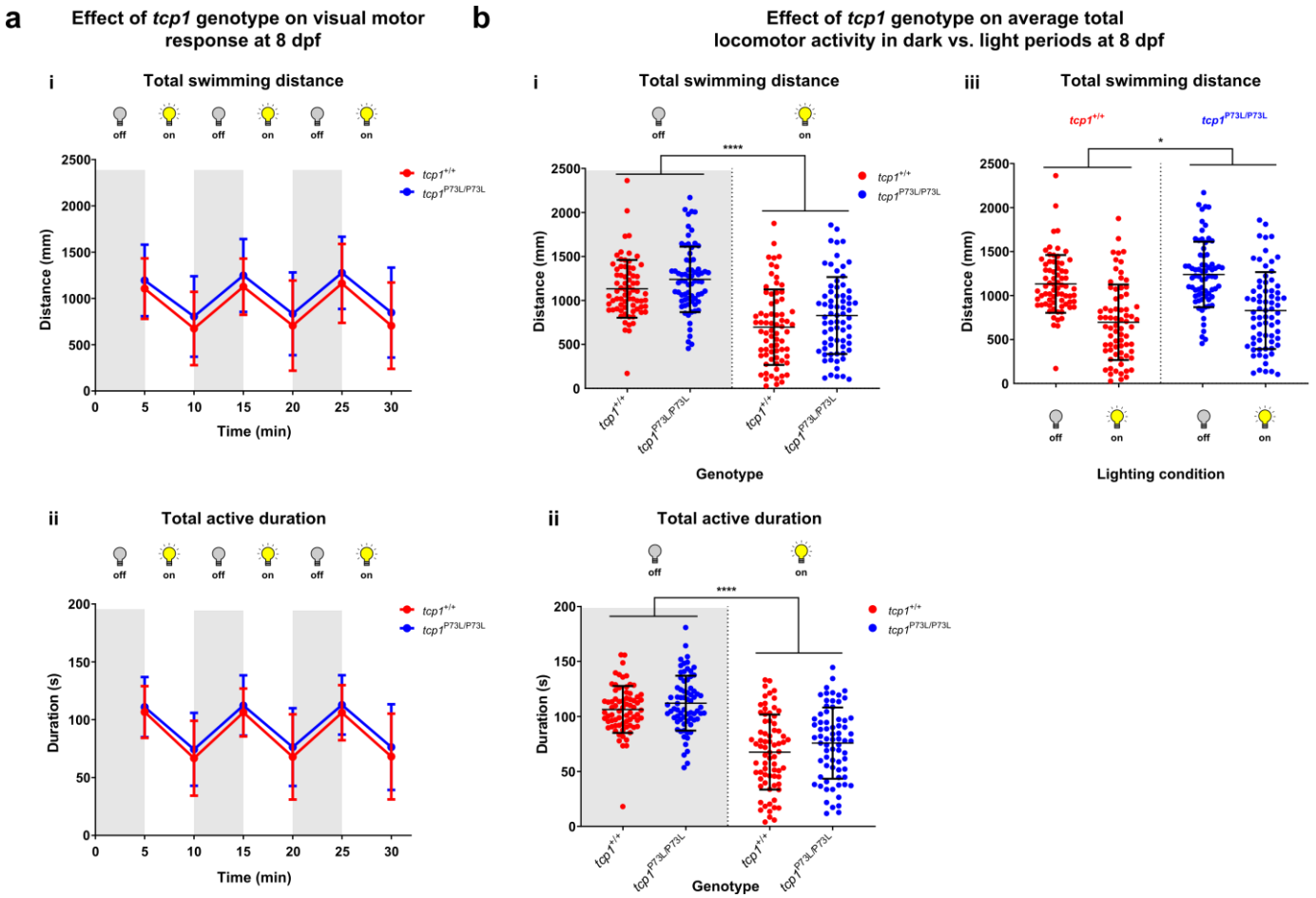

Figure 5.10. Maternal zygotic *tcp1*^{P73L} mutant zebrafish larvae do not exhibit impaired locomotion in response to light and dark stimuli at 8 dpf. (**a**) Graphs illustrating the effects of alternating dark/light cycles on (**i**) total swimming distance and (**ii**) total active duration of wild-type and *tcp1*^{P73L} mutant larvae at 8 dpf. (**b**) Graphs showing (**i,iii**) total swimming distance and (**ii**) total active duration of wild-type and *tcp1*^{P73L} mutant larvae at 8 dpf, averaged across all three dark periods and all three light periods (N.B. **bi** and **biii** contain the same data points but are plotted separately to illustrate significant effects of lighting (**bi**) and genotype (**biii**) on total swimming distance). For all graphs, error bars represent standard deviations for n = 72 wild-type and n = 71 homozygous mutant larvae from three independent experimental replicates (individual larvae are represented by individual points in (**bi**), (**bii**) and (**biii**). Statistical significance of the effects of genotype and lighting condition on locomotion were determined in GraphPad Prism 8.3.1, by performing two-way repeated measures ANOVA. Levels of significance are indicated by asterisks (* = $p < 0.05$, **** = $p < 0.0001$). See Appendix 2 for a summary of ANOVA

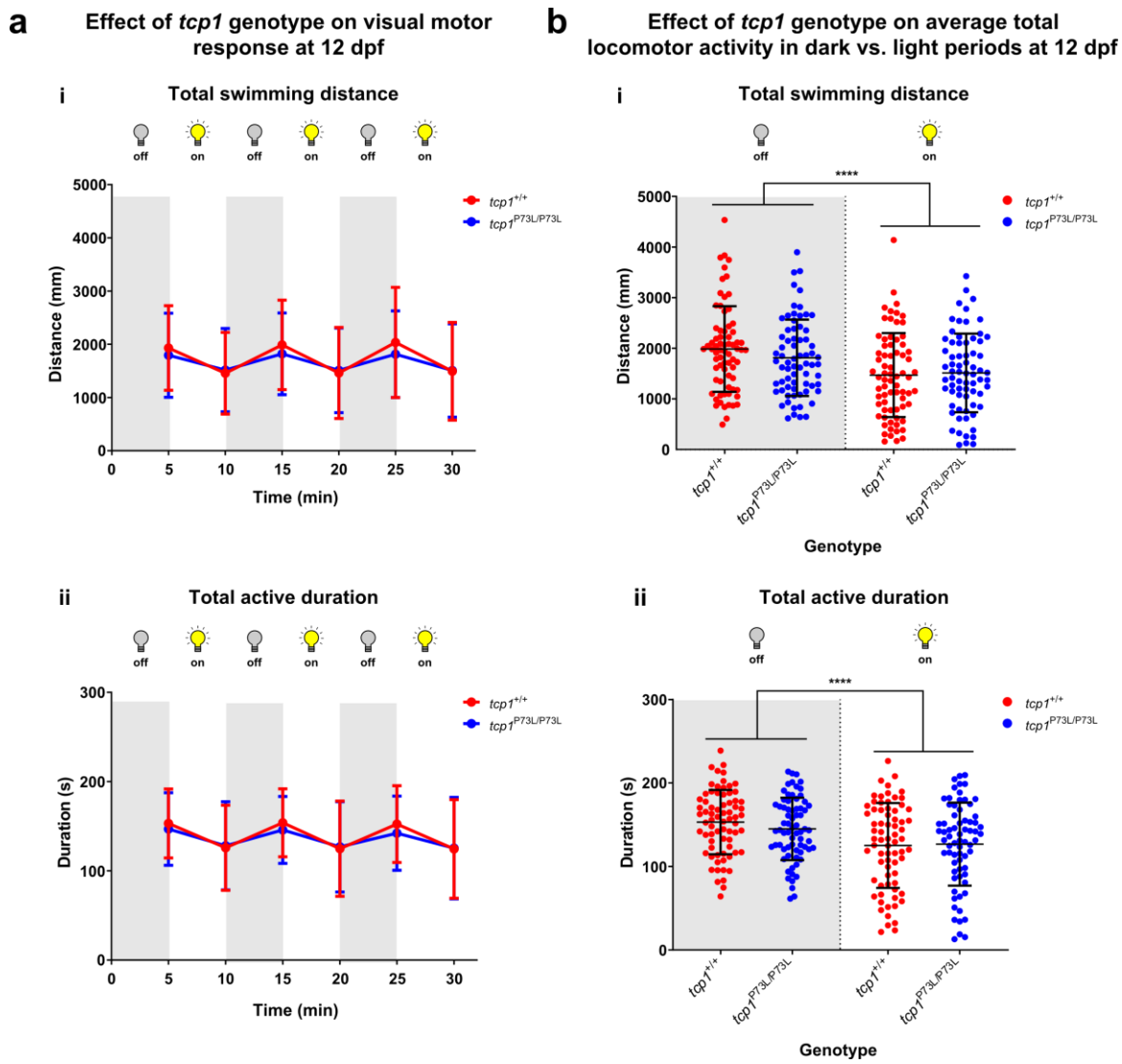

Figure 5.11. Maternal zygotic *tcp1*^{P73L} mutant zebrafish larvae do not exhibit impaired locomotion in response to light and dark stimuli at 12 dpf. (**a**) Graphs illustrating the effects of alternating dark/light cycles on (**i**) total swimming distance and (**ii**) total active duration of wild-type and *tcp1*^{P73L} mutant larvae at 12 dpf. (**b**) Graphs showing (**i**) total swimming distance and (**ii**) total active duration of wild-type and *tcp1*^{P73L} mutant larvae at 12 dpf, averaged across all three dark periods and all three light periods. For all graphs, error bars represent standard deviations for n = 72 wild-type and n = 70 homozygous mutant larvae from three independent experimental replicates (individual larvae are represented by individual points in (**bi**) and (**bii**). Statistical significance of the effects of genotype and lighting condition on locomotion were determined in GraphPad Prism 8.3.1, by performing two-way repeated measures ANOVA followed by Sidak's multiple comparisons test where appropriate. Significant effects of lighting condition on locomotion are indicated by asterisks (**** = $p < 0.0001$). See Appendix 2 for a summary of ANOVA results.

To determine whether the *tcp1*^{P73L} mutant larvae swim at similar speeds to wild-type larvae, we then measured the amount of time that they spend swimming at fast (≥ 10 mm/s) or slow (5 ≤ *x* < 10 mm/s) speeds in response to light and dark stimuli. For larvae from incrosses of F2 *tcp1*^{P73L} heterozygotes (Figure 5.12), we observed no significant interacting effects between lighting condition and genotype on the duration of fast or slow swimming at any stage. We observed a statistically significant effect ($p = 0.04$) of genotype on the duration of fast swimming at 12 dpf, irrespective of lighting condition (Figure 5.12cii, Table 8.20, Appendix 3); however, post-hoc multiple comparisons did not reveal any significant differences in the total duration of fast swimming between wild-type and heterozygous *tcp1*^{P73L} mutants or between wild-type and homozygous *tcp1*^{P73L} mutants (Table 8.21, Appendix 3).

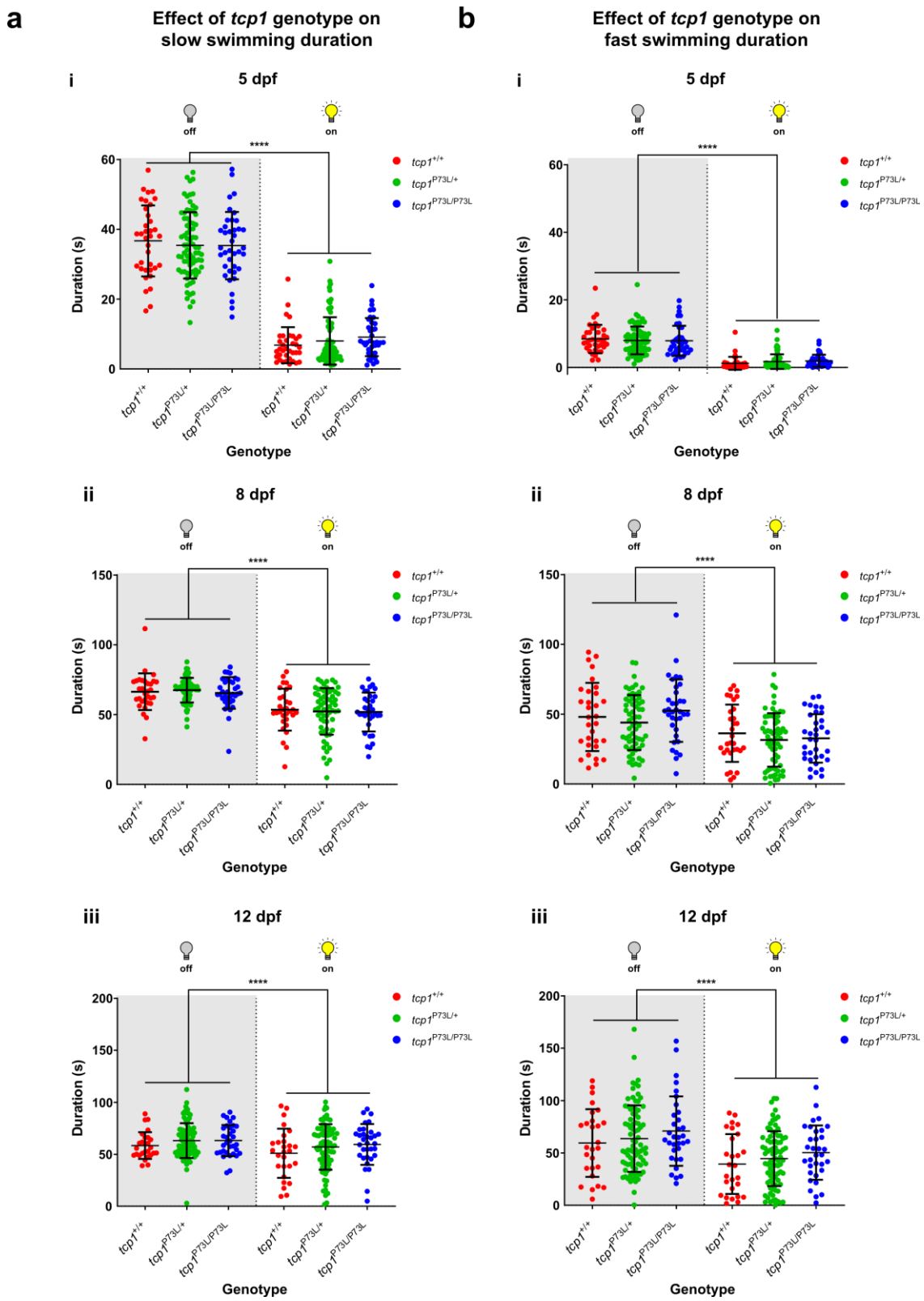

Figure 5.12. Fast and slow swimming behaviour in response to light and dark stimuli in zygotic *tcp1*^{P73L} mutant zebrafish larvae. Graphs showing (**a**) total duration of slow swimming and (**b**) total duration of fast swimming for wild-type and *tcp1*^{P73L} mutant larvae at (**i**) 5 dpf, (**ii**) 8 dpf and (**iii**) 12 dpf, averaged across all three dark periods and all three light periods. For all graphs, error bars represent standard deviations for larvae from at least three independent experimental replicates (individual larvae are represented by individual points; see Figures 5.6-5.8 for exact numbers used in each experiment). Statistical significance of the effects of genotype and lighting condition on locomotion were determined in GraphPad Prism 8.3.1, by performing two-way repeated measures ANOVA followed by Sidak's multiple comparisons test, where appropriate. Significant effects of lighting condition on locomotion are indicated by asterisks (**** = $p < 0.0001$). See Appendix 3 for a summary of ANOVA results.

For offspring from incrosses of F3 wild types and F3 *tcp1*^{P73L} homozygotes (Figure 5.13), we identified a significant interacting effect ($p = 0.013$) between lighting condition and genotype on the duration of fast swimming at 12 dpf (Figure 5.13cii, Table 8.27, Appendix 4). This is consistent with our earlier observation of a significant interacting effect on total swimming distance in these larvae at this time point; however, this only accounted for just over 0.5% of the total variation among the data (Table 8.27, Appendix 4). Moreover, post-hoc comparisons revealed no significant difference in fast swimming duration between wild-type and mutant larvae in either the light or the dark periods, indicating that motor function at fast swimming speeds is not compromised in the *tcp1*^{P73L} mutants.

We observed a significant effect ($p = 0.0136$) of genotype on the duration of fast swimming at 8 dpf (Figure 5.13biv, Table 8.25, Appendix 4), indicating that *tcp1*^{P73L} mutant larvae spend longer swimming at fast speeds at this stage compared with wild-type larvae (21% increase in mean fast swimming duration vs wild-type, 95% CI 4-37%). This is consistent with our earlier finding that the total swimming distance of *tcp1*^{P73L} mutant larvae was greater than that of wild-type larvae at this stage.

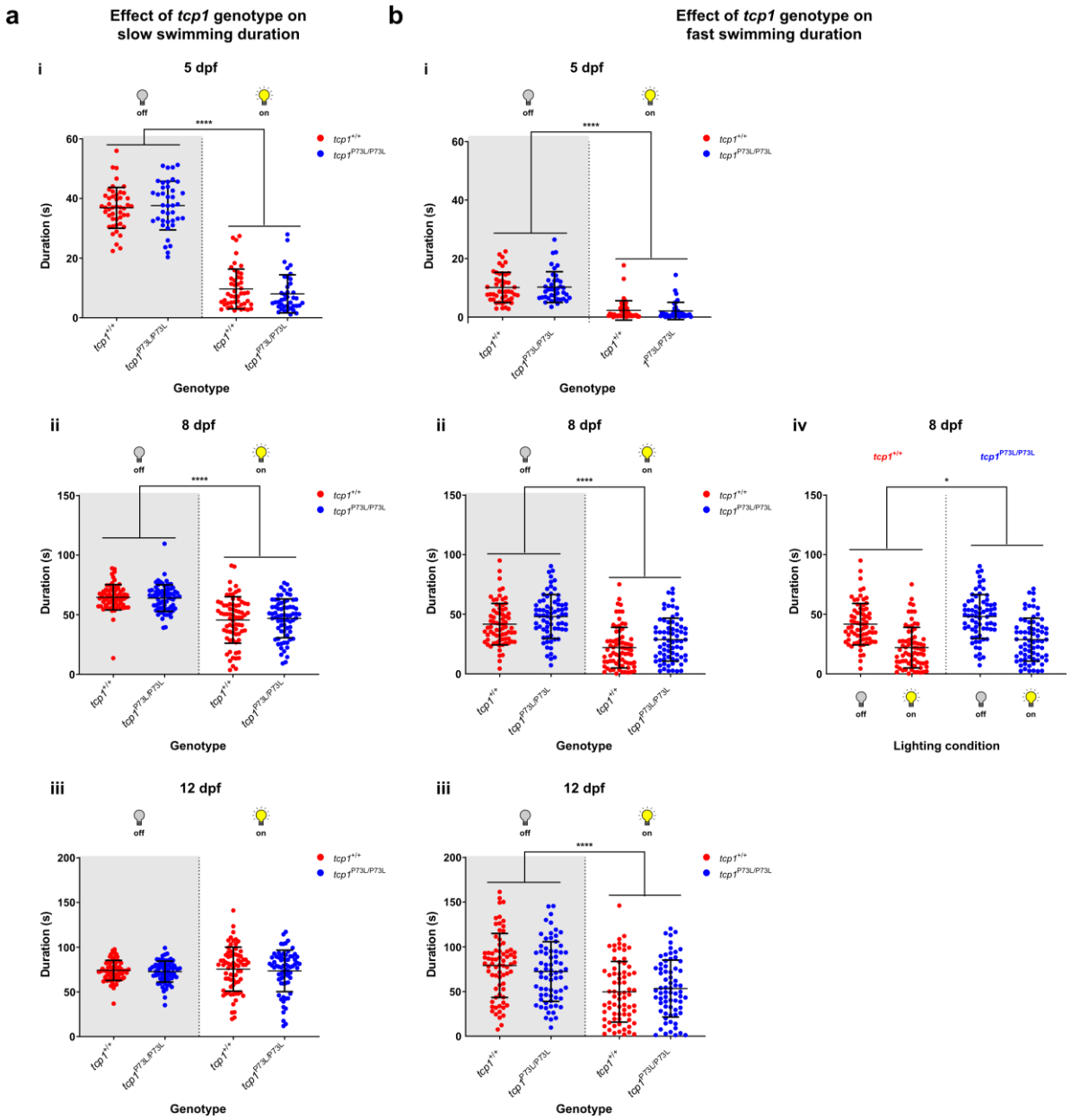

Figure 5.13. Fast and slow swimming behaviour in response to light and dark stimuli in maternal zygotic *tcp1*^{P73L} mutant zebrafish larvae. Graphs showing (**a**) total duration of slow swimming and (**b**) total duration of fast swimming for wild-type and *tcp1*^{P73L} mutant larvae at (**i**) 5 dpf, (**ii**,**iv**) 8 dpf and (**iii**) 12 dpf, averaged across all three dark periods and all three light periods. (N.B. **bii** and **biv** contain the same data points but are plotted separately to illustrate significant effects of lighting (**bii**) and genotype (**biv**) on fast swimming at 8 dpf). For all graphs, error bars represent standard deviations for larvae from three independent experimental replicates (individual larvae are represented by individual points; see Figures 5.9-5.11 for exact numbers used in each experiment). Statistical significance of the effects of genotype and lighting condition on locomotion were determined in GraphPad Prism 8.3.1, by performing two-way repeated measures ANOVA, followed by Sidak's multiple comparisons test where appropriate. Significant effects of lighting condition (**i**,**ii**,**iii**) and genotype (**iv**) on locomotion are indicated by asterisks (* = $p < 0.05$, **** = $p < 0.0001$). See Appendix 4 for a summary of ANOVA results.

5.5 The *tcp1*^{P73L} mutation does not result in reduced swimming endurance in adult zebrafish

As we detected little evidence to suggest that motor function is impaired in homozygous *tcp1*^{P73L} mutant zebrafish at larval stages, we decided to investigate whether these mutants develop a motor defect with age. To do this, we employed the established swim tunnel test (Figure 5.14a), which provides a read-out of swimming endurance and has previously been used to demonstrate motor dysfunction in adult zebrafish models of neurological disease (Chapman et al., 2013; Ramesh et al., 2010; Shaw et al., 2018).

We measured the swimming endurance of sex-matched wild-type and homozygous *tcp1*^{P73L} mutant zebrafish at 6 months and 9 months post-fertilisation (see legend for Figure 5.14 for details of numbers and sexes of fish). However, we did not identify any significant difference in critical swimming velocity between the genotypes at either stage (Figure 5.14b), indicating that the motor function of these mutants is not impaired up to 9 months of age.

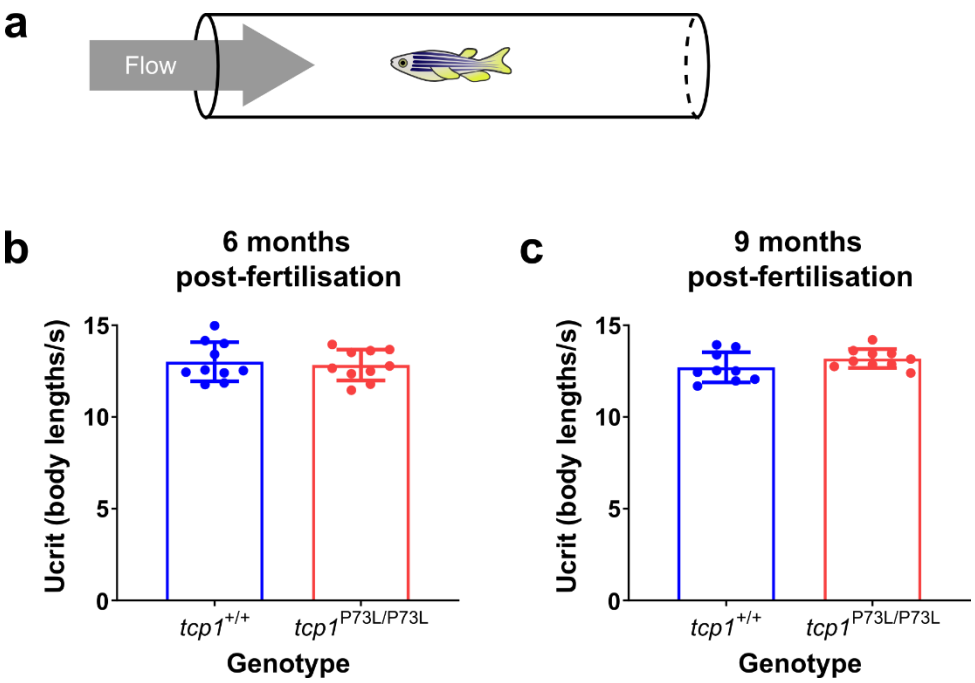

Figure 5.14. Motor endurance is not impaired in adult *tcp1*^{P73L} mutant zebrafish. (**a**) Schematic diagram of the swim tunnel used to test the swimming endurance of adult zebrafish. Fish are placed into a transparent tunnel, in which they swim against a flow of water. The speed of the water flow is incrementally increased at 5-minute intervals until the fish reaches exhaustion. (**b**,**c**) Bar graph showing mean critical swimming velocities for wild-type (**red**) and homozygous *tcp1*$^{P73L/P73L}$ mutant (**blue**) zebrafish at (**b**) 6 months and (**c**) 9 months post-fertilisation. Error bars represent standard deviation of critical swimming velocities of (**b**) n = 10 (5 male, 5 female) wild-type zebrafish and n = 10 (5 male, 5 female) *tcp1*^{P73L} mutant zebrafish or (**c**) n = 9 (4 male, 5 female) wild-type and n = 10 (5 male, 5 female) mutant zebrafish (9 months). Individual fish are represented by individual data points. Statistical significance was assessed using using GraphPad Prism 8.3.1, by performing unpaired t tests between wild-type and mutant fish at each time point.

5.6 Homozygous *tcp1*^{P73L} mutant zebrafish larvae display altered colour preference

Our observation that homozygous *tcp1*^{P73L} mutant larvae respond in the expected manner to the light and dark stimuli in the experiments described above suggests that these mutants are not completely blind. However, this assay does not tell us whether they have any subtle visual defects that might be more relevant to the phenotypes observed in the human patients with the *TCP1*^{P70L} mutation.

One of the key features of the visual phenotype in patients is colour blindness. A cross-maze with different coloured arms was previously used to demonstrate that zebrafish larvae display an innate colour preference by 5 dpf (Park et al., 2016). This preference was found to manifest hierarchically, with larvae exhibiting a strong preference for blue and red areas (blue > red) over green and yellow areas (green > yellow). In mutant zebrafish larvae harbouring a null mutation in the tyrosinase gene (*tyr*), which has been linked to colour vision deficits in human patients (Liu et al., 2014), this larval colour preference was abolished (Park et al., 2016).

We reasoned that we could use a similar approach to determine whether homozygous *tcp1*^{P73L} mutant larvae display any colour vision deficits by investigating whether their behaviour toward different colours was altered compared to wild-type larvae. We placed groups of wild-type or homozygous *tcp1*^{P73L} mutant larvae into a cross-maze similar to the one described by Park et al. (2016) (Figure 5.15a), and we recorded their activity over a 10-minute period. We then counted the number of larvae in each arm of the maze at 5-second intervals and expressed this as a proportion of the total fish from each group occupying each coloured arm, averaged across all quantified frames (Figure 5.15b).

In agreement with previous findings (Park et al., 2016), we observed a hierarchical colour preference in wild-type larvae; they displayed the strongest preference for blue, followed by red, then green; and they displayed a strong aversion to the yellow arm (solid bars, Figure 5.15b). The general pattern of behaviour was similar in homozygous *tcp1*^{P73L}

mutant larvae (empty bars, Figure 5.15b); however, the magnitude of preference for each colour differed, with mutant larvae spending significantly more time in the blue arm than wild-type larvae. The mutants also appeared to spend less time occupying the red arm than wild-type larvae, though this difference was not statistically significant. Together, these data indicate that the behavioural response to colour is altered in *tcp1*^{P73L} mutant larvae.

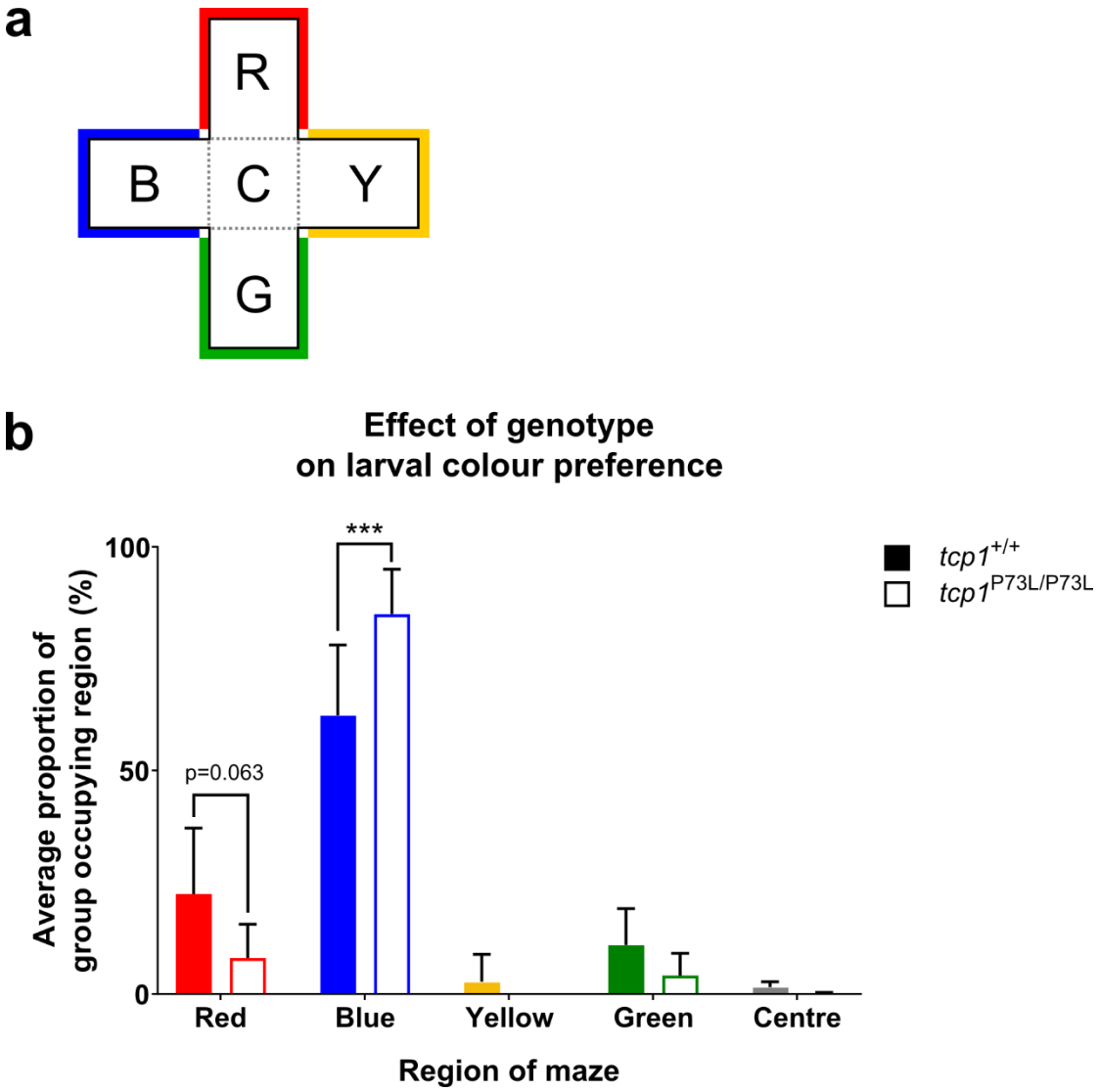

Figure 5.15. *tcp1*^{P73L} mutant larvae exhibit altered colour preference behaviour. (**a**) Schematic diagram of the cross-maze used to assess colour preference of zebrafish larvae, illustrating the defined regions corresponding to each coloured arm, or the centre of the maze (B = blue, R = red, Y = yellow, G = green, C = centre). (**b**) Bar graph showing the average percentage of wild-type (solid bars) or mutant (empty bars) larvae that occupied each region of the maze at any given point. Bars represent the mean percentage occupancy of each region across n = 5 experimental replicates for both genotypes, and error bars represent the standard deviations of the percentage occupancies in the five experiments. Statistical significance was determined in GraphPad Prism 8.3.1 by performing two-way ANOVA followed by Sidak's multiple comparisons test between wild-type and homozygous mutants for each individual coloured region.

5.7 Discussion

In this chapter, we aimed to investigate whether zebrafish *tcp1* mutations affect functions of relevance to human *TCP1*-linked disease, so that we could further test our hypothesis that the *TCP1*^{P70L} mutation causes the patients' phenotypes. We specifically aimed to do this by using behavioural assays to measure motor and visual function, as these are key components of the phenotype observed in patients. Our findings showed that homozygous *tcp1*^{I57fs} larvae exhibit severe motor dysfunction, but we did not detect any obvious motor defects in *tcp1*^{P73L} mutants at larval or adult stages. However, we did obtain some data that may indicate a colour vision defect in *tcp1*^{P73L} mutant larvae.

5.7.1 Effects of *tcp1* mutations on motor function

We examined the motor function of homozygous *tcp1*^{I57fs} mutant larvae at 3 dpf and found that their touch-evoked escape response was severely impaired. When we investigated the source of this motor dysfunction, we identified abnormalities in several components of the main circuit responsible for facilitating the escape response. The most obvious defect was in the skeletal muscle of the trunk, where we found that *tcp1*^{I57fs} mutants had fewer myofibrils than their siblings, which is likely to contribute to their motor dysfunction. This finding is consistent with phenotypes that were previously observed in larvae with insertional mutations in *tcp1*, *cct2*, *cct5* and *cct8*, a CRISPR-induced frameshift mutation in *cct4*, or an ENU-induced splice site mutation in *cct3* (Berger et al., 2018) and supports an important role for TRiC/CCT in skeletal muscle development. This finding is in line with our earlier observation that *tcp1* mRNA is highly expressed in the somites of wild-type embryos.

TRiC/CCT is known to be involved in folding actin (Sternlicht et al., 1993) and myosin (Srikakulam and Winkelmann, 1999), both of which are major components of skeletal muscle. Berger et al. (2018) proposed that the skeletal muscle defects they observed in *cct3* mutant larvae were more likely to be a result of defective actin folding than defective

myosin folding. They observed reduced trunk birefringence (a read-out of muscle integrity) in *cct3* mutant larvae, and were unable to rescue this through treatment with a small molecule that was previously shown to be capable of refolding myosin (Radke et al., 2014) and rescued birefringence phenotypes associated with misfolded myosin in *unc45b* morphant larvae (Berger et al., 2018; Etard et al., 2015). Moreover, they observed defective incorporation of GFP-tagged α-actin into myofibrils in these mutants (Berger et al., 2018). Our earlier finding that *actb1* mRNA was upregulated in *tcp1*^{I57fs} mutants also points to a role for actin misfolding due to loss of *tcp1* in these larvae; however, we cannot directly link this finding to the muscle phenotype we observed, as skeletal muscle is predominantly composed of α-cardiac muscle actin and α-skeletal muscle actin, which are encoded by *actc1a*, *actc1b*, *acta1a* and *actc1b* (Sztal et al., 2018).

We also detected abnormalities in the Mauthner cells of *tcp1*^{I57fs} larvae. One of our observations was that the relative intensity of the 3A10 immunostaining in the cell bodies and axons of the Mauthner cells differed in wild-type and mutant larvae. The epitope for the 3A10 antibody is a neurofilament-associated antigen, previously characterised as a short amino acid sequence found in several proteins that are expressed during mammalian brain development (Harada et al., 1999); however, the significance of the increased relative staining intensity of Mauthner cell bodies in the *tcp1*^{I57fs} mutant larvae is unclear. Moreover, we do not know whether the abnormalities we observed are linked to a functional defect in these cells and if/how such a defect contributes to the aberrant escape response we observed in these mutants. To address this, we would need to perform further functional assessments; for example, by conducting electrophysiological measurements or calcium imaging of the Mauthner cells (Takahashi et al., 2002).

In contrast, we did not see any obvious morphological changes in the spinal motor neurons of *tcp1*^{I57fs} mutant larvae, though we did not look in any detail at specific subclasses of motor neuron to determine whether there are any more subtle morphological changes. We also did not examine whether there are any functional defects in these cells, or whether

neuromuscular junction integrity is affected. Furthermore, we did not assess whether the sensory Rohon-Beard neurons, which also form part of the escape response circuit, are affected. These would be suitable avenues for further investigation of the factors contributing to motor dysfunction in *tcp1*^{I57fs} larvae. For example, we could perform immunohistochemistry to assess the health of the neuromuscular junction by measuring the degree of co-localisation between α-bungarotoxin (a postsynaptic marker) and anti-synaptic vesicle protein 2 (SV2; a pre-synaptic marker), which has been shown to be altered in zebrafish models of motor neuron disease and peripheral neuropathy (Chapman et al., 2013; Ramesh et al., 2010; Sakowski et al., 2012). We could also perform immunohistochemical analysis of the Rohon-Beard neurons using antibodies against islet-1/2 (Jao et al., 2012) and acetylated α-tubulin (Svoboda et al., 2001), or the zn-12 antibody (Faucherre et al., 2013) to determine whether they are affected by loss of *tcp1*.

In contrast to the *tcp1*^{I57fs} mutants, we did not observe such a striking motor phenotype in homozygous *tcp1*^{P73L} larvae. We failed to detect any obvious evidence of a defective locomotor response to alternating light and dark stimuli in *tcp1*^{P73L} larvae, and this did not appear to be due to the phenotype being masked by the presence of wild-type maternal transcripts early in development. We did detect a significant overall increase in the total swimming distance and the duration of fast swimming in maternal zygotic *tcp1*^{P73L} mutant larvae compared with wild-type larvae at 8 dpf; however, this effect was not present at any other time point and is unlikely to be relevant to motor function. Moreover, the wild-type and maternal zygotic *tcp1*^{P73L} mutant larvae that we used in this experiment were obtained from independent incrosses, so there is a possibility that any differences between the genotypes in terms of their locomotor activity might be due to the presence of unrelated variants outside the *tcp1* gene. Because we saw no obvious motor dysfunction in *tcp1*^{P73L} mutant larvae, we then assessed the motor endurance of adult *tcp1*^{P73L} mutants using the swim tunnel test. However, we saw no evidence that their motor function was impaired compared to wild-type zebrafish.

These approaches have successfully revealed defects in zebrafish models of human diseases affecting the motor system (Chapman et al., 2013; Ramesh et al., 2010; Shaw et al., 2018). However, it is possible that motor dysfunction in *tcp1*^{P73L} mutant larvae is below the threshold that can be detected using these assays. It is also worth noting that the assays we have used here may not provide the most relevant read-out of cerebellar function. Although patients with the *TCP1*^{P70L} mutation were not reported to exhibit typical cerebellar signs such as tremor or nystagmus upon clinical examination, we do not know to what extent their cerebellar atrophy, and any resulting cerebellar dysfunction, might be contributing to their phenotypes. Tests such as the optokinetic response and the optomotor response, which involve measuring visually guided larval behaviours that are thought to be regulated by the cerebellum (Kist and Portugues, 2019; Knogler et al., 2019, 2017), may be useful for further investigating the possibility of functional cerebellar defects in *tcp1*^{P73L} mutant larvae. Indeed, the optokinetic response assay previously revealed aberrant eye movements underpinned by Purkinje cell pathology in a zebrafish model of spinocerebellar ataxia (Namikawa et al., 2019). However, a drawback of measuring motor function using behavioural assays that require sensory visual input is that abnormal behavioural responses could also arise as a result of visual dysfunction. This is particularly relevant in the context of modelling the *TCP1*-linked disorder, which also manifests with visual defects. We would therefore need to corroborate any findings from these behavioural assays using other approaches, such as measuring neuronal activity in the cerebellum.

5.7.2 Effects of *tcp1* mutations on visual function

We did not see any impairment in the locomotor response of *tcp1*^{P73L} larvae to alternating light and dark stimuli, indicating that these mutants are able to detect light and dark. However, mutant larvae that develop without eyes, as well as larvae whose eyes have been surgically removed, have previously been shown to be capable of responding to changes in light and dark due to the presence of photoreceptive cells in the brain

(Fernandes et al., 2012); therefore, this finding may not rule out the possibility that the *tcp1*^{P73L} mutants have defects in retinal function. However, although the assays performed by Fernandes et al. (2012) assess the larval response to changes in light intensity, it is not the same as the assay we used; therefore, we would need to determine how larvae without eyes behave in the assay we used to be able to draw a direct comparison with the *tcp1*^{P73L} mutant larvae.

This test also does not give us any information about any specific visual defects that might be relevant to the patients' phenotypes. Since the patients with the *TCP1*^{P70L} mutation have colour vision defects, we assessed the behavioural response of the *tcp1*^{P73L} mutant larvae to different colours. In doing this, we found that *tcp1*^{P73L} mutant larvae behaved differently to wild-type larvae in a colour preference maze. Specifically, the mutants spent significantly more time occupying the blue arm of the maze than wild-type larvae, and they also spent slightly less time occupying the red and green arms of the maze (though this was not statistically significant).

One possible explanation for this is that the mutants have a functional defect in a particular subset of cone photoreceptors, which could cause certain colours to appear differently than usual. This may, in turn, cause the larvae to exhibit altered behaviour in response to these colours. To illustrate this point, Figure 5.16 shows a simulation of what the coloured arms of the maze might look like to humans with different forms of colour blindness corresponding to deficiencies in the three cone subtypes. With colour blindness caused by red cone deficiency (protanopia) or green cone deficiency (deuteranopia), it becomes difficult to distinguish between the red and green arms of the maze, and both become more yellow in appearance.

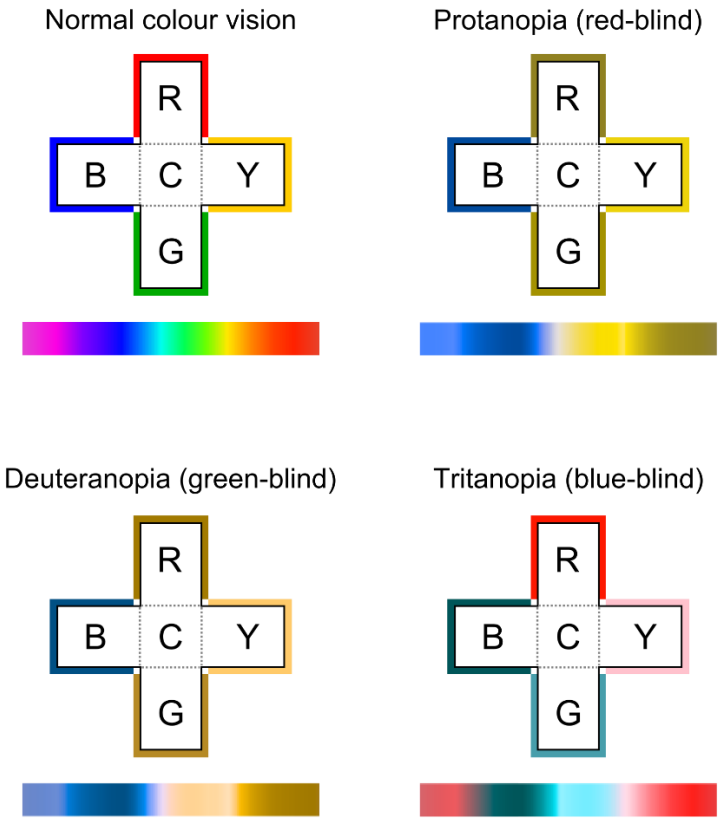

Figure 5.16. Schematic diagram of cross-maze used for larval colour preference assay, with simulations of how the colours might appear to humans with different types of colour vision deficiency. Simulated colour blindness images were created by uploading the original schematic diagram of the cross-maze and visible light spectrum to the Color Blindness Simulator tool (Colblindor, accessible at: color-blindness.com/coblis-color-blindness-simulator/)

Considering the innate aversion of zebrafish larvae towards yellow (Park et al., 2016), if the *tcp1*^{P73L} mutant larvae have a red or green cone deficiency, we might expect them to avoid the 'yellow-appearing' red and green arms as well as the yellow arm itself. This would be consistent with our observation that these mutants spend a greater proportion of their time in the blue arm than wild-type larvae and may be indicative of a red or green cone defect in these larvae. However, it is possible that this finding is unrelated to the *tcp1*^{P73L} mutants' ability to detect colour. Indeed, one caveat associated with this experiment is that we did not control for lighting intensity in the maze; therefore, our results could also have been influenced by the response of the larvae to the intensity of light in each of the coloured arms.

To obtain further evidence to help us interpret this result and determine whether it corresponds to a functional defect in the retina, it would be useful to compare ERG recordings from wild-type and mutant retinae so that we can assess whether there are any alterations in the electrical response to light in the different subclasses of photoreceptor, or in other retinal neurons. It would also be beneficial to perform more sophisticated behavioural tests to assess whether our findings are linked to a colour vision defect. For example, we could apply a modified version of the optokinetic response assay, which involves measuring larval eye movements in response to coloured patterns, to determine whether the *tcp1*^{P73L} mutant larvae are able to distinguish between different colours, while controlling for lighting intensity (Klaassen et al., 2011). It may also be beneficial to test for possible non-colour-related visual defects using other behavioural assays, such as the optomotor response assay (Neuhauss, 2003; Stujenske et al., 2011); or by assessing visual function at low light levels using an escape response assay (Maaswinkel et al., 2005). However, most of these assays come with the limitation that any behavioural abnormalities could be driven by motor dysfunction as well as visual dysfunction; therefore, they would be best employed in combination with electrophysiological analyses.

5.7.3 Conclusions

In summary, we have shown that loss of zebrafish *tcp1* causes severe defects in the larval touch-evoked escape response, which is likely to be predominantly explained by gross morphological abnormalities in the skeletal muscles of the trunk. We also uncovered some evidence to suggest that the health of the Mauthner cells may be affected by loss of *tcp1*; however, we would need to conduct further experiments to determine whether these abnormalities, or abnormalities in any other components of the circuit governing this response, contribute to the motor dysfunction we observed. Contrastingly, our data did not suggest that motor function is compromised in homozygous *tcp1*^{P73L} mutant fish at either the larval or the adult stage, but we cannot rule out the possibility that motor function could be impaired at a low level that may not have been detected by the assays we used.

With regard to assessing the visual function of the *tcp1*^{P73L} mutant larvae, we found that these mutants displayed an altered behavioural response to colour compared with wild-type larvae. However, we would need to examine their phenotypes in further detail using electrophysiological and more advanced behavioural approaches to determine whether this corresponds to a colour vision defect and to investigate whether any other aspects of visual function are impaired.

Chapter 6

Discussion

6.1 Rationale for this investigation

Rare genetic diseases present a significant problem for translational research. These disorders are collectively common and often present with debilitating clinical phenotypes, but effective disease-modifying treatments are currently scarce. This is partly due to the challenge of obtaining accurate molecular diagnoses for rare diseases (especially for disorders that are only known to affect a small number of patients from the same family), and partly due to a lack of experimental research into the mechanisms underpinning these conditions, because research efforts have tended to focus predominantly on common disorders.

Recent advances in DNA sequencing technology, together with the establishment of large-scale rare disease research networks, have been hugely advantageous for uncovering novel causative variants for rare diseases. However, we are now faced with the task of experimentally confirming the pathogenicity of a growing pool of candidate variants and deciphering how they cause disease. These investigations will not only aid our understanding of the genetic and pathophysiological aetiologies of these specific conditions but will also provide us with opportunities to gain novel insights into human gene function.

The zebrafish offers numerous advantages as an *in vivo* model system for studying these diseases, combining conserved vertebrate genetic and physiological features with an amenability to genetic and experimental manipulation. In this project, we aimed to apply these characteristics to study a novel homozygous variant in *TCP1* (*TCP1*^{P70L}), which has been linked to a rare neurological disorder in three siblings born to consanguineous parents.

6.2 Specific hypotheses and aims of this thesis

To date, the *TCP1*^{P70L} mutation has only been reported in these three siblings, and there are currently no other published reports of *TCP1* mutations causing similar disorders in any unrelated patients. Therefore, we cannot conclude that the *TCP1*^{P70L} mutation is pathogenic without further evidence to substantiate this. In line with this, our first hypothesis was that the patients' phenotypes are caused by the homozygous *TCP1*^{P70L} mutation. To test this hypothesis, we generated a *tcp1* knock-in mutant zebrafish line (*tcp1*^{P73L}) harbouring a mutation equivalent to the human *TCP1*^{P70L} variant, and we characterised this model to determine whether phenotypic features of the human disease were recapitulated.

These patients represent the first direct link between *TCP1* and neurological disease, and their phenotypes imply that *TCP1* plays a critical role in specific components of the nervous system. Accordingly, our second hypothesis was that *TCP1* is important for the development and/or maintenance of the cerebellum and retina, which are the key tissues affected in patients with the *TCP1*^{P70L} mutation. To test this hypothesis, we generated a mutant zebrafish harbouring a frameshift mutation in *tcp1*, so that we could study how loss of *tcp1* affects tissues that are relevant to the human disease.

6.3 Do *tcp1*^{P73L} mutant zebrafish recapitulate the phenotypes of the human *TCP1*^{P70L}-linked disorder?

The patients with the novel *TCP1*^{P70L} mutation presented with pathology affecting the cerebellum, retina and peripheral nervous system, manifesting clinically as mild motor and visual dysfunction. We therefore characterised our *tcp1*^{P73L} mutant zebrafish to determine whether we could identify any relevant defects that might help us to confirm the pathogenicity of the *TCP1*^{P70L} mutation.

We uncovered no evidence to indicate that there are morphological abnormalities in the cerebellum or retina of homozygous *tcp1*^{P73L} mutant larvae up to 5 dpf, and our findings also suggest that these mutants have no defects in motor function during larval stages or in adulthood. Furthermore, we detected little evidence of compensatory activation of molecular pathways that might be connected to TRiC/CCT dysfunction in these larvae, which might indicate that this mutation does not result in a broad loss of chaperone activity.

We did, however, find that the *tcp1*^{P73L} larvae behaved differently to wild-type zebrafish in a colour preference test. This result is consistent with these mutants having a colour vision deficit, which is one of the clinical features of the human disease. However, we would need to corroborate this finding by performing more detailed assessments of visual function in our model before we can definitively conclude that colour vision is impaired in the *tcp1*^{P73L} mutant larvae.

Taken together, we currently have limited evidence to robustly support the hypothesis that the *TCP1*^{P70L} mutation causes the patients' neurological phenotypes based on data from the *tcp1*^{P73L} mutant zebrafish alone. There are several possible justifications for this; firstly, it may be that our hypothesis is incorrect, and the patients' phenotypes are not caused by the *TCP1*^{P70L} mutation, which could explain why we see little evidence of neurological dysfunction in the *tcp1*^{P73L} mutant zebrafish. It is also possible that a mutation in another gene modulates the patients' phenotypes alongside the *TCP1* mutation. At this point, it is relevant to consider that, although the *TCP1*^{P70L} mutation was identified as the most promising candidate mutation for this disorder, it was not the only candidate variant uncovered in these patients. To identify the mutation responsible for the neurological disorder in this pedigree, whole-exome sequencing data was initially filtered to pinpoint rare variants that were homozygous in an affected patient, but not in an unaffected sibling. Of these, variants producing a CADD score (a tool for scoring the likely deleteriousness of human variants) (Rentzsch et al., 2019) of less than 15 were excluded, as these are generally considered to be benign. The candidate variants that remained after these

filtering steps are listed in Table 6.1 (unpublished findings from the Sheridan group, University of Leeds), along with the scores obtained from various predictive tools relating to their likely deleteriousness to protein function.

Table 6.1. Summary of homozygous candidate variants identified in patients with cerebellar atrophy and retinal dystrophy

		Scores predicting likely deleteriousness of variant			
		CADD*	**SIFT#**	**PolyPhen-2^**	**SNAP2º**
Candidate mutations	***TCP1*** **p.P70L** **c.209C>T**	31	0.00	1.00 (probably damaging)	70
	DLL3 **p.G458R** **c.1372G>C**	28.5	0.00	1.00 (probably damaging)	65
	CLPTM1 **p.R477Q** **c.1430G>A**	18.69	0.04	0.437 (benign)	51
	CATSPERG **p.W983L** **c.2948G>T**	16.96	0.00	1.00 (probably damaging)	65
	KLHL9 **p.F348L** **c.1044T>G**	15.84	0.00	0.997 (probably damaging)	35
	ARL6IP1 **p.S144P** **c.430T>C**	15.8	0.32	0.939 (possibly damaging)	42

*Higher CADD score = greater likelihood of deleteriousness, <15 unlikely to be associated with disease
#Lower SIFT score = greater likelihood of deleteriousness, <0.05 considered to be damaging
^Higher PolyPhen-2 score = greater likelihood of deleteriousness, >0.85 predicted to be damaging
ºHigher SNAP2 score = greater likelihood of effect on protein function (<50 = weak signal for effect, >50 = strong signal for effect

The candidate mutation identified in *DLL3* (delta-like canonical notch ligand 3) is predicted to have deleterious effects on protein function (Table 6.1); however, autosomal recessive mutations in this gene have previously been shown to cause segmentation defects of the vertebrae (Bulman et al., 2000; Turnpenny et al., 2003). It is therefore unlikely that this variant would cause or modulate the neurological phenotypes observed in these patients.

The *CLPTM1* (cleft lip and palate transmembrane protein 1) gene encodes a protein involved in controlling the trafficking of $GABA_A$ receptors to the postsynaptic membrane, thus regulating inhibitory synaptic transmission (Ge et al., 2018). Since synaptic

dysfunction has been implicated in the pathology of various neurodevelopmental and neurodegenerative disorders (Ardiles et al., 2017), it is conceivable that dysfunction of this gene could result in a neurological phenotype. It is worth noting, however, that the scores obtained from the predictive tools for the *CLPTM1* mutation provide a much weaker indication of deleteriousness than the scores for the *TCP1* mutation (Table 6.1), making it a less likely candidate for this disorder.

The *CATSPERG* (cation channel sperm associated auxiliary subunit gamma) gene encodes a protein involved in the process of regulating calcium entry into sperm cells, thereby playing a role in sperm motility and male fertility (Wang et al., 2009). Although the predictive scores for the *CATSPERG* mutation suggest that it may have damaging effects on protein function (Table 6.1), there is no obvious rationale for linking the neurological phenotypes observed in these patients to CATSPERG dysfunction.

Kelch-like protein 9, encoded by *KLHL9*, is a component of a complex which controls the detachment of aurora B kinase from chromosomes during mitosis, thereby facilitating proper mitotic cell division (Sumara et al., 2007). Mitotic defects resulting in aneuploidy have been linked to the pathogenesis of various neurodegenerative and neurodevelopmental disorders (Potter et al., 2019). It is therefore feasible that dysfunction of *KLHL9* might disrupt mitosis and cause a neurological phenotype to arise in these patients in a similar manner; however, the candidate mutation identified in *KLHL9* is not as strongly predicted to have damaging consequences as some of the other candidates (Table 6.1).

The *ARL6IP1* gene, encoding ADP-ribosylation factor-like protein 6-interacting protein 1, has previously been implicated in neurological disease. Specifically, biallelic mutations in *ARL6IP1* have been shown to cause an autosomal recessive form of spastic paraplegia (Chukhrova et al., 2019; Nizon et al., 2018; Wakil et al., 2019). However, the *ARL6IP1* mutation identified here is not strongly predicted to have deleterious effects (Table 6.1); therefore, it is unlikely that it contributes to the neurological phenotypes of these patients.

Based on this predictive information, the *TCP1*^{P70L} mutation remains the most likely candidate for this disorder; however, given the links between *CLPTM1* and GABAergic synapse function, it would be interesting to experimentally explore the functionality of the *CLPTM1* candidate mutation to assess whether it might also modulate the patients' phenotypes. It may also be informative to determine the effects of the *KLHL9* candidate mutation, to assess whether it might contribute pathologically to this condition by initiating cell cycle defects.

Another potential reason for the apparent lack of pathology in our *tcp1*^{P73L} mutant zebrafish model is that we have not yet performed sufficiently detailed characterisation to reveal a phenotype in these fish. This is supported by our finding that the *tcp1*^{P73L} mutant larvae displayed altered behaviour in the colour preference assay, consistent with a subtle level of dysfunction that requires more in-depth characterisation. This may be related to the fact that the patients' phenotypes are relatively mild.

To explore this possibility, we would need to further analyse the phenotypes of the *tcp1*^{P73L} mutant zebrafish. At the morphological level, it would be useful to examine the Purkinje cells and photoreceptors in greater detail to assess whether there are any subtle morphological defects in these cells that our assays were not sensitive enough to detect. We could also investigate whether other key cell types in the cerebellum and/or retina are affected by the mutation. It would additionally be beneficial to explore functional phenotypes in more detail; for example, by employing more sophisticated behavioural approaches to measure motor and visual function, or by using electrophysiological approaches to determine whether there is any evidence for impaired activity in relevant neuronal populations. Because our characterisation of these mutants has predominantly been focused on identifying defects at the larval stage, we would also need to extend our investigations to conduct more detailed analyses in juvenile and adult fish, since morphological or functional phenotypes associated with the mutation may not become apparent until later in development.

Another potential reason for the apparent lack of phenotype in the *tcp1*^{P73L} mutant zebrafish is that the mutation may exert its effects in a species-specific manner, causing neurological dysfunction in humans but no pathology in zebrafish. This could arise as a result of inherent interspecies differences in the organisation of the nervous system. Notably, the zebrafish nervous system is less complex than the human nervous system, so it is possible that the mutation affects pathways that are important for development and function of the human nervous system but are dispensable for the development of the zebrafish nervous system. If this were the case, the mutation may still have an effect in zebrafish at the biochemical level. Although we saw no evidence of compensatory gene expression that might point towards chaperone dysfunction in the *tcp1*^{P73L} larvae, we cannot rule out the possibility that TRiC/CCT function and/or substrate folding are impaired in these mutants to an extent that does not impact on neurological function. This is another area that could be addressed by future experiments.

In interpreting our findings from the *tcp1*^{P73L} mutant zebrafish, it is also relevant to consider the fact that the zebrafish possesses an innate and widespread capacity for regeneration of many tissues, including those of the nervous system (Zambusi and Ninkovic, 2020). In contrast, the inborn capacity for neuronal regeneration in humans is comparatively restricted (Jessberger, 2016). This superior regenerative ability of the zebrafish may be enough to overcome a subtle degenerative effect of the *tcp1*^{P73L} mutation, which could cause disease-relevant phenotypes to become masked.

When we examined Purkinje cells in the *tcp1*^{P73L} larvae at 5 dpf, we saw no obvious differences compared to wild-type siblings. It has previously been shown that zebrafish Purkinje cells are capable of regenerating after injury during juvenile stages, but that this ability becomes impeded in adult zebrafish due to the pool of Purkinje cell progenitors at the ventricular zone becoming depleted over time (Kaslin et al., 2017). It would be interesting to assess the health of Purkinje cells in the adult *tcp1*^{P73L} zebrafish to determine

whether degeneration of these cells becomes apparent when their regenerative capacity is diminished.

Similarly, the zebrafish retina has a well-characterised ability to regenerate after injury at both larval and adult stages (Angueyra and Kindt, 2018). To test whether this may be contributing to the apparent lack of retinal pathology in the *tcp1*^{P73L} larvae, we could determine whether retinal degeneration occurs in these mutants when the regenerative capacity of this tissue is experimentally suppressed: for example, through the activation of γ-aminobutyric acid (GABA) signalling (Rao et al., 2017).

6.4 How does *TCP1* contribute to vertebrate development?

Our second hypothesis for this investigation was centred around the idea that the experimental study of genes linked to rare human disease can enhance our understanding of human gene function. Considering the phenotypes associated with the *TCP1*^{P70L} mutation, we specifically hypothesised that *TCP1* plays an important role in the development and maintenance of the cerebellum and retina. To test this, we investigated the phenotypic consequences of loss of *tcp1* in the zebrafish using our *tcp1*^{I57fs} mutant line.

Consistent with the hypothesis, we observed severe retinal degeneration in *tcp1*^{I57fs} mutants, along with an absence of cerebellar Purkinje cells, indicating that *tcp1* does indeed play an important role in these tissues. We also detected evidence of more general pathology, with homozygous *tcp1*^{I57fs} mutants displaying reduced survival and delayed development, together with optic tectum and skeletal muscle abnormalities, suggesting that the requirements for *tcp1* extend beyond the tissues that are affected in patients with the *TCP1*^{P70L} mutation.

Some of our observations from the *tcp1*^{I57fs} mutant zebrafish are consistent with phenotypes that have been reported for other models in which TRiC/CCT subunits have been ablated. For example, as we have discussed in previous chapters, retinal degeneration and optic tectum abnormalities are common features of several zebrafish

TRiC/CCT mutants (Berger et al., 2018; Matsuda and Mishina, 2004; Minegishi et al., 2018), and TRiC/CCT function has also been shown to be critical to the health of murine photoreceptors (Posokhova et al., 2011; Sinha et al., 2014). Together with our data, these findings strongly implicate *TCP1* and the TRiC/CCT complex in the maintenance of the vertebrate retina.

Skeletal muscle defects are also prevalent amongst zebrafish TRiC/CCT mutants (Berger et al., 2018), and cardiac-specific knockdown of TRiC/CCT subunits in *Drosophila melanogaster* was previously shown to result in defective myofibril organisation (Melkani et al., 2017). Taken with our findings, these data also support an important role for TRiC/CCT in muscle development and/or maintenance.

To date, we are not aware of any other studies in which specific roles for *TCP1* or TRiC/CCT in the cerebellum have been explored. However, our observation that the *tcp1*^{l57fs} mutant larvae completely lack cerebellar Purkinje cells at 3 dpf strongly supports a crucial role for *tcp1* in the development and/or maintenance of the cerebellum. Further investigations would be required to determine whether this is a common phenotypic feature that arises as a result of TRiC/CCT mutations (but has not yet been explored in other models), or whether this is a specific effect caused by loss of *tcp1*.

Combined with results from previous studies, our findings therefore support the hypothesis that *TCP1* is important for tissues implicated in the human disease. Our data are also consistent with the notion that TRiC/CCT plays a role in skeletal muscle formation, as well as being critical for general zebrafish development and survival. However, we would need to conduct further experiments to fully uncover the precise functions of *tcp1* in these tissues during development and to understand the pathophysiological mechanisms underpinning the phenotypes we observed in the *tcp1*^{l57fs} mutants. Bearing in mind our data showing that transcripts for TRiC/CCT substrates are differentially expressed and that heat shock genes are upregulated in these mutants, one reasonable next step would be

to further explore the possible contribution of misfolding of TRiC/CCT substrates and impaired proteostasis to the pathology we observed.

6.5 Is the *TCP1*^{P70L} mutation responsible for the patients' phenotypes?

The gold standard proof of pathogenicity for a novel candidate variant is the identification of unrelated patients who present with similar clinical phenotypes and have mutations in the same gene (MacArthur et al., 2014). This can be achieved by using tools such as GeneMatcher (Sobreira et al., 2015) to determine whether any other candidate variants in the gene have been reported by other groups. However, no other candidate variants are known to have been reported for *TCP1* at present.

Without evidence from unrelated patients, the next best strategy for confirming that a candidate variant causes a rare disease is to collect predictive and experimental information about the mutation to determine the likelihood of its pathogenicity (MacArthur et al., 2014). Prior to our investigations, the *TCP1*^{P70L} variant had already been shown to segregate appropriately with the phenotype in the family, had not been identified in healthy individuals in the general population, and was proposed to have deleterious effects on protein structure and/or function, based on the results of a number of computational predictions (Adzhubei et al., 2010; Hecht et al., 2015; Vaser et al., 2016). Moreover, the *TCP1* gene is evolutionarily highly conserved and is likely to be highly intolerant of loss-of-function mutations according to the Genome Aggregation Database (Karczewski et al., 2019). Although these findings support the pathogenicity of the mutation, more robust experimental evidence is required to determine whether it causes the patients' phenotypes.

The main goal of this thesis was to further explore the potential pathogenicity of the *TCP1*^{P70L} mutation by creating and characterising a *tcp1*^{P73L} mutant zebrafish line; however, as we discussed earlier, we observed little evidence of pathology in these mutants to support our hypothesis. Contrastingly, the phenotypes we observed in our

tcp1^{I57fs} mutant zebrafish are consistent with *tcp1* playing an important role in the development and/or maintenance of the tissues affected in the patients. Taken together with the predicted pathogenicity of the *TCP1*^{P70L} mutation, our findings from the *tcp1*^{I57fs} mutant zebrafish support our hypothesis that the *TCP1*^{P70L} mutation causes the patients' phenotypes; however, we would need to perform further functional analysis of the variant in our *tcp1*^{P73L} zebrafish, and possibly in other model systems, before we can conclude that the *TCP1*^{P70L} variant is definitely responsible for the patients' disease.

6.6 Advantages and limitations of studying specific human disease-linked mutations using knock-in zebrafish models

As discussed above, the primary motivation behind this thesis was to test the specific hypotheses relating to the pathogenicity of the novel *TCP1*^{P70L} variant and the functions of *TCP1* during vertebrate development. However, we reasoned that our findings would also allow us to comment more broadly on the utility and feasibility of creating and using novel CRISPR knock-in mutant zebrafish to assess the pathogenicity of candidate rare disease variants. This is especially relevant in light of the substantial number of novel human variants being linked to rare disease through large-scale NGS efforts such as the 100,000 Genomes Project (Turnbull et al., 2018). Many of these newly identified variants will require further experimental analysis to establish their functional significance, and it is imperative that we implement appropriate and practical strategies for doing so.

As we have already discussed, the zebrafish has been identified as a particularly useful experimental system in which to study rare genetic diseases (Adamson et al., 2018; Varga et al., 2018), not least due to its genetic tractability, which allows the zebrafish genome to be manipulated to study the phenotypic consequences of targeted mutations and their relationship to human disease. These benefits of the zebrafish as a model system for studying rare disorders are already being exploited as part of the strategy of large-scale

rare disease programmes such as the Undiagnosed Diseases Network (UDN) (Wangler et al., 2017).

Classically, strategies for using the zebrafish to assess how a mutation in a human disease-linked gene contributes to pathogenesis have focused on genetically ablating the function of the zebrafish orthologue to determine whether this gives rise to phenotypes that are relevant to the human disorder. However, this may not always be the most suitable approach, especially if the human mutation of interest is dominantly inherited and is thought to act through a gain-of-function mechanism, or if it is expected to have a hypomorphic effect. In these cases, it may be more useful to precisely recapitulate the human mutation in the zebrafish genome, so that its phenotypic consequences can be more accurately assessed. Here, we chose to apply this approach to assess the pathogenicity of the *TCP1*^{P70L} variant. This highlighted some benefits and pitfalls of modelling precise disease-linked mutations in the zebrafish, which we will discuss in the following sections.

6.6.1 Accurate recapitulation of human disease phenotypes

In theory, zebrafish knock-in models offer an advantage over knock-out models in that they should allow subtle phenotypes associated with specific partial loss-of-function mutations to be more accurately recapitulated than in knock-out models, where phenotypes are likely to present more severely than in patients with hypomorphic mutations. This was highlighted by our investigations; we found that loss of zebrafish *tcp1* did give rise to defects in the tissues that are implicated in the human disorder, but the phenotypes were much more severe than those described in patients with the *TCP1*^{P70L} mutation. Moreover, the *tcp1*^{I57fs} mutants also displayed pathology affecting tissues (e.g. skeletal muscle) that are not known to be involved in the human disease, and they also exhibited more general evidence of abnormal development. For this reason, future mechanistic investigations into

the phenotypes we observed the *tcp1*^{I57fs} mutant zebrafish may not yield results that are directly applicable to the pathogenesis of the human disorder.

In contrast, we found very little evidence of pathology in the *tcp1*^{P73L} mutant zebrafish; the only difference we observed in these mutants compared to wild-type fish was their behaviour in the colour preference assay. Although this result requires further validation to determine whether it corresponds to a true visual defect, it reinforces the notion that knock-in zebrafish models may allow us to study subtler phenotypes that are more relevant to human disease.

On the other hand, our findings also highlighted the challenges associated with being able to identify such subtle defects in zebrafish, as more sensitive assays will likely be required to reveal milder phenotypes. It is therefore advisable to consider the practicality of characterising phenotypes associated with the disease before using this strategy to model hypomorphic human mutations linked to milder disease phenotypes. This approach is perhaps best suited to modelling diseases that present with specific phenotypes that can be easily confirmed by examining particular cell types or by measuring the activities of certain proteins; however, this relies on a degree of prior knowledge about the pathological features of the disease, which will be limited for many rare disorders.

6.6.2 Technical considerations for modelling precise rare disease-linked mutations in the zebrafish

In the context of using the zebrafish as an experimental tool to investigate the pathogenicity of the huge number of novel variants emerging from large-scale rare disease programmes, it is also important to consider the technical challenges associated with modelling precise human mutations in the zebrafish, as we discuss below.

6.6.2.1 Limitations of creating knock-in zebrafish models using CRISPR/Cas9 and HDR

Here, we used CRISPR/Cas9 to generate our *tcp1*^{P73L} knock-in mutant zebrafish through HDR by designing short ssODN repair templates containing the P73L mutation. Although we were eventually successful in creating our knock-in model, our results highlighted the inefficiency of this approach. We only observed germline transmission of the correctly-repaired knock-in sequence from 2% (1/50) of founders that were injected with the NT repair template and 7.14% (1/14) of founders that were injected with the T repair template. Moreover, we also identified some founders that were transmitting erroneously repaired alleles, indicating that accuracy of the repair may also be a problem when using this strategy.

Low knock-in efficiency is widely recognised as a limitation of using CRISPR/Cas9 to introduce precise mutations into the zebrafish genome (Boel et al., 2018; Prykhozhij et al., 2018). Given the potential utility of knock-in zebrafish models for many applications, including creating more genetically accurate disease models, several groups have endeavoured to test different strategies for knocking precise mutations into the zebrafish genome with a view to optimising the approach so that it becomes more widely applicable.

Table 6.2 summarises some of the successful strategies that have been used to date and highlights how these approaches relate to some of the factors that have been proposed to influence knock-in efficiency, which we will discuss further in the following section.

Table 6.2. Summary of approaches that have successfully been used to introduce precise mutations into the zebrafish genome by CRISPR/Cas9 + HDR-mediated knock-in

Reference	Edited locus	Approach/ aim	Findings relating to factors proposed to influence CRISPR/HDR-mediated knock-in efficiency in zebrafish									Overall knock-in efficiency achieved
			Distance between cut site and desired mutation	gRNA efficiency (cutting efficiency)	Mutation of PAM/ gRNA target sequence in repair template	Overall repair template length	Target vs non-target strand repair templates	Symmetrical vs asymmetrical repair templates	Chemical repair template modifications	Single stranded vs double stranded repair templates	Use of HDR-enhancing/ NHEJ-inhibiting drugs	
Armstrong et al. (2016)	*tardbp*	Introduce single base-pair substitutions using short ssODN repair templates	Effects on efficiency were not tested, but mutations for both loci were located within 5 bp of cut site	Did not test effects on knock-in efficiency, but demonstrated by restriction fragment length analysis that gRNAs reliably facilitate target site mutagenesis by NHEJ (resulting in 21% germline transmission of indels for *tardbp* and 17% for *fus*)	Used templates with/without gRNA target site mutations but did not specifically compare efficiencies of knock-in using these templates	Did not specifically test this, but compared 23- and 100-nt templates for tardbp and observed slight increase in germline transmission efficiency with 100-nt (3/77 founders transmitting precise mutation vs. 1/46 for 23-nt template)	Not compared	Only tested symmetrical templates	Not tested	Only tested single-stranded templates	Not tested	Injected embryos were not screened directly. Germline transmission rates calculated as 2-4% of founders transmitting correct sequence, depending on locus/repair template used
	fus											
Bai et al. (2020)	*tyr*	Compare efficacy of zLOST (zebrafish long single-stranded DNA templates) vs other template types for correcting loss-of-function mutation which abolishes pigment development	Effects on efficiency were not tested but desired mutations were located close to cut site	Did not test effects on knock-in efficiency, but demonstrated target site mutagenesis by T7 endonuclease digestion	Did not specifically test effects on knock-in efficiency, but gRNA target sites and/or PAM were disrupted by knock-in for all loci	zLOST (~300-nt) reported to perform considerably better (98.5% efficiency) than other template designs, including short ssODNs (105-nt, 39.1% efficiency),circular dsDNA templates (~1500-nt, 2-5.4% efficiency), and linear dsDNA templates (0-3.0% efficiency). Efficiency was quantified as percentage of embryos containing pigmented melanphores, though this includes embryos in which the amount of pigment rescue was very small.	Not tested	Did not see any significant difference in efficiency between asymmetrical and symmetrical repair templates (but only tested this for double-stranded repair templates)	Not tested	Double-stranded templates performed much worse than single-stranded templates	Anecdotally reported no increase in knock-in efficiency using zLOST when using SCR7 (NHEJ inhibitor) or RS1 (HDR stimulator)	zLOST produced correct HDR efficiency between 5.11-17.86% in injected embroys (assessed by percentage of correct NGS reads). Germline transmission rates between 9.5-31.8% (percentage of founders transmitting desired edit through germline)
	th	Assess efficacy of zLOST for introducing desired edits at various loci		Not reported		zLOST reported to perform better (5.11-17.86% efficiency) than short ssODNs (0.09-0.54% efficiency) or circular dsDNA templates (0.6-1.62% efficiency). Efficiencies were reported as percentage of NGS reads containing precise edits in injected embryos		Not tested		Not tested		
	nop56											
	rps14											
	twist2											
	rpl18											

Table 6.2 (cont.)

Reference	Edited locus	Approach/ aim	Distance between cut site and desired mutation	gRNA efficiency (Cas9 cutting efficiency)	Mutation of PAM/ gRNA target sequence in repair template	Overall template length	Target vs non-target strand repair templates	Symmetrical vs asymmetrical templates	Chemical template modifications	Single stranded vs double stranded repair templates	Use of HDR-enhancing/ NHEJ-inhibiting drugs	Overall knock-in efficiency achieved
Boel et al. (2018)	*smad6a*	Test efficacy of different ssODN repair template designs to introduce single base-pair substitutions	Generally more efficient knock-in of edits located close to cut site	Not reported	Inserted silent mutations in PAM/gRNA target sequence for all loci, but effects on editing efficiency were not investigated	Reported increased HDR efficiency with 120-nt templates compared to 60-nt templates for 3 out of 4 targets, but increase is mostly accounted for by increased frequency of erroneous repair. Frequency of precise repair for symmetrical repair templates does not appear to be affected by repair template length	No significant overall effect of target vs non-target strand templates on knock-in efficiency.	No significant overall effect of asymmetrical vs symmetrical repair templates. However, found that 120-nt asymmetrical non-target strand templates with longer left homology arm tended to perform better than 120-nt symmetrical non-target strand templates, and 120-nt target strand templates with longer right homology arm tended to outperform 120-nt symmetrical target strand templates	Not tested	Only tested single-stranded repair templates	No significant effects on knock-in efficiency using NHEJ inhibitors (SCR7, NU7441, KU0060648) or HDR stimulators (RS1, L755507)	1-4% maximum knock-in efficiency in injected embryos (measured as % of correct NGS reads). Identified germ cells with precise HDR in 5/8 founders for *smad6a* locus and 1/8 founders for *slc2a10* locus
	tprkb											
	pls3											
	slc2a10											
DiNapoli et al. (2020)	*mitfa*	Test potential of synthetic repair templates to introduce precise edits to rescue pigmentation defect caused by missense mutation in *mitfa*	Desired missense mutation was located ~20-nt away from the cut site. Observed higher incorporation of silent mutations located closest to PAM than those located further away (only measured for one repair template)	Not reported	Disrupted gRNA target site and PAM in repair template sequences	951 bp asymmetric template performed better (9% efficiency) than 2000 bp asymmetric template (6% efficiency) or 318 bp asymmetric template (1% efficiency), though efficiency of 951 bp template dropped to 5% when sequence was shifted by 50 or 100 bp. Efficiency was measured as percentage of injected embryos showing pigment rescue	Successful pigment rescue was only observed with asymmetric templates (though did not measure editing efficiency within individual injected embryos)		Not tested	Most templates were double-stranded. No pigmentation rescue observed with single-stranded templates	Not tested	Up to 9% of embryos showed evidence of pigment rescue. Did not directly quantify precisely repaired sequences in injected embryos, or germline transmission rates
Hwang et al. (2013a)	*fh*	Test potential of ssODNs to introduce small targeted insertions or single base-pair substitutions by CRISPR	Effects on efficiency were not tested, but intended mutations were located at, or close to, the cut site	Effects on knock-in efficiency were not tested but gRNAs were previously shown by T7 endonuclease digestion assay to have mutagenesis efficiencies of 27.1% (*gsk3b*) or 52.7% (*fh*)	Saw increased knock-in efficiency (5.1% of sequences from injected embryos containing precise knock-in) when final guanine of PAM site was mutated than when the single base-pair substitution was located 5 bp from the PAM, within the gRNA target site (1% of sequences from injected embryos containing precise knock-in)	Not investigated. All templates were short (~50-nt) ssODNs	Non-target strand template gave higher precise knock-in efficiency for *fh* locus, but target strand template gave higher precise knock-in efficiency for *gsk3b* locus	Not tested. All templates had symmetrical homology arms.	Not tested	Not tested. All templates were single-stranded.	Not tested	0-8.3% precise knock-in efficiency (quantified as percentage of precisely repaired sequences identified in injected embryos). Germline transmission efficiency was not assessed.
	gsk3b				Not tested							

Table 6.2 (cont.)

Reference	Edited locus	Approach/ aim	Distance between cut site and desired mutation	gRNA efficiency (Cas9 cutting efficiency)	Mutation of PAM/ gRNA target sequence in repair template	Overall repair template length	Target vs non-target strand repair templates	Symmetrical vs asymmetrical repair templates	Chemical repair template modifications	Single stranded vs double stranded repair templates	Use of HDR-enhancing/ NHEJ-inhibiting drugs	Overall knock-in efficiency achieved
Irion et al. (2014)	*alb*	Test potential of different repair templates to correct loss-of-function mutation which abolishes pigment development	Not tested. Desired single base-pair substitution located >40 bp from the cut site	Effects on knock-in efficiency were not measured but gRNA/Cas9 were shown to induce defects in pigmentation in >95% of wild-type injected embryos	Effects on knock-in efficiency were not investigated, but several silent mutations were introduced into the target site	Long circular DNA templates (875 bp) containing gRNA target sites performed better (19.3-47.2% efficiency) than 206-3800 bp linear DNA templates (0-1.2% efficiency) or 986-3800 bp circular DNA (2.4-2.5% efficiency). Efficiencies calculated as percentage of injected embryos with pigment rescue at 5 dpf.	Not tested		Not tested	All tested templates were double-stranded	Not tested	Efficiency within injected embryos not measured. Germline transmission from ~10% of founders, to 3-24% of progeny
Prykhozhij et al. (2018)	*tp53* (1)	Test efficacy of different ssODN repair template designs to introduce missense mutations	Did not specifically investigate this, but observed higher efficiency knock-in at *cdh5* locus where desired mutations were located directly next to cut site (assessed by intensity of products amplified by AS-PCR, and highest germline transmission frequency to F1 (~21.4% of founders transmitting correct sequence))	Did not formally quantify cutting efficiency, but ensured effective gRNA choice by assessing mutagenesis indirectly using T7 endonuclease digestion or heteroduplex mobility assay	Inserted silent mutations in PAM/gRNA target sequence for all loci, but effects on editing efficiency were not investigated	Not tested. All templates were ~123-136-nt in length	Target strand asymmetrical repair templates increased precise knock-in efficiency compared to non-target strand symmetrical repair templates (assessed by sequencing DNA amplified from injected embryos – quantified as 2.72-fold increase in efficiency for *tp53* locus 1 and 9.5-fold increase for *tp53* locus 2).		Not tested	Only tested single-stranded templates	Not tested	0.57-2% maximum knock-in efficiency in injected embryos (measured as % of correct NGS reads). Germline transmission rates calculated as 0-21.4% of founders transmitting correct sequence, depending on locus/repair template used
	tp53 (2)											
	cdh5											
	lmna			Not tested					Improved knock-in efficiency by modifying repair template with phosphor-thiorate linkages (~1.4-fold increase in intensity of AS-PCR products)			

Table 6.2 (cont.)

Reference	Edited locus	Approach/ aim	Distance between cut site and desired mutation	gRNA efficiency (Cas9 cutting efficiency)	Mutation of PAM/ gRNA target sequence in repair template	Overall template length	Target vs non-target strand repair templates	Symmetrical vs asymmetrical templates	Chemical template modifications	Single stranded vs double stranded repair templates	Use of HDR-enhancing/ NHEJ-inhibiting drugs	Overall knock-in efficiency achieved
Zhang et al. (2018)	*ybx1*	Identify factors that may optimise knock-in of point mutations by CRISPR/Cas9 + HDR in zebrafish	Not tested, but desired edit was located at cut site	Did not specifically investigate effects on knock-in efficiency, but chose gRNA which induced mutagenesis with 80% efficiency (8/10 injected embryos found have target site mutagenesis by HRM analysis)	Did not test effects on knock-in efficiency, but inserted several silent mutations into gRNA target sequence in repair templates	~800 bp dsDNA template in plasmid performed better (induced correct mutagenesis in 15-16% of injected embryos) than ~800 bp linear dsDNA template (induced correct mutagenesis in 8-10% of injected embryos) and 50-nt ssODN (induced correct mutagenesis in 0-5% of injected embryos). Mutagenesis determined by qPCR analysis using HDR allele-specific primers.	Not tested		Not tested	Long double-stranded template (linear or plasmid) better than short single-stranded	Slight increase in knock-in efficiency (~1.6-fold compared to DMSO) using RS1 (HDR stimulator). ~3.5-fold increase in knock-in efficiency compared to DMSO using SCR7 (NHEJ inhibitor). Greatest increase in knock-in efficiency (~4.9-fold compared to DMSO) when SCR7 and RS1 were combined.	Knock-in efficiency within injected embryos was not measured. Up to 12% of founders injected with repair template and Cas9 protein found to transmit desired mutation to F1 progeny at rates between 8.3-33.3%).
Our data	*tcp1*	Introduce a precise missense mutation into the zebrafish genome	Not tested, but desired edit was located at PAM site	Did not investigate effects on knock-in efficiency, but demonstrated by HRM analysis that gRNA induces target site mutagenesis	Did not test effects on knock-in efficiency, but inserted several silent mutations into gRNA target sequence in repair template	Only tested short (65-nt) repair templates	Target strand repair template gave rise to greater proportion of founders transmitting the correctly repaired sequence through the germline than the non-target strand repair template.	Did not test	Not tested	Only tested single-stranded templates	Not tested	Knock-in efficiency within injected embryos was not measured. 2% of founders injected with the non-target strand repair template and 7.14% of founders injected with the target strand repair template found to transmit desired mutation to F1 progeny at a frequency of approximately 14.5%.

6.6.2.2 Factors influencing HDR-mediated knock-in efficiency by CRISPR/Cas9

Before considering whether these studies provide any consensus on the most efficient approach for achieving HDR-mediated knock-in of precise mutations by CRISPR/Cas9, it is important to note that knock-in efficiency has not been quantified and reported using the same method in every study. Some groups qualitatively assessed efficiency by recording the extent to which a visible phenotype (usually lack of pigment formation) was rescued by the knock-in (Bai et al., 2020; DiNapoli et al., 2020; Irion et al., 2014). For some studies, injected embryos were sequenced to measure how efficiently the correct mutation was introduced (Bai et al., 2020; Boel et al., 2018; Hwang et al., 2013a; Prykhozhij et al., 2018). Notably, this approach also provides a read-out of the accuracy of the approach, allowing incorrectly repaired alleles to be uncovered. Some, but not all, of the studies also reported knock-in efficiency in terms of germline transmission frequency (as we did for our approach) (Bai et al., 2020; Boel et al., 2018; Irion et al., 2014; Prykhozhij et al., 2018; Zhang et al., 2018).

Because a consistent measure of knock-in efficiency is lacking across these studies, it is difficult to draw direct comparisons between these approaches. However, these investigations, and the work we have presented here in relation to generating the *tcp1*^{P73L} mutant line, have highlighted some common features that appear to be key to success when using this approach, as discussed below.

6.6.2.2.1 Selection of an appropriate gRNA

A consistent feature of most of these successful approaches, including ours, is that the gRNA and HDR template are designed so that the Cas9 cut site and the desired edit are in close proximity to one another. The distance between the cut site and the desired mutation was shown to correlate with the efficiency of HDR-mediated knock-in in zebrafish (Boel et al., 2018; DiNapoli et al., 2020), with smaller distances generally resulting in greater knock-in efficiency. This is also consistent with findings from cell culture-based

experiments (Paquet et al., 2016). It can sometimes be challenging to achieve this, as it relies on the presence of a suitable gRNA target site close to the mutation of interest. For *Streptococcus pyogenes* Cas9, this is restricted by the requirement for a 5'-NGG-3' PAM; however, the identification of a number of Cas variants with alternative PAM requirements which have been shown to facilitate targeted gene editing in zebrafish (Feng et al., 2016; Fernandez et al., 2018; Kleinstiver et al., 2015; Liu et al., 2019; Moreno-Mateos et al., 2017) will help to address this problem. One Cas variant of particular interest in the context of HDR-mediated knock-in is Cas12a (Zetsche et al., 2015). Members of the Cas12a family of nucleases recognise 'T-rich' PAM sequences, thereby expanding the range of potential CRISPR target sites (Tóth et al., 2020). Moreover, Cas12a may facilitate more efficient knock-in by HDR in zebrafish than Cas9-based approaches (Moreno-Mateos et al., 2017). This is thought to be because Cas12a creates its double-stranded breaks downstream of the target site, and further away (18-23 nt) from the PAM than Cas9 (Moreno-Mateos et al., 2017). This reduces the chance of the PAM and gRNA target site from becoming destroyed by NHEJ-mediated indels, which may increase the likelihood of successful HDR, by allowing Cas12a to repeatedly re-cut the target site following unsuccessful HDR (Moreno-Mateos et al., 2017).

Another common feature of successful knock-in appears to be the selection of an efficient gRNA. Several groups reported that they assessed the cutting efficiency of their gRNA while designing their knock-in approach (Armstrong et al., 2016; Bai et al., 2020; Hwang et al., 2013a; Irion et al., 2014; Prykhozhij et al., 2018; Zhang et al., 2018) to ensure that the target site would be efficiently cleaved and thereby increase the chances of successful knock-in. There are several approaches that can be used to test gRNA efficiency experimentally. Many of these involve assessing heteroduplex formation in DNA from injected embryos by T7 endonuclease I digestion (Bai et al., 2020; Hwang et al., 2013a; Prykhozhij et al., 2018), heteroduplex mobility assays (Prykhozhij et al., 2018) or HRM analysis (Zhang et al., 2018). However, it is worth noting that some groups report efficiency

in terms of the proportion of injected embryos containing mutations (Irion et al., 2014; Zhang et al., 2018), whereas others reported the mutagenesis efficiency within individual injected embryos to determine what proportion of the cells were likely to contain CRISPR-induced mutations (Armstrong et al., 2016; Bai et al., 2020; Hwang et al., 2013a; Prykhozhij et al., 2018). In our investigation, we did not formally quantify the efficiency of our gRNA; however, we did demonstrate by HRM analysis that it could induce mutagenesis at the target site before we attempted to introduce the P73L mutation by HDR.

As we discussed above, the selection of an appropriate gRNA for CRISPR/Cas9-mediated knock-in is largely constrained by the requirement for the Cas9 cleavage site to be located close to the intended knock-in site. For some targets, however, there may be a choice of several gRNAs (as was the case for our *tcp1* target). In this case, one option would be to test a few gRNAs to determine which is most efficient; however, several gRNA design tools (such as the DeskGen design tool we used) are now able to provide rankings for gRNAs based on their predicted cutting efficiencies, which can negate the need to test numerous gRNAs for each target. As more information is gathered about the sequence requirements for efficient gRNAs (Chari et al., 2015; Doench et al., 2016; Hiranniramol et al., 2020; Wong et al., 2015; Xu et al., 2015), more advanced prediction and design tools continue to be developed (Concordet and Haeussler, 2018; Hiranniramol et al., 2020; Kaur et al., 2016; Montague et al., 2014; Wong et al., 2015; Xie et al., 2014). This will aid us in identifying the best gRNAs for targets of interest.

6.6.2.2.2 Designing an appropriate HDR template

Another factor that has been investigated extensively in relation to its impact on HDR-mediated knock-in efficiency by CRISPR/Cas9 is the design of the repair template used to introduce the mutation of interest. Among the successful approaches we have considered in Table 6.2, numerous repair template designs have been tested. These templates vary

widely in terms of the lengths of their homology arms; whether their homology arms are symmetrical or asymmetrical; whether they are single- or double-stranded, linear or circular; whether they have been chemically modified; and, in the case of single-stranded templates, whether they share homology with the strand of genomic DNA to which the gRNA binds (the target strand) or the opposite strand (the non-target strand). So far, there appears to be no single template design that has reliably performed better in all cases across all studies, suggesting that knock-in efficiency is likely to be partly dictated by the specific locus being edited. However, a recent study (Bai et al., 2020) aimed to systematically test various different template designs and generated results suggesting that long single-stranded DNA templates (zLOST) give rise to more efficient knock-in of precise mutations than several other template designs, and that they are able to do this across several different loci. Nonetheless, further investigations by other groups would be required to corroborate these findings to determine whether this type of template performs consistently better across a wider range of targets.

There have also been some reports suggesting that phosphorothioate modification of repair templates may increase knock-in efficiency by CRISPR/Cas9 in cell culture and murine models (Renaud et al., 2016). This approach has also been tested for introducing precise mutations into the zebrafish genome (Prykhozhij et al., 2018); however, there is currently limited evidence to support it as a consistent strategy for increasing knock-in efficiency in zebrafish.

A notable feature of most successful repair templates used for knock-in of precise mutations in zebrafish, including ours, is the introduction of silent mutations within the PAM or gRNA target site. These aim to prevent further target cleavage by Cas9 following a knock-in event. This strategy was previously shown to enhance knock-in rates in human cells (Paquet et al., 2016), and many groups have adopted it as part of their strategy for achieving successful HDR-mediated knock-in of precise mutations in zebrafish (Armstrong

et al., 2016; Bai et al., 2020; Boel et al., 2018; DiNapoli et al., 2020; Hwang et al., 2013a; Irion et al., 2014; Prykhozhij et al., 2018; Zhang et al., 2018).

6.6.2.2.3 Use of small molecules to enhance HDR-mediated knock-in efficiency

A number of small molecules that have been reported to either enhance HDR or inhibit components of the NHEJ repair pathway have also been tested for their potential utility in increasing CRISPR/Cas9-mediated knock-in efficiency in zebrafish (Aksoy et al., 2019; Bai et al., 2020; Boel et al., 2018; Zhang et al., 2018). However, the consensus on this strategy is mixed, with some groups reporting more efficient knock-in when using these compounds (Aksoy et al., 2019; Zhang et al., 2018), while others report that they have no effect on knock-in efficiency (Bai et al., 2020; Boel et al., 2018). It may be that the efficacy of these compounds for improving HDR efficiency is dependent on factors such as the specific target being edited, the type of mutation being introduced, or the design of the repair template; however, further investigations would be required to determine whether this is the case.

Importantly, although these studies have revealed some useful considerations that may increase the likelihood of success when designing an HDR-mediated knock-in strategy, the overall efficiency of HDR that has been achieved using these approaches remains very low (see final column, Table 6.2). This highlights the importance of developing efficient screening approaches to maximise the chances of identifying founders that are transmitting the mutation of interest through the germline (Prykhozhij et al., 2018), as we discussed in Chapter 3.

6.6.2.3 Emerging technologies for modelling precise disease-linked mutations in the zebrafish genome

Since many human genetic diseases, including the *TCP1*-linked disorder that we have investigated here, are caused by missense mutations, the specific goal of many zebrafish

knock-in experiments is to recreate a precise single base-pair substitution. As we have discussed above, the efficiency of introducing this type of mutation via CRISPR/Cas9 and HDR is currently limited, thereby reducing the scope for modelling these mutations on a large scale. However, it may become more efficient to develop this type of model with the use of more recently introduced CRISPR/Cas9-based technologies, such as base editors (Qin et al., 2018; Zhang et al., 2017b) and prime editing tools (Anzalone et al., 2019).

Base editing allows specific bases to be converted directly with the use of dCas9 conjugated to a deaminase enzyme (Gaudelli et al., 2017; Komor et al., 2016). Base editors can be used to introduce specific point mutations in zebrafish (Qin et al., 2018; Zhang et al., 2017b), and initial reports suggest that this may represent a more efficient strategy than HDR-based knock-in for introducing single point mutations (Zhang et al., 2017b). However, further investigations will be required to assess the efficacy of this approach to determine whether it represents a viable strategy for modelling human diseases on a large scale. Unpublished preliminary observations from our own laboratory suggest that base editing with a Cas9-cytidine deaminase base editor (obtained from Zhang et al.) is very inefficient, despite using gRNAs that appear to have high efficiency for generating indels using the prototypical Cas9 endonuclease. It may be that base editors have different sequence requirements for efficient gRNAs, as has previously been proposed for CRISPRi and dCas9 (Xu et al., 2015). A further limitation is that current base editors only allow selected base-pair substitutions to be made (specifically, C to T, T to C, A to G, and G to A), and editing is restricted to bases that lie within an optimal 'editing window' relative to the PAM, with other bases that fall within this window also being vulnerable to off-target editing (Gaudelli et al., 2017; Komor et al., 2016).

Prime editing is a more recently developed tool (Anzalone et al., 2019). This approach is based on the use of an RNA-guided Cas9-reverse transcriptase fusion protein, which 'rewrites' the DNA sequence at the chosen target site. In human cells, it has been shown to offer greater efficacy and accuracy than HDR-mediated knock-in (Anzalone et al., 2019).

It also offers many more possibilities in terms of the mutations that can be introduced compared with base editors (Anzalone et al., 2019). However, there are currently no reports of prime editing having successfully been used to introduce precise mutations into the zebrafish genome. Further studies will therefore be required to assess whether this represents an alternative, more efficient strategy for introducing precise disease-linked mutations into the zebrafish genome.

6.7 Conclusions

In summary, the goal of this thesis was to develop and use novel zebrafish models to test two key hypotheses: a) that the *TCP1*^{P70L} mutation identified in three siblings with a rare neurological disease is responsible for their phenotypes, and b) that *TCP1* plays an important role in the tissues affected by disease in these patients (the cerebellum and retina).

Based on the data we have presented here, we currently lack sufficient evidence to conclude that the patients' phenotypes are definitely caused by the *TCP1*^{P70L} mutation. However, our findings relating to the phenotypic consequences of loss of *tcp1* in the zebrafish, combined with previous observations on the phenotypes associated with loss of TRiC/CCT function in other models, have provided some experimental evidence to support this hypothesis.

In relation to our second hypothesis, we found that, in zebrafish, *tcp1* does appear to play an important role in tissues that are relevant to human disease, though further investigations will be required to decipher precisely how *tcp1* contributes to the development and/or maintenance of these tissues.

In a broader context, we have also illustrated that it is technically feasible to model human disease-linked point mutations in the zebrafish by CRISPR/Cas9 and HDR with the use of short ssODN repair templates, in agreement with previous reports. However, as we have discussed, HDR-mediated knock-in remains an inefficient approach for modelling precise

disease-linked mutations. As such, it is currently unlikely to represent a feasible strategy for modelling rare genetic diseases in the zebrafish on a large scale, without a large and dedicated team of researchers. Nonetheless, the efficiency of generating point mutant zebrafish models using CRISPR/Cas9 and HDR may improve with further research into the requirements for efficient HDR template design. Moreover, as more recently introduced genome editing techniques, such as base editing and prime editing, are further developed and optimised, these may expand the tools available for modelling precise disease-linked mutations in zebrafish in the future.

References

Adamson, K.I., Sheridan, E., Grierson, A.J., 2018. Use of zebrafish models to investigate rare human disease. J Med Genet 55, 641–654. doi:10.1136/jmedgenet-2018-105358

Adzhubei, I.A., Schmidt, S., Peshkin, L., Ramensky, V.E., Gerasimova, A., Bork, P., Kondrashov, A.S., Sunyaev, S.R., 2010. A method and server for predicting damaging missense mutations. Nat Methods 7, 248–249. doi:10.1038/nmeth0410-248

Aguilar, A., Meunier, A., Strehl, L., Martinovic, J., Bonniere, M., Attie-Bitach, T., Encha-Razavi, F., Spassky, N., 2012. Analysis of human samples reveals impaired SHH-dependent cerebellar development in Joubert syndrome/Meckel syndrome. Proc Natl Acad Sci U S A 109, 16951–16956. doi:10.1073/pnas.1201408109

Akizu, N., Cantagrel, V., Zaki, M.S., Al-Gazali, L., Wang, X., Rosti, R.O., Dikoglu, E., Gelot, A.B., Rosti, B., Vaux, K.K., Scott, E.M., Silhavy, J.L., Schroth, J., Copeland, B., Schaffer, A.E., Gordts, P.L.S.M., Esko, J.D., Buschman, M.D., Field, S.J., Napolitano, G., Abdel-Salam, G.M., Ozgul, R.K., Sagıroglu, M.S., Azam, M., Ismail, S., Aglan, M., Selim, L., Mahmoud, I.G., Abdel-Hadi, S., Badawy, A. El, Sadek, A.A., Mojahedi, F., Kayserili, H., Masri, A., Bastaki, L., Temtamy, S., Müller, U., Desguerre, I., Casanova, J.-L., Dursun, A., Gunel, M., Gabriel, S.B., de Lonlay, P., Gleeson, J.G., 2015. Biallelic mutations in SNX14 cause a syndromic form of cerebellar atrophy and lysosome-autophagosome dysfunction. Nat Genet 47, 528–34. doi:10.1038/ng.3256

Aksoy, Y.A., Nguyen, D.T., Chow, S., Chung, R.S., Guillemin, G.J., Cole, N.J., Hesselson, D., 2019. Chemical reprogramming enhances homology-directed genome editing in zebrafish embryos. Commun Biol 2, 1–9. doi:10.1038/s42003-019-0444-0

Almeida, R., Lyons, D., 2016. Oligodendrocyte Development in the Absence of Their Target Axons In Vivo. PLoS One 11, e0164432. doi:10.1371/journal.pone.0164432

Amini, R., Rocha-Martins, M., Norden, C., 2018. Neuronal migration and lamination in the vertebrate retina. Front Neurosci. doi:10.3389/fnins.2017.00742

Anderson, J.L., Mulligan, T.S., Shen, M.C., Wang, H., Scahill, C.M., Tan, F.J., Du, S.J., Busch-Nentwich, E.M., Farber, S.A., 2017. mRNA processing in mutant zebrafish lines generated by chemical and CRISPR-mediated mutagenesis produces unexpected transcripts that escape nonsense-mediated decay. PLoS Genet 13. doi:10.1371/journal.pgen.1007105

Angelis, A., Tordrup, D., Kanavos, P., 2015. Socio-economic burden of rare diseases: A systematic review of cost of illness evidence. Health Policy (New York) 119, 964–979. doi:10.1016/j.healthpol.2014.12.016

Angueyra, J.M., Kindt, K.S., 2018. Leveraging zebrafish to study retinal degenerations. Front Cell Dev Biol. doi:10.3389/fcell.2018.00110

Anzalone, A. V., Randolph, P.B., Davis, J.R., Sousa, A.A., Koblan, L.W., Levy, J.M., Chen, P.J., Wilson, C., Newby, G.A., Raguram, A., Liu, D.R., 2019. Search-and-replace genome editing without double-strand breaks or donor DNA. Nature 576, 149–157. doi:10.1038/s41586-019-1711-4

Arai, Y., Maeda, A., Hirami, Y., Ishigami, C., Kosugi, S., Mandai, M., Kurimoto, Y., Takahashi, M., 2015. Retinitis Pigmentosa with EYS Mutations Is the Most Prevalent Inherited Retinal Dystrophy in Japanese Populations. J Ophthalmol 2015, 1–10. doi:10.1155/2015/819760

Ardiles, A.O., Grabrucker, A.M., Scholl, F.G., Rudenko, G., Borsello, T., 2017. Molecular and cellular mechanisms of synaptopathies. Neural Plast. doi:10.1155/2017/2643943

Armstrong, G.A.B., Liao, M., You, Z., Lissouba, A., Chen, B.E., Drapeau, P., 2016. Homology Directed Knockin of Point Mutations in the Zebrafish tardbp and fus Genes in ALS Using the CRISPR/Cas9 System. PLoS One 11, e0150188. doi:10.1371/journal.pone.0150188

Asano, T., Kawamura, S., Tachibanaki, S., 2019. Transducin activates cGMP phosphodiesterase by trapping inhibitory γ subunit freed reversibly from the catalytic subunit in solution. Sci Rep 9. doi:10.1038/s41598-019-43675-9

Auer, T.O., Duroure, K., De Cian, A., Concordet, J.P., Del Bene, F., 2014. Highly efficient CRISPR/Cas9-mediated knock-in in zebrafish by homology-independent DNA repair. Genome Res 24, 142–153. doi:10.1101/gr.161638.113

Avanesov, A., Malicki, J., 2010. Analysis of the retina in the zebrafish model, Methods in Cell Biology. doi:10.1016/B978-0-12-384892-5.00006-2

Avdesh, A., Martin-Iverson, M.T., Mondal, A., Chen, M., Askraba, S., Morgan, N., Lardelli, M., Groth, D.M., Verdile, G., Martins, R.N., 2012. Evaluation of color preference in zebrafish for learning and memory. J Alzheimer's Dis 28, 459–469. doi:10.3233/JAD-2011-110704

Bae, Y.K., Kani, S., Shimizu, T., Tanabe, K., Nojima, H., Kimura, Y., Higashijima, S. ichi, Hibi, M., 2009. Anatomy of zebrafish cerebellum and screen for mutations affecting its development. Dev Biol 330, 406–426. doi:10.1016/j.ydbio.2009.04.013

Bai, H., Liu, L., An, K., Lu, X., Harrison, M., Zhao, Y., Yan, R., Lu, Z., Li, S., Lin, S., Liang, F., Qin, W., 2020. CRISPR/Cas9-mediated precise genome modification by a long ssDNA template in zebrafish. BMC Genomics 21, 67. doi:10.1186/s12864-020-6493-4

Bally-Cuif, L., Vernier, P., 2010. Organization and physiology of the zebrafish nervous system, in: Fish Physiology. pp. 25–80. doi:10.1016/S1546-5098(10)02902-X

Basnet, R.M., Zizioli, D., Taweedet, S., Finazzi, D., Memo, M., 2019. Zebrafish larvae as a behavioral model in neuropharmacology. Biomedicines. doi:10.3390/BIOMEDICINES7010023

Beaulieu, C.L., Majewski, J., Schwartzentruber, J., Samuels, M.E., Fernandez, B.A., Bernier, F.P., Brudno, M., Knoppers, B., Marcadier, J., Dyment, D., Adam, S., Bulman, D.E., Jones, S.J.M., Avard, D., Nguyen, M.T., Rousseau, F., Marshall, C., Wintle, R.F., Shen, Y., Scherer, S.W., FORGE Canada Consortium, F.C., Friedman, J.M., Michaud, J.L., Boycott, K.M., 2014. FORGE Canada Consortium: outcomes of a 2-year national rare-disease gene-discovery project. Am J Hum Genet 94, 809–17. doi:10.1016/j.ajhg.2014.05.003

Behrends, C., Langer, C.A., Boteva, R., Böttcher, U.M., Stemp, M.J., Schaffar, G., Rao, B.V., Giese, A., Kretzschmar, H., Siegers, K., Hartl, F.U., 2006. Chaperonin TRiC Promotes the Assembly of polyQ Expansion Proteins into Nontoxic Oligomers. Mol Cell 23, 887–897. doi:10.1016/j.molcel.2006.08.017

Ben-Arie, N., Bellen, H.J., Armstrong, D.L., McCall, A.E., Gordadze, P.R., Guo, Q., Matzuk, M.M., Zoghbi, H.Y., 1997. Math1 is essential for genesis of cerebellar granule neurons. Nature 390, 169–172. doi:10.1038/36579

Bendikov-Bar, I., Maor, G., Filocamo, M., Horowitz, M., 2013. Ambroxol as a pharmacological chaperone for mutant glucocerebrosidase. Blood Cells, Mol Dis 50, 141–145. doi:10.1016/j.bcmd.2012.10.007

Bercier, V., Hubbard, J.M., Fidelin, K., Duroure, K., Auer, T.O., Revenu, C., Wyart, C., Del

Bene, F., 2019. Dynactin1 depletion leads to neuromuscular synapse instability and functional abnormalities. Mol Neurodegener 14, 1–22. doi:10.1186/s13024-019-0327-3

Berezniuk, I., Vu, H.T., Lyons, P.J., Sironi, J.J., Xiao, H., Burd, B., Setou, M., Angeletti, R.H., Ikegami, K., Fricker, L.D., 2012. Cytosolic carboxypeptidase 1 is involved in processing ??- and ??-tubulin. J Biol Chem 287, 6503–6517. doi:10.1074/jbc.M111.309138

Berger, J., Berger, S., Li, M., Jacoby, A.S., Arner, A., Bavi, N., Stewart, A.G., Currie, P.D., 2018. In Vivo Function of the Chaperonin TRiC in α-Actin Folding during Sarcomere Assembly. Cell Rep. doi:10.1016/j.celrep.2017.12.069

Bigotti, M.G., Clarke, A.R., 2008. Chaperonins: The hunt for the Group II mechanism. Arch Biochem Biophys. doi:10.1016/j.abb.2008.03.015

Bittles, A., 2008. Consanguinity and its relevance to clinical genetics. Clin Genet 60, 89–98. doi:10.1034/j.1399-0004.2001.600201.x

Boel, A., De Saffel, H., Steyaert, W., Callewaert, B., De Paepe, A., Coucke, P.J., Willaert, A., 2018. CRISPR/Cas9-mediated homology-directed repair by ssODNs in zebrafish induces complex mutational patterns resulting from genomic integration of repair-template fragments. DMM Dis Model Mech 11. doi:10.1242/dmm.035352

Booth, C.R., Meyer, A.S., Cong, Y., Topf, M., Sali, A., Ludtke, S.J., Chiu, W., Frydman, J., 2008. Mechanism of lid closure in the eukaryotic chaperonin TRiC/CCT. Nat Struct Mol Biol 15, 746–753. doi:10.1038/nsmb.1436

Bouhouche, A., Benomar, A., Bouslam, N., Chkili, T., Yahyaoui, M., 2006. Mutation in the epsilon subunit of the cytosolic chaperonin-containing t-complex peptide-1 (Cct5) gene causes autosomal recessive mutilating sensory neuropathy with spastic paraplegia. J Med Genet 43, 441–443. doi:10.1136/jmg.2005.039230

Bowie, E., Goetz, S.C., 2020. Ttbk2 and primary cilia are essential for the connectivity and survival of cerebellar purkinje neurons. Elife 9. doi:10.7554/eLife.51166

Boycott, K.M., Vanstone, M.R., Bulman, D.E., MacKenzie, A.E., 2013. Rare-disease genetics in the era of next-generation sequencing: discovery to translation. Nat Rev Genet 14, 681–691. doi:10.1038/nrg3555

Brady, R.O., Kanfer, J.N., Bradley, R.M., Shapiro, D., 1966. Demonstration of a deficiency of glucocerebroside-cleaving enzyme in Gaucher's disease. J Clin Invest 45, 1112–5. doi:10.1172/JCI105417

Bras, J., Alonso, I., Barbot, C., Costa, M.M., Darwent, L., Orme, T., Sequeiros, J., Hardy, J., Coutinho, P., Guerreiro, R., 2015. Mutations in PNKP cause recessive ataxia with oculomotor apraxia type 4. Am J Hum Genet 96, 474–479. doi:10.1016/j.ajhg.2015.01.005

Brehme, M., Voisine, C., Rolland, T., Wachi, S., Soper, J.H., Zhu, Y., Orton, K., Villella, A., Garza, D., Vidal, M., Ge, H., Morimoto, R.I., 2014. A chaperome subnetwork safeguards proteostasis in aging and neurodegenerative disease. Cell Rep 9, 1135–1150. doi:10.1016/j.celrep.2014.09.042

Briscoe, S.D., Ragsdale, C.W., 2019. Evolution of the Chordate Telencephalon. Curr Biol. doi:10.1016/j.cub.2019.05.026

Brockerhoff, S.E., Hurley, J.B., Niemi, G.A., Dowling, J.E., 1997. A new form of inherited red-blindness identified in zebrafish. J Neurosci 17, 4236–4242. doi:10.1523/jneurosci.17-11-04236.1997

Bulman, M.P., Kusumi, K., Frayling, T.M., McKeown, C., Garrett, C., Lander, E.S., Krumlauf, R., Hattersley, A.T., Ellard, S., Turnpenny, P.D., 2000. Mutations in the human Delta homologue, DLL3, cause axial skeletal defects in spondylocostal dysostosis. Nat Genet 24, 438–441. doi:10.1038/74307

Burns, D.T., Donkervoort, S., Müller, J.S., Knierim, E., Bharucha-Goebel, D., Faqeih, E.A., Bell, S.K., AlFaifi, A.Y., Monies, D., Millan, F., Retterer, K., Dyack, S., MacKay, S., Morales-Gonzalez, S., Giunta, M., Munro, B., Hudson, G., Scavina, M., Baker, L., Massini, T.C., Lek, M., Hu, Y., Ezzo, D., AlKuraya, F.S., Kang, P.B., Griffin, H., Foley, A.R., Schuelke, M., Horvath, R., Bönnemann, C.G., 2018. Variants in EXOSC9 Disrupt the RNA Exosome and Result in Cerebellar Atrophy with Spinal Motor Neuronopathy. Am J Hum Genet 102, 858–873. doi:10.1016/j.ajhg.2018.03.011

Butts, T., Green, M.J., Wingate, R.J.T., 2014. Development of the cerebellum: Simple steps to make a 'little brain.' Dev. doi:10.1242/dev.106559

Camasses, A., Bogdanova, A., Shevchenko, A., Zachariae, W., 2003. The CCT chaperonin promotes activation of the anaphase-promoting complex through the generation of functional Cdc20. Mol Cell 12, 87–100. doi:10.1016/S1097-2765(03)00244-2

Chaplin, N., Tendeng, C., Wingate, R.J.T., 2010. Absence of an external germinal layer in zebrafish and shark reveals a distinct, anamniote ground plan of cerebellum development. J Neurosci 30, 3048–3057. doi:10.1523/JNEUROSCI.6201-09.2010

Chapman, A.L., Bennett, E.J., Ramesh, T.M., De Vos, K.J., Grierson, A.J., 2013. Axonal Transport Defects in a Mitofusin 2 Loss of Function Model of Charcot-Marie-Tooth Disease in Zebrafish. PLoS One 8, e67276. doi:10.1371/journal.pone.0067276

Chari, R., Mali, P., Moosburner, M., Church, G.M., 2015. Unraveling CRISPR-Cas9 genome engineering parameters via a library-on-library approach. Nat Methods 12, 823–826. doi:10.1038/nmeth.3473

Chen, J., Patel, R., Friedman, T.C., Jones, K.S., 2010. The Behavioral and Pharmacological Actions of NMDA Receptor Antagonism are Conserved in Zebrafish Larvae. Int J Comp Psychol 23, 82–90.

Chiyonobu, T., Inoue, N., Morimoto, M., Kinoshita, T., Murakami, Y., 2014. Glycosylphosphatidylinositol (GPI) anchor deficiency caused by mutations in PIGW is associated with West syndrome and hyperphosphatasia with mental retardation syndrome. J Med Genet 51, 203–207. doi:10.1136/jmedgenet-2013-102156

Chrispell, J.D., Rebrik, T.I., Weiss, E.R., 2015. Electroretinogram analysis of the visual response in zebrafish larvae. J Vis Exp 2015. doi:10.3791/52662

Chukhrova, A.L., Akimova, I.A., Shchagina, O.A., Kadnikova, V.A., Ryzhkova, O.P., Polyakov, A. V., 2019. A new case of infantile-onset hereditary spastic paraplegia with complicated phenotype (<scp>SPG</scp> 61) in a consanguineous Russian family. Eur J Neurol 26, e61–e62. doi:10.1111/ene.13880

Cnossen, W.R., Te Morsche, R.H.M., Hoischen, A., Gilissen, C., Chrispijn, M., Venselaar, H., Mehdi, S., Bergmann, C., Veltman, J.A., Drenth, J.P.H., 2014. Whole-exome sequencing reveals LRP5 mutations and canonical Wnt signaling associated with hepatic cystogenesis. PNAS 111, 5343–5348. doi:10.1073/pnas.1309438111

Colledge, W.H., Abella, B.S., Southern, K.W., Ratcliff, R., Jiang, C., Cheng, S.H., MacVinish, L.J., Anderson, J.R., Cuthbert, A.W., Evans, M.J., 1995. Generation and characterization of a delta F508 cystic fibrosis mouse model. Nat Genet 10, 445–52. doi:10.1038/ng0895-445

Concordet, J.-P., Haeussler, M., 2018. CRISPOR: intuitive guide selection for CRISPR/Cas9 genome editing experiments and screens. Nucleic Acids Res 46, W242–W245. doi:10.1093/nar/gky354

Cong, L., Ran, F.A., Cox, D., Lin, S., Barretto, R., Habib, N., Hsu, P.D., Wu, X., Jiang, W., Marraffini, L.A., Zhang, F., 2013. Multiplex genome engineering using CRISPR/Cas systems. Science (80-) 339, 819–823. doi:10.1126/science.1231143

Corrales, J.M.D., Blaess, S., Mahoney, E.M., Joyner, A.L., 2006. The level of sonic hedgehog signaling regulates the complexity of cerebellar foliation. Development 133, 1811–1821. doi:10.1242/dev.02351

Dawkins, H.J., Draghia-Akli, R., Lasko, P., Lau, L.P., Jonker, A.H., Cutillo, C.M., Rath, A., Boycott, K.M., Baynam, G., Lochmüller, H., Kaufmann, P., Cam, Y. Le, Hivert, V., Austin, C.P., International Rare Diseases Research Consortium (IRDiRC), 2017. Progress in rare diseases research 2010-2016: an IRDiRC perspective. Clin Transl Sci. doi:10.1111/cts.12501

Deciphering Developmental Disorders Study, 2017. Prevalence and architecture of de novo mutations in developmental disorders. Nature 542, 433–438. doi:10.1038/nature21062

Deciphering Developmental Disorders Study, 2015. Large-scale discovery of novel genetic causes of developmental disorders. Nature 519, 223–8. doi:10.1038/nature14135

Dillon, C., Goda, Y., 2005. The Actin Cytoskeleton: Integrating Form and Function at the Synapse. Annu Rev Neurosci 28, 25–55. doi:10.1146/annurev.neuro.28.061604.135757

DiNapoli, S.E., Martinez-Mcfaline, R., Gribbin, C.K., Wrighton, P.J., Balgobin, C.A., Nelson, I., Leonard, A., Maskin, C.R., Shwartz, A., Quenzer, E.D., Mailhiot, D., Kao, C., Mcconnell, S.C., De Jong, J.L.O., Goessling, W., Houvras, Y., 2020. OUP accepted manuscript. Nucleic Acids Res. doi:10.1093/nar/gkaa085

Doench, J.G., Fusi, N., Sullender, M., Hegde, M., Vaimberg, E.W., Donovan, K.F., Smith, I., Tothova, Z., Wilen, C., Orchard, R., Virgin, H.W., Listgarten, J., Root, D.E., 2016. Optimized sgRNA design to maximize activity and minimize off-target effects of CRISPR-Cas9. Nat Biotechnol 34, 184–191. doi:10.1038/nbt.3437

Dona, M., Slijkerman, R., Lerner, K., Broekman, S., Wegner, J., Howat, T., Peters, T., Hetterschijt, L., Boon, N., de Vrieze, E., Sorusch, N., Wolfrum, U., Kremer, H., Neuhauss, S., Zang, J., Kamermans, M., Westerfield, M., Phillips, J., van Wijk, E., 2018. Usherin defects lead to early-onset retinal dysfunction in zebrafish. Exp Eye Res 173, 148–159. doi:10.1016/j.exer.2018.05.015

Dow, L.E., Lowe, S.W., 2012. Life in the Fast Lane: Mammalian Disease Models in the Genomics Era. Cell 148, 1099–1109. doi:10.1016/j.cell.2012.02.023

Doyon, Y., McCammon, J.M., Miller, J.C., Faraji, F., Ngo, C., Katibah, G.E., Amora, R., Hocking, T.D., Zhang, L., Rebar, E.J., Gregory, P.D., Urnov, F.D., Amacher, S.L., 2008. Heritable targeted gene disruption in zebrafish using designed zinc-finger nucleases. Nat Biotechnol 26, 702–708. doi:10.1038/nbt1409

Driever, W., Solnica-Krezel, L., Schier, A.F., Neuhauss, S.C.F., Malicki, J., Stemple, D.L., Stainier, D.Y.R., Zwartkruis, F., Abdelilah, S., Rangini, Z., Belak, J., Boggs, C., 1996. A genetic screen for mutations affecting embryogenesis in zebrafish. Development 123, 37–46. doi:10.5167/uzh-215

Driever, W., Stemple, D., Schier, A., Solnica-Krezel, L., 1994. Zebrafish: genetic tools for studying vertebrate development. Trends Genet. doi:10.1016/0168-9525(94)90091-4

DuVal, M., Allison, Wt., 2017. Impacts of the retinal environment and photoreceptor type on functional regeneration. Neural Regen Res 12, 376. doi:10.4103/1673-5374.202930

Ebdali, S., Hashemi, B., Hashemi, H., Jafarzadehpur, E., Asgari, S., 2018. Time and frequency components of ERG responses in retinitis pigmentosa. Int Ophthalmol 38, 2435–2444. doi:10.1007/s10792-017-0748-3

Erzurumluoglu, A.M., Shihab, H.A., Rodriguez, S., Gaunt, T.R., Day, I.N.M., 2016. Importance of Genetic Studies in Consanguineous Populations for the Characterization of Novel Human Gene Functions. Ann Hum Genet 80, 187–196. doi:10.1111/ahg.12150

Etard, C., Armant, O., Roostalu, U., Gourain, V., Ferg, M., Strähle, U., 2015. Loss of function of myosin chaperones triggers Hsf1-mediated transcriptional response in skeletal muscle cells. Genome Biol 16, 267. doi:10.1186/s13059-015-0825-8

EURORDIS, 2010. WHY Research on Rare Diseases. [WWW Document]. www.eurordis.org. URL http://www.eurordis.org/sites/default/files/publications/why_rare_disease_research.pdf (accessed 1.23.18).

EURORDIS, 2007. What is a rare disease? [WWW Document]. www.eurordis.org. URL http://www.eurordis.org/sites/default/files/publications/Fact_Sheet_RD.pdf (accessed 2.7.18).

EURORDIS, 2005. Rare diseases: understanding this Public Health Priority [WWW Document]. www.eurordis.org. URL http://www.eurordis.org/IMG/pdf/princeps_document-EN.pdf (accessed 2.7.18).

Faucherre, A., Nargeot, J., Mangoni, M.E., Jopling, C., 2013. piezo2b regulates vertebrate light touch response. J Neurosci 33, 17089–17094. doi:10.1523/JNEUROSCI.0522-13.2013

Feng, Y., Chen, C., Han, Y., Chen, Z., Lu, X., Liang, F., Li, S., Qin, W., Lin, S., 2016. Expanding CRISPR/Cas9 genome editing capacity in Zebrafish using SaCas9. G3 Genes, Genomes, Genet 6, 2517–2521. doi:10.1534/g3.116.031914

Fernandes, A.M., Fero, K., Arrenberg, A.B., Bergeron, S.A., Driever, W., Burgess, H.A., 2012. Deep brain photoreceptors control light-seeking behavior in zebrafish larvae. Curr Biol 22, 2042–2047. doi:10.1016/j.cub.2012.08.016

Fernandez, J.P., Vejnar, C.E., Giraldez, A.J., Rouet, R., Moreno-Mateos, M.A., 2018. Optimized CRISPR-Cpf1 system for genome editing in zebrafish. Methods 150, 11–18. doi:10.1016/j.ymeth.2018.06.014

Gagliardi, M., Strazzullo, M., Matarazzo, M.R., 2018. DNMT3B functions: Novel insights from human disease. Front Cell Dev Biol. doi:10.3389/fcell.2018.00140

Gahl, W.A., Mulvihill, J.J., Toro, C., Markello, T.C., Wise, A.L., Ramoni, R.B., Adams, D.R., Tifft, C.J., 2016. The NIH Undiagnosed Diseases Program and Network: Applications to modern medicine. Mol Genet Metab. doi:10.1016/j.ymgme.2016.01.007

Gallina, I., Colding, C., Henriksen, P., Beli, P., Nakamura, K., Offman, J., Mathiasen, D.P., Silva, S., Hoffmann, E., Groth, A., Choudhary, C., Lisby, M., 2015. Cmr1/WDR76 defines a nuclear genotoxic stress body linking genome integrity and protein quality

control. Nat Commun 6, 1–16. doi:10.1038/ncomms7533

Gama Sosa, M.A., De Gasperi, R., Elder, G.A., 2012. Modeling human neurodegenerative diseases in transgenic systems. Hum Genet 131, 535–563. doi:10.1007/s00439-011-1119-1

Gasic, I., Boswell, S.A., Mitchison, T.J., 2019. Tubulin mRNA stability is sensitive to change in microtubule dynamics caused by multiple physiological and toxic cues. PLoS Biol 17. doi:10.1371/journal.pbio.3000225

Gaudelli, N.M., Komor, A.C., Rees, H.A., Packer, M.S., Badran, A.H., Bryson, D.I., Liu, D.R., 2017. Programmable base editing of A•T to G•C in genomic DNA without DNA cleavage. Nature. doi:10.1038/nature24644

Ge, Y., Kang, Y., Cassidy, R.M., Moon, K.M., Lewis, R., Wong, R.O.L., Foster, L.J., Craig, A.M., 2018. Clptm1 Limits Forward Trafficking of GABAA Receptors to Scale Inhibitory Synaptic Strength. Neuron 97, 596-610.e8. doi:10.1016/j.neuron.2017.12.038

Gibbs, H.C., Chang-Gonzalez, A., Hwang, W., Yeh, A.T., Lekven, A.C., 2017. Midbrain-hindbrain boundary morphogenesis: At the intersection of wnt and Fgf signaling. Front Neuroanat. doi:10.3389/fnana.2017.00064

Gilbert, L.A., Larson, M.H., Morsut, L., Liu, Z., Brar, G.A., Torres, S.E., Stern-Ginossar, N., Brandman, O., Whitehead, E.H., Doudna, J.A., Lim, W.A., Weissman, J.S., Qi, L.S., 2013. CRISPR-Mediated Modular RNA-Guided Regulation of Transcription in Eukaryotes. Cell 154, 442–451. doi:10.1016/j.cell.2013.06.044

Gilmore, J.M., Sardiu, M.E., Groppe, B.D., Thornton, J.L., Liu, X., Dayebgadoh, G., Banks, C.A., Slaughter, B.D., Unruh, J.R., Workman, J.L., Florens, L., Washburn, M.P., 2016. WDR76 Co-Localizes with heterochromatin related proteins and rapidly responds to DNA damage. PLoS One 11, e0155492. doi:10.1371/journal.pone.0155492

Glasauer, S.M.K., Neuhauss, S.C.F., 2014. Whole-genome duplication in teleost fishes and its evolutionary consequences. Mol Genet Genomics. doi:10.1007/s00438-014-0889-2

Goker-Alpan, O., Schiffmann, R., LaMarca, M.E., Nussbaum, R.L., McInerney-Leo, A., Sidransky, E., 2004. Parkinsonism among Gaucher disease carriers. J Med Genet 41, 937–940. doi:10.1136/jmg.2004.024455

Grunwald, D.J., Streisinger, G., 1992. Induction of Recessive Lethal and Specific Locus Mutations in the Zebrafish with Ethyl Nitrosourea. Genet Res 59, 103–116. doi:10.1017/S0016672300030317

Guerrero, C., Milenković, T., Pržulj, N., Kaiser, P., Huang, L., 2008. Characterization of the proteasome interaction network using a QTAX-based tag-team strategy and protein interaction network analysis. Proc Natl Acad Sci U S A 105, 13333–13338. doi:10.1073/pnas.0801870105

Gui, H., Schriemer, D., Cheng, W.W., Chauhan, R.K., Antiňolo, G., Berrios, C., Bleda, M., Brooks, A.S., Brouwer, R.W.W., Burns, A.J., Cherny, S.S., Dopazo, J., Eggen, B.J.L., Griseri, P., Jalloh, B., Le, T.-L., Lui, V.C.H., Luzón-Toro, B., Matera, I., Ngan, E.S.W., Pelet, A., Ruiz-Ferrer, M., Sham, P.C., Shepherd, I.T., So, M.-T., Sribudiani, Y., Tang, C.S.M., van den Hout, M.C.G.N., van der Linde, H.C., van Ham, T.J., van IJcken, W.F.J., Verheij, J.B.G.M., Amiel, J., Borrego, S., Ceccherini, I., Chakravarti, A., Lyonnet, S., Tam, P.K.H., Garcia-Barceló, M.-M., Hofstra, R.M.W., 2017. Whole exome sequencing coupled with unbiased functional analysis reveals new Hirschsprung disease genes. Genome Biol 18, 48. doi:10.1186/s13059-017-1174-6

Haag, N., Schwintzer, L., Ahuja, R., Koch, N., Grimm, J., Heuer, H., Qualmann, B., Kessels, M.M., 2012. The actin nucleator Cobl is crucial for Purkinje cell development and works in close conjunction with the F-actin binding protein Abp1. J Neurosci 32, 17842–56. doi:10.1523/JNEUROSCI.0843-12.2012

Haffter, P., Granato, M., Brand, M., Mullins, M.C., Hammerschmidt, M., Kane, D.A., Odenthal, J., Van Eeden, F.J.M., Jiang, Y.J., Heisenberg, C.P., Kelsh, R.N., Furutani-Seiki, M., Vogelsang, E., Beuchle, D., Schach, U., Fabian, C., Nüsslein-Volhard, C., 1996. The identification of genes with unique and essential functions in the development of the zebrafish, Danio rerio. Development 123, 1–36.

Haldipur, P., Bharti, U., Govindan, S., Sarkar, C., Iyengar, S., Gressens, P., Mani, S., 2012. Expression of sonic hedgehog during cell proliferation in the human cerebellum. Stem Cells Dev 21, 1059–1068. doi:10.1089/scd.2011.0206

Hamamy, H., 2012. Consanguineous marriages preconception consultation in primary health care settings. J Community Genet. doi:10.1007/s12687-011-0072-y

Hamling, K.R., Tobias, Z.J.C., Weissman, T.A., 2015. Mapping the development of cerebellar Purkinje cells in zebrafish. Dev Neurobiol 75, 1174–1188. doi:10.1002/dneu.22275

Harada, A., Takeuchi, K.I., Dohmae, N., Takio, K., Uenaka, T., Aoki, J., Inoue, K., Umeda, M., 1999. A monoclonal antibody, 3A10, recognizes a specific amino acid sequence present on a series of developmentally expressed brain proteins. J Biochem 125, 443–448. doi:10.1093/oxfordjournals.jbchem.a022306

Hari, M., Wang, Y., Veeraraghavan, S., Cabral, F., 2003. Mutations in α- and β-tubulin that stabilize microtubules and confer resistance to colcemid and vinblastine. Mol Cancer Ther 2, 597–605.

Hartl, F.U., Bracher, A., Hayer-Hartl, M., 2011. Molecular chaperones in protein folding and proteostasis. Nature 475, 324–332. doi:10.1038/nature10317

Hashimoto, M., Hibi, M., 2012. Development and evolution of cerebellar neural circuits. Dev Growth Differ. doi:10.1111/j.1440-169X.2012.01348.x

Heap, L.A., Goh, C.C., Kassahn, K.S., Scott, E.K., 2013. Cerebellar Output in Zebrafish: An Analysis of Spatial Patterns and Topography in Eurydendroid Cell Projections. Front Neural Circuits 7. doi:10.3389/fncir.2013.00053

Hecht, M., Bromberg, Y., Rost, B., 2015. Better prediction of functional effects for sequence variants. BMC Genomics 16. doi:10.1186/1471-2164-16-S8-S1

Heidari, A., Tongsook, C., Najafipour, R., Musante, L., Vasli, N., Garshasbi, M., Hu, H., Mittal, K., McNaughton, A.J.M., Sritharan, K., Hudson, M., Stehr, H., Talebi, S., Moradi, M., Darvish, H., Rafiq, M.A., Mozhdehipanah, H., Rashidinejad, A., Samiei, S., Ghadami, M., Windpassinger, C., Gillessen-Kaesbach, G., Tzschach, A., Ahmed, I., Mikhailov, A., James Stavropoulos, D., Carter, M.T., Keshavarz, S., Ayub, M., Najmabadi, H., Liu, X., Ropers, H.H., Macheroux, P., Vincent, J.B., 2015. Mutations in the histamine N-methyltransferase gene, HNMT, are associated with nonsyndromic autosomal recessive intellectual disability. Hum Mol Genet 24, 5697–5710. doi:10.1093/hmg/ddv286

Heintze, J., Luft, C., Ketteler, R., 2013. A CRISPR CASe for high-throughput silencing. Front Genet 4, 1–6. doi:10.3389/fgene.2013.00193

Heman-Ackah, S.M., Bassett, A.R., Wood, M.J.A., 2016. Precision Modulation of Neurodegenerative Disease-Related Gene Expression in Human iPSC-Derived

Neurons. Sci Rep 6, 28420. doi:10.1038/srep28420

Hiranniramol, K., Chen, Y., Liu, W., Wang, X., 2020. Generalizable sgRNA design for improved CRISPR/Cas9 editing efficiency. Bioinformatics. doi:10.1093/bioinformatics/btaa041

Hisano, Y., Sakuma, T., Nakade, S., Ohga, R., Ota, S., Okamoto, H., Yamamoto, T., Kawahara, A., 2015. Precise in-frame integration of exogenous DNA mediated by CRISPR/Cas9 system in zebrafish. Sci Rep 5, 8841. doi:10.1038/srep08841

Hoon, M., Okawa, H., Della Santina, L., Wong, R.O.L., 2014. Functional architecture of the retina: Development and disease. Prog Retin Eye Res. doi:10.1016/j.preteyeres.2014.06.003

Hoshijima, K., Jurynec, M.J., Klatt Shaw, D., Jacobi, A.M., Behlke, M.A., Grunwald, D.J., 2019. Highly Efficient CRISPR-Cas9-Based Methods for Generating Deletion Mutations and F0 Embryos that Lack Gene Function in Zebrafish. Dev Cell 51, 645-657.e4. doi:10.1016/j.devcel.2019.10.004

Howe, K., Clark, M.D., Torroja, C.F., Torrance, J., Berthelot, C., Muffato, M., Collins, J.E.J.E., Humphray, S., McLaren, K., Matthews, L., McLaren, S., Sealy, I., Caccamo, M., Churcher, C., Scott, C., Barrett, J.C., Koch, R., Rauch, G.-J.J., White, S., Chow, W., Kilian, B., Quintais, L.T., Guerra-Assunção, J.A., Zhou, Y., Gu, Y., Yen, J., Vogel, J.-H.H., Eyre, T., Redmond, S., Banerjee, R., Chi, J., Fu, B., Langley, E., Maguire, S.F., Laird, G.K., Lloyd, D., Kenyon, E., Donaldson, S., Sehra, H., Almeida-King, J., Loveland, J., Trevanion, S., Jones, M., Quail, M., Willey, D., Hunt, A., Burton, J., Sims, S., McLay, K., Plumb, B., Davis, J., Clee, C., Oliver, K., Clark, R., Riddle, C., Eliott, D., Threadgold, G., Harden, G., Ware, D., Mortimer, B., Kerry, G., Heath, P., Phillimore, B., Tracey, A., Corby, N., Dunn, M., Johnson, C., Wood, J., Clark, S., Pelan, S., Griffiths, G., Smith, M., Glithero, R., Howden, P., Barker, N., Stevens, C., Harley, J., Holt, K., Panagiotidis, G., Lovell, J., Beasley, H., Henderson, C., Gordon, D., Auger, K., Wright, D., Collins, J.E.J.E., Raisen, C., Dyer, L., Leung, K., Robertson, L., Ambridge, K., Leongamornlert, D., McGuire, S., Gilderthorp, R., Griffiths, C., Manthravadi, D., Nichol, S., Barker, G., Whitehead, S., Kay, M., Brown, J., Murnane, C., Gray, E., Humphries, M., Sycamore, N., Barker, D., Saunders, D., Wallis, J., Babbage, A., Hammond, S., Mashreghi-Mohammadi, M., Barr, L., Martin, S., Wray, P., Ellington, A., Matthews, N., Ellwood, M., Woodmansey, R., Clark, G., Cooper, J.D., Tromans, A., Grafham, D., Skuce, C., Pandian, R., Andrews, R., Harrison, E., Kimberley, A., Garnett, J., Fosker, N., Hall, R., Garner, P., Kelly, D., Bird, C., Palmer, S., Gehring, I., Berger, A., Dooley, C.M., Ersan-Ürün, Z., Eser, C., Geiger, H., Geisler, M., Karotki, L., Kirn, A., Konantz, J., Konantz, M., Oberländer, M., Rudolph-Geiger, S., Teucke, M., Osoegawa, K., Zhu, B., Rapp, A., Widaa, S., Langford, C., Yang, F., Carter, N.P., Harrow, J., Ning, Z., Herrero, J., Searle, S.M.J., Enright, A., Geisler, R., Plasterk, R.H.A., Lee, C., Westerfield, M., de Jong, P.J., Zon, L.I., Postlethwait, J.H., Nüsslein-Volhard, C., Hubbard, T.J.P., Roest Crollius, H., Rogers, J., Stemple, D.L., Elliot, D., Eliott, D., Threadgold, G., Harden, G., Ware, D., Begum, S., Mortimore, B., Mortimer, B., Kerry, G., Heath, P., Phillimore, B., Tracey, A., Corby, N., Dunn, M., Johnson, C., Wood, J., Clark, S., Pelan, S., Griffiths, G., Smith, M., Glithero, R., Howden, P., Barker, N., Lloyd, C., Stevens, C., Harley, J., Holt, K., Panagiotidis, G., Lovell, J., Beasley, H., Henderson, C., Gordon, D., Auger, K., Wright, D., Collins, J.E.J.E., Raisen, C., Dyer, L., Leung, K., Robertson, L., Ambridge, K., Leongamornlert, D., McGuire, S., Gilderthorp, R., Griffiths, C., Manthravadi, D., Nichol, S., Barker, G., Whitehead, S., Kay, M., Brown, J., Murnane, C., Gray, E., Humphries, M., Sycamore, N., Barker, D., Saunders, D., Wallis, J., Babbage, A., Hammond, S., Mashreghi-Mohammadi, M., Barr, L., Martin, S., Wray, P., Ellington, A., Matthews, N., Ellwood, M., Woodmansey, R., Clark, G., Cooper, J.D., Cooper, J.D., Tromans, A., Grafham, D., Skuce, C., Pandian, R., Andrews, R., Harrison, E.,

Kimberley, A., Garnett, J., Fosker, N., Hall, R., Garner, P., Kelly, D., Bird, C., Palmer, S., Gehring, I., Berger, A., Dooley, C.M., Ersan-Ürün, Z., Eser, C., Geiger, H., Geisler, M., Karotki, L., Kirn, A., Konantz, J., Konantz, M., Oberländer, M., Rudolph-Geiger, S., Teucke, M., Lanz, C., Raddatz, G., Osoegawa, K., Zhu, B., Rapp, A., Widaa, S., Langford, C., Yang, F., Schuster, S.C., Carter, N.P., Harrow, J., Ning, Z., Herrero, J., Searle, S.M.J., Enright, A., Geisler, R., Plasterk, R.H.A., Lee, C., Westerfield, M., de Jong, P.J., Zon, L.I., Postlethwait, J.H., Nüsslein-Volhard, C., Hubbard, T.J.P., Roest Crollius, H., Rogers, J., Stemple, D.L., 2013. The zebrafish reference genome sequence and its relationship to the human genome. Nature 496, 498–503. doi:10.1038/nature12111

Huang, Y.Y., Neuhauss, S.C.F., 2008. The optokinetic response in zebrafish and its applications. Front Biosci. doi:10.2741/2810

Hwang, W.Y., Fu, Y., Reyon, D., Maeder, M.L., Kaini, P., Sander, J.D., Joung, J.K., Peterson, R.T., Yeh, J.R.J., 2013a. Heritable and Precise Zebrafish Genome Editing Using a CRISPR-Cas System. PLoS One 8. doi:10.1371/journal.pone.0068708

Hwang, W.Y., Fu, Y., Reyon, D., Maeder, M.L., Tsai, S.Q., Sander, J.D., Peterson, R.T., Yeh, J.-R.R.J., Joung, J.K., 2013b. Efficient genome editing in zebrafish using a CRISPR-Cas system. Nat Biotechnol 31, 227–229. doi:10.1038/nbt.2501

Iijima, M., Shimizu, H., Tanaka, Y., Urushihara, H., 1998. A Dictyostelium discoideum homologue to Tcp-1 is essential for growth and development. Gene 213, 101–6. doi:10.1016/s0378-1119(98)00190-5

Ilkovski, B., Pagnamenta, A.T., O'Grady, G.L., Kinoshita, T., Howard, M.F., Lek, M., Thomas, B., Turner, A., Christodoulou, J., Sillence, D., Knight, S.J.L., Popitsch, N., Keays, D.A., Anzilotti, C., Goriely, A., Waddel, L.B., Brilot, F., North, K.N., Kanzawa, N., Macarthur, D.G., Taylor, J.C., Kini, U., Murakami, Y., Clarke, N.F., 2015. Mutations in PIGY: Expanding the phenotype of inherited glycosylphosphatidylinositol deficiencies. Hum Mol Genet 24, 6146–6159. doi:10.1093/hmg/ddv331

Iribarne, M., 2019. Zebrafish Photoreceptor Degeneration and Regeneration Research to Understand Hereditary Human Blindness, in: Visual Impairment and Blindness [Working Title]. IntechOpen. doi:10.5772/intechopen.88758

Irion, U., Krauss, J., Nüsslein-Volhard, C., 2014. Precise and efficient genome editing in zebrafish using the CRISPR/Cas9 system. Development 141.

Irons, T.D., MacPhail, R.C., Hunter, D.L., Padilla, S., 2010. Acute neuroactive drug exposures alter locomotor activity in larval zebrafish. Neurotoxicol Teratol 32, 84–90. doi:10.1016/j.ntt.2009.04.066

Jao, L.E., Appel, B., Wente, S.R., 2012. A zebrafish model of lethal congenital contracture syndrome 1 reveals Gle 1 function in spinal neural precursor survival and motor axon arborization. Development 139, 1316–1326. doi:10.1242/dev.074344

Jessberger, S., 2016. Stem Cell-Mediated Regeneration of the Adult Brain. Transfus Med Hemotherapy. doi:10.1159/000447646

Jin, Z.B., Huang, X.F., Lv, J.N., Xiang, L., Li, D.Q., Chen, J., Huang, C., Wu, J., Lu, F., Qu, J., 2014. SLC7A14 linked to autosomal recessive retinitis pigmentosa. Nat Commun 5, 3517. doi:10.1038/ncomms4517

Kaisari, S., Sitry-Shevah, D., Miniowitz-Shemtov, S., Teichner, A., Hershko, A., 2017. Role of CCT chaperonin in the disassembly of mitotic checkpoint complexes. Proc Natl Acad Sci 114, 201620451. doi:10.1073/pnas.1620451114

Kamei, M., Isogai, S., Pan, W., Weinstein, B.M., 2010. Imaging blood vessels in the zebrafish, in: Methods in Cell Biology. pp. 27–54. doi:10.1016/B978-0-12-384892-5.00002-5

Kani, S., Bae, Y.K., Shimizu, T., Tanabe, K., Satou, C., Parsons, M.J., Scott, E., Higashijima, S.I., Hibi, M., 2010. Proneural gene-linked neurogenesis in zebrafish cerebellum. Dev Biol 343, 1–17. doi:10.1016/j.ydbio.2010.03.024

Karczewski, K.J., Francioli, L.C., Tiao, G., Cummings, B.B., Alföldi, J., Wang, Q., Collins, R.L., Laricchia, K.M., Ganna, A., Birnbaum, D.P., Gauthier, L.D., Brand, H., Solomonson, M., Watts, N.A., Rhodes, D., Singer-Berk, M., England, E.M., Seaby, E.G., Kosmicki, J.A., Walters, R.K., Tashman, K., Farjoun, Y., Banks, E., Poterba, T., Wang, A., Seed, C., Whiffin, N., Chong, J.X., Samocha, K.E., Pierce-Hoffman, E., Zappala, Z., O'Donnell-Luria, A.H., Minikel, E.V., Weisburd, B., Lek, M., Ware, J.S., Vittal, C., Armean, I.M., Bergelson, L., Cibulskis, K., Connolly, K.M., Covarrubias, M., Donnelly, S., Ferriera, S., Gabriel, S., Gentry, J., Gupta, N., Jeandet, T., Kaplan, D., Llanwarne, C., Munshi, R., Novod, S., Petrillo, N., Roazen, D., Ruano-Rubio, V., Saltzman, A., Schleicher, M., Soto, J., Tibbetts, K., Tolonen, C., Wade, G., Talkowski, M.E., Consortium, T.G.A.D., Neale, B.M., Daly, M.J., MacArthur, D.G., 2019. Variation across 141,456 human exomes and genomes reveals the spectrum of loss-of-function intolerance across human protein-coding genes. bioRxiv 531210. doi:10.1101/531210

Kasher, P.R., Namavar, Y., van Tijn, P., Fluiter, K., Sizarov, A., Kamermans, M., Grierson, A.J., Zivkovic, D., Baas, F., 2011. Impairment of the tRNA-splicing endonuclease subunit 54 (tsen54) gene causes neurological abnormalities and larval death in zebrafish models of pontocerebellar hypoplasia. Hum Mol Genet 20, 1574–1584. doi:10.1093/hmg/ddr034

Kaslin, J., Kroehne, V., Ganz, J., Hans, S., Brand, M., 2017. Distinct roles of neuroepithelial-like and radial glia-like progenitor cells in cerebellar regeneration. Dev 144, 1462–1471. doi:10.1242/dev.144907

Kastenhuber, E., Kern, U., Bonkowsky, J.L., Chien, C. Bin, Driever, W., Schweitzer, J., 2009. Netrin-DCC, robo-slit, and heparan sulfate proteoglycans coordinate lateral positioning of longitudinal dopaminergic diencephalospinal axons. J Neurosci 29, 8914–8926. doi:10.1523/JNEUROSCI.0568-09.2009

Kaur, K., Gupta, A.K., Rajput, A., Kumar, M., 2016. ge-CRISPR - An integrated pipeline for the prediction and analysis of sgRNAs genome editing efficiency for CRISPR/Cas system. Sci Rep. doi:10.1038/srep30870

Kefalov, V.J., 2011. Rod and Cone Visual Pigments and Phototransduction through Pharmacological, Genetic, and Physiological Approaches *. doi:10.1074/jbc.R111.303008

Kettleborough, R.N.W., Busch-Nentwich, E.M., Harvey, S.A., Dooley, C.M., de Bruijn, E., van Eeden, F., Sealy, I., White, R.J., Herd, C., Nijman, I.J., Fényes, F., Mehroke, S., Scahill, C., Gibbons, R., Wali, N., Carruthers, S., Hall, A., Yen, J., Cuppen, E., Stemple, D.L., 2013. A systematic genome-wide analysis of zebrafish protein-coding gene function. Nature 496, 494–497. doi:10.1038/nature11992

Khan, S.A., Muhammad, N., Khan, M.A., Kamal, A., Rehman, Z.U., Khan, S., 2016. Genetics of human Bardet-Biedl syndrome, an update. Clin Genet. doi:10.1111/cge.12737

Khanna, H., 2015. Photoreceptor Sensory Cilium: Traversing the Ciliary Gate. Cells 4, 674–686. doi:10.3390/cells4040674

Kim, A.R., Choi, K.W., 2019. TRiC/CCT chaperonins are essential for organ growth by interacting with insulin/TOR signaling in Drosophila. Oncogene 38, 4739–4754. doi:10.1038/s41388-019-0754-1

Kim, K., Ryu, S.-M., Kim, S.-T., Baek, G., Kim, D., Lim, K., Chung, E., Kim, S., Kim, J.-S., 2017. Highly efficient RNA-guided base editing in mouse embryos. Nat Biotechnol 35, 435–437. doi:10.1038/nbt.3816

Kim, Y.B., Komor, A.C., Levy, J.M., Packer, M.S., Zhao, K.T., Liu, D.R., 2017. Increasing the genome-targeting scope and precision of base editing with engineered Cas9-cytidine deaminase fusions. Nat Biotechnol 35, 371–376. doi:10.1038/nbt.3803

Kimmel, C.B., 1993. PATTERNING THE BRAIN OF THE ZEBRAFISH EMBRYO, Annu. Rev. Neurosci.

Kimmel, C.B., Ballard, W.W., Kimmel, S.R., Ullmann, B., Schilling, T.F., 1995. Stages of embryonic development of the zebrafish. Dev Dyn 203, 253–310. doi:10.1002/aja.1002030302

Kist, A.M., Portugues, R., 2019. Optomotor Swimming in Larval Zebrafish Is Driven by Global Whole-Field Visual Motion and Local Light-Dark Transitions. CellReports 29, 659-670.e3. doi:10.1016/j.celrep.2019.09.024

Kitagawa, R., Kastan, M.B., 2005. The ATM-dependent DNA damage signaling pathway, in: Cold Spring Harbor Symposia on Quantitative Biology. pp. 99–109. doi:10.1101/sqb.2005.70.002

Kitamura, A., Kubota, H., Pack, C.-G., Matsumoto, G., Hirayama, S., Takahashi, Y., Kimura, H., Kinjo, M., Morimoto, R.I., Nagata, K., 2006. Cytosolic chaperonin prevents polyglutamine toxicity with altering the aggregation state. Nat Cell Biol 8, 1163–1170. doi:10.1038/ncb1478

Klaassen, L.J., Sun, Z., Steijaert, M.N., Bolte, P., Fahrenfort, I., Sjoerdsma, T., Klooster, J., Claassen, Y., Shields, C.R., Ten Eikelder, H.M.M., Janssen-Bienhold, U., Zoidl, G., McMahon, D.G., Kamermans, M., 2011. Synaptic transmission from horizontal cells to cones is impaired by loss of connexin hemichannels. PLoS Biol 9. doi:10.1371/journal.pbio.1001107

Kleinstiver, B.P., Prew, M.S., Tsai, S.Q., Topkar, V. V., Nguyen, N.T., Zheng, Z., Gonzales, A.P.W., Li, Z., Peterson, R.T., Yeh, J.-R.J.R.J., Aryee, M.J., Joung, J.K., 2015. Engineered CRISPR-Cas9 nucleases with altered PAM specificities. Nature 523, 481–485. doi:10.1038/nature14592

Knaus, A., Kortüm, F., Kleefstra, T., Stray-Pedersen, A., Đukić, D., Murakami, Y., Gerstner, T., van Bokhoven, H., Iqbal, Z., Horn, D., Kinoshita, T., Hempel, M., Krawitz, P.M., 2019. Mutations in PIGU Impair the Function of the GPI Transamidase Complex, Causing Severe Intellectual Disability, Epilepsy, and Brain Anomalies. Am J Hum Genet 105, 395–402. doi:10.1016/j.ajhg.2019.06.009

Knogler, L.D., Kist, A.M., Portugues, R., 2019. Motor context dominates output from purkinje cell functional regions during reflexive visuomotor behaviours. Elife 8. doi:10.7554/eLife.42138

Knogler, L.D., Markov, D.A., Dragomir, E.I., Štih, V., Portugues, R., 2017. Sensorimotor Representations in Cerebellar Granule Cells in Larval Zebrafish Are Dense, Spatially Organized, and Non-temporally Patterned. Curr Biol 27, 1288–1302. doi:10.1016/j.cub.2017.03.029

Koboldt, D.C., Steinberg, K.M., Larson, D.E., Wilson, R.K., Mardis, E.R., 2013. The next-

generation sequencing revolution and its impact on genomics. Cell 155, 27. doi:10.1016/j.cell.2013.09.006

Koike, M., Shibata, M., Sunabori, T., Yamaguchi, J., Sakimura, K., Komatsu, M., Tanaka, K., Uchiyama, Y., 2017. Purkinje Cells Are More Vulnerable to the Specific Depletion of Cathepsin D Than to That of Atg7. Am J Pathol 187, 1586–1600. doi:10.1016/j.ajpath.2017.02.020

Kok, F.O., Shin, M., Ni, C.W., Gupta, A., Grosse, A.S., VanImpel, A., Kirchmaier, B.C., Peterson-Maduro, J., Kourkoulis, G., Male, I., DeSantis, D.F., Sheppard-Tindell, S., Ebarasi, L., Betsholtz, C., Schulte-Merker, S., Wolfe, S.A., Lawson, N.D., 2015. Reverse genetic screening reveals poor correlation between morpholino-induced and mutant phenotypes in zebrafish. Dev Cell 32, 97–108. doi:10.1016/j.devcel.2014.11.018

Komor, A.C., Kim, Y.B., Packer, M.S., Zuris, J.A., Liu, D.R., 2016. Programmable editing of a target base in genomic DNA without double-stranded DNA cleavage. Nature 533, 420–424. doi:10.1038/nature17946

Kostic, C., Arsenijevic, Y., 2016. Animal modelling for inherited central vision loss. J Pathol 238, 300–310. doi:10.1002/path.4641

Kozol, R.A., Abrams, A.J., James, D.M., Buglo, E., Yan, Q., Dallman, J.E., 2016. Function Over Form: Modeling Groups of Inherited Neurological Conditions in Zebrafish. Front Mol Neurosci 9. doi:10.3389/fnmol.2016.00055

Krawitz, P.M., Murakami, Y., Hecht, J., Krüger, U., Holder, S.E., Mortier, G.R., Delle Chiaie, B., De Baere, E., Thompson, M.D., Roscioli, T., Kielbasa, S., Kinoshita, T., Mundlos, S., Robinson, P.N., Horn, D., 2012. Mutations in PIGO, a member of the GPI-anchor-synthesis pathway, cause hyperphosphatasia with mental retardation. Am J Hum Genet 91, 146–151. doi:10.1016/j.ajhg.2012.05.004

Kubota, S., Kubota, H., Nagata, K., 2006. Cytosolic chaperonin protects folding intermediates of Gβ from aggregation by recognizing hydrophobic β-strands. Proc Natl Acad Sci U S A 103, 8360–8365. doi:10.1073/pnas.0600195103

Lai, E.C., 2010. Cerebellar Disease, in: Neurology Secrets. Elsevier Inc., pp. 157–167. doi:10.1016/B978-0-323-05712-7.00010-6

Langenau, D.M., Ferrando, A.A., Traver, D., Kutok, J.L., Hezel, J.-P.P.D., Kanki, J.P., Zon, L.I., Look, A.T., Trede, N.S., 2004. In vivo tracking of T cell development, ablation, and engraftment in transgenic zebrafish. PNAS 101, 7369–7374. doi:10.1073/pnas.0402248101

Larson, M.H., Gilbert, L.A., Wang, X., Lim, W.A., Weissman, J.S., Qi, L.S., 2013. CRISPR interference (CRISPRi) for sequence-specific control of gene expression. Nat Protoc 8, 2180–2196. doi:10.1038/nprot.2013.132

Lee, M.J., Stephenson, D.A., Groves, M.J., Sweeney, M.G., Davis, M.B., An, S.F., Houlden, H., Salih, M.A.M., Timmerman, V., de Jonghe, P., Auer-Grumbach, M., Di Maria, E., Scaravilli, F., Wood, N.W., Reilly, M.M., 2003. Hereditary sensory neuropathy is caused by a mutation in the delta subunit of the cytosolic chaperonin-containing t-complex peptide-1 (Cct4) gene. Hum Mol Genet 12, 1917–1925. doi:10.1093/hmg/ddg198

Legradi, J., el Abdellaoui, N., van Pomeren, M., Legler, J., 2014. Comparability of behavioural assays using zebrafish larvae to assess neurotoxicity. Environ Sci Pollut Res 22, 16277–16289. doi:10.1007/s11356-014-3805-8

Li, H.L., Gee, P., Ishida, K., Hotta, A., 2016. Efficient genomic correction methods in human iPS cells using CRISPR-Cas9 system. Methods. doi:10.1016/j.ymeth.2015.10.015

Li, L., Dowling, J.E., 1997. A dominant form of inherited retinal degeneration caused by a non-photoreceptor cell-specific mutation. Proc Natl Acad Sci U S A 94, 11645–11650. doi:10.1073/pnas.94.21.11645

Liang, X., Potter, J., Kumar, S., Ravinder, N., Chesnut, J.D., 2017. Enhanced CRISPR/Cas9-mediated precise genome editing by improved design and delivery of gRNA, Cas9 nuclease, and donor DNA. J Biotechnol 241, 136–146. doi:10.1016/j.jbiotec.2016.11.011

Liu, J., Zhou, Y., Qi, X., Chen, J., Chen, W., Qiu, G., Wu, Z., Wu, N., 2016. CRISPR/Cas9 in zebrafish: an efficient combination for human genetic diseases modeling. Hum Genet 1–12. doi:10.1007/s00439-016-1739-6

Liu, K., Petree, C., Requena, T., Varshney, P., Varshney, G.K., 2019. Expanding the CRISPR toolbox in zebrafish for studying development and disease. Front Cell Dev Biol. doi:10.3389/fcell.2019.00013

Liu, K.S., Fetcho, J.R., 1999. Laser ablations reveal functional relationships of segmental hindbrain neurons in zebrafish. Neuron 23, 325–335. doi:10.1016/S0896-6273(00)80783-7

Liu, N., Kong, X.D., Shi, H.R., Wu, Q.H., Jiang, M., 2014. Tyrosinase gene mutations in the Chinese Han population with OCA1. Genet Res (Camb) 96, e14. doi:10.1017/S0016672314000160

Liu, X., Lin, C.-Y., Lei, M., Yan, S., Zhou, T., Erikson, R.L., 2005. CCT Chaperonin Complex Is Required for the Biogenesis of Functional Plk1 25, 4993–5010. doi:10.1128/MCB.25.12.4993–5010.2005

Liu, Y., Lee, J.W., Ackerman, S.L., 2015. Mutations in the Microtubule-Associated Protein 1A (Map1a) Gene Cause Purkinje Cell Degeneration. J Neurosci 35, 4587–4598. doi:10.1523/JNEUROSCI.2757-14.2015

Liu, Y.C., Hale, M.E., 2017. Local Spinal Cord Circuits and Bilateral Mauthner Cell Activity Function Together to Drive Alternative Startle Behaviors. Curr Biol 27, 697–704. doi:10.1016/j.cub.2017.01.019

Lobanova, E.S., Finkelstein, S., Li, J., Travis, A.M., Hao, Y., Klingeborn, M., Skiba, N.P., Deshaies, R.J., Arshavsky, V.Y., 2018. Increased proteasomal activity supports photoreceptor survival in inherited retinal degeneration. Nat Commun 9. doi:10.1038/s41467-018-04117-8

Lobanova, E.S., Finkelstein, S., Skiba, N.P., Arshavsky, V.Y., 2013. Proteasome overload is a common stress factor in multiple forms of inherited retinal degeneration. Proc Natl Acad Sci U S A 110, 9986–9991. doi:10.1073/pnas.1305521110

Low, S.E., Amburgey, K., Horstick, E., Linsley, J., Sprague, S.M., Cui, W.W., Zhou, W., Hirata, H., Saint-Amant, L., Hume, R.I., Kuwada, J.Y., 2011. TRPM7 is required within zebrafish sensory neurons for the activation of touch-evoked escape behaviors. J Neurosci 31, 11633–11644. doi:10.1523/JNEUROSCI.4950-10.2011

Low, S.E., Ryan, J., Sprague, S.M., Hirata, H., Cui, W.W., Zhou, W., Hume, R.I., Kuwada, J.Y., Saint-Amant, L., 2010a. touché is required for touch-evoked generator potentials within vertebrate sensory neurons. J Neurosci 30, 9359–9367. doi:10.1523/JNEUROSCI.1639-10.2010

Low, S.E., Zhou, W., Choong, I., Saint-Amant, L., Sprague, S.M., Hirata, H., Cui, W.W., Hume, R.I., Kuwada, J.Y., 2010b. NaV1.6a is required for normal activation of motor circuits normally excited by tactile stimulation. Dev Neurobiol 70, 508–522. doi:10.1002/dneu.20791

Lu, Z., Hu, X., Liu, F., Soares, D.C., Liu, X., Yu, S., Gao, M., Han, S., Qin, Y., Li, C., Jiang, T., Luo, D., Guo, A.-Y., Tang, Z., Liu, M., 2017. Ablation of EYS in zebrafish causes mislocalisation of outer segment proteins, F-actin disruption and cone-rod dystrophy. Sci Rep 7, 46098. doi:10.1038/srep46098

Lukov, G.L., Baker, C.M., Ludtke, P.J., Hu, T., Carter, M.D., Hackett, R.A., Thulin, C.D., Willardson, B.M., 2006. Mechanism of assembly of G protein βγ subunits by protein kinase CK2-phosphorylated phosducin-like protein and the cytosolic chaperonin complex. J Biol Chem 281, 22261–22274. doi:10.1074/jbc.M601590200

Lundin, V.F., Srayko, M., Hyman, A.A., Leroux, M.R., 2008. Efficient chaperone-mediated tubulin biogenesis is essential for cell division and cell migration in C. elegans. Dev Biol 313, 320–334. doi:10.1016/j.ydbio.2007.10.022

Luzzatto, L., Hollak, C.E.M., Cox, T.M., Schieppati, Arrigo, Licht, Christoph, Kääriäinen, H., Merlini, G., Schaefer, F., Simoens, Steven, Pani, L., Garattini, S., Remuzzi, G., Schieppati, A, Henter, J., Daina, E., Aperia, A., Communities, C. of the E., Hillmen, P., Hall, C., Marsh, J., Al., E., Parker, C., Legendre, C., Licht, C, Muus, P., Al., E., O'Sullivan, B., Orenstein, D., Milla, C., Picavet, E., Annemans, L., Cleemput, I., Cassiman, D., Simoens, S, Hyry, H., Stern, A., Cox, T., Roos, J., Wyden, R., Grassley, C., 2015. Rare diseases and effective treatments: are we delivering? Lancet 385, 750–752. doi:10.1016/S0140-6736(15)60297-5

Maaswinkel, H., Riesbeck, L.E., Riley, M.E., Carr, A.L., Mullin, J.P., Nakamoto, A.T., Li, L., 2005. Behavioral screening for nightblindness mutants in zebrafish reveals three new loci that cause dominant photoreceptor cell degeneration. Mech Ageing Dev 126, 1079–1089. doi:10.1016/j.mad.2005.03.025

MacArthur, D.G., Manolio, T.A., Dimmock, D.P., Rehm, H.L., Shendure, J., Abecasis, G.R., Adams, D.R., Altman, R.B., Antonarakis, S.E., Ashley, E.A., Barrett, J.C., Biesecker, L.G., Conrad, D.F., Cooper, G.M., Cox, N.J., Daly, M.J., Gerstein, M.B., Goldstein, D.B., Hirschhorn, J.N., Leal, S.M., Pennacchio, L.A., Stamatoyannopoulos, J.A., Sunyaev, S.R., Valle, D., Voight, B.F., Winckler, W., Gunter, C., 2014. Guidelines for investigating causality of sequence variants in human disease. Nature 508, 469–476. doi:10.1038/nature13127

MacPhail, R.C., Brooks, J., Hunter, D.L., Padnos, B., Irons, T.D., Padilla, S., 2009. Locomotion in larval zebrafish: Influence of time of day, lighting and ethanol. Neurotoxicology 30, 52–58. doi:10.1016/j.neuro.2008.09.011

Majczenko, K., Davidson, A.E., Camelo-Piragua, S., Agrawal, P.B., Manfready, R.A., Li, X., Joshi, S., Xu, J., Peng, W., Beggs, A.H., Li, J.Z., Burmeister, M., Dowling, J.J., 2012. Dominant mutation of CCDC78 in a unique congenital myopathy with prominent internal nuclei and atypical cores. Am J Hum Genet 91, 365–371. doi:10.1016/j.ajhg.2012.06.012

Makrythanasis, P., Kato, M., Zaki, M.S., Saitsu, H., Nakamura, K., Santoni, F.A., Miyatake, S., Nakashima, M., Issa, M.Y., Guipponi, M., Letourneau, A., Logan, C. V., Roberts, N., Parry, D.A., Johnson, C.A., Matsumoto, N., Hamamy, H., Sheridan, E., Kinoshita, T., Antonarakis, S.E., Murakami, Y., 2016. Pathogenic Variants in PIGG Cause Intellectual Disability with Seizures and Hypotonia. Am J Hum Genet 98, 615–626. doi:10.1016/j.ajhg.2016.02.007

Mandegar, M.A., Huebsch, N., Frolov, E.B., Shin, E., Truong, A., Olvera, M.P., Chan, A.H., Miyaoka, Y., Holmes, K., Spencer, C.I., Judge, L.M., Gordon, D.E., Eskildsen, T.V., Villalta, J.E., Horlbeck, M.A., Gilbert, L.A., Krogan, N.J., Sheikh, S.P., Weissman, J.S., Qi, L.S., So, P.-L., Conklin, B.R., 2016. CRISPR Interference Efficiently Induces Specific and Reversible Gene Silencing in Human iPSCs. Cell Stem Cell 18, 541–553. doi:10.1016/j.stem.2016.01.022

Mangos, S., Lam, P., Zhao, A., Liu, Y., Mudumana, S., Vasilyev, A., Liu, A., Drummond, I.A., 2010. The ADPKD genes pkd1a/b and pkd2 regulate extracellular matrix formation. Dis Model Mech 3, 354–365. doi:10.1242/dmm.003194

Mannu, G.S., 2014. Retinal phototransduction. Neurosciences (Riyadh) 19, 275–80.

Manto, M., Bower, J.M., Conforto, A.B., Delgado-García, J.M., Da Guarda, S.N.F., Gerwig, M., Habas, C., Hagura, N., Ivry, R.B., Marien, P., Molinari, M., Naito, E., Nowak, D.A., Ben Taib, N.O., Pelisson, D., Tesche, C.D., Tilikete, C., Timmann, D., 2012. Consensus paper: Roles of the cerebellum in motor control-the diversity of ideas on cerebellar involvement in movement, in: Cerebellum. pp. 457–487. doi:10.1007/s12311-011-0331-9

Markaki, M., Tavernarakis, N., 2010. Modeling human diseases in Caenorhabditis elegans. Biotechnol J. doi:10.1002/biot.201000183

Matsuda, N., Mishina, M., 2004. Identification of chaperonin CCTγ subunit as a determinant of retinotectal development by whole-genome subtraction cloning from zebrafish no tectal neuron mutant. Development 131, 1913–1925. doi:10.1242/dev.01085

Matsui, H., Namikawa, K., Babaryka, A., Köster, R.W., 2014. Functional regionalization of the teleost cerebellum analyzed in vivo. Proc Natl Acad Sci U S A 111, 11846–11851. doi:10.1073/pnas.1403105111

Matsui, T., Sasaki, A., Akazawa, N., Otani, H., Bessho, Y., 2012. Celf1 regulation of dmrt2a is required for somite symmetry and left-right patterning during zebrafish development. Dev 139, 3553–3560. doi:10.1242/dev.077263

Maydan, G., Noyman, I., Har-Zahav, A., Neriah, Z. Ben, Pasmanik-Chor, M., Yeheskel, A., Albin-Kaplanski, A., Maya, I., Magal, N., Birk, E., Simon, A.J., Halevy, A., Rechavi, G., Shohat, M., Straussberg, R., Basel-Vanagaite, L., 2011. Multiple congenital anomalies-hypotonia-seizures syndrome is caused by a mutation in PIGN. J Med Genet 48, 383–389. doi:10.1136/jmg.2010.087114

McCurley, A.T., Callard, G. V., 2008. Characterization of housekeeping genes in zebrafish: Male-female differences and effects of tissue type, developmental stage and chemical treatment. BMC Mol Biol 9, 102. doi:10.1186/1471-2199-9-102

Meier, A., Nelson, R., Connaughton, V.P., 2018. Color processing in zebrafish retina. Front Cell Neurosci. doi:10.3389/fncel.2018.00327

Melkani, G.C., Bhide, S., Han, A., Vyas, J., Livelo, C., Bodmer, R., Bernstein, S.I., 2017. TRiC/CCT chaperonins are essential for maintaining myofibril organization, cardiac physiological rhythm, and lifespan. FEBS Lett. doi:10.1002/1873-3468.12860

Messchaert, M., Dona, M., Broekman, S., Peters, T.A., Corral-Serrano, J.C., Slijkerman, R.W.N., van Wijk, E., Collin, R.W.J., 2018. Eyes shut homolog is important for the maintenance of photoreceptor morphology and visual function in zebrafish. PLoS One 13. doi:10.1371/journal.pone.0200789

Minegishi, Y., Nakaya, N., Tomarev, S.I., 2018. Mutation in the Zebrafish cct2 gene leads

to abnormalities of cell cycle and cell death in the Retina: A model of CCT2-related leber congenital amaurosis. Investig Ophthalmol Vis Sci 59, 995–1004. doi:10.1167/iovs.17-22919

Minegishi, Y., Sheng, X., Yoshitake, K., Sergeev, Y., Iejima, D., Shibagaki, Y., Monma, N., Ikeo, K., Furuno, M., Zhuang, W., Liu, Y., Rong, W., Hattori, S., Iwata, T., 2016. CCT2 Mutations Evoke Leber Congenital Amaurosis due to Chaperone Complex Instability. Sci Rep 6, 33742. doi:10.1038/srep33742

Moens, C.B., Donn, T.M., Wolf-Saxon, E.R., Ma, T.P., 2008. Reverse genetics in zebrafish by TILLING. Briefings Funct Genomics Proteomics 7, 454–459. doi:10.1093/bfgp/eln046

Montague, T.G., Cruz, J.M., Gagnon, J.A., Church, G.M., Valen, E., 2014. CHOPCHOP: a CRISPR/Cas9 and TALEN web tool for genome editing. Nucleic Acids Res 42, W401–W407. doi:10.1093/nar/gku410

Moreno-Mateos, M.A., Fernandez, J.P., Rouet, R., Vejnar, C.E., Lane, M.A., Mis, E., Khokha, M.K., Doudna, J.A., Giraldez, A.J., 2017. CRISPR-Cpf1 mediates efficient homology-directed repair and temperature-controlled genome editing. Nat Commun 8, 2024. doi:10.1038/s41467-017-01836-2

Morris, A.C., Fadool, J.M., 2005. Studying rod photoreceptor development in zebrafish. Physiol Behav 86, 306–313. doi:10.1016/j.physbeh.2005.08.020

Moshiri, A., Humpal, D., Leonard, B.C., Imai, D.M., Tham, A., Bower, L., Clary, D., Glaser, T.M., Lloyd, K.C.K., Murphy, C.J., 2017. Arap1 deficiency causes photoreceptor degeneration in mice. Investig Ophthalmol Vis Sci 58, 1709–1718. doi:10.1167/iovs.16-20062

Moulton, M.J., Letsou, A., 2016. Modeling congenital disease and inborn errors of development in Drosophila melanogaster. Dis Model Mech 9, 253–269. doi:10.1242/dmm.023564

Mullen, R.J., Eichert, E.M., Sidman, R.L., 1976. Purkinje cell degeneration, a new neurological mutation in the mouse. Genetics 73, 208–212. doi:10.1073/pnas.73.1.208

Muto, A., Kawakami, K., 2011. Imaging functional neural circuits in zebrafish with a new GCaMP and the Gal4FF-UAS system. Commun Integr Biol 4, 566. doi:10.4161/CIB.4.5.15848

Myers, K.R., Casanova, J.E., 2008. Regulation of actin cytoskeleton dynamics by Arf-family GTPases. Trends Cell Biol 18, 184–92. doi:10.1016/j.tcb.2008.02.002

Nachury, M. V., Loktev, A. V., Zhang, Q., Westlake, C.J., Peränen, J., Merdes, A., Slusarski, D.C., Scheller, R.H., Bazan, J.F., Sheffield, V.C., Jackson, P.K., 2007. A Core Complex of BBS Proteins Cooperates with the GTPase Rab8 to Promote Ciliary Membrane Biogenesis. Cell 129, 1201–1213. doi:10.1016/j.cell.2007.03.053

Nakashima, M., Kashii, H., Murakami, Y., Kato, M., Tsurusaki, Y., Miyake, N., Kubota, M., Kinoshita, T., Saitsu, H., Matsumoto, N., 2014. Novel compound heterozygous PIGT mutations caused multiple congenital anomalies-hypotonia-seizures syndrome 3. Neurogenetics 15, 193–200. doi:10.1007/s10048-014-0408-y

Namikawa, K., Dorigo, A., Zagrebelsky, M., Russo, G., Kirmann, T., Fahr, W., Dübel, S., Korte, M., Köster, R.W., 2019. Modeling neurodegenerative spinocerebellar ataxia type 13 in zebrafish using a Purkinje neuron specific tunable coexpression system. J Neurosci 39, 3948–3969. doi:10.1523/JNEUROSCI.1862-18.2019

Nasevicius, A., Ekker, S.C., 2000. Effective targeted gene 'knockdown' in zebrafish. Nat Genet 26, 216–220. doi:10.1038/79951

Nasevicius, A., Larson, J., Ekker, S.C., 2000. Distinct Requirements for Zebrafish Angiogenesis Revealed by a *VEGF-A* Morphant. Yeast 1, 294–301. doi:10.1002/1097-0061(200012)17:4<294::AID-YEA54>3.0.CO;2-5

Neef, D.W., Jaeger, A.M., Frydman, J., Correspondence, D.J.T., Gomez-Pastor, R., Willmund, F., Thiele, D.J., 2014. A Direct Regulatory Interaction between Chaperonin TRiC and Stress-Responsive Transcription Factor HSF1. CellReports 9, 955–966. doi:10.1016/j.celrep.2014.09.056

Neuhauss, S.C.F., 2003. Behavioral genetic approaches to visual system development and function in zebrafish. J Neurobiol. doi:10.1002/neu.10165

Ng, B.G., Hackmann, K., Jones, M.A., Eroshkin, A.M., He, P., Wiliams, R., Bhide, S., Cantagrel, V., Gleeson, J.G., Paller, A.S., Schnur, R.E., Tinschert, S., Zunich, J., Hegde, M.R., Freeze, H.H., 2012. Mutations in the glycosylphosphatidylinositol gene PIGL cause CHIME syndrome. Am J Hum Genet 90, 685–688. doi:10.1016/j.ajhg.2012.02.010

Nguyen, T.T.M., Murakami, Y., Sheridan, E., Ehresmann, S., Rousseau, J., St-Denis, A., Chai, G., Ajeawung, N.F., Fairbrother, L., Reimschisel, T., Bateman, A., Berry-Kravis, E., Xia, F., Tardif, J., Parry, D.A., Logan, C. V., Diggle, C., Bennett, C.P., Hattingh, L., Rosenfeld, J.A., Perry, M.S., Parker, M.J., Le Deist, F., Zaki, M.S., Ignatius, E., Isohanni, P., Lönnqvist, T., Carroll, C.J., Johnson, C.A., Gleeson, J.G., Kinoshita, T., Campeau, P.M., 2017. Mutations in GPAA1, Encoding a GPI Transamidase Complex Protein, Cause Developmental Delay, Epilepsy, Cerebellar Atrophy, and Osteopenia. Am J Hum Genet 101, 856–865. doi:10.1016/j.ajhg.2017.09.020

Nishiyama, J., Miura, E., Mizushima, N., Watanabe, M., Yuzaki, M., 2007. Aberrant membranes and double-membrane structures accumulate in the axons of Atg5-null Purkinje cells before neuronal death. Autophagy 3, 591–596. doi:10.4161/auto.4964

Nizon, M., Küry, S., Péréon, Y., Besnard, T., Quinquis, D., Boisseau, P., Marsaud, T., Magot, A., Mussini, J.M., Mayrargue, E., Barbarot, S., Bézieau, S., Isidor, B., 2018. ARL6IP1 mutation causes congenital insensitivity to pain, acromutilation and spastic paraplegia. Clin Genet 93, 169–172. doi:10.1111/cge.13048

Oliveira, J., Silveira, M., Chacon, D., Luchiari, A., 2015. The Zebrafish World of Colors and Shapes: Preference and Discrimination. Zebrafish 12, 166–173. doi:10.1089/zeb.2014.1019

Oura, Y., Nakamura, M., Takigawa, T., Fukushima, Y., Wakabayashi, T., Tsujikawa, M., Nishida, K., 2018. High-Temperature Requirement A 1 Causes Photoreceptor Cell Death in Zebrafish Disease Models. Am J Pathol 188, 2729–2744. doi:10.1016/j.ajpath.2018.08.012

Pandey, U.B., Nichols, C.D., 2011. Human disease models in Drosophila melanogaster and the role of the fly in therapeutic drug discovery. Pharmacol Rev 63, 411–436. doi:10.1124/pr.110.003293

Panula, P., Sallinen, V., Sundvik, M., Kolehmainen, J., Torkko, V., Tiittula, A., Moshnyakov, M., Podlasz, P., 2006. Modulatory neurotransmitter systems and behavior: Towards zebrafish models of neurodegenerative diseases. Zebrafish. doi:10.1089/zeb.2006.3.235

Paquet, D., Kwart, D., Chen, A., Sproul, A., Jacob, S., Teo, S., Moore Olsen, K., Gregg, A., Noggle, S., Tessier-Lavigne, M., 2016. Efficient introduction of specific

homozygous and heterozygous mutations using CRISPR/Cas9. Nature 533, 125–142. doi:10.1038/nature17664

Park, J.S., Ryu, J.H., Choi, T.I., Bae, Y.K., Lee, S., Kang, H.J., Kim, C.H., 2016. Innate color preference of zebrafish and its use in behavioral analyses. Mol Cells 39, 750–755. doi:10.14348/molcells.2016.0173

Pascual, M., Abasolo, I., Meur, A.M. Le, Martínez, A., Del Rio, J.A., Wright, C.V.E., Real, F.X., Soriano, E., 2007. Cerebellar GABAergic progenitors adopt an external granule cell-like phenotype in the absence of Ptf1a transcription factor expression. Proc Natl Acad Sci U S A 104, 5193–5198. doi:10.1073/pnas.0605699104

Pavel, M., Imarisio, S., Menzies, F.M., Jimenez-Sanchez, M., Siddiqi, F.H., Wu, X., Renna, M., O'Kane, C.J., Crowther, D.C., Rubinsztein, D.C., 2016. CCT complex restricts neuropathogenic protein aggregation via autophagy. Nat Commun 7, 13821. doi:10.1038/ncomms13821

Perles, Z., Moon, S., Ta-Shma, A., Yaacov, B., Francescatto, L., Edvardson, S., Rein, A.J., Elpeleg, O., Katsanis, N., 2015. A human laterality disorder caused by a homozygous deleterious mutation in *MMP21*. J Med Genet 52, 840–847. doi:10.1136/jmedgenet-2015-103336

Pietri, T., Roman, A.-C., Guyon, N., Romano, S.A., Washbourne, P., Moens, C.B., de Polavieja, G.G., Sumbre, G., 2013. The first mecp2-null zebrafish model shows altered motor behaviors. Front Neural Circuits 7. doi:10.3389/fncir.2013.00118

Plimpton, R.L., Cuéllar, J., Lai, C.W.J., Aoba, T., Makaju, A., Franklin, S., Mathis, A.D., Prince, J.T., Carrascosa, J.L., Valpuesta, J.M., Willardson, B.M., 2015. Structures of the Gβ-CCT and PhLP1-Gβ-CCT complexes reveal a mechanism for G-protein β-subunit folding and Gβγ dimer assembly. Proc Natl Acad Sci U S A 112, 2413–2418. doi:10.1073/pnas.1419595112

Posokhova, E., Song, H., Belcastro, M., Higgins, L.A., Bigley, L.R., Michaud, N.A., Martemyanov, K.A., Sokolov, M., 2011. Disruption of the chaperonin containing TCP-1 function affects protein networks essential for rod outer segment morphogenesis and survival. Mol Cell Proteomics 10. doi:10.1074/mcp.M110.000570

Potter, H., Chial, H.J., Caneus, J., Elos, M., Elder, N., Borysov, S., Granic, A., 2019. Chromosome Instability and Mosaic Aneuploidy in Neurodegenerative and Neurodevelopmental Disorders. Front Genet 10, 1092. doi:10.3389/fgene.2019.01092

Presnyak, V., Alhusaini, N., Chen, Y.H., Martin, S., Morris, N., Kline, N., Olson, S., Weinberg, D., Baker, K.E., Graveley, B.R., Coller, J., 2015. Codon optimality is a major determinant of mRNA stability. Cell 160, 1111–1124. doi:10.1016/j.cell.2015.02.029

Prykhozhij, S. V., Fuller, C., Steele, S.L., Veinotte, C.J., Razaghi, B., Robitaille, J.M., McMaster, C.R., Shlien, A., Malkin, D., Berman, J.N., 2018. Optimized knock-in of point mutations in zebrafish using CRISPR/Cas9. Nucleic Acids Res 46. doi:10.1093/nar/gky512

Purves, D., Augustine, G.J., Fitzpatrick, D., Katz, L.C., LaMantia, A.-S., McNamara, J.O., Williams, S.M., 2001. The Retina.

Putri, R.R., Chen, L., 2018. Spatiotemporal control of zebrafish (Danio rerio) gene expression using a light-activated CRISPR activation system. Gene 677, 273–279. doi:10.1016/j.gene.2018.07.077

Qin, W., Lu, X., Liu, Y., Bai, H., Li, S., Lin, S., 2018. Precise A.T to G.C base editing in the zebrafish genome. BMC Biol 16, 139. doi:10.1186/s12915-018-0609-1

Radke, M.B., Taft, M.H., Stapel, B., Hilfiker-Kleiner, D., Preller, M., Manstein, D.J., 2014. Small molecule-mediated refolding and activation of myosin motor function. Elife 2014, e01603. doi:10.7554/eLife.01603

Raghupathy, R., Patnaik, S., Shu, X., 2013. Transgenic Zebrafish Models for Understanding Retinitis Pigmentosa. Cloning Transgenes 02. doi:10.4172/2168-9849.1000110

Ramesh, T., Lyon, A.N., Pineda, R.H., Wang, C., Janssen, P.M.L., Canan, B.D., Burghes, A.H.M., Beattie, C.E., 2010. A genetic model of amyotrophic lateral sclerosis in zebrafish displays phenotypic hallmarks of motoneuron disease. DMM Dis Model Mech 3, 652–662. doi:10.1242/dmm.005538

Ramoni, R.B., Mulvihill, J.J., Adams, D.R., Allard, P., Ashley, E.A., Bernstein, J.A., Gahl, W.A., Hamid, R., Loscalzo, J., McCray, A.T., Shashi, V., Tifft, C.J., Wise, A.L., Adams, D.R., Adams, C.J., Alejandro, M.E., Allard, P., Ashley, E.A., Azamian, M.S., Bacino, C.A., Balasubramanyam, A., Barseghyan, H., Beggs, A.H., Bellen, H.J., Bernick, D., Bernstein, J.A., Bican, A., Bick, D.P., Birch, C.L., Boone, B.E., Briere, L.C., Brown, D.M., Brownstein, C.A., Brush, M., Burke, E.A., Burrage, L.C., Chao, K.R., Clark, G.D., Cogan, J.D., Cooper, C.M., Craigen, W.J., Davids, M., Dayal, J.G., Dell'Angelica, E.C., Dhar, S.U., Dipple, K.M., Donnell-Fink, L.A., Dorrani, N., Dorset, D.C., Draper, D.D., Dries, A.M., Eastwood, R., Eckstein, D.J., Emrick, L.T., Eng, C.M., Esteves, C., Estwick, T., Fisher, P.G., Frisby, T.S., Frost, K., Gahl, W.A., Gartner, V., Godfrey, R.A., Goheen, M., Golas, G.A., Goldstein, D.B., Gordon, M. "Gracie" G., Gould, S.E., Gourdine, J.-P.F., Graham, B.H., Groden, C.A., Gropman, A.L., Hackbarth, M.E., Haendel, M., Hamid, R., Hanchard, N.A., Handley, L.H., Hardee, I., Herzog, M.R., Holm, I.A., Howerton, E.M., Iglesias, B., Jacob, H.J., Jain, M., Jiang, Y., Johnston, J.M., Jones, A.L., Koehler, A.E., Koeller, D.M., Kohane, I.S., Kohler, J.N., Krasnewich, D.M., Krieg, E.L., Krier, J.B., Kyle, J.E., Lalani, S.R., Latham, L., Latour, Y.L., Lau, C.C., Lazar, J., Lee, B.H., Lee, H., Lee, P.R., Levy, S.E., Levy, D.J., Lewis, R.A., Liebendorder, A.P., Lincoln, S.A., Loomis, C.R., Loscalzo, J., Maas, R.L., Macnamara, E.F., MacRae, C.A., Maduro, V. V., Malicdan, M.C. V., Mamounas, L.A., Manolio, T.A., Markello, T.C., Martin, C., Mazur, P., McCarty, A.J., McConkie-Rosell, A., McCray, A.T., Metz, T.O., Might, M., Moretti, P.M., Mulvihill, J.J., Murphy, J.L., Muzny, D.M., Nehrebecky, M.E., Nelson, S.F., Newberry, J.S., Newman, J.H., Nicholas, S.K., Novacic, D., Orange, J.S., Pallais, J.C., Palmer, C.G.S., Papp, J.C., Pena, L.D.M., Phillips, J.A., Posey, J.E., Postlethwait, J.H., Potocki, L., Pusey, B.N., Ramoni, R.B., Robertson, A.K., Rodan, L.H., Rosenfeld, J.A., Sadozai, S., Schaffer, K.E., Schoch, K., Schroeder, M.C., Scott, D.A., Sharma, P., Shashi, V., Silverman, E.K., Sinsheimer, J.S., Soldatos, A.G., Spillmann, R.C., Splinter, K., Stoler, J.M., Stong, N., Strong, K.A., Sullivan, J.A., Sweetser, D.A., Thomas, S.P., Tifft, C.J., Tolman, N.J., Toro, C., Tran, A.A., Valivullah, Z.M., Vilain, E., Waggott, D.M., Wahl, C.E., Walley, N.M., Walsh, C.A., Wangler, M.F., Warburton, M., Ward, P.A., Waters, K.M., Webb-Robertson, B.-J.M., Weech, A.A., Westerfield, M., Wheeler, M.T., Wise, A.L., Wolfe, L.A., Worthey, E.A., Yamamoto, S., Yang, Y., Yu, G., Zornio, P.A., 2017. The Undiagnosed Diseases Network: Accelerating Discovery about Health and Disease. Am J Hum Genet 100, 185–192. doi:10.1016/j.ajhg.2017.01.006

Rao, M.B., Didiano, D., Patton, J.G., 2017. Neurotransmitter-Regulated Regeneration in the Zebrafish Retina. Stem Cell Reports 8, 831–842. doi:10.1016/j.stemcr.2017.02.007

Raymond, F.L., Whibley, A., Stratton, M.R., Gecz, J., 2009. Lessons learnt from large-scale exon re-sequencing of the X chromosome. Hum Mol Genet 18, R60-4.

doi:10.1093/hmg/ddp071

Reissmann, S., Joachimiak, L.A., Chen, B., Meyer, A.S., Nguyen, A., Frydman, J., 2012. A Gradient of ATP Affinities Generates an Asymmetric Power Stroke Driving the Chaperonin TRIC/CCT Folding Cycle. CellReports 2, 866–877. doi:10.1016/j.celrep.2012.08.036

Renaud, J.B., Boix, C., Charpentier, M., De Cian, A., Cochennec, J., Duvernois-Berthet, E., Perrouault, L., Tesson, L., Edouard, J., Thinard, R., Cherifi, Y., Menoret, S., Fontanière, S., de Crozé, N., Fraichard, A., Sohm, F., Anegon, I., Concordet, J.P., Giovannangeli, C., 2016. Improved Genome Editing Efficiency and Flexibility Using Modified Oligonucleotides with TALEN and CRISPR-Cas9 Nucleases. Cell Rep 14, 2263–2272. doi:10.1016/j.celrep.2016.02.018

Rentzsch, P., Witten, D., Cooper, G.M., Shendure, J., Kircher, M., 2019. CADD: predicting the deleteriousness of variants throughout the human genome. Nucleic Acids Res 47. doi:10.1093/nar/gky1016

Richardson, C.D., Ray, G.J., DeWitt, M.A., Curie, G.L., Corn, J.E., 2016. Enhancing homology-directed genome editing by catalytically active and inactive CRISPR-Cas9 using asymmetric donor DNA. Nat Biotechnol 34, 339–44. doi:10.1038/nbt.3481

Richardson, R., Tracey-White, D., Webster, A., Moosajee, M., 2017. The zebrafish eye-a paradigm for investigating human ocular genetics. Eye. doi:10.1038/eye.2016.198

Ritter, D.A., Bhatt, D.H., Fetcho, J.R., 2001. In vivo imaging of zebrafish reveals differences in the spinal networks for escape and swimming movements. J Neurosci 21, 8956–8965. doi:10.1523/jneurosci.21-22-08956.2001

Robles, E., Laurell, E., Baier, H., 2014. The retinal projectome reveals brain-area-specific visual representations generated by ganglion cell diversity. Curr Biol 24, 2085–2096. doi:10.1016/j.cub.2014.07.080

Roostaei, T., Nazeri, A., Sahraian, M.A., Minagar, A., 2014. The human cerebellum: A review of physiologic neuroanatomy. Neurol Clin. doi:10.1016/j.ncl.2014.07.013

Rossi, A., Kontarakis, Z., Gerri, C., Nolte, H., Hölper, S., Krüger, M., Stainier, D.Y.R., 2015. Genetic compensation induced by deleterious mutations but not gene knockdowns. Nature Aug 13, 230–233. doi:10.1038/nature14580

Roy, B., Ali, D.W., 2013. Patch clamp recordings from embryonic zebrafish mauthner cells. J Vis Exp. doi:10.3791/50551

Roy, B., Ferdous, J., Ali, D.W., 2015. NMDA receptors on zebrafish Mauthner cells require CaMKII-α for normal development. Dev Neurobiol 75, 145–162. doi:10.1002/dneu.22214

Rupik, W., Jasik, K., Bembenek, J., Widłak, W., 2011. The expression patterns of heat shock genes and proteins and their role during vertebrate's development. Comp Biochem Physiol - A Mol Integr Physiol. doi:10.1016/j.cbpa.2011.04.002

Saint-Amant, L., Drapeau, P., 1998. Time course of the development of motor behaviors in the zebrafish embryo. J Neurobiol 37, 622–632. doi:10.1002/(SICI)1097-4695(199812)37:4<622::AID-NEU10>3.0.CO;2-S

Sakowski, S.A., Lunn, J.S., Busta, A.S., Oh, S.S., Zamora-Berridi, G., Palmer, M., Rosenberg, A.A., Philip, S.G., Dowling, J.J., Feldman, E.L., 2012. Neuromuscular effects of G93A-SOD1 expression in zebrafish, Molecular Neurodegeneration.

Sander, J.D., Cade, L., Khayter, C., Reyon, D., Peterson, R.T., Joung, J.K., Yeh, J.-R.J.,

2011. Targeted gene disruption in somatic zebrafish cells using engineered TALENs. Nat Biotechnol 29, 697–698. doi:10.1038/nbt.1934

Santoriello, C., Zon, L.I., 2012. Hooked! Modeling human disease in zebrafish. J Clin Invest. doi:10.1172/JCI60434

Sassen, A., Köster, R.W., 2015. A molecular toolbox for genetic manipulation of zebrafish. Adv Genomics Genet 5, 151–163. doi:10.2147/AGG.S57585

Savitsky, K., Bar-Shira, A., Gilad, S., Rotman, G., Ziv, Y., Vanagaite, L., Tagle, D.A., Smith, S., Uziel, T., Sfez, S., Ashkenazi, M., Pecker, I., Frydman, M., Harnik, R., Patanjali, S.R., Simmons, A., Clines, G.A., Sartiel, A., Gatti, R.A., Chessa, L., Sanal, O., Lavin, M.F., Jaspers, N.G., Taylor, A.M., Arlett, C.F., Miki, T., Weissman, S.M., Lovett, M., Collins, F.S., Shiloh, Y., 1995. A single ataxia telangiectasia gene with a product similar to PI-3 kinase. Science (80-) 268, 1749–1753. doi:10.1126/science.7792600

Schaar, B.T., McConnell, S.K., 2005. Cytoskeletal coordination during neuronal migration. Proc Natl Acad Sci U S A 102, 13652–13657. doi:10.1073/pnas.0506008102

Schmahmann, J.D., 2019. The cerebellum and cognition. Neurosci Lett. doi:10.1016/j.neulet.2018.07.005

Schmitt, E., Claudie, P., Beauchemin, M., Richard, B., 2007. DNA-damage response network at the crossroads of cell-cycle checkpoints, cellular senescence and apoptosis *. J Zhejiang Univ Sci B 8, 377–397. doi:10.1631/jzus.2007.B0377

Schmitt, E.A., Dowling, J.E., 1999. Early retinal development in the zebrafish,Danio rerio: Light and electron microscopic analyses. J Comp Neurol 404, 515–536. doi:10.1002/(SICI)1096-9861(19990222)404:4<515::AID-CNE8>3.0.CO;2-A

Schmittgen, T.D., Livak, K.J., 2008. Analyzing real-time PCR data by the comparative CT method. Nat Protoc 3, 1101–1108. doi:10.1038/nprot.2008.73

Seixas, C., Cruto, T., Tavares, A., Gaertig, J., Soares, H., 2010. CCTα and CCTδ Chaperonin Subunits Are Essential and Required for Cilia Assembly and Maintenance in Tetrahymena. PLoS One 5, e10704. doi:10.1371/journal.pone.0010704

Seo, S., Baye, L.M., Schulz, N.P., Beck, J.S., Zhang, Q., Slusarski, D.C., Sheffield, V.C., 2010. BBS6, BBS10, and BBS12 form a complex with CCT/TRiC family chaperonins and mediate BBSome assembly. Proc Natl Acad Sci U S A 107, 1488–93. doi:10.1073/pnas.0910268107

Shankaran, S.S., Dahlem, T.J., Bisgrove, B.W., Yost, H.J., Tristani-Firouzi, M., 2017. CRISPR/Cas9-directed gene editing for the generation of loss-of-function mutants in high-throughput zebrafish F0 screens. Curr Protoc Mol Biol 2017, 31.9.1-31.9.22. doi:10.1002/cpmb.42

Shaw, M.P., Higginbottom, A., McGown, A., Castelli, L.M., James, E., Hautbergue, G.M., Shaw, P.J., Ramesh, T.M., 2018. Stable transgenic C9orf72 zebrafish model key aspects of the ALS/FTD phenotype and reveal novel pathological features. Acta Neuropathol Commun 6, 125. doi:10.1186/s40478-018-0629-7

She, J., Wu, Y., Lou, B., Lodd, E., Klems, A., Schmoehl, F., Yuan, Z., Noble, F. Le, Kroll, J., 2019. Genetic compensation by *epob* in pronephros development in *epoa* mutant zebrafish. Cell Cycle 18, 2683–2696. doi:10.1080/15384101.2019.1656019

Shen, T., Lee, A., Shen, C., Lin C Jimmy, 2015. The long tail and rare disease research: the impact of next-generation sequencing for rare Mendelian disorders. Genet Res Cambridge 97, e15. doi:http://dx.doi.org/10.1017/S0016672315000166

Sheridan, E., Wright, J., Small, N., Corry, P.C., Oddie, S., Whibley, C., Petherick, E.S., Malik, T., Pawson, N., Mckinney, P.A., Parslow, R.C., 2013. Risk factors for congenital anomaly in a multiethnic birth cohort: an analysis of the Born in Bradford study. Lancet 382, 1350–1359. doi:10.1016/S0140-6736(13)61132-0

Silverman, G.A., Luke, C.J., Bhatia, S.R., Long, O.S., Vetica, A.C., Perlmutter, D.H., Pak, S.C., 2009. Modeling Molecular and Cellular Aspects of Human Disease Using the Nematode Caenorhabditis elegans. Pediatr Res 65, 10–18. doi:10.1203/PDR.0b013e31819009b0

Sinha, S., Belcastro, M., Datta, P., Seo, S., Sokolov, M., 2014. Essential role of the chaperonin CCT in rod outer segment biogenesis. Investig Ophthalmol Vis Sci 55, 3775–3784. doi:10.1167/iovs.14-13889

Smith, K.A., Joziasse, I.C., Chocron, S., Van Dinther, M., Guryev, V., Verhoeven, M.C., Rehmann, H., Van Der Smagt, J.J., Doevendans, P.A., Cuppen, E., Mulder, B.J., Ten Dijke, P., Bakkers, J., 2009. Dominant-negative alk2 allele associates with congenital heart defects. Circulation 119, 3062–3069. doi:10.1161/CIRCULATIONAHA.108.843714

Smith, L.L., Beggs, A.H., Gupta, V.A., 2013. Analysis of skeletal muscle defects in larval zebrafish by birefringence and touch-evoke escape response assays. J Vis Exp. doi:10.3791/50925

Sobreira, N., Schiettecatte, F., Valle, D., Hamosh, A., 2015. GeneMatcher: A Matching Tool for Connecting Investigators with an Interest in the Same Gene. Hum Mutat 36, 928–930. doi:10.1002/humu.22844

Solnica-Krezel, L., Schier, A.F., Driever, W., 1994. Efficient recovery of ENU-induced mutations from the zebrafish germline. Genetics 136, 1401–1420.

Sot, B., Rubio-Muñoz, A., Leal-Quintero, A., Martínez-Sabando, J., Marcilla, M., Roodveldt, C., Valpuesta, J.M., 2017. The chaperonin CCT inhibits assembly of α-synuclein amyloid fibrils by a specific, conformation-dependent interaction. Sci Rep 7. doi:10.1038/srep40859

Spassky, N., Han, Y.G., Aguilar, A., Strehl, L., Besse, L., Laclef, C., Romaguera Ros, M., Garcia-Verdugo, J.M., Alvarez-Buylla, A., 2008. Primary cilia are required for cerebellar development and Shh-dependent expansion of progenitor pool. Dev Biol 317, 246–259. doi:10.1016/j.ydbio.2008.02.026

Spiess, C., Meyer, A.S., Reissmann, S., Frydman, J., 2004. Mechanism of the eukaryotic chaperonin: protein folding in the chamber of secrets. Trends Cell Biol 14, 598–604. doi:10.1016/j.tcb.2004.09.015

Srikakulam, R., Winkelmann, D.A., 1999. Myosin II folding is mediated by a molecular chaperonin. J Biol Chem 274, 27265–27273. doi:10.1074/jbc.274.38.27265

Stainier, D.Y.R., Raz, E., Lawson, N.D., Ekker, S.C., Burdine, R.D., Eisen, J.S., Ingham, P.W., Schulte-Merker, S., Yelon, D., Weinstein, B.M., Mullins, M.C., Wilson, S.W., Ramakrishnan, L., Amacher, S.L., Neuhauss, S.C.F., Meng, A., Mochizuki, N., Panula, P., Moens, C.B., 2017. Guidelines for morpholino use in zebrafish. PLoS Genet 13. doi:10.1371/journal.pgen.1007000

Stearns, G., Evangelista, M., Fadool, J.M., Brockerhoff, S.E., 2007. A mutation in the cone-specific pde6 gene causes rapid cone photoreceptor degeneration in zebrafish. J Neurosci 27, 13866–13874. doi:10.1523/JNEUROSCI.3136-07.2007

Sternlicht, H., Farr, G.W., Sternlicht, M.L., Driscoll, J.K., Willison, K., Yaffe, M.B., 1993.

The t-complex polypeptide 1 complex is a chaperonin for tubulin and actin in vivo. Proc Natl Acad Sci U S A 90, 9422–6.

Strata, P., 2015. The Emotional Cerebellum. Cerebellum. doi:10.1007/s12311-015-0649-9

Stujenske, J.M., Dowling, J.E., Emran, F., 2011. The bugeye mutant zebrafish exhibits visual deficits that arise with the onset of an enlarged eye phenotype. Investig Ophthalmol Vis Sci 52, 4200–4207. doi:10.1167/iovs.10-6434

Sumara, I., Quadroni, M., Frei, C., Olma, M.H., Sumara, G., Ricci, R., Peter, M., 2007. A Cul3-Based E3 Ligase Removes Aurora B from Mitotic Chromosomes, Regulating Mitotic Progression and Completion of Cytokinesis in Human Cells. Dev Cell 12, 887–900. doi:10.1016/j.devcel.2007.03.019

Sun, Y., Zhang, B., Luo, L., Shi, D.L., Wang, H., Cui, Z., Huang, H., Cao, Y., Shu, X., Zhang, W., Zhou, J., Li, Y., Du, J., Zhao, Q., Chen, J., Zhong, H., Zhong, T.P., Li, L., Xiong, J.W., Peng, J., Xiao, W., Zhang, J., Yao, J., Yin, Z., Mo, X., Peng, G., Zhu, J., Chen, Y., Zhou, Y., Liu, D., Pan, W., Zhang, Y., Ruan, H., Liu, F., Zhu, Z., Meng, A., 2020. Systematic genome editing of the genes on zebrafish Chromosome 1 by CRISPR/Cas9. Genome Res 30, 118–126. doi:10.1101/gr.248559.119

Sung, J.J., Jeon, J., Lee, J.J., Kim, C.G., 2009. Zebrafish Jak2a plays a crucial role in definitive hematopoiesis and blood vessel formation. Biochem Biophys Res Commun 378, 629–633. doi:10.1016/j.bbrc.2008.11.116

Sunyaev, S.R., 2012. Inferring causality and functional significance of human coding dna variants. Hum Mol Genet 21, R10–R17. doi:10.1093/hmg/dds385

Suzuki, S.C., Bleckert, A., Williams, P.R., Takechi, M., Kawamura, S., Wong, R.O.L., 2013. Cone photoreceptor types in zebrafish are generated by symmetric terminal divisions of dedicated precursors. Proc Natl Acad Sci U S A 110, 15109–15114. doi:10.1073/pnas.1303551110

Svoboda, K.R., Linares, A.E., Ribera, A.B., 2001. Activity regulates programmed cell death of zebrafish Rohon-Beard neurons. Development 128, 3511–3520.

Sweeney, P., Park, H., Baumann, M., Dunlop, J., Frydman, J., Kopito, R., McCampbell, A., Leblanc, G., Venkateswaran, A., Nurmi, A., Hodgson, R., 2017. Protein misfolding in neurodegenerative diseases: implications and strategies. Transl Neurodegener 6, 6. doi:10.1186/s40035-017-0077-5

Sympson, C.J., Singleton, D., Geoghegan, T.E., 1993. Cytochalasin D-induced actin gene expression in murine erythroleukemia cells. Exp Cell Res 205, 225–231. doi:10.1006/excr.1993.1080

Szaflik, J.P., Janik-Papis, K., Synowiec, E., Ksiazek, D., Zaras, M., Wozniak, K., Szaflik, J., Blasiak, J., 2009. DNA damage and repair in age-related macular degeneration. Mutat Res Mol Mech Mutagen 669, 169–176. doi:10.1016/j.mrfmmm.2009.06.008

Sztal, T.E., McKaige, E.A., Williams, C., Ruparelia, A.A., Bryson-Richardson, R.J., 2018. Genetic compensation triggered by actin mutation prevents the muscle damage caused by loss of actin protein. PLOS Genet 14, e1007212. doi:10.1371/journal.pgen.1007212

Sztal, T.E., Ruparelia, A.A., Williams, C., Bryson-Richardson, R.J., 2016. Using touch-evoked response and locomotion assays to assess muscle performance and function in zebrafish. J Vis Exp 2016. doi:10.3791/54431

Takahashi, M., Narushima, M., Oda, Y., 2002. In Vivo Imaging of Functional Inhibitory

Networks on the Mauthner Cell of Larval Zebrafish. J Neurosci 22, 3929–3938. doi:10.1523/jneurosci.22-10-03929.2002

Takeuchi, M., Matsuda, K., Yamaguchi, S., Asakawa, K., Miyasaka, N., Lal, P., Yoshihara, Y., Koga, A., Kawakami, K., Shimizu, T., Hibi, M., 2015. Establishment of Gal4 transgenic zebrafish lines for analysis of development of cerebellar neural circuitry. Dev Biol 397, 1–17. doi:10.1016/j.ydbio.2014.09.030

Takeuchi, M., Yamaguchi, S., Sakakibara, Y., Hayashi, T., Matsuda, K., Hara, Y., Tanegashima, C., Shimizu, T., Kuraku, S., Hibi, M., 2017. Gene expression profiling of granule cells and Purkinje cells in the zebrafish cerebellum. J Comp Neurol 525, 1558–1585. doi:10.1002/cne.24114

Talbot, J.C., Amacher, S.L., 2014. A streamlined CRISPR pipeline to reliably generate zebrafish frameshifting alleles. Zebrafish 11, 583–585. doi:10.1089/zeb.2014.1047

Tam, S., Geller, R., Spiess, C., Frydman, J., 2006. The chaperonin TRiC controls polyglutamine aggregation and toxicity through subunit-specific interactions. Nat Cell Biol 8, 1155–1162. doi:10.1038/ncb1477

Tarailo-Graovac, M., Sinclair, G., Stockler-Ipsiroglu, S., Van Allen, M., Rozmus, J., Shyr, C., Biancheri, R., Oh, T., Sayson, B., Lafek, M., Ross, C.J., Robinson, W.P., Wasserman, W.W., Rossi, A., van Karnebeek, C., 2015. The genotypic and phenotypic spectrum of PIGA deficiency. Orphanet J Rare Dis 10, 23. doi:10.1186/s13023-015-0243-8

Taruscio, D., Groft, S.C., Cederroth, H., Melegh, B., Lasko, P., Kosaki, K., Baynam, G., McCray, A., Gahl, W.A., 2015. Undiagnosed Diseases Network International (UDNI): White paper for global actions to meet patient needs. Mol Genet Metab. doi:10.1016/j.ymgme.2015.11.003

Tian, G., Vainberg, I.E., Tap, W.D., Lewis, S.A., Cowan, N.J., 1995. Specificity in chaperonin-mediated protein folding. Nature. doi:10.1038/375250a0

Tischfield, M.A., Cederquist, G.Y., Gupta, M.L., Engle, E.C., Engle, E.C., 2011. Phenotypic spectrum of the tubulin-related disorders and functional implications of disease-causing mutations. Curr Opin Genet Dev 21, 286–94. doi:10.1016/j.gde.2011.01.003

Tokumoto, M., Horiguchi, R., Nagahama, Y., Ishikawa, K., Tokumoto, T., 2000. Two proteins, a goldfish 20S proteasome subunit and the protein interacting with 26S proteasome, change in the meiotic cell cycle. Eur J Biochem 267, 97–103. doi:10.1046/j.1432-1327.2000.00962.x

Tóth, E., Varga, É., Kulcsár, P.I., Kocsis-Jutka, V., Krausz, S.L., Nyeste, A., Welker, Z., Huszár, K., Ligeti, Z., Tálas, A., Welker, E., 2020. Improved LbCas12a variants with altered PAM specificities further broaden the genome targeting range of Cas12a nucleases. Nucleic Acids Res. doi:10.1093/nar/gkaa110

Tracy, C.M., Kolesnikov, A. V., Blake, D.R., Chen, C.K., Baehr, W., Kefalov, V.J., Willardson, B.M., 2015. Retinal cone photoreceptors require phosducin-like protein 1 for G protein complex assembly and signaling. PLoS One 10. doi:10.1371/journal.pone.0117129

Trinidad, A.G.G.A.G., Muller, P.A.J.P.A.P.A.J., Cuellar, J., Klejnot, M., Nobis, M., Valpuesta, J.M.M.J.M., Vousden, K.H.H.K.H., Abe, Y., Yoon, S.O., Kubota, K., Mendoza, M.C., Gygi, S.P., Blenis, J., Adorno, M., Cordenonsi, M., Montagner, M., Dupont, S., Wong, C., Hann, B., Solari, A., Bobisse, S., Rondina, M.B., Guzzardo, V., al., et, Andrews, P., He, Y.J., Xiong, Y., Bom, A.P.A., Rangel, L.P., Costa, D.C., Oliveira, G.A. de, Sanches, D., Braga, C.A., Gava, L.M., Ramos, C.H., Cepeda, A.O.,

Stumbo, A.C., al., et, Beckerman, R., Prives, C., Blagosklonny, M.V., Toretsky, J., Bohen, S., Neckers, L., Bullock, A.N., Henckel, J., DeDecker, B.S., Johnson, C.M., Nikolova, P.V., Proctor, M.R., Lane, D.P., Fersht, A.R., Bullock, A.N., Henckel, J., Fersht, A.R., Candau, R., Scolnick, D.M., Darpino, P., Ying, C.Y., Halazonetis, T.D., Berger, S.L., Coffill, C.R., Muller, P.A.J.P.A.P.A.J., Oh, H.K., Neo, S.P., Hogue, K.A., Cheok, C.F., Vousden, K.H.H.K.H., Lane, D.P., Blackstock, W.P., Gunaratne, J., Collavin, L., Lunardi, A., Sal, G. Del, Douglas, N.R., Reissmann, S., Zhang, J., Chen, B., Jakana, J., Kumar, R., Chiu, W., Frydman, J., Feldman, D.E., Spiess, C., Howard, D.E., Frydman, J., Freed-Pastor, W.A., Prives, C., Friedlander, P., Legros, Y., Soussi, T., Prives, C., Frydman, J., Nimmesgern, E., Ohtsuka, K., Hartl, F.U., Gannon, J.V., Greaves, R., Iggo, R., Lane, D.P., Gómez-Puertas, P., Martín-Benito, J., Carrascosa, J.L., Willison, K.R., Valpuesta, J.M.M.J.M., Grantham, J., Brackley, K.I., Willison, K.R., Hartl, F.U., Bracher, A., Hayer-Hartl, M.K., Hayer-Hartl, M.K., Ewbank, J.J., Creighton, T.E., Hartl, F.U., Hollstein, M., Hainaut, P., Joerger, A.C., Fersht, A.R., Joly, E.C., Tremblay, E., Tanguay, R.M., Wu, Y., Bibor-Hardy, V., Kitamura, A., Kubota, H., Pack, C.G., Matsumoto, G., Hirayama, S., Takahashi, Y., Kimura, H., Kinjo, M., Morimoto, R.I., Nagata, K., Kussie, P.H., Gorina, S., Marechal, V., Elenbaas, B., Moreau, J., Levine, A.J., Pavletich, N.P., Lee, C.W., Arai, M., Martinez-Yamout, M.A., Dyson, H.J., Wright, P.E., Liu, X., Lin, C.Y., Lei, M., Yan, S., Zhou, T., Erikson, R.L., Liu, B., Larsson, L., Caballero, A., Hao, X., Oling, D., Grantham, J., Nyström, T., Matus, D.Q., Li, X.Y., Durbin, S., Agarwal, D., Chi, Q., Weiss, S.J., Sherwood, D.R., Mayer, M.P., Mayer, S., Rüdiger, S., Ang, H.C., Joerger, A.C., Fersht, A.R., Meek, D.W., Anderson, C.W., Melville, M.W., McClellan, A.J., Meyer, A.S., Darveau, A., Frydman, J., Meyer, A.S., Gillespie, J.R., Walther, D., Millet, I.S., Doniach, S., Frydman, J., Michalovitz, D., Halevy, O., Oren, M., Milner, J., Cook, A., Sheldon, M., Muller, P.A.J.P.A.P.A.J., Caswell, P.T., Doyle, B., Iwanicki, M.P., Tan, E.H., Karim, S.A., Lukashchuk, N., Gillespie, D.A., Ludwig, R.L., Gosselin, P., al., et, Muller, P.A.J.P.A.P.A.J., Vousden, K.H.H.K.H., Norman, J.C., Muller, P.A.J.P.A.P.A.J., Trinidad, A.G.G.A.G., Timpson, P., Morton, J.P., Zanivan, S., Berghe, P.V. van den, Nixon, C., Karim, S.A., Caswell, P.T., Noll, J.E., al., et, Nikolaev, A.Y., Li, M., Puskas, N., Qin, J., Gu, W., Siegers, K., Waldmann, T., Leroux, M.R., Grein, K., Shevchenko, A., Schiebel, E., Hartl, F.U., Tam, S., Geller, R., Spiess, C., Frydman, J., Thulasiraman, V., Yang, C.F., Frydman, J., Valpuesta, J.M.M.J.M., Martín-Benito, J., Gómez-Puertas, P., Carrascosa, J.L., Willison, K.R., Vousden, K.H.H.K.H., Prives, C., Walerych, D., Olszewski, M.B., Gutkowska, M., Helwak, A., Zylicz, M., Zylicz, A., Wilcken, R., Wang, G., Boeckler, F.M., Fersht, A.R., Willison, K.R., Lewis, V., Zuckerman, K.S., Cordell, J., Dean, C., Miller, K., Lyon, M.F., Marsh, M., Xu, J., Reumers, J., Couceiro, J.R., Smet, F. De, Gallardo, R., Rudyak, S., Cornelis, A., Rozenski, J., Zwolinska, A., Marine, J.C., al., et, Yam, A.Y., Xia, Y., Lin, H.T., Burlingame, A., Gerstein, M., Frydman, J., Yébenes, H., Mesa, P., Muñoz, I.G., Montoya, G., Valpuesta, J.M.M.J.M., Zhang, W., Guo, X.Y., Hu, G.Y., Liu, W.B., Shay, J.W., Deisseroth, A.B., 2013. No Title 50. doi:10.1016/j.molcel.2013.05.002

Turnbull, C., Scott, R.H., Thomas, E., Jones, L., Murugaesu, N., Pretty, F.B., Halai, D., Baple, E., Craig, C., Hamblin, A., Henderson, S., Patch, C., O'Neill, A., Devereaux, A., Smith, K., Martin, A.R., Sosinsky, A., McDonagh, E.M., Sultana, R., Mueller, M., Smedley, D., Toms, A., Dinh, L., Fowler, T., Bale, M., Hubbard, T., Rendon, A., Hill, S., Caulfield, M.J., 2018. The 100 000 Genomes Project: Bringing whole genome sequencing to the NHS. BMJ 361, k1687. doi:10.1136/bmj.k1687

Turnpenny, P.D., Whittock, N., Duncan, J., Dunwoodie, S., Kusumi, K., Ellard, S., 2003. Novel mutations in DLL3, a somitogenesis gene encoding a ligand for the Notch signalling pathway, cause a consistent pattern of abnormal vertebral segmentation in spondylocostal dysostosis. J Med Genet 40, 333–339. doi:10.1136/jmg.40.5.333

Ursic, D., Sedbrook, J.C., Himmel, K.L., Culbertson, M.R., 1994. The essential yeast Tcp1

protein affects actin and microtubules. Mol Biol Cell 5, 1065–1080. doi:10.1091/mbc.5.10.1065

Vabulas, R.M., Raychaudhuri, S., Hayer-Hartl, M., Hartl, F.U., 2010. Protein folding in the cytoplasm and the heat shock response. Cold Spring Harb Perspect Biol. doi:10.1101/cshperspect.a004390

Vacaru, A.M., Unlu, G., Spitzner, M., Mione, M., Knapik, E.W., Sadler, K.C., 2014. In vivo cell biology in zebrafish - providing insights into vertebrate development and disease. J Cell Sci 127, 485–495. doi:10.1242/jcs.140194

Vang, S., Corydon, T.J., Børglum, A.D., Scott, M.D., Frydman, J., Mogensen, J., Gregersen, N., Bross, P., 2005. Actin mutations in hypertrophic and dilated cardiomyopathy cause inefficient protein folding and perturbed filament formation. FEBS J 272, 2037–2049. doi:10.1111/j.1742-4658.2005.04630.x

Varga, M., Ralbovszki, D., Balogh, E., Hamar, R., Keszthelyi, M., Tory, K., 2018. Zebrafish Models of Rare Hereditary Pediatric Diseases. Diseases 6, 43. doi:10.3390/diseases6020043

Varshney, G.K., Huang, H., Zhang, S., Lu, J., Gildea, D.E., Yang, Z., Wolfsberg, T.G., Lin, S., Burgess, S.M., 2013. The Zebrafish Insertion Collection (ZInC): A web based, searchable collection of zebrafish mutations generated by DNA insertion. Nucleic Acids Res 41, D861-864. doi:10.1093/nar/gks946

Varshney, G.K., Pei, W., LaFave, M.C., Idol, J., Xu, L., Gallardo, V., Carrington, B., Bishop, K., Jones, M., Li, M., Harper, U., Huang, S.C., Prakash, A., Chen, W., Sood, R., Ledin, J., Burgess, S.M., 2015. High-throughput gene targeting and phenotyping in zebrafish using CRISPR/Cas9. Genome Res 25, 1030–1042. doi:10.1101/gr.186379.114

Vaser, R., Adusumalli, S., Leng, S.N., Sikic, M., Ng, P.C., 2016. SIFT missense predictions for genomes. Nat Protoc 11, 1–9. doi:10.1038/nprot.2015.123

Vaz, R., Hofmeister, W., Lindstrand, A., 2019. Zebrafish models of neurodevelopmental disorders: Limitations and benefits of current tools and techniques. Int J Mol Sci. doi:10.3390/ijms20061296

Veldman, M.B., Lin, S., 2008. Zebrafish as a developmental model organism for pediatric research. Pediatr Res. doi:10.1203/PDR.0b013e318186e609

Wakil, S.M., Alhissi, S., Al Dossari, H., Alqahtani, A., Shibin, S., Melaiki, B.T., Finsterer, J., Al-Hashem, A., Bohlega, S., Alazami, A.M., 2019. Truncating ARL6IP1 variant as the genetic cause of fatal complicated hereditary spastic paraplegia. BMC Med Genet 20. doi:10.1186/s12881-019-0851-6

Wang, H., Liu, J., Cho, K.H., Ren, D., 2009. A novel, single, transmembrane protein CATSPERG is associated with CATSPER1 channel protein. Biol Reprod 81, 539–544. doi:10.1095/biolreprod.109.077107

Wangler, M.F., Yamamoto, S., Chao, H.-T., Posey, J.E., Westerfield, M., Postlethwait, J., Hieter, P., Boycott, K.M., Campeau, P.M., Bellen, H.J., Bellen, H.J., 2017. Model Organisms Facilitate Rare Disease Diagnosis and Therapeutic Research. Genetics 207, 9–27. doi:10.1534/genetics.117.203067

Ward, J.M., La Spada, A.R., 2015. Ataxin-3, DNA Damage Repair, and SCA3 Cerebellar Degeneration: On the Path to Parsimony? PLoS Genet 11, e1004937. doi:10.1371/journal.pgen.1004937

Wasfy, M.M., Matsui, J.I., Miller, J., Dowling, J.E., Perkins, B.D., 2014. Myosin 7aa-/- mutant zebrafish show mild photoreceptor degeneration and reduced

electroretinographic responses. Exp Eye Res 122, 65–76. doi:10.1016/j.exer.2014.03.007

Waters, A.M., Beales, P.L., 2011. Ciliopathies: An expanding disease spectrum. Pediatr Nephrol. doi:10.1007/s00467-010-1731-7

Weber, T., Namikawa, K., Winter, B., Müller-Brown, K., Kühn, R., Wurst, W., Köster, R.W., 2016. Caspase-mediated apoptosis induction in zebrafish cerebellar Purkinje neurons. Dev 143, 4279–4287. doi:10.1242/dev.122721

Willison, K.R., 2018. The substrate specificity of eukaryotic cytosolic chaperonin CCT. Philos Trans R Soc B Biol Sci. doi:10.1098/rstb.2017.0192

Wong, N., Liu, W., Wang, X., 2015. WU-CRISPR: characteristics of functional guide RNAs for the CRISPR/Cas9 system. Genome Biol 16, 218. doi:10.1186/s13059-015-0784-0

Wong, Y.C., Krainc, D., 2016. Lysosomal trafficking defects link Parkinson's disease with Gaucher's disease. Mov Disord 31, 1610–1618. doi:10.1002/mds.26802

Wood, V., Lock, A., Harris, M.A., Rutherford, K., Bähler, J., Oliver, S.G., 2019. Hidden in plain sight: what remains to be discovered in the eukaryotic proteome? Open Biol 9, 180241. doi:10.1098/rsob.180241

Woods, C.G., Cox, J., Springell, K., Hampshire, D.J., Mohamed, M.D., McKibbin, M., Stern, R., Raymond, F.L., Sandford, R., Sharif, S.M., Karbani, G., Ahmed, M., Bond, J., Clayton, D., Inglehearn, C.F., 2006. Quantification of homozygosity in consanguineous individuals with autosomal recessive disease. Am J Hum Genet 78, 889–896. doi:10.1086/503875

Wright, C.F., Fitzgerald, T.W., Jones, W.D., Clayton, S., McRae, J.F., van Kogelenberg, M., King, D.A., Ambridge, K., Barrett, D.M., Bayzetinova, T., Bevan, A.P., Bragin, E., Chatzimichali, E.A., Gribble, S., Jones, P., Krishnappa, N., Mason, L.E., Miller, R., Morley, K.I., Parthiban, V., Prigmore, E., Rajan, D., Sifrim, A., Swaminathan, G.J., Tivey, A.R., Middleton, A., Parker, M., Carter, N.P., Barrett, J.C., Hurles, M.E., FitzPatrick, D.R., Firth, H. V, DDD study, 2015. Genetic diagnosis of developmental disorders in the DDD study: a scalable analysis of genome-wide research data. Lancet (London, England) 385, 1305–14. doi:10.1016/S0140-6736(14)61705-0

Wu, Q., Medina, S.G., Kushawah, G., Devore, M.L., Castellano, L.A., Hand, J.M., Wright, M., Bazzini, A.A., 2019. Translation affects mRNA stability in a codon-dependent manner in human cells. Elife 8. doi:10.7554/eLife.45396

Wullimann, M.F., Rupp, B., Reichert, H., 1996. Neuroanatomy of the zebrafish brain : a topological atlas. Birkhäuser Verlag.

Xie, S., Shen, Bin, Zhang, C., Huang, X., Zhang, Y., Cong, L., Ran, F., Cox, D., Lin, S., Barretto, R., Mali, P., Yang, L., Esvelt, K., Aach, J., Guell, M., Mali, P., Aach, J., Stranges, P., Esvelt, K., Moosburner, M., Cheng, A., Wang, H., Yang, H., Shi, L., Katz, Y., Qi, L., Larson, M., Gilbert, L., Doudna, J., Weissman, J., Larson, M., Gilbert, L., Wang, X., Lim, W., Weissman, J., Barrangou, R., Fremaux, C., Deveau, H., Richards, M., Boyaval, P., Marraffini, L., Sontheimer, E., Niu, Y., Shen, B, Cui, Y., Chen, Y., Wang, J., Matsunaga, T., Yamashita, J., Yang, H., Wang, H., Shivalila, C., Cheng, A., Shi, L., Zhou, J., Shen, B, Zhang, W., Wang, J., Yang, J., Sung, Y., Kim, J., Kim, H., Lee, J., Jeon, J., Fujii, W., Kawasaki, K., Sugiura, K., Naito, K., Ma, Y., Zhang, X., Shen, B, Lu, Y., Chen, W., Auer, T., Duroure, K., Cian, A. De, Concordet, J., Bene, F. Del, Hisano, Y., Ota, S., Kawahara, A., Jao, L., Wente, S., Chen, W., Chang, N., Sun, C., Gao, L., Zhu, D., Xu, X., Ren, X., Sun, J., Housden, B., Hu, Y., Roesel, C., Bassett, A., Liu, J., Dickinson, D., Ward, J., Reiner, D., Goldstein, B., Wu,

Y., Liang, D., Wang, Y., Bai, M., Tang, W., Hsu, P., Scott, D., Weinstein, J., Ran, F., Konermann, S., Pattanayak, V., Lin, S., Guilinger, J., Ma, E., Doudna, J., Fu, Y., Foden, J., Khayter, C., Maeder, M., Reyon, D., Carroll, D., Ran, F., Hsu, P., Lin, C., Gootenberg, J., Konermann, S., Jiang, H., Wong, W., Wang, T., Wei, J., Sabatini, D., Lander, E., Jiang, W., Zhou, H., Bi, H., Fromm, M., Yang, B., Bikard, D., Marraffini, L., Jiang, W., Bikard, D., Cox, D., Zhang, F., Marraffini, L., Ma, M., Ye, A., Zheng, W., Kong, L., Heigwer, F., Kerr, G., Boutros, M., 2014. sgRNAcas9: A Software Package for Designing CRISPR sgRNA and Evaluating Potential Off-Target Cleavage Sites. PLoS One 9, e100448. doi:10.1371/journal.pone.0100448

Xu, H., Xiao, T., Chen, C.H., Li, W., Meyer, C.A., Wu, Q., Wu, D., Cong, L., Zhang, F., Liu, J.S., Brown, M., Liu, X.S., 2015. Sequence determinants of improved CRISPR sgRNA design. Genome Res 25, 1147–1157. doi:10.1101/gr.191452.115

Yam, A.Y., Xia, Y., Lin, H.-T.J., Burlingame, A., Gerstein, M., Frydman, J., 2008. Defining the TRiC/CCT interactome links chaperonin function to stabilization of newly made proteins with complex topologies. Nat Struct Mol Biol 15, 1255–62. doi:10.1038/nsmb.1515

Yin, J., Brocher, J., Linder, B., Hirmer, A., Sundaramurthi, H., Fischer, U., Winkler, C., 2012. The 1D4 antibody labels outer segments of long double cone but not rod photoreceptors in zebrafish. Investig Ophthalmol Vis Sci 53, 4943–4951. doi:10.1167/iovs.12-9511

Yuan, Q., Zhao, M., Tandon, B., Maili, L., Liu, X., Zhang, A., Baugh, E.H., Tran, T., Silva, R.M., Hecht, J.T., Swindell, E.C., Wagner, D.S., Letra, A., 2017. Role of *WNT10A* in failure of tooth development in humans and zebrafish. Mol Genet Genomic Med 5, 730–741. doi:10.1002/mgg3.332

Zambusi, A., Ninkovic, J., 2020. Regeneration of the central nervous system-principles from brain regeneration in adult zebrafish. World J Stem Cells. doi:10.4252/wjsc.v12.i1.8

Zeiher, B.G., Eichwald, E., Zabner, J., Smith, J.J., Puga, A.P., McCray, P.B., Capecchi, M.R., Welsh, M.J., Thomas, K.R., 1995. A mouse model for the delta F508 allele of cystic fibrosis. J Clin Invest 96, 2051–2064. doi:10.1172/JCI118253

Zetsche, B., Gootenberg, J.S., Abudayyeh, O.O., Slaymaker, I.M., Makarova, K.S., Essletzbichler, P., Volz, S.E., Joung, J., Van Der Oost, J., Regev, A., Koonin, E. V., Zhang, F., 2015. Cpf1 Is a Single RNA-Guided Endonuclease of a Class 2 CRISPR-Cas System. Cell 163, 759–771. doi:10.1016/j.cell.2015.09.038

Zhang, F., Kurokawa, K., Lassoued, A., Crowell, J.A., Miller, D.T., 2019. Cone photoreceptor classification in the living human eye from photostimulation-induced phase dynamics. Proc Natl Acad Sci U S A 116, 7951–7956. doi:10.1073/pnas.1816360116

Zhang, J., Wang, C., Shen, Y., Chen, N., Wang, L., Liang, L., Guo, T., Yin, X., Ma, Z., Zhang, B., Yang, L., 2016. A mutation in ADIPOR1 causes nonsyndromic autosomal dominant retinitis pigmentosa. Hum Genet 135, 1375–1387. doi:10.1007/s00439-016-1730-2

Zhang, Y., Ear, J., Yang, Z., Morimoto, K., Zhang, B., Lin, S., 2014. Defects of protein production in erythroid cells revealed in a zebrafish Diamond–Blackfan anemia model for mutation in RPS19. Cell Death Dis 5, e1352. doi:10.1038/cddis.2014.318

Zhang, Y., Huang, H., Zhao, G., Yokoyama, T., Vega, H., Huang, Y., Sood, R., Bishop, K., Maduro, V., Accardi, J., Toro, C., Boerkoel, C.F., Lyons, K., Gahl, W.A., Duan, X., Malicdan, M.C. V., Lin, S., 2017a. ATP6V1H Deficiency Impairs Bone Development

through Activation of MMP9 and MMP13. PLoS Genet 13, e1006481. doi:10.1371/journal.pgen.1006481

Zhang, Y., Qin, W., Lu, X., Xu, J., Huang, H., Bai, H., Li, S., Lin, S., 2017b. Programmable base editing of zebrafish genome using a modified CRISPR-Cas9 system. Nat Commun 8, 118. doi:10.1038/s41467-017-00175-6

Zhang, Y., Zhang, Z., Ge, W., 2018. An efficient platform for generating somatic point mutations with germline transmission in the zebrafish by CRISPR/Cas9-mediated gene editing. J Biol Chem 293, 6611–6622. doi:10.1074/jbc.RA117.001080

Appendices

8.1 Appendix 1: ANOVA summary tables to accompany Figure 5.6, Figure 5.7 and Figure 5.8

Table 8.1 Summary of ANOVA results for effects of lighting and *tcp1*^{P73L} genotype on total swimming distance at 5 dpf (corresponding to data in Figure 5.6bi)

Source of Variation	% of total variation	p value	p value summary	Significant?
Lighting x genotype interaction	0.236	0.2411	ns	No
Lighting main effect	60.55	<0.0001	****	Yes
Genotype main effect	0.007126	0.975	ns	No
Individual fish	20.84	0.0006	***	Yes

Table 8.2 Summary of ANOVA results for effects of lighting and *tcp1*^{P73L} genotype on total active duration at 5 dpf (corresponding to data in Figure 5.6bii)

Source of Variation	% of total variation	p value	p value summary	Significant?
Lighting x genotype interaction	0.1992	0.2263	ns	No
Lighting main effect	65.4	<0.0001	****	Yes
Genotype main effect	0.01493	0.94	ns	No
Individual fish	17.84	0.0002	***	Yes

Table 8.3 Summary of ANOVA results for effects of lighting and *tcp1*^{P73L} genotype on total swimming distance at 8 dpf (corresponding to data in Figure 5.7bi)

Source of Variation	% of total variation	p value	p value summary	Significant?
Lighting x genotype interaction	0.5097	0.0888	ns	No
Lighting main effect	11.23	<0.0001	****	Yes
Genotype main effect	1.104	0.3912	ns	No
Individual fish	73.54	<0.0001	****	Yes

Table 8.4 Summary of ANOVA results for effects of lighting and *tcp1*^{P73L} genotype on total active duration at 8 dpf (corresponding to data in Figure 5.7bii)

Source of Variation	% of total variation	p value	p value summary	Significant?
Lighting x genotype interaction	0.2611	0.2494	ns	No
Lighting main effect	17.96	<0.0001	****	Yes
Genotype main effect	0.4011	0.6904	ns	No
Individual fish	67.99	<0.0001	****	Yes

Table 8.5 Summary of ANOVA results for effects of lighting and *tcp1*^{P73L} genotype on total swimming distance at 12 dpf (corresponding to data in Figure 5.8bi)

Source of Variation	% of total variation	p value	p value summary	Significant?
Lighting x genotype interaction	0.04867	0.8155	ns	No
Lighting main effect	6.146	<0.0001	****	Yes
Genotype main effect	1.665	0.2117	ns	No
Individual fish	74.26	<0.0001	****	Yes

Table 8.6 Summary of ANOVA results for effects of lighting and *tcp1*^{P73L} genotype on total active duration at 12 dpf (corresponding to data in Figure 5.8bii)

Source of Variation	% of total variation	p value	p value summary	Significant?
Lighting x genotype interaction	0.01417	0.9102	ns	No
Lighting main effect	6.626	<0.0001	****	Yes
Genotype main effect	1.671	0.2336	ns	No
Individual fish	79.59	<0.0001	****	Yes

8.2 Appendix 2: ANOVA summary tables to accompany Figure 5.9, Figure 5.10 and Figure 5.11

Table 8.7 Summary of ANOVA results for effects of lighting and *tcp1*^{P73L} genotype on total swimming distance at 5 dpf (corresponding to data in Figure 5.9bi)

Source of Variation	% of total variation	p value	p value summary	Significant?
Lighting x genotype interaction	0.06307	0.489	ns	No
Lighting main effect	70.73	<0.0001	****	Yes
Genotype main effect	0.00728	0.8532	ns	No
Individual fish	17.97	0.0138	*	Yes

Table 8.8 Summary of ANOVA results for effects of lighting and *tcp1*^{P73L} genotype on total active duration at 5 dpf (corresponding to data in Figure 5.9bii)

Source of Variation	% of total variation	p value	p value summary	Significant?
Lighting x genotype interaction	0.1045	0.2998	ns	No
Lighting main effect	77.37	<0.0001	****	Yes
Genotype main effect	0.01378	0.7755	ns	No
Individual fish	14.31	0.0052	**	Yes

Table 8.9 Summary of ANOVA results for effects of lighting and *tcp1*^{P73L} genotype on total swimming distance at 8 dpf (corresponding to data in Figure 5.10bi,iii)

Source of Variation	% of total variation	p value	p value summary	Significant?
Lighting x genotype interaction	0.02039	0.6823	ns	No
Lighting main effect	22.22	<0.0001	****	Yes
Genotype main effect	1.795	0.04	*	Yes
Individual fish	58.87	<0.0001	****	Yes

Table 8.10 Summary of ANOVA results for effects of lighting and *tcp1*^{P73L} genotype on total active duration at 8 dpf (corresponding to data in Figure 5.10bii)

Source of Variation	% of total variation	p value	p value summary	Significant?
Lighting x genotype interaction	0.03137	0.6037	ns	No
Lighting main effect	29.97	<0.0001	****	Yes
Genotype main effect	1.014	0.1015	ns	No
Individual fish	52.63	<0.0001	****	Yes

Table 8.11 Summary of ANOVA results for effects of lighting and *tcp1*^{P73L} genotype on total swimming distance at 12 dpf (corresponding to data in 5.11bi)

Source of Variation	% of total variation	p value	p value summary	Significant?
Lighting x genotype interaction	0.4259	0.0398	*	Yes
Lighting main effect	6.066	<0.0001	****	Yes
Genotype main effect	0.1599	0.5964	ns	No
Individual fish	79.45	<0.0001	****	Yes

Table 8.12 Summary of Sidak's multiple comparisons test results for simple main effects of *tcp1*^{P73L} genotype on total swimming distance in light and dark periods at 12 dpf (corresponding to data in Figure 5.11 bi and Table 8.11)

Comparison	Predicted (LS) mean diff.	95.00% CI of diff.	Significant?	Summary	Adjusted p Value
***tcp1*$^{+/+}$ vs. *tcp1*$^{P73L/P73L}$ (Dark)**	173.9	-129.4 to 477.1	No	ns	0.3574
***tcp1*$^{+/+}$ vs. *tcp1*$^{P73L/P73L}$ (Light)**	-41.76	-345.0 to 261.5	No	ns	0.9410

Table 8.13 Summary of Sidak's multiple comparisons test results for simple main effects of dark and light periods on total swimming distance in wild-type and *tcp1*^{P73L} mutant larvae at 12 dpf (corresponding to data in 5.11bi and Table 8.11)

Comparison	Predicted (LS) mean diff.	95.00% CI of diff.	Significant?	Summary	Adjusted p Value
Dark vs. Light (*tcp1*$^{+/+}$)	514.7	349.7 to 679.6	Yes	****	<0.0001
Dark vs. Light (*tcp1*$^{P73L/P73L}$)	299.1	131.8 to 466.3	Yes	***	0.0002

Table 8.14 Summary of ANOVA results for effects of lighting and *tcp1*^{P73L} genotype on total active duration at 12 dpf (corresponding to data in Figure 5.11bii)

Source of Variation	% of total variation	p value	p value summary	Significant?
Lighting x genotype interaction	0.2865	0.0809	ns	No
Lighting main effect	6.357	<0.0001	****	Yes
Genotype main effect	0.1248	0.6415	ns	No
Individual fish	80.22	<0.0001	****	Yes

8.3 Appendix 3: ANOVA summary tables to accompany Figure 5.12

Table 8.15 Summary of ANOVA results for effects of lighting and *tcp1*^{P73L} genotype on duration of slow swimming at 5 dpf (corresponding to data in Figure 5.12ai)

Source of Variation	% of total variation	p value	p value summary	Significant?
Lighting x genotype interaction	0.1696	0.2374	ns	No
Lighting main effect	67.57	<0.0001	****	Yes
Genotype main effect	0.01881	0.9192	ns	No
Individual fish	16.51	<0.0001	****	Yes

Table 8.16 Summary of ANOVA results for effects of lighting and *tcp1*^{P73L} genotype on duration of fast swimming at 5 dpf (corresponding to data in Figure 5.12bi)

Source of Variation	% of total variation	p value	p value summary	Significant?
Lighting x genotype interaction	0.2661	0.3932	ns	No
Lighting main effect	44.55	<0.0001	****	Yes
Genotype main effect	0.004681	0.9885	ns	No
Individual fish	30.02	0.0148	*	Yes

Table 8.17 Summary of ANOVA results for effects of lighting and *tcp1*^{P73L} genotype on duration of slow swimming at 8 dpf (corresponding to data in Figure 5.12aii)

Source of Variation	% of total variation	p value	p value summary	Significant?
Lighting x genotype interaction	0.1106	0.677	ns	No
Lighting main effect	19.5	<0.0001	****	Yes
Genotype main effect	0.1378	0.8644	ns	No
Individual fish	59.52	<0.0001	****	Yes

Table 8.18 Summary of ANOVA results for effects of lighting and *tcp1*^{P73L} genotype on duration of fast swimming at 8 dpf (corresponding to data in Figure 5.12bii)

Source of Variation	% of total variation	p value	p value summary	Significant?
Lighting x genotype interaction	0.6272	0.0545	ns	No
Lighting main effect	10.49	<0.0001	****	Yes
Genotype main effect	1.165	0.3738	ns	No
Individual fish	74.01	<0.0001	****	Yes

Table 8.19 Summary of ANOVA results for effects of lighting and *tcp1*^{P73L} genotype on duration of slow swimming at 12 dpf (corresponding to data in Figure 5.12ci)

Source of Variation	% of total variation	p value	p value summary	Significant?
Lighting x genotype interaction	0.09931	0.6009	ns	No
Lighting main effect	1.789	<0.0001	****	Yes
Genotype main effect	1.458	0.2936	ns	No
Individual fish	82.55	<0.0001	****	Yes

Table 8.20 Summary of ANOVA results for effects of lighting and *tcp1*^{P73L} genotype on duration of fast swimming at 12 dpf (corresponding to data in Figure 5.12cii)

Source of Variation	% of total variation	p value	p value summary	Significant?
Lighting x genotype interaction	0.0005456	0.9971	ns	No
Lighting main effect	8.871	<0.0001	****	Yes
Genotype main effect	3.392	0.04	*	Yes
Individual fish	72.07	<0.0001	****	Yes

Table 8.21 Summary of Sidak's multiple comparisons test results for main effect of *tcp1*^{P73L} genotype on duration of fast swimming at 12 dpf (corresponding to data in Figure 5.12cii and Table 8.20)

Comparison	Predicted (LS) mean diff.	95.00% CI of diff.	Significant?	Summary	Adjusted p Value
***tcp1*$^{+/+}$ vs. *tcp1*$^{P73L/+}$**	2.583	-10.50 to 15.67	No	ns	0.8818
***tcp1*$^{+/+}$ vs. *tcp1*$^{P73L/P73L}$**	-11.16	-26.49 to 4.168	No	ns	0.1936

8.4 Appendix 4: ANOVA summary tables to accompany Figure 5.13

Table 8.22 Summary of ANOVA results for effects of lighting and *tcp1*^{P73L} genotype on duration of slow swimming at 5 dpf (corresponding to data in Figure 5.13ai)

Source of Variation	% of total variation	p value	p value summary	Significant?
Lighting x genotype interaction	0.1396	0.1745	ns	No
Lighting main effect	80.49	<0.0001	****	Yes
Genotype main effect	0.02054	0.7153	ns	No
Individual fish	13.04	0.0005	***	Yes

Table 8.23 Summary of ANOVA results for effects of lighting and *tcp1*^{P73L} genotype on duration of fast swimming at 5 dpf (corresponding to data in Figure 5.13aii)

Source of Variation	% of total variation	p value	p value summary	Significant?
Lighting x genotype interaction	0.01752	0.7909	ns	No
Lighting main effect	46.62	<0.0001	****	Yes
Genotype main effect	0.0007497	0.9646	ns	No
Individual fish	32.15	0.0263	*	Yes

Table 8.24 Summary of ANOVA results for effects of lighting and *tcp1*^{P73L} genotype on duration of slow swimming at 8 dpf (corresponding to data in Figure 5.13bi)

Source of Variation	% of total variation	p value	p value summary	Significant?
Lighting x genotype interaction	0.09123	0.4586	ns	No
Lighting main effect	27.17	<0.0001	****	Yes
Genotype main effect	0.009805	0.8674	ns	No
Individual fish	49.41	<0.0001	****	Yes

Table 8.25 Summary of ANOVA results for effects of lighting and *tcp1*^{P73L} genotype on duration of fast swimming at 8 dpf (corresponding to data in Figure 5.13bii,iv)

Source of Variation	% of total variation	p value	p value summary	Significant?
Lighting x genotype interaction	0.001727	0.9027	ns	No
Lighting main effect	22.84	<0.0001	****	Yes
Genotype main effect	2.585	0.0136	*	Yes
Individual fish	58.33	<0.0001	****	Yes

Table 8.26 Summary of ANOVA results for effects of lighting and *tcp1*^{P73L} genotype on duration of slow swimming at 12 dpf (corresponding to data in Figure 5.13ci)

Source of Variation	% of total variation	p value	p value summary	Significant?
Lighting x genotype interaction	0.005844	0.8705	ns	No
Lighting main effect	0.08723	0.5291	ns	No
Genotype main effect	0.2011	0.5241	ns	No
Individual fish	69.03	<0.0001	****	Yes

Table 8.27 Summary of ANOVA results for effects of lighting and *tcp1*^{P73L} genotype on duration of fast swimming at 12 dpf (corresponding to data in Figure 5.13cii)

Source of Variation	% of total variation	p value	p value summary	Significant?
Lighting x genotype interaction	0.5264	0.013	*	Yes
Lighting main effect	11.45	<0.0001	****	Yes
Genotype main effect	0.04779	0.7675	ns	No
Individual fish	76.26	<0.0001	****	Yes

Table 8.28 Summary of Sidak's multiple comparisons test results for simple main effects of *tcp1*^{P73L} genotype on fast swimming duration in light and dark periods at 12 dpf (corresponding to data in Figure 5.13cii and Table 8.27)

Comparison	Predicted (LS) mean diff.	95.00% CI of diff.	Significant?	Summary	Adjusted p Value
***tcp1*$^{+/+}$ vs. *tcp1*$^{P73L/P73L}$ (Dark)**	6.752	-5.990 to 19.50	No	ns	0.4140
***tcp1*$^{+/+}$ vs. *tcp1*$^{P73L/P73L}$ (Light)**	-3.625	-16.37 to 9.118	No	ns	0.7724

Table 8.29 Summary of Sidak's multiple comparisons test results for simple main effects of dark and light periods on fast swimming duration in wild-type and *tcp1*^{P73L} mutant larvae at 12 dpf (corresponding to data in Figure 5.13cii and Table 8.27)

Comparison	Predicted (LS) mean diff.	95.00% CI of diff.	Significant?	Summary	Adjusted p Value
Dark – Light (*tcp1*$^{+/+}$)	29.39	22.84 to 35.94	Yes	****	<0.0001
Dark – Light (*tcp1*$^{P73L/P73L}$)	19.01	12.37 to 25.65	Yes	****	<0.0001